KATHOLIEKE UNIVERSITEIT
LEUVEN

Arenberg Doctoral School of Science, Engineering & Technology
K.U.Leuven Kulak
Subfaculty of Science

Simulations as a guidance to support and optimize experimental techniques for ultrasonic non-destructive testing

Steven DELRUE

Dissertation presented in partial
fulfilment of the requirements for
the degree of Doctor
in Science

November 2011

Simulations as a guidance to support and optimize experimental techniques for ultrasonic nondestructive testing

Steven DELRUE

Jury:
Prof. dr. ir. M. Wevers, chair
Prof. dr. K. Van Den Abeele, promotor
Dr. E. Blomme, co-promotor
Prof. dr. ir. H. De Gersem, co-promotor
Prof. dr. ir. L. De Lathauwer
Prof. dr. C. Glorieux
Prof. dr. O. Bou Matar
(Lille)
Prof. dr. M. Scalerandi
(Torino)

Dissertation presented in partial
fulfilment of the requirements for
the degree of Doctor
in Science

November 2011

E. Sabbelaan 53, B-8500 Kortrijk(Belgium)

D/2011/10.705/82
ISBN 978-90-8649-464-4

Preface

While I am writing this preface of my thesis, I realize that four years of research have almost come to an end. Research is not always easy, but I had the luck of benefiting from the help and support of many people, who made it a little bit easier.

First of all, I am very thankful to my promotor, Koen Van Den Abeele. He introduced me to the interesting problems discussed in this thesis. His enthusiasm and his friendship have always been a great support for me. During the past four years, he guided me through this research with his experience, knowledge and ideas. I can only thank him for our collaboration and I will always remember our interesting discussions, his fruitful advices and the time he made for me.

I would also like to thank the team of the NCU lab of KATHO, for providing me with the experimental data needed for this study. It was a pleasure collaborating with them and I learned a lot from the discussions we had.

I am also grateful to my colleagues at the University Campus of the K.U.Leuven at Kortrijk, and specially the signal processing and wave propagation research group, for their support, useful comments and suggestions. All of them have contributed in their own way to a wonderful and warm working atmosphere.

I am also indebted to the members of the jury of this thesis for the time they have spent applying their expert knowledge to the examination of this thesis. Their valuable criticism and useful comments certainly have contributed to the improvement of this text.

I would also like to thank my family and friends for their support, their interest and for always being there when I needed them most. Special thanks go to my parents for their love and constant encouragement during my whole life. They gave me the opportunity to study and instilled into me the personal qualities, values and motivation that have helped me to successfully end this thesis.

The last words of thank are devoted to the dearest persons in my life who have been the source of strength and inspiration for me. First, I would like to thank my wife, Liesbeth, for her emotional support, unconditional love and trust. Without her, I could not have completed this work. She has motivated and encouraged me over and over again. I would also like to thank my daughter, Yune. Although she's just a few months old, she helped me a lot to go through the last few months of this project. Coming home after a day at the office, her beautiful smile made me forget the stress and gave me renewed courage and strength to continue the work.

Thank you all,

Steven

Abstract

In today's rapidly growing industrial world where the requirement of reliability is increasing day by day and where newer and advanced materials are being introduced on a large scale, non-destructive testing (NDT) techniques have a very important role to play. The goal of NDT methodologies and techniques is to detect the presence of damage and inclusions, and to image components or structures to find defect locations, without destroying the material. Among the variety of non-destructive testing and evaluation (NDT&E) techniques, ultrasonic methods (20 kHz - 100 MHz) are perhaps the most frequently used. Stimulated by an intensive research over the last few decades, several important techniques in the field of ultrasonic NDT&E have emerged recently. Nonlinear elastic wave spectroscopy (NEWS) and non-contact ultrasonic (NCU) techniques proclaim to be very promising techniques for the detection of defects and/or discontinuities, while time reversed acoustics (TRA) techniques have become very important for the characterization and localization of material inhomogeneities and defects.

In the present work, fundamental research is conducted to support and optimize NEWS, NCU and TRA techniques. This is realized by constructing and implementing practical models for a realistic description of elastic wave phenomena in materials. Two different finite element models (a spectral solution and a time domain solution) are developed and implemented in the commercially available software package COMSOL Multiphysics. The spectral solution is first used for the simulation of various cases of non-contact inspection of materials and is later adapted for the simulation of particular time reversal experiments in reverberant and non-reverberant media. The time domain solution is used for describing the behaviour of nonlinear defects (delaminations and cracks) in composite materials and metals. Starting from the numerical models, a parameter study and basic experimental verification are performed allowing to get a better understanding in the existing NCU, NEWS and TRA techniques and to explore the potential of and increase confidence in new NDT techniques.

Beknopte samenvatting

In de huidige snel groeiende industriële wereld waar steeds hogere eisen worden gesteld betreffende betrouwbaarheid en duurzaamheid en waar nieuwere en geavanceerde materialen op grote schaal worden ontwikkeld, spelen niet-destructieve test (NDT) technieken een zeer belangrijke rol. NDT methoden en technieken kunnen de aanwezigheid van schade en insluitsels in materialen detecteren en lokaliseren zonder daarbij het onderzochte materiaal te beschadigen. Binnen de verscheidenheid aan niet-destructieve test en evaluatie (NDT&E) technieken nemen de ultrasone technieken (20 kHz - 100 MHz) een vooraanstaande positie in. Gestimuleerd door intensief onderzoek in de voorbije decennia, zijn er binnen het domein van ultrasoon NDT&E een aantal belangrijke technieken ontstaan. Niet-lineaire elastische golf spectroscopie en contactloos ultrasoon onderzoek zijn bijvoorbeeld veelbelovende technieken voor de detectie van defecten en/of discontinuïteiten. Tijdsomkeringstechnieken daarentegen, zijn dan weer zeer belangrijk geworden voor de karakterisatie en lokalisatie van inhomogeniteiten en defecten in materialen.

In dit werk wordt er fundamenteel onderzoek verricht ter ondersteuning en optimalisatie van deze NDT detectie en lokalisatie technieken. We ontwikkelen en implementeren daarvoor adequate modellen die elastische golfvoortplantingsfenomenen in materialen op een realistische manier beschrijven. Twee verschillende eindige elementen modellen (één in het frequentiedomein en één in het tijdsdomein) worden ontwikkeld en geïmplementeerd in het softwarepakket COMSOL Multiphysics. Het spectrale model wordt eerst gebruikt voor de simulatie van contactloze ultrasone experimenten en wordt daarna aangepast voor de simulatie van tijdsomkeringsexperimenten in enerzijds sterk en anderzijds weinig reverbererende materialen. Het tweede model wordt gebruikt voor het beschrijven van het gedrag van niet-lineaire defecten (delaminaties en scheuren) in composieten en metalen. Een uitvoerige parameterstudie, gebaseerd op de numerieke modellen, en een experimentele verificatie van de modellen en methodologieën laten ons toe om de verschillende gekende NDT technieken beter te begrijpen en om meer vertrouwen te krijgen in nieuwe NDT technieken.

List of Symbols

Abbreviations

ACU	Air-Coupled Ultrasound
CAN	Contact Acoustic Nonlinearity
CFRP	Carbon Fiber Reinforced Plastic
CW	Continuous Wave
FEM	Finite Element Method
FNR	Focus-to-Noise Ratio
GFRE	Glass Fiber Reinforced Epoxy
IF	Inverse Filtering
IR	Integrated Response
LED	Light-Emitting Diode
NACE	Nonlinear Air-Coupled Emission
NCU	Non-Contact Ultrasound
NDT&E	Non-Destructive Testing and Evaluation
NEWS	Nonlinear Elastic Wave Spectroscopy
PCB	Printed Circuit Board
PDE	Partial Differential Equation
PML	Perfectly Matching Layer
SSM	Scaling Subtraction Method
TR	Time Reversal
TRA	Time Reversed Acoustics

Arabic symbols

$\mathbf{a}$	acceleration vector
A_n	n^{th} asymmetric Lamb mode
B	bulk modulus, chirp bandwidth
c	wave propagation velocity

d	plate thickness
E	Young's modulus
f	frequency
f_c	chirp central frequency
f_{exc}	excitation frequency
f_s	chirp starting frequency
G	shear modulus
i	imaginary unit
$\mathbf{k}$	wave vector
k_L	longitudinal wave number
k_{Lamb}	Lamb wave number
k_R	Rayleigh wave number
k_T	shear wave number
S_n	n^{th} symmetric Lamb mode
T	pulse duration, period
t_c	central time
t_F	focal time
$\mathbf{u}$	displacement vector
$\mathbf{v}$	velocity vector
v_{air}	wave velocity in air
v_L	longitudinal wave velocity
v_{Lamb}	Lamb wave velocity
v_R	Rayleigh wave velocity
v_T	transversal wave velocity

Greek symbols

ε	strain
γ	absorption coefficient
κ	bulk modulus
λ	wavelength, first Lamé parameter
λ_R	Rayleigh wavelength
μ	second Lamé parameter
ν	Poisson's ratio
ρ	density
σ	standard deviation
$\boldsymbol{\tau}$	stress tensor
θ	angle of incidence
ϕ	displacement potential (scalar field)
$\boldsymbol{\psi}$	displacement potential (vector field)
ω	angular frequency

Contents

List of Figures

List of Tables

Chapter 1

Introduction

1.1 Problem statement

Engineering components and structures in industry are usually subjected to complex service environments, such as for instance exposure to elevated temperature, mechanical loading, physico-chemically hostile media, etc. In due course, extended or repeated external loading causes the formation and growth of defects, corrosion, creep and fatigue damage. In addition, discontinuities and heterogeneities may be present in the raw material stage or might have been introduced during machining, fabrication, heat treatment and assembling. The presence of defects in materials, including for example inclusions, voids, lack of fusion or penetration in welds, cracks and delaminations, can lead to failure when growing to a critical size. Therefore, early detection and characterization of defects is essential to avoid damage and loss of structural integrity of the affected component.

For over sixty years, non-destructive testing (NDT) or non-destructive evaluation (NDE) of materials has been an area of continued growth [8, 14, 17]. The need for developing NDT methodologies and techniques that can detect the presence of damage and inclusions, and image the component or structure to find defect locations has increased dramatically in recent years for various reasons such as product safety, in-line diagnostics, quality control, health monitoring, security testing, etc. There are currently several different non-destructive testing and evaluation (NDT&E) techniques to allow inspection of materials, e.g. radiography, electrical and magnetic methods, thermal methods, optical testing, etc. However, the ultrasonic methods are still the most popular because of their capability, flexibility, and relative cost effectiveness [15, 16, 26].

Ultrasonic techniques are based on transmission and reflection of ultrasonic waves, with frequencies starting from 20 kHz (i.e. beyond the upper limit of human hearing) and propagating through the inside of the material. For decades, these techniques have been excellent tools for NDT, and they still are. However, social (safety) and economical drives (efficiency) in industrial activities constantly push forward the acceptance limits for permanent health monitoring, quality assurance and characterization techniques of industrial products. The requests from industry generally deal with a more sensitive detection of performance degradation (early stages of fatigue cracking for instance), and a more practical realization of ultrasonic techniques (avoiding contact fluids for instance). Driven by these desires, there has been a substantial interest in Nonlinear Elastic Wave Spectroscopy (NEWS) [13, 19, 21, 23, 24] and Non-Contact Ultrasound (NCU) [2, 3, 5–7, 20, 22] research over the last decades.

Conventional ultrasonic NDT techniques are commonly based on reflection, diffraction and scattering of acoustic waves by defects (e.g. inclusions) causing amplitude and/or phase variations of the output signal, but the frequency content of the input and output signals is the same. The efficiency of the interaction depends on the size of the defects and a degradation of linear material properties caused by the damage. However, for incipient damage in the form of microcracks or delaminations, traditional linear ultrasonic techniques may fail to detect such defects due to a lack of acoustic impedance contrast. Nonlinear ultrasound (and especially NEWS techniques), on the other hand, have proven to be extremely sensitive to early damage evaluation in materials. The field of nonlinear acoustics in solids deals with the investigation of the amplitude dependence of material parameters (moduli, velocities, attenuation), which can for instance be evidenced by thorough analysis of modifications in the spectral content. The degree to which these material properties depend on the applied dynamic amplitude can be quantified by various nonlinear parameters. Through the instantaneous detection of the nonlinearity parameters, the internal damage in a material can be measured very efficiently.

Traditional linear and nonlinear ultrasonic NDT generally involves the use of an emitting transducer and a receiving transducer (in some cases one transducer can be used as emitter as well as receiver). The emitter generates an ultrasonic wave which propagates in the test sample. The sound field is influenced by borders, obstacles and defects, and is finally received by the second transducer. To enable optimal transmission of sound waves into the inspection material, and likewise reception at the receiver, a coupling medium (e.g. water, glue or grease) is commonly used between the transducer and the material. Even though this is the most common way of ultrasonic testing, the use of coupling media reduces the range of applications. For example, some materials can be damaged when using liquid couplants. Other materials cannot be tested by immersion since they are too large or because discontinuities in the material can be filled with the couplant. When using glue, the couplant needs to be removed after testing, which can be very difficult or time consuming. For a more practical realization of ultrasonic techniques NCU can be used. In NCU (more and more referred to as ACU, air-coupled ultrasound), the ultrasound is generated and used to test materials without the generating sensor making direct or indirect contact with the test material. The "coupling medium" is simply formed by a layer of air between the transducer and the material to be tested. Once the transmitted ultrasonic wave passes the air-layer and reaches the surface of the test material, part of the wave is reflected while the other part of the wave propagates further in the material. Information about the test specimen is finally obtained from manual or automatic measurements with normal or oblique incidence of the transmitted (direct transmission mode) or reflected waves (single-sided transmission mode), usually by means of a similar NCU transducer working in reception mode.

Apart from the detection of defects using linear and nonlinear, contact and non-contact NDT techniques, there is also a high need for localization schemes for quantitative material and defect characterization. An established localization technique, which has become a hot topic of innovative research in ultrasonic applications in the last 15 years, is time reversal (TR) [10–12, 18]. Time reversed acoustics (TRA) is the process of recording a signal from a remote source with an array of transducers, and then replaying the signal in a time reversed fashion from the same array to focus the sound back in space and time to where it came from, or to scattering targets inside the region which were acting as sources. Doing so, the TR technique enables us to locate strong linear scatterers (inclusions and interfaces with high impedance contrast) or, when combined to NEWS, to focus selectively on weaker nonlinear defects (microcracks, delaminations, etc.).

1.2 Research objectives

The current industrial (r)evolution imposes high demands regarding permanent process control, quality assurance and characterization of industrial products, for instance, in the development of new materials as well as in the production and health monitoring of existing components. As a result, the optimization of new and existing NDT detection and localization techniques with increased practicability and increased sensitivity becomes imperative. One way to improve the performance of a promising technique is to initiate and enhance a support platform for accurate simulations and to couple it to basic experimental verification. Simulations are crucial to increase confidence in new NDT techniques. Both NEWS and NCU for detection of defects and TRA for localization of defects proclaim to be promising tools for NDT applications. Since the applicative use of these techniques till now is still quite limited, they may benefit from intense numerical assistance, thereby solving fundamental problems that may occur.

A number of numerical algorithms and techniques for elastic wave propagation have been developed over the last few decades. This includes for instance finite difference time-domain and finite element models [4, 9, 25]. All of these methods have been thoroughly studied and their stability and accuracy have been analysed for standard configurations and verified for a large number of examples, especially wave scattering problems. Simulations of NEWS for the detection of microdamage are more difficult to obtain, due to the nonlinear material characteristics which have to be modelled. Similarly, for NCU modelling, the problem arises that the acoustic wavelengths in the testing objects and in the surrounding air are at least an order of magnitude different, and thus much smaller than the dimensions of the object itself. As a result, simulations require huge amounts of computer time and an appropriate simulation procedure for such situations has to be realized. Other important aspects are the use of numerical simulation models to infer material properties from available experimental data (e.g. through inverse least-square modelling), to support precise localization of inclusions and defects, and to optimize experimental setup and operational parameters in function of the required accuracy and resolution.

In the last few years, the improvement of commercial ultrasonic wave simulation packages towards higher applicability, reliability and efficiency is remarkable. The majority of elastic wave simulation tasks can be carried out by commercially available software tools for the simulation of ultrasonic wave propagation. One of these software packages based on the finite element method is Comsol Multiphysics [1], a program that can be used for simulating multi-physics and single-physics applications in 1D, 2D or 3D, but has no cut-and-dried solution for the implementation of typical NCU, NEWS and TRA experiments. However, thanks to its large number of predefined modelling interfaces (physics modes containing the underlying equations and PDE modes to specify your own equations) and due to its flexibility for the implementation of arbitrary geometrical problems, we chose to use this tool for modelling and simulating NCU, TRA and NEWS problems.

The main goal of this thesis is to develop appropriate simulation techniques in order to support the qualitative process of gathering observable facts concerning wave propagation in heterogeneous and/or nonlinear materials in view of NCU and NEWS experiments, to assist in the design and testing of localization using TRA and to provide quantitative comparison for experimental results. In short, we will develop an efficient implementation of various cases of air-coupled inspection of materials and particular TR experiments in reverberant and non-reverberant samples using COMSOL PDE modes and an implementation of composite materials and metals containing nonlinear defects (respectively delaminations and cracks) using COMSOL physics modes. Then, starting from the numerical model, concrete simulations and basic experimental verification are performed to get a better understanding of existing NDT techniques, to increase confidence in new NDT techniques and to focus on the optimization (increased practicability and sensitivity) of NCU, TRA and NEWS techniques.

1.3 Outline of the thesis

In the second chapter of this thesis, a mathematical description of surface waves, guided waves and standing waves in solid materials is developed. First, we recall the wave equation for waves propagating in an unbounded, homogeneous, isotropic and linear elastic medium. By specifying particular boundary conditions for a semi-infinite half-space, for a plate configuration and for a bounded medium, expressions for guided waves and standing waves can be deduced. Using the obtained expressions, special characteristics of these types of waves are studied.

As we intend to numerically simulate several ultrasonic NDT techniques using the commercially available finite element based software package COMSOL Multiphysics, a short introduction to the software and the underlying finite element method is given in the third chapter. In the first part of the chapter, the basic concepts of the method are given, without going into detail on the theory. In the second part of the chapter, a short description of the COMSOL Multiphysics software is given and the different predefined modelling interfaces (physics modes and PDE modes) used in the simulations are briefly discussed.

In chapter 4, we focus on NCU techniques for the non-destructive testing of materials. In the first part of the chapter, a typical NCU test configuration (the air-coupled ultrasonic single-sided pitch-catch technique) is discussed and an experiment using this technique on an aluminium bar with a borehole is described. This experiment is then simulated using two distinctive simulation methods, a ray tracing (shadow) method and a spectral solution implemented within COMSOL Multiphysics. Both methods are thoroughly described in the chapter. In the second part of the chapter, observations and simulations obtained from the single-sided air-coupled pitch-catch experiment are compared, showing a good qualitative agreement between both. In the last part of the chapter, the developed finite element method is used for simulations of more complex problems. In particular, the ultrasonic testing of an aluminium plate with varying cross-section and a LED-rail profile are discussed. Based on the simulation results, air-coupled techniques for the testing of both samples are proposed.

In chapter 5, the developed finite element model in Comsol Multiphysics is adapted for the simulation of TRA experiments. In the first part of the chapter, time reversal in a reverberant medium is described. Due to the high number of reflections in such a medium, a time reversal technique using only one channel can be used. It is illustrated how this technique can be used to focus high levels of acoustic energy at one or multiple points in the medium and to focus selectively or collectively along each of the spatial directions. In the second part of the chapter, the concept of a chaotic cavity transducer (a transducer glued on a cavity of chaotic shape) is introduced to focus energy in a non-reverberant sample. Performing finite element simulations, the feasibility and capability of the chaotic cavity transducer is tested and the use of a chaotic cavity transducer as a virtual array of transducers to focus energy in any point in a medium is illustrated.

The sixth chapter concerns nonlinear ultrasonic spectroscopy of delaminations and surface breaking cracks, which are often referred to as contact acoustic nonlinearities (CANs). In the first part of the chapter, the basics of CANs are discussed. Then, a three-dimensional finite element model of a composite material containing a closed delamination is developed within Comsol Multiphysics. In contrast to the spectral models used in the previous two chapters, the finite element simulation for CANs is based on a pure time domain model. In addition, the model makes use of local node splitting and the nonlinear constitutive behaviour of the defect is implemented by means of spring-damper elements at the defects interface. In the next part of the chapter, an intensive parametric study is performed in order to gain a better understanding of the behaviour of a dynamically excited delamination. Different techniques for the detection and localization of delaminations are discussed. In the last part of the chapter, we adapted the developed model to the study of surface breaking cracks.

Finally, in the conclusions of this thesis, the major achievements of this work are summarized and several directions for future research are discussed.

Bibliography

[1] *COMSOL Multiphysics User's Guide, Version 3.3*, 2006.

[2] Blomme, E., Bulcaen, D., and Declercq, F. Air-coupled ultrasonic NDE: experiments in the frequency range 750 kHz - 2 MHz. *NDT&E Int. 35* (2002), 417–426.

[3] Blomme, E., Bulcaen, D., and Declercq, F. Recent observations with air-coupled NDE in the frequency range of 650 kHz to 1.2 MHz. *Ultrasonics 40* (2002), 153–157.

[4] Bou Matar, O., Galopin, E., Li, Y., and Ducloux, O. An optimized convolution-perfectly matched layer (C-PML) absorbing boundary condition for the second-order elastic wave equation - Application to surface and Lamb waves propagation. In *Proceedings of the COMSOL users Conference* (Grenoble, October 2007).

[5] Castaings, M., and Cawley, P. The generation, propagation, and detection of Lamb waves in plates using air-coupled ultrasonic transducers. *J. Acoust. Soc. Am. 100* (1996), 3070–3077.

[6] Castaings, M., Cawley, P., Farlow, R., and Hayward, G. Single sided inspection of composite materials using air coupled ultrasound. *J. Nondestruct. Eval. 17* (1998), 37–45.

[7] Castaings, M., and Hosten, B. Air-coupled measurement of plane wave, ultrasonic plate transmission for characterising anisotropic, viscoelastic materials. *Ultrasonics 38* (2000), 781–786.

[8] Chen, C., Ed. *Ultrasonic and advanced methods for nondestructive testing and material characterization.* World Scientific, 2007.

[9] Fellinger, P., Marklein, R., Langenberg, K., and Klaholz, S. Numerical modeling of elastic wave propagation and scattering with EFIT - elastodynamic finite integration technique. *Wave Motion 21* (1995), 47–66.

[10] Fink, M. Time reversed acoustics. *Phys. Today 50* (1997), 34–40.

[11] Fink, M. Time-reversed acoustics. *Sci. Am. 281* (1999), 91–97.

[12] Fink, M., Cassereau, D., Derode, A., Prada, C., Roux, P., Tanter, M., Thomas, J., and Wu, F. Time-reversed acoustics. *Rep. Prog. Phys. 63* (2000), 1933–1995.

[13] Guyer, R., and Johnson, P. *Nonlinear Mesoscopic Elasticity : The Complex Behaviour of Granular Media Including Rocks and Soil.* Wiley-VCH, 2009.

[14] Hellier, C. *Handbook of nondestructive evaluation.* McGRAW-HILL, 2003.

[15] Krautkramer, J., and Krautkramer, H. *Ultrasonic testing of materials.* Springer, 1990.

[16] Kundu, T., Ed. *Ultrasonic nondestructive evaluation: Engineering and biological material characterization.* CRC Press, 2004.

[17] Mix, P. *Introduction to nondestructive testing.* John Wiley & Sons, 2005.

[18] Roux, P., and Fink, M. Time reversal in a waveguide: Study of the temporal and spatial focusing. *J. Acoust. Soc. Am. 107* (2000), 2418–2429.

[19] Solodov, I. Ultrasonics of non-linear contacts: propagation, reflection and NDE-applications. *Ultrasonics 36* (1998), 383–390.

[20] Solodov, I., Döring, D., and Busse, G. Mapping of elastic anisotropy with air-coupled phonon-focusing of guided and surface waves. In *Proceedings of the European Conference on Non-Destructive Testing* (Berlin, September 2006).

[21] Solodov, I., Krohn, N., and Busse, G. CAN: an example of nonclassical acoustic nonlinearity in solids. *Ultrasonics 40* (2002), 621–625.

[22] Solodov, I., Stoessel, R., and Busse, G. Material characterization and NDE using focused slanted transmission mode of air-coupled ultrasound. *Res. Nondestruct. Eval. 15* (2004), 65–85.

[23] Van Den Abeele, K., Carmeliet, J., Ten Cate, J., and Johnson, P. Nonlinear elastic wave spectroscopy (NEWS) techniques to discern material damage, Part II: Single-mode nonlinear resonance acoustic spectroscopy. *Res. Nondestruct. Eval. 12* (2000), 31–42.

[24] Van Den Abeele, K., Johnson, P., and Sutin, A. Nonlinear elastic wave spectroscopy (NEWS) techniques to discern material damage, Part I: Nonlinear wave modulation spectroscopy (NWMS). *Res. Nondestruct. Eval. 12* (2000), 17–30.

[25] Van Den Abeele, K., and Vanaverbeke, S. *Universality of nonclassical nonlinearity: Multiscale approach and simulations of wave propagation and resonance in media with localized microdamage: 1-D and 2-D cases.* Springer, 2006, ch. 12, pp. 177–201.

[26] Victorov, I. *Rayleigh and Lamb Waves.* Plenum Press New York, 1967.

Chapter 2

Wave propagation and boundary interaction

In general, the use of ultrasonic waves is well established in the NDT industry. Bulk wave are most commonly used, because they offer the advantage of being easy to understand and easy to use. As the terminology suggests, bulk waves can only propagate in the bulk of an object, far from any boundaries, where the longitudinal and shear waves are uncoupled. At surfaces of the object and at interfaces between different materials, the bulk waves interact with these boundaries and create new waves by means of reflection and refraction. In addition, mode conversion between longitudinal and shear waves may occur at the interface. In particular situations, such boundary interactions eventually lead to the development of elastodynamic guided waves. Guided waves either travel at the boundaries (Rayleigh waves) or between the boundaries (Lamb waves). It should be noted that bulk and guided waves behave differently but are actually governed by the same set of partial differential wave equations. The difference in the mathematical description of the two types of waves is entirely due to the boundary conditions. In the case of bulk waves, there is no need for boundary conditions, whereas guided waves do not develop in the absence of boundaries. Apart from bulk and guided waves, one also distinguishes standing waves. Standing waves occur when a wave is propagating through a medium bounded in all directions. Waves reflected from the boundaries will interact with waves incident towards the boundaries, creating a typical wave pattern in the medium. At specific frequencies, the created pattern has a very regular shape, which is called a standing wave pattern.

In the first part of this chapter the basic concepts of ultrasonic guided waves propagating in a solid material are introduced. Since the basic principles of guided waves are well known and several textbooks have discussed the topic [2, 4], only the main characteristics are reviewed in this chapter. First, we recall the wave equation for bulk waves propagating in an unbounded, homogeneous, isotropic, linear elastic medium. Then, the resulting system of differential equations is solved for a semi-infinite half-space and a plate configuration, leading to guided Rayleigh and Lamb waves. Using the obtained expressions, special characteristics of both types of waves can be studied. In the last part of this chapter, we focus on the description of standing waves in a three-dimensional rectangular domain.

2.1 Propagation in unbounded media

The general description of guided waves starts with the definition of strain and stress and with Hooke's law, which describes the relation between stress and strain, and leads to the derivation of the wave equation of motion. The mathematical solutions of the wave equation determine the types of waves that can propagate in a solid medium.

2.1.1 Strain

Let $\mathbf{u}(\mathbf{x}, t)$ be the three-dimensional displacement vector of a point P in a solid body in which a wave propagates with constant amplitude. The point P is localized by the position vector $\mathbf{x} = (x, y, z)$ and t denotes the time. Direct strains in the medium in the vicinity of P are represented by $\varepsilon_{xx}, \varepsilon_{yy}$ and ε_{zz} and the shear components of strain by ε_{xy}, ε_{yz} and ε_{xz}. The strain tensor $\boldsymbol{\varepsilon}$, containing the relative deformations in each physical direction, is then defined as:

$$\varepsilon_{ij} = \frac{1}{2}\left(\frac{\partial u_i}{\partial j} + \frac{\partial u_j}{\partial i}\right) \quad \text{with} \quad i, j \in \{x, y, z\} \tag{2.1}$$

The strain tensor is symmetric and the above equation is only valid in the case of small deformations.

2.1.2 Stress

The stress is a force over a unit area. To describe the forces on an elemental area of a body, nine stress components τ_{ij} are used. As the strain tensor, the stress tensor is also symmetric. This implies that only six of the nine components of both tensors are needed to fully describe the stress and strain of a body.

2.1.3 Stress-strain relations

The general form of Hooke's law states that the six components of both the stress tensor and the strain tensor can be linked to each other by using 36 components of the elasticity tensor $\mathbf{c}$. Hooke's law is then given by the following relation:

$$\tau_{ij} = \sum_{k,l} c_{ijkl}\varepsilon_{kl} \quad \text{with} \quad i,j,k,l \in \{x,y,z\} \tag{2.2}$$

In the simplest case, a solid medium can be assumed to be isotropic, and the number of independent elastic constants is reduced to 2, the Lamé constants λ and μ, which are determined by the properties of the solid. Therefore, Hooke's law for an isotropic solid is:

$$\tau_{ij} = \lambda(\varepsilon_{xx} + \varepsilon_{yy} + \varepsilon_{zz})\delta_{ij} + 2\mu\varepsilon_{ij} \quad \text{with} \quad i,j \in \{x,y,z\} \tag{2.3}$$

with δ_{ij} the Kronecker delta. Lamé's constants λ and μ completely define the elastic stress-strain behaviour of the material. In some applications, Lamé's constants are replaced by four related elastic constants:

$$E = \frac{\mu(3\lambda + 2\mu)}{\lambda + \mu}, \quad \nu = \frac{\lambda}{2(\lambda + \mu)}, \quad B = \lambda + \frac{2\mu}{3}, \quad G = \mu \tag{2.4}$$

$$\lambda = \frac{\nu E}{(1+\nu)(1-2\nu)}, \quad \mu = \frac{E}{2(1+\nu)} \tag{2.5}$$

where E is Young's modulus, ν is Poisson's ratio, B is the bulk modulus and G is the shear modulus.

Later on in this thesis we will also consider more complex symmetries (e.g. orthotropic composites) for which a higher number of elastic constants is required.

2.1.4 The equation of motion

Applying Newton's second law, the temporal evolution of the displacement field $\mathbf{u}$ can be investigated. When the material has a uniform density ρ and the body forces are neglected, the equation of motion can be written as follows:

$$\rho \frac{\partial^2 u_i}{\partial t^2} = \frac{\partial \tau_{ix}}{\partial x} + \frac{\partial \tau_{iy}}{\partial y} + \frac{\partial \tau_{iz}}{\partial z} \quad \text{with} \quad i \in \{x, y, z\} \tag{2.6}$$

This equation, which describes the motion in a solid, is obtained by considering stress variations across an element. Substitution of equations (2.1) and (2.3) yields:

$$\rho \frac{\partial^2 u_i}{\partial t^2} = \mu \sum_j \frac{\partial^2 u_i}{\partial j^2} + (\lambda + \mu) \sum_j \frac{\partial^2 u_j}{\partial i \partial j} \quad \text{with} \quad i, j \in \{x, y, z\} \tag{2.7}$$

or in vector notation:

$$\rho \ddot{\mathbf{u}} = \mu \nabla^2 \mathbf{u} + (\lambda + \mu) \nabla (\nabla \cdot \mathbf{u}) \tag{2.8}$$

These equations of motion must be satisfied by all elastic waves propagating in the material and will be referred to as the wave equations. Since the wave equations are linear, the superposition of two or more valid solutions will still provide a valid solution.

The wave equation (2.8) cannot be integrated directly. Also, the three displacement components are coupled, which makes it difficult to interpret or solve. One way of manipulating the wave equation is to use a Helmholtz decomposition [2] to split the displacement field $\mathbf{u}$ into a rotational component $\nabla \times \boldsymbol{\psi}$ and an irrotational component $\nabla \phi$:

$$\mathbf{u} = \nabla \phi + \nabla \times \boldsymbol{\psi} \tag{2.9}$$

where $\boldsymbol{\psi}$ has zero divergence:

$$\nabla \cdot \boldsymbol{\psi} = 0 \tag{2.10}$$

Substitution of these potential functions into the wave equation (2.8), means that the equation of motion can be separated into two independent wave equations:

$$\nabla^2 \phi = \frac{1}{v_L^2} \ddot{\phi} \tag{2.11}$$

and

$$\nabla^2 \boldsymbol{\psi} = \frac{1}{v_T^2} \ddot{\boldsymbol{\psi}} \tag{2.12}$$

Equation (2.11), containing the scalar potential which governs the irrotational part of the displacement, describes longitudinal waves in solids, while equation (2.12), containing the vector potential and thus related to the divergence free part of $\mathbf{u}$, refers to the shear motion of the waves. v_L and v_T are the velocities of longitudinal and shear waves in the infinite isotropic medium and can be expressed as follows:

$$v_L = \sqrt{\frac{\lambda + 2\mu}{\rho}} \quad \text{and} \quad v_T = \sqrt{\frac{\mu}{\rho}} \tag{2.13}$$

This reveals that there are only two types of bulk waves which can propagate in an unbounded isotropic medium. Equations (2.11) and (2.12) are independent of each other, meaning that longitudinal and shear waves can propagate without interaction in unbounded media.

2.2 Guided waves

The wave equations (2.11) and (2.12), for bulk waves, can now be used to describe the propagation of a plane harmonic wave in a semi-infinite medium (half-space) or in plates with parallel surfaces. In order to simplify the calculations, the coordinate system is chosen so that the waves are independent of the y-direction and thus, displacements and stresses are along the x- or z-axis. Consequently, the vector potential $\boldsymbol{\psi}$ will only have a non-zero component along the y-axis, which we will further denote by ψ. Wave equations (2.11) and (2.12) can now be written as:

$$\frac{\partial^2 \phi}{\partial x^2} + \frac{\partial^2 \phi}{\partial z^2} = \frac{1}{v_L^2}\frac{\partial^2 \phi}{\partial t^2} \tag{2.14}$$

$$\frac{\partial^2 \psi}{\partial x^2} + \frac{\partial^2 \psi}{\partial z^2} = \frac{1}{v_T^2}\frac{\partial^2 \psi}{\partial t^2} \tag{2.15}$$

Furthermore, if we assume the interface of the half-space and the surfaces of the plates to be perpendicular to the (x, y)-plane (i.e. in a plane described by $z = z_0$), and we consider the propagation of plane harmonic waves in the positive x-direction, we can propose the general solution to expressions (2.14) and (2.15) in the form of:

$$\phi = \Phi(z)e^{i(kx-\omega t)} \tag{2.16}$$

$$\psi = \Psi(z)e^{i(kx-\omega t)} \tag{2.17}$$

where x is the spatial coordinate of the wave, t is the time variable, k is the wave number and ω is the angular frequency. Substitution of these solutions into wave equations (2.14) and (2.15), yields two differential equations for both $\Phi(z)$ and $\Psi(z)$:

$$\frac{d^2\Phi(z)}{dz^2} - (k^2 - k_L^2)\Phi(z) = 0 \tag{2.18}$$

$$\frac{d^2\Psi(z)}{dz^2} - (k^2 - k_T^2)\Psi(z) = 0 \tag{2.19}$$

with

$$k_L^2 = \frac{\omega^2}{v_L^2} \tag{2.20}$$

the longitudinal wave number and

$$k_T^2 = \frac{\omega^2}{v_T^2} \tag{2.21}$$

the shear wave number.

When the potentials ϕ and ψ are known, the corresponding displacement fields can be calculated by using equation (2.9). In two dimensions, we get:

$$u_x = \frac{\partial\phi}{\partial x} - \frac{\partial\psi}{\partial z} \tag{2.22}$$

$$u_z = \frac{\partial\phi}{\partial z} + \frac{\partial\psi}{\partial x} \tag{2.23}$$

Similarly, by using Hooke's law (2.3), the stress components can be calculated. In two dimensions, we get three independent components:

$$\tau_{xx} = \lambda\left(\frac{\partial^2\phi}{\partial x^2} + \frac{\partial^2\phi}{\partial z^2}\right) + 2\mu\left(\frac{\partial^2\phi}{\partial x^2} - \frac{\partial^2\psi}{\partial x\partial z}\right) \tag{2.24}$$

$$\tau_{zz} = \lambda\left(\frac{\partial^2\phi}{\partial x^2} + \frac{\partial^2\phi}{\partial z^2}\right) + 2\mu\left(\frac{\partial^2\phi}{\partial z^2} + \frac{\partial^2\psi}{\partial x\partial z}\right) \tag{2.25}$$

$$\tau_{xz} = \mu\left(2\frac{\partial^2\phi}{\partial x\partial z} + \frac{\partial^2\psi}{\partial x^2} - \frac{\partial^2\psi}{\partial z^2}\right) \tag{2.26}$$

We will now study two different configurations: the semi-infinite half-space and the (parallel) plate configuration. In both configurations the potentials ϕ and ψ can be determined by using the boundary conditions associated with each configuration.

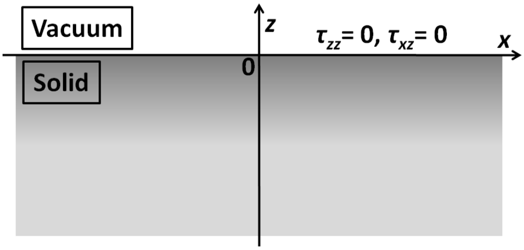

Figure 2.1: Semi-infinite half-space: a solid material is located at $z < 0$, for $z > 0$ vacuum is assumed.

2.2.1 Propagation in a semi-infinite half-space

The first configuration under study is the semi-infinite half-space, as depicted in figure 2.1. A homogeneous, isotropic, linear elastic solid material is located at $z < 0$. For $z > 0$ vacuum is assumed. We will now search for suitable solutions for the potentials ϕ and ψ by solving the differential equations (2.18) and (2.19). We do this by proposing the following solutions for $\Phi(z)$ and $\Psi(z)$:

$$\Phi(z) = Ae^{pz} + A'e^{-pz} \tag{2.27}$$

$$\Psi(z) = Be^{qz} + B'e^{-qz} \tag{2.28}$$

with $p^2 = k^2 - k_L^2$ and $q^2 = k^2 - k_T^2$. Both, p^2 and q^2 are positive (we will later show that $k^2 > k_T^2 > k_L^2$). The integration constants A, A', B and B' need to be determined by the boundary conditions.

Since the potentials need to be bounded for $z \to -\infty$, the integration constants A' and B' should be set to zero. The potentials ϕ and ψ defined in equations (2.16) and (2.17) thus become:

$$\phi = Ae^{pz}e^{i(kx-\omega t)} \tag{2.29}$$

$$\psi = Be^{qz}e^{i(kx-\omega t)} \tag{2.30}$$

The two remaining constants can be determined by implementing appropriate boundary conditions at the boundary. The solid has a free surface at $z = 0$, meaning that the normal and tangential stress components should be equal to zero at $z = 0$, thus:

$$\tau_{zz}\big|_{z=0} = 0 \tag{2.31}$$

$$\tau_{xz}\big|_{z=0} = 0 \tag{2.32}$$

After introducing equations (2.29) and (2.30) in equations (2.25) and (2.26) for the stress components τ_{zz} and τ_{xz}, the above boundary conditions give rise to the following system of equations:

$$\begin{bmatrix} (\lambda + 2\mu)p^2 - \lambda k^2 & 2i\mu kq \\ 2ikp & -(q^2 + k^2) \end{bmatrix} \cdot \begin{bmatrix} A \\ B \end{bmatrix} = 0 \tag{2.33}$$

This system of equations has a non-zero solution if the determinant of its coefficient matrix (known as the Rayleigh determinant) is zero. This yields an equation for the wave number k:

$$4k^2pq - (k^2 + q^2)^2 = 0 \tag{2.34}$$

Solving this equation gives the wave number k_R and the velocity $v_R = \omega/k_R$ for a wave that can propagate along the surface of the semi-infinite medium. This wave is known as the Rayleigh wave (in the following, subscript R is always associated with the Rayleigh wave). The equation has no analytical solution and thus has to be solved numerically. Victorov [4] showed that k_R can be approximated by the following expression:

$$k_R = \frac{1 + \nu}{0.87 + 1.12\nu} k_T \tag{2.35}$$

The theoretical value of Poisson's ratio ν for an isotropic material is between -1.0 and 0.5, but most isotropic materials have Poisson's ratio values ranging between 0 and 0.5 [3]. Consequently, the wave number of the Rayleigh wave will be larger than the wave numbers of the transversal and longitudinal wave and thus, the assumption that p^2 and q^2 are positive values was justified..

By substitution of equations (2.29) and (2.30) in equations (2.22) and (2.23), the entire displacement field can be calculated. Using one of the relations in (2.33) and keeping only the real parts, we get the following displacement components:

$$u_x = -Ak_R \left(e^{p_R z} - \frac{2p_R q_R}{q_R^2 + k_R^2} e^{q_R z} \right) \sin(k_R x - \omega t) \tag{2.36}$$

$$u_z = Ap_R \left(e^{p_R z} - \frac{2k_R^2}{q_R^2 + k_R^2} e^{q_R z} \right) \cos(k_R x - \omega t) \tag{2.37}$$

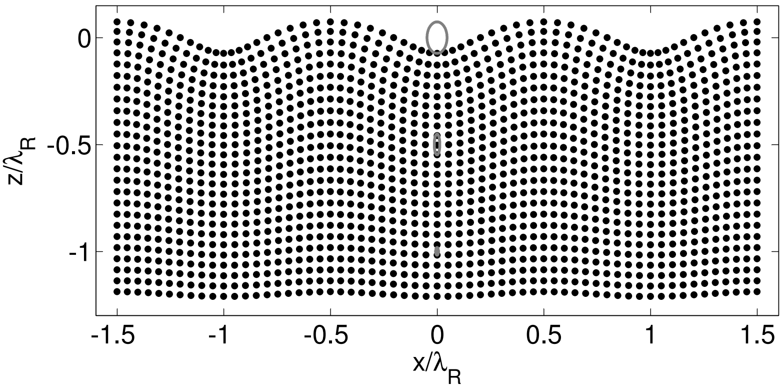

Figure 2.2: Snapshot of the displacement field of a 500 kHz Rayleigh wave at the boundary of an aluminium half-space. The ellipses shown, are the paths followed by three different points within the aluminium sample.

A typical displacement field at the boundary of an aluminium half-space ($\rho = 2700$ kg/m^3, $v_L = 6320$ m/s and $v_T = 3130$ m/s) is shown in figure 2.2. The figure shows a snapshot of the displacement field of a 500 kHz Rayleigh wave. The displacement components u_x and u_z are calculated and each point is shifted proportionally to this amount in its respective direction. In order to have a clear representation of the displacement field, the displacement amplitude was made much higher than its actual value. It is clear that the Rayleigh wave is located at the boundary of the sample and the displacement amplitudes decrease exponentially with increasing distance from the surface. This behaviour can also be observed in figure 2.3, where the displacement amplitudes are plotted as a function of depth. The displacement amplitudes are normalized with respect to the normal displacement amplitude u_z at the boundary of the sample.

If we have a closer look to the equations (2.36) and (2.37), we see that the particles in a solid, through which a Rayleigh wave passes, move in elliptical paths. In figure 2.3 we see that the normal displacement component u_z is systematically larger than the displacement component u_x parallel to the surface, meaning that the major axis of the ellipse is perpendicular to the surface of the solid. Typical paths followed by three different points are shown in figure 2.2. The eccentricity of the ellipses depends on the distance to the surface. In a Rayleigh wave, particles at the surface trace out a counter-clockwise ellipse, while particles at a depth of more than 1/5th of a wavelength trace out clockwise ellipses. This is due to the change of sign of the displacement component u_x at

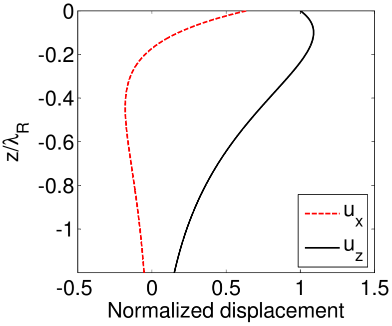

Figure 2.3: Displacement amplitudes as a function of depth for a 500 kHz Rayleigh wave at the boundary of an aluminium half-space. The displacement amplitudes are normalized with respect to the normal displacement amplitude u_z at the boundary of the sample.

$z = -0.2\lambda_R$. At depths larger than one wavelength the motion of the particles becomes extremely small. Since the wavelength is inversely proportional to the frequency the penetration depth of surface waves is thus frequency dependent.

2.2.2 Propagation in a plate

The second configuration under study is the plate configuration, as depicted in figure 2.4. A homogeneous, isotropic, linear elastic solid material is located at $-d/2 < z < d/2$. For $z < -d/2$ and $z > d/2$ vacuum is assumed. As with Rayleigh waves, we will search for suitable solutions for the potentials ϕ and ψ. The following solutions $\Phi(z)$ and $\Psi(z)$ of differential equations (2.18) and (2.19) are proposed:

$$\Phi(z) = A\cosh(pz) + A'\sinh(pz) \tag{2.38}$$

$$\Psi(z) = B\cosh(qz) + B'\sinh(qz) \tag{2.39}$$

with p and q defined as in (2.27) and (2.28) and integration constants A, A', B and B'. The potentials ϕ and ψ defined in equations (2.16) and (2.17) become:

$$\phi = (A\cosh(pz) + A'\sinh(pz))\, e^{i(kx-\omega t)} \tag{2.40}$$

$$\psi = (B\cosh(qz) + B'\sinh(qz))\, e^{i(kx-\omega t)} \tag{2.41}$$

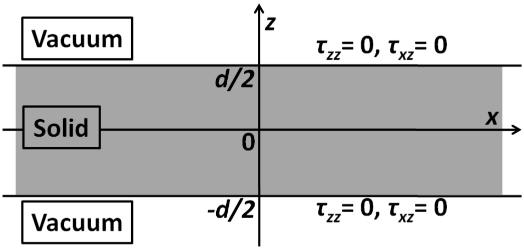

Figure 2.4: Plate configuration: a solid material is located at $-d/2 < z < d/2$, for $z < -d/2$ and $z > d/2$ vacuum is assumed.

The four integration constants can be determined by implementing stress-free boundary conditions at the free surfaces of the solid, thus:

$$\tau_{zz}|_{z=\pm d/2} = 0 \tag{2.42}$$

$$\tau_{xz}|_{z=\pm d/2} = 0 \tag{2.43}$$

This can only be satisfied simultaneously if the stress components τ_{zz} and τ_{xz} are either even or odd functions of z. Introducing equations (2.40) and (2.41) in equations (2.25) and (2.26) and requiring the normal and tangential stress to be either even or odd, yields that either the integration constants A and B' or the constants A' and B need to be equal to zero.

In the first case ($A = B' = 0$), the above boundary conditions give rise to the following system of equations:

$$\begin{bmatrix} \left(-\lambda(k^2 - p^2) + 2\mu p^2\right)\sinh(pd/2) & 2i\mu kq\sinh(qd/2) \\ 2i\mu kp\cosh(pd/2) & -\mu(k^2+q^2)\cosh(qd/2) \end{bmatrix} \cdot \begin{bmatrix} A' \\ B \end{bmatrix} = 0 \tag{2.44}$$

In the second case ($A' = B = 0$), the stress-free boundary conditions give rise to the following system of equations:

$$\begin{bmatrix} \left(-\lambda(k^2 - p^2) + 2\mu p^2\right)\cosh(pd/2) & 2i\mu kq\cosh(qd/2) \\ 2i\mu kp\sinh(pd/2) & -\mu(k^2+q^2)\sinh(qd/2) \end{bmatrix} \cdot \begin{bmatrix} A \\ B' \end{bmatrix} = 0 \tag{2.45}$$

Both systems of equations have a non-zero solution if the determinant of its corresponding coefficient matrix is zero. This yields the following equations for the wave number k:

$$\frac{\tanh(qd/2)}{\tanh(pd/2)} = \frac{(k^2+q^2)^2}{4k^2pq} \tag{2.46}$$

$$\frac{\tanh(qd/2)}{\tanh(pd/2)} = \frac{4k^2pq}{(k^2+q^2)^2} \tag{2.47}$$

The above equations are called the Lamb wave dispersion equations. Solving these equations gives the wave number k_{Lamb} and the velocity $v_{Lamb} = \omega/k_{Lamb}$ for a Lamb wave, which propagates through a solid material of thickness d at a given frequency f. As in the case of Rayleigh waves, the above equations have no explicit analytical solution and have to be solved numerically. Equations (2.46) and (2.47) give rise to two classes of solutions: anti-symmetric (A) and symmetric (S) modes, with respect to the central horizontal axis ($z = 0$) through the plate. The number of anti-symmetric modes at a specific frequency is determined by the number of real roots of equation (2.46), the number of symmetric modes by the real roots of equation (2.47). In addition to a finite number of real roots, both equations have also an infinite set of purely imaginary roots. These roots correspond to in-phase motions of the plate which decay or grow exponentially along the x-axis.

As an illustration, the dispersion curves are calculated for an aluminium plate ($\rho = 2700$ kg/m^3, $v_L = 6320$ m/s, $v_T = 3130$ m/s). First, a frequency f is selected. Then, we search for velocities v which are a solution of the dispersion equations. This procedure is then repeated for each frequency. The result of this approach is depicted in figure 2.5. Since several velocities appear to be a solution of the dispersion equations at a given frequency, several curves can be distinguished. Each of these velocities can be attributed to a specific plate mode. In the figure, anti-symmetric modes are plotted in grey, symmetric modes are plotted in black. For a frequency-thickness product (fd) close to zero, equations (2.46) and (2.47) have only one root each. These roots correspond to the zeroth order anti-symmetric mode A_0 and the zeroth order symmetric mode S_0. As fd increases, the number of roots increases. The new roots correspond to the higher order anti-symmetric ($A_1, A_2, A_3, A_4, \ldots$) and symmetric ($S_1, S_2, S_3, S_4, \ldots$) modes. Higher order modes only appear above a certain cut-off frequency, below this frequency the corresponding mode doesn't exist. The cut-off frequencies can be pictured as the resonant frequencies for longitudinal and shear waves propagating perpendicular to the plane of the plate, i.e:

$$f_n = \frac{n v_{L,T}}{2d} \tag{2.48}$$

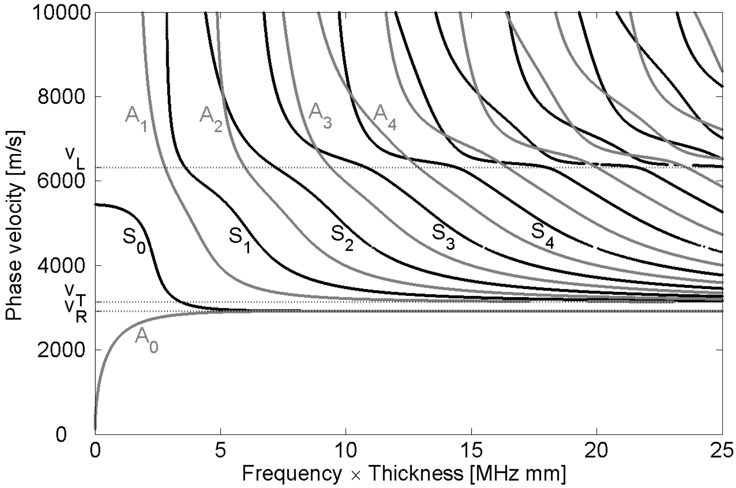

Figure 2.5: Dispersion curves for an aluminium plate. Anti-symmetric plate modes are plotted in grey, symmetric plate modes are plotted in black. The horizontal lines mark the longitudinal velocity ($v_L = 6320$ m/s), the shear velocity ($v_T = 3130$ m/s) and the Rayleigh velocity ($v_R = 2920$ m/s) for aluminium.

where n is any positive integer and $v_{L,T}$ are the longitudinal and shear wave propagation velocities. For each resulting set of resonances, the corresponding Lamb modes are alternately symmetrical and anti-symmetrical. At its cut-off frequency, each of the higher order modes has an infinite phase velocity. For $fd \to \infty$, the phase velocity of the zeroth order modes converges to the Rayleigh wave velocity ($v_R = 2920$ m/s), while the phase velocity of the higher order modes converges to the shear wave velocity v_T. Moreover, for the higher order modes, there appear to be intervals of fd in which the phase velocity remains almost constant. In these intervals the phase velocity approaches the longitudinal wave velocity v_L.

As in the case of Rayleigh waves, the entire displacement field can be calculated by substitution of the potentials ϕ en ψ (equations (2.40) and (2.41)) in equations (2.22) and (2.23). Again, we distinguish between the two cases: $A = B' = 0$ and $A' = B = 0$. In the first case we get the following displacement components:

$$u_x = (ikA' \sinh(pz) - qB \sinh(qz))\, e^{i(kx-\omega t)} \tag{2.49}$$

$$u_z = (pA' \cosh(pz) + ikB \cosh(qz))\, e^{i(kx-\omega t)} \tag{2.50}$$

We note that both u_x and u_z are asymmetrical with respect to the z-axis (i.e. the displacement u_x has opposite signs, the displacement u_z has the same signs in the upper and lower halves of the plate). Waves in which the displacement components have this behaviour are called anti-symmetric Lamb waves. In the second case we get the following displacement components:

$$u_x = (ikA\cosh(pz) - qB'\cosh(qz))\, e^{i(kx-\omega t)} \tag{2.51}$$

$$u_z = (pA\sinh(pz) + ikB'\sinh(qz))\, e^{i(kx-\omega t)} \tag{2.52}$$

Here, both u_x and u_z are symmetric with respect to the z-axis (i.e. the displacement u_x has the same signs, the displacement u_z has opposite signs in the upper and lower halves of the plate). These waves are called symmetric Lamb waves.

Typical displacement fields of a 500 kHz Lamb wave in an aluminium plate with thickness $d = 5$ mm are shown in figure 2.6. If we look at the dispersion curves in figure 2.5, we see that at this frequency the zeroth order anti-symmetric A_0 mode and symmetric S_0 mode have wave propagation velocities equal to $v_{Lamb} = 2762$ m/s for the A_0 mode and $v_{Lamb} = 3841$ m/s for the S_0 mode. In figure 2.6, a snapshot of the displacement field of these modes is shown. In order to have a clear representation, the displacement amplitude in both cases was made much larger than its actual value. In figure 2.6(a), the anti-symmetric A_0 mode is depicted, while figure 2.6(b) visualizes the symmetric S_0 mode.

The displacement amplitudes as a function of depth for both modes are plotted in figure 2.7. The displacement amplitudes are normalized with respect to the normal displacement amplitude u_z at the boundary of the sample. Figure 2.7(a) shows the displacement amplitudes for the anti-symmetric A_0 mode, figure 2.7(b) shows the displacement amplitudes for the symmetric S_0 mode. In both figures 2.6 and 2.7 we clearly see that for the anti-symmetric mode $u_x(z) = -u_x(-z)$ and $u_z(z) = u_z(-z)$, implying that the tangential displacement u_x will always be zero in the centre of the plate. For the symmetric mode $u_x(z) = u_x(-z)$ and $u_z(z) = -u_z(-z)$, i.e. the normal displacement u_z should be zero in the centre of the plate. This behaviour is also found in the higher order Lamb modes.

As already mentioned, for $fd \to \infty$, the phase velocities of the fundamental modes converge to the Rayleigh wave velocity, meaning that the zeroth order Lamb waves behave more and more like a Rayleigh wave. The displacements become localized near the free boundaries of the plate and the displacement amplitudes decrease exponentially with increasing distance from the boundaries. This can be illustrated by looking at the A_0 and S_0 Lamb waves in an aluminium plate with thickness 5 mm at a frequency of 5 MHz. At this frequency both

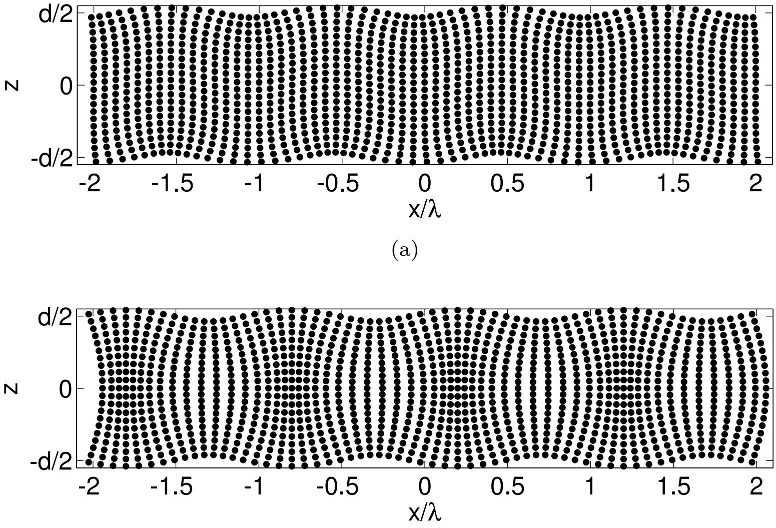

(a)

(b)

Figure 2.6: Snapshot of the displacement field of 500 kHz zeroth order Lamb waves in an aluminium plate with thickness $d = 5$ mm. (a) Anti-symmetric Lamb mode A_0 with wave propagation velocity $v_{Lamb} = 2762$ m/s, (b) Symmetric Lamb mode S_0 with wave propagation velocity $v_{Lamb} = 3841$ m/s.

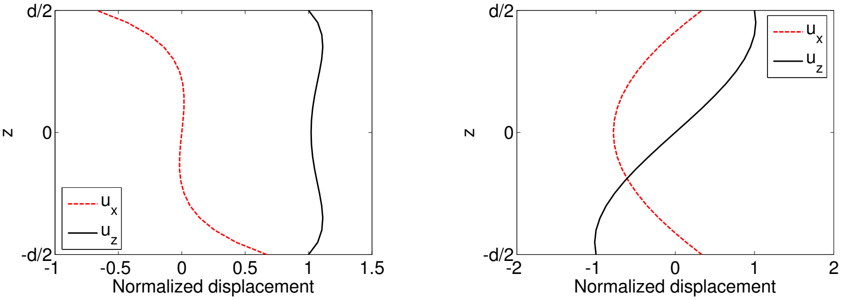

(a) (b)

Figure 2.7: Displacement amplitudes as a function of depth for a 500 kHz zeroth order Lamb wave in an aluminium plate with thickness $d = 5$ mm. The amplitudes are normalized with respect to the normal displacement amplitude u_z at the boundary of the sample. (a) Anti-symmetric Lamb mode A_0 with wave propagation velocity $v_{Lamb} = 2762$ m/s, (b) Symmetric Lamb mode S_0 with wave propagation velocity $v_{Lamb} = 3841$ m/s.

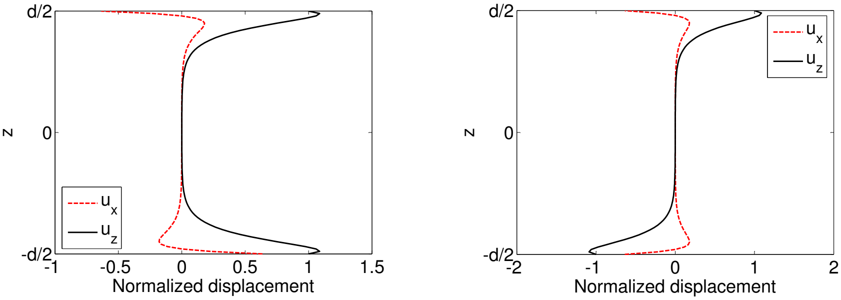

(a)

(b)

Figure 2.8: Displacement amplitudes as a function of depth for a 5 MHz zeroth order Lamb wave in an aluminium plate with thickness $d = 5$ mm. The amplitudes are normalized with respect to the normal displacement amplitude u_z at the boundary of the sample. (a) Anti-symmetric Lamb mode A_0 with wave propagation velocity $v_{Lamb} \approx v_R = 2920$ m/s, (b) Symmetric Lamb mode S_0 with wave propagation velocity $v_{Lamb} \approx v_R = 2920$ m/s.

Lamb waves propagate with a velocity close to the Rayleigh wave velocity (see figure 2.5). In figure 2.8, the displacement amplitudes for both Lamb waves are plotted as a function of depth. As we can see, for both waves the largest displacement amplitudes are found near the free boundaries of the sample, at the centre of the plate the tangential and normal displacements are close to zero. This distribution of the displacements in each of the waves is similar to the distribution of the displacements in the Rayleigh wave (see figure 2.3). For $fd \to \infty$, each of the fundamental modes A_0 and S_0 gives rise to two Rayleigh waves propagating along the free surfaces of the plate.

We already studied the behaviour of the fundamental modes A_0 and S_0 for $fd \to \infty$. We now look at the motion for the higher order Lamb waves. In figures 2.9 to 2.12, the displacement amplitudes as a function of depth are shown for the first order and second order anti-symmetric and symmetric modes (A_1, S_1, A_2, S_2) in an aluminium plate with thickness $d = 5$ mm. The displacement amplitudes have been calculated for each of the modes for four different frequency-thickness products (fd is indicated at the top of each graph). All amplitudes are normalized with respect to the maximum of the absolute value of the tangential and normal displacement amplitudes. From the figures, it is clear that the distribution of the displacements within the plate is described by complicated oscillating functions. With increasing order of the mode, the number of oscillations increases. The number of oscillations also increases with increasing value of fd. Victorov [4] showed that a maximum number of oscillations is

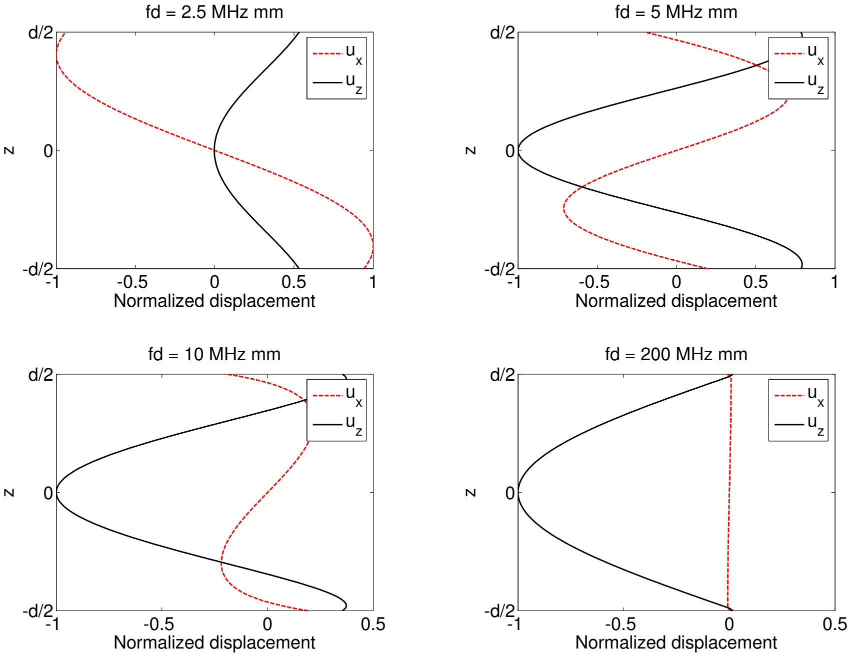

Figure 2.9: Displacement amplitudes as a function of depth for the anti-symmetric A_1 mode in an aluminium plate with thickness $d = 5$ mm. The displacement amplitudes are given for four different frequency-thickness products. The values for fd are indicated in each graph. The amplitudes are normalized with respect to the maximum of the absolute value of the tangential and normal displacement amplitudes.

reached at values of fd where the condition $k_{Lamb}^2 + q^2 = 0$ is satisfied. For higher fd-values, the number of oscillations decreases, resulting in a very simple distribution of the displacements. For example, if $fd = 200$ MHz mm, we see that all four waves have a very small tangential displacement u_x, compared to the normal displacement u_z, implying that, for $fd \to \infty$, these higher order Lamb modes behave more and more like shear waves. For this reason, their phase velocity converges to the shear wave velocity v_T for large frequency-thickness products (see figure 2.5). In addition, the amplitude of the normal displacement is tending to zero at the boundaries of the sample, while high normal displacement amplitudes are found within the plate. This means that, for sufficiently large plate thicknesses, the motion in each higher order Lamb mode becomes localized in the thickness and does not emerge to the surface, in contrast to the fundamental modes S_0 and A_0.

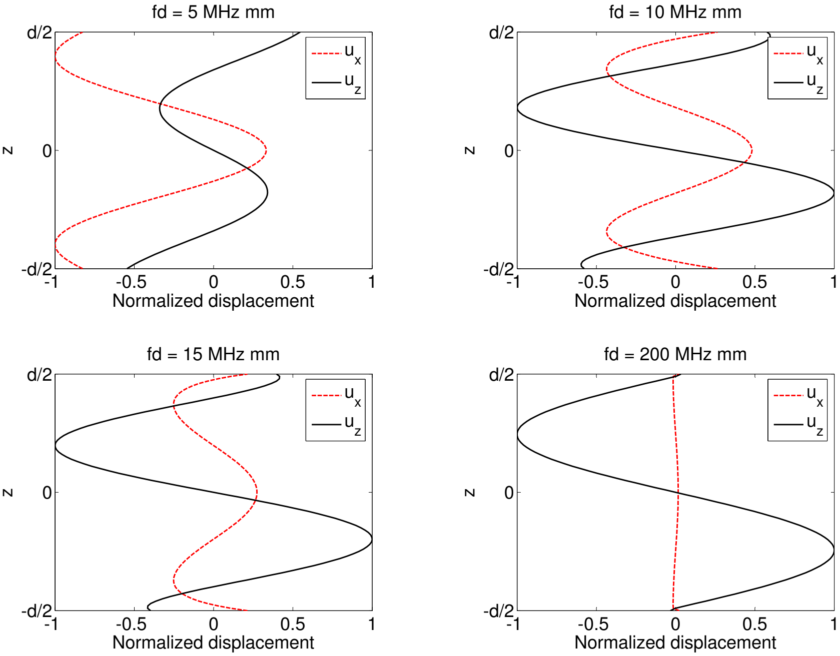

Figure 2.10: Displacement amplitudes as a function of depth for the symmetric S_1 mode in an aluminium plate with thickness $d = 5$ mm. The displacement amplitudes are given for four different frequency-thickness products. The values for fd are indicated in each graph. The amplitudes are normalized with respect to the maximum of the absolute value of the tangential and normal displacement amplitudes.

2.2.3 Excitation of guided waves

In most non-destructive testing (NDT) applications, the sample under study is surrounded by a liquid (e.g. water, air). Strictly speaking, Rayleigh waves and Lamb waves, as described earlier, exist respectively on a free half-space and in free plates. However, if the density of the surrounding liquid is small compared to the density of the solid, the waves propagating along the liquid-solid interface are very similar to the Rayleigh and Lamb waves. These waves are called leaky Rayleigh and leaky Lamb waves and their velocities can be approximated by the Rayleigh and Lamb wave velocities respectively. The influence of the liquid on the attenuation of the leaky Rayleigh and Lamb waves is far more pronounced than the velocity change. This is due to the continuous radiation of energy into the liquid.

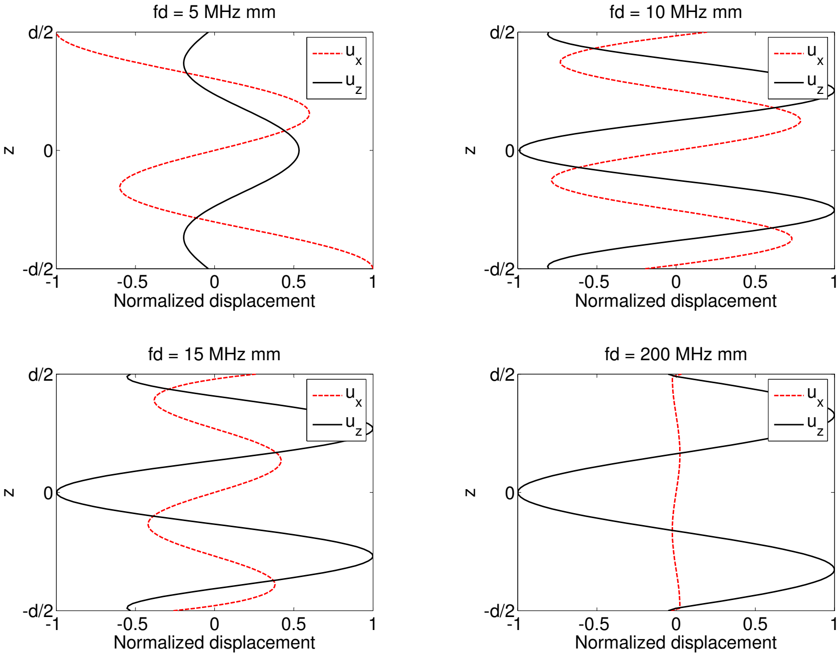

Figure 2.11: Displacement amplitudes as a function of depth for the anti-symmetric A_2 mode in an aluminium plate with thickness $d = 5$ mm. The displacement amplitudes are given for four different frequency-thickness products. The values for fd are indicated in each graph. The amplitudes are normalized with respect to the maximum of the absolute value of the tangential and normal displacement amplitudes.

For the excitation of ultrasonic Rayleigh and Lamb waves, several methods are available. The most commonly used technique is by insonifying the sample with a longitudinal wave that is incident on the sample surface at an oblique angle. This can be done directly by an ultrasonic wave from a piezoelectric transducer glued to the sloping surface of a prism or wedge which is acoustically coupled through one of its faces to the surface of the sample (contact method), or indirectly by an ultrasonic wave from a transducer which is not in contact with the sample (immersion method). In both situations, the transmitted longitudinal wave impinges on the boundary of the sample at an angle θ. This causes a refracted longitudinal wave and a mode converted shear wave to propagate in the sample.

Typically, for Lamb waves, the longitudinal and shear waves will propagate within a plate along zigzagging paths and the Lamb waves may be derived by the

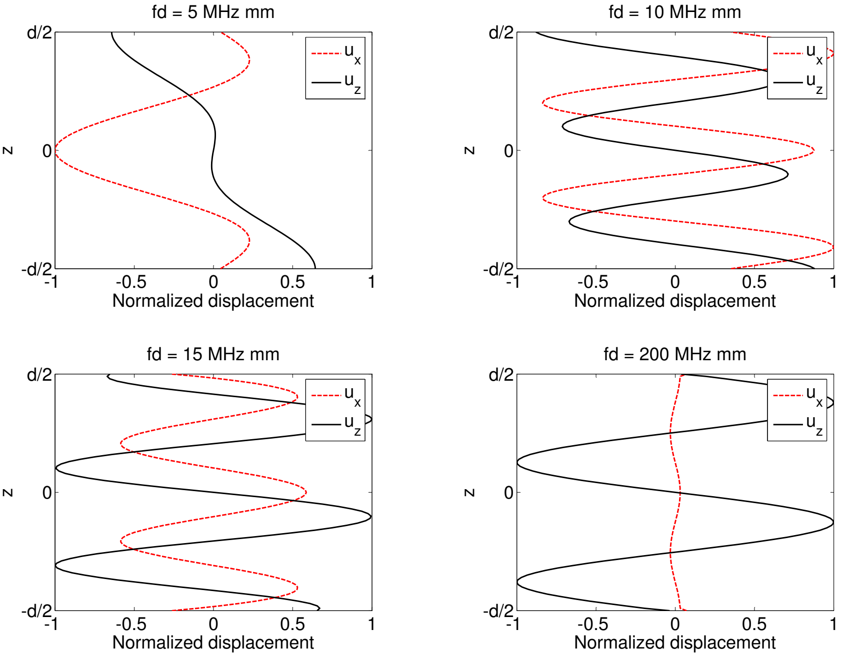

Figure 2.12: Displacement amplitudes as a function of depth for the symmetric S_2 mode in an aluminium plate with thickness $d = 5$ mm. The displacement amplitudes are given for four different frequency-thickness products. The values for fd are indicated in each graph. The amplitudes are normalized with respect to the maximum of the absolute value of the tangential and normal displacement amplitudes.

combined effect of incident and reflected waves throughout the plate thickness. Figure 2.13 explains the formation of a Lamb wave from the zigzagging wave model. For simplicity, we illustrate here only the shear waves in the plate. For a narrow beam, as in figure 2.13(a), the single sections of the zigzag wave do not influence each other. By broadening the beam (figure 2.13(b)), the two sections travelling in the same direction approach each other resulting in an overlap if the beam is broad enough (figure 2.13(c)). In this case, interference may take place. However, the interference shown in figure 2.13(c) is destructive. By choosing another angle of incidence for the incident longitudinal wave, the interference may be constructive resulting in a Lamb wave as in figure 2.13(d). In order to generate a guided wave, the angle of incidence θ should be chosen such that the velocity at the surface of the sample is equal to the Rayleigh or

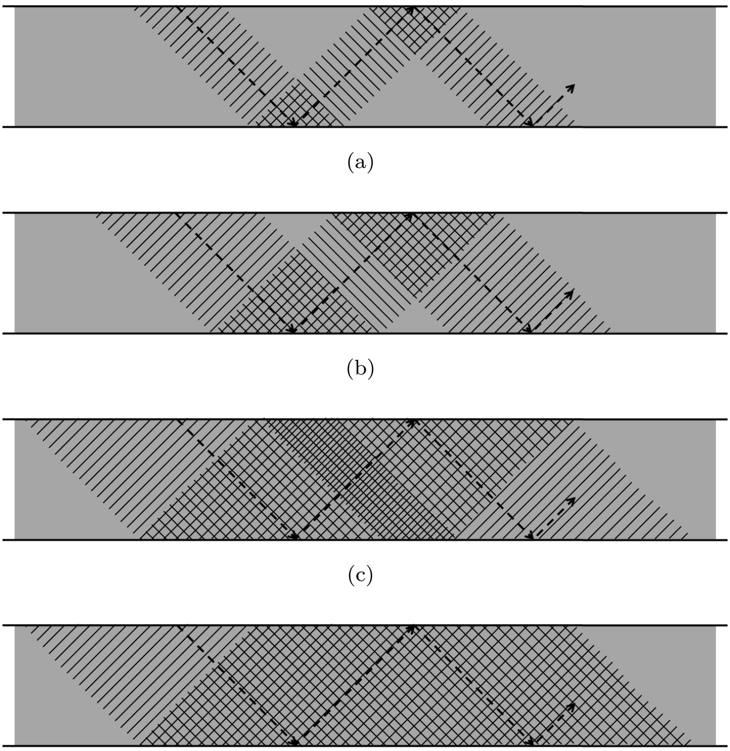

(a)

(b)

(c)

(d)

Figure 2.13: Generation of a Lamb wave from a zigzag-reflected shear wave: (a) narrow beam obliquely reflected, (b) broader beam obliquely reflected, (c) broad beam with unfavourable phase, (d) broad beam with favourable phase obtained by using the right angle of incidence.

Lamb wave velocity. By using Snell's law, we get:

$$\sin\theta = \frac{v_{inc}}{v_{R,Lamb}} \tag{2.53}$$

where v_{inc} is the longitudinal velocity of the incident wave in the wedge or in the surrounding fluid and $v_{R,Lamb}$ is the velocity of the Rayleigh wave or Lamb wave in the sample, propagating in the positive x-direction.

To illustrate this method, a Rayleigh wave and an A_1 and S_1 Lamb mode were simulated using COMSOL Multiphysics, which is a commercially available finite element based program for simulating multi-physics and single-physics

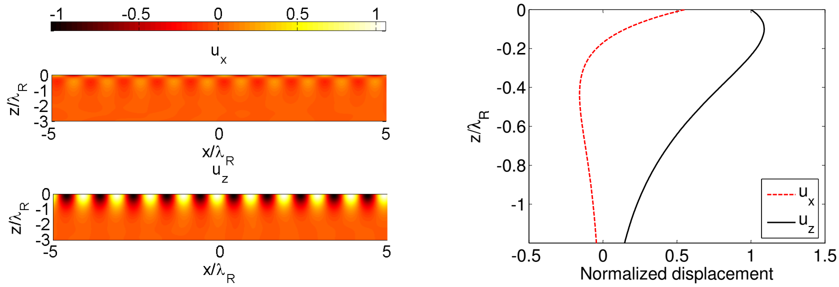

(a) (b)

Figure 2.14: Simulation of a 500 kHz Rayleigh wave at the boundary of an aluminium half-space. The wave was generated using an angle of incidence $\theta = 6.7°$. (a) Snapshots of the normal and tangential displacement fields of the Rayleigh wave. The colour scale goes from white (for the largest values) to black (for the lowest values). (b) Displacement amplitudes as a function of depth for $x = 0$. The displacement amplitudes in (a) and (b) are normalized with respect to the maximum of the normal displacement amplitude u_z at the boundary of the sample.

applications [1]. The simulated results can be compared with the theoretical results from sections 2.2.1 and 2.2.2. For the Rayleigh wave an aluminium half-space is used, while for the Lamb waves an aluminium plate with thickness $d = 5$ mm is used. Both samples are surrounded by air and the guided waves are excited by the immersion method ($v_{inc} = 340$ m/s).

A Rayleigh wave on an aluminium half-space has velocity $v_R = 2920$ m/s. Introducing this velocity in equation (2.53) we know that the angle θ of the incident longitudinal wave should be equal to 6.7°. In figure 2.14(a) snapshots of the normal and tangential displacement fields of a 500 kHz Rayleigh wave at the boundary of the aluminium sample are shown. From this figure, it is clear that the Rayleigh wave propagates along the surface of the sample, as the largest amplitudes are found near the boundary of the sample. Figure 2.14(b) shows the displacement amplitudes as a function of depth for $x = 0$. The amplitudes are normalized with respect to the normal displacement amplitude u_z at the boundary of the sample. Comparing the distribution of the displacements in this figure with the one from figure 2.3 we observe a similar behaviour, meaning that the simulated leaky Rayleigh wave can indeed be approximated by the Rayleigh wave discussed in section 2.2.1.

In figures 2.15 and 2.16 the results of the simulated 1 MHz anti-symmetric A_1 mode and symmetric S_1 mode in an aluminium plate with thickness $d = 5$ mm are shown. Looking at the dispersion curves in figure 2.5, we see that the

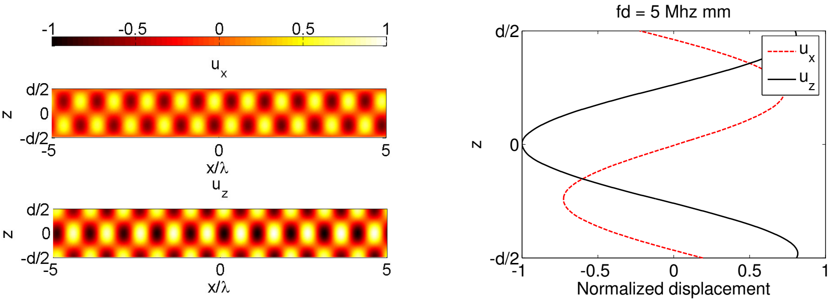

(a) (b)

Figure 2.15: Simulation of a 1 MHz anti-symmetric A_1 Lamb wave in an aluminium plate. The wave was generated using an angle of incidence $\theta = 4.9°$. (a) Snapshots of the normal and tangential displacement fields of the Lamb wave. The colour scale goes from white (for the largest values) to black (for the lowest values). (b) Displacement amplitudes as a function of depth for $x = 0$. The displacement amplitudes in (a) and (b) are normalized with respect to the maximum of the absolute value of the normal displacement amplitude u_z.

wave propagation velocities of both Lamb modes are respectively 3962 m/s and 5603 m/s. Both Lamb modes can thus be generated by a longitudinal wave insonifying the sample at respectively 4.9° and 3.5°. Figures 2.15(a) and 2.16(a) show snapshots of the normal and tangential displacement fields of both Lamb waves. In figures 2.15(b) and 2.16(b), the displacement amplitudes as a function of depth for $x = 0$ are shown. The displacement amplitudes are normalized with respect to the maximum of the absolute value of the tangential and normal displacement amplitudes. The simulated amplitudes can now be compared with the theoretical results from figures 2.9 and 2.10. Again, a good agreement between the theoretical results and the simulation results is found.

2.3 Standing waves

Until now, we studied waves propagating through a medium that was infinitely extended in both x- and y-directions so that the waves could propagate indefinitely in both directions. However, if a wave is propagating through a medium bounded in all directions, the wave will quickly reach the interfaces of the material and interact with these interfaces by means of reflection. Any reflected portion of the wave will then interfere with the portion of the wave that is incident towards the boundary. This interference will create a rather

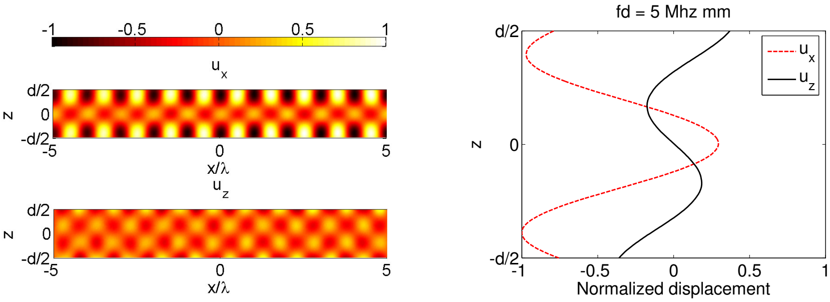

(a) (b)

Figure 2.16: Simulation of a 1 MHz symmetric S_1 Lamb wave in an aluminium plate. The wave was generated using an angle of incidence $\theta = 3.5°$. (a) Snapshots of the normal and tangential displacement fields of the Lamb wave. The colour scale goes from white (for the largest values) to black (for the lowest values). (b) Displacement amplitudes as a function of depth for $x = 0$. The displacement amplitudes in (a) and (b) are normalized with respect to the maximum of the absolute value of the tangential displacement amplitude u_x.

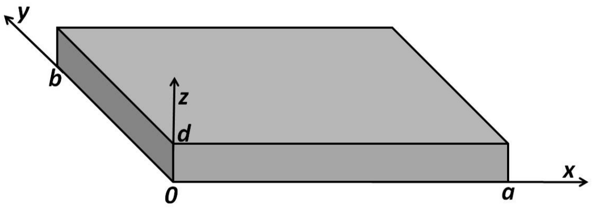

Figure 2.17: Three-dimensional rectangular domain located at $0 < x < a$, $0 < y < b$ and $0 < z < d$.

irregular and non-repeating wave pattern in the medium. However, when the vibrational frequency of the source causes reflected waves from the boundaries of the medium to interfere with incident waves in such a manner that specific points along the medium appear to be standing still (node points), while the displacement of other points along the medium changes over time in a regular manner, a regular wave pattern is produced. Since the observed wave pattern is characterized by points that appear to be standing still, the pattern is often called a standing wave pattern. Such patterns are only created within the medium at specific frequencies of vibration, called the eigenfrequencies of the medium.

For simple shapes, the main characteristics of the standing wave solutions can be easily described analytically. As an illustration, we will discuss the propagation of a wave in a three-dimensional rectangular domain of length a, width b and height d, as depicted in figure 2.17. The propagation of the wave in this domain is governed by the following partial differential equation:

$$\frac{\partial^2 u_z}{\partial t^2} = c^2 \left(\frac{\partial^2 u_z}{\partial x^2} + \frac{\partial^2 u_z}{\partial y^2} + \frac{\partial^2 u_z}{\partial z^2} \right) \tag{2.54}$$

where $u_z(x, y, z, t)$ defines the normal displacement of a point at position (x, y, z) and at time t, c is the wave propagation velocity and $0 < x < a$, $0 < y < b$ and $0 < z < d$. Supposing that the boundaries of the domain are free, the solution has to satisfy the following boundary conditions:

$$\frac{\partial u_z}{\partial x}(0, y, z, t) = \frac{\partial u_z}{\partial x}(a, y, z, t) = 0 \tag{2.55}$$

$$\frac{\partial u_z}{\partial y}(x, 0, z, t) = \frac{\partial u_z}{\partial y}(x, b, z, t) = 0 \tag{2.56}$$

$$\frac{\partial u_z}{\partial z}(x, y, 0, t) = \frac{\partial u_z}{\partial z}(x, y, d, t) = 0 \tag{2.57}$$

To solve the differential equation we use the method of separation of variables in which it is assumed that $u_z(x, y, z, t)$ consists of the product of four distinct functions each depending on one variable only:

$$u_z(x, y, z, t) = X(x)Y(y)Z(z)T(t) \tag{2.58}$$

Substituting equation (2.58) into (2.54) and dividing both sides of the resulting equation by $c^2 X(x)Y(y)Z(z)T(t)$ we obtain:

$$\frac{1}{c^2}\frac{T''(t)}{T(t)} = \frac{X''(x)}{X(x)} + \frac{Y''(y)}{Y(y)} + \frac{Z''(z)}{Z(z)} \tag{2.59}$$

It is easily observed that the left hand side depends only on t and the right hand side depends only on x, y and z. This means that the equality holds only if both sides are equal to the same constant. Assuming that the right hand side is a constant, it is valid to assume that it is the sum of three constants. This allows to reduce the partial differential equation (2.54) to a set of four second order ordinary differential equations:

$$X''(x) + k_x^2 X(x) = 0 \tag{2.60}$$

$$Y''(y) + k_y^2 Y(y) = 0 \tag{2.61}$$

$$Z''(z) + k_z^2 Z(z) = 0 \tag{2.62}$$

$$T''(t) + \omega^2 T(t) = 0 \tag{2.63}$$

where k_x, k_y, k_z and ω are constants, and

$$\omega^2 = c^2 \left(k_x^2 + k_y^2 + k_z^2\right). \tag{2.64}$$

Solving the second order differential equations (2.60) to (2.62), we obtain the following solutions:

$$X(x) = A\cos(k_x x) + B\sin(k_x x) \tag{2.65}$$

$$Y(y) = C\cos(k_y y) + D\sin(k_y y) \tag{2.66}$$

$$Z(z) = E\cos(k_z z) + F\sin(k_z z) \tag{2.67}$$

where A, B, C, D, E and F are constants. Using the proper boundary conditions (2.55) to (2.57) into equations (2.65) to (2.67) we find:

$$B = 0, \quad k_x = \frac{l\pi}{a}, \quad l \in \mathbb{N} \tag{2.68}$$

$$D = 0, \quad k_y = \frac{m\pi}{b}, \quad m \in \mathbb{N} \tag{2.69}$$

$$F = 0, \quad k_z = \frac{n\pi}{d}, \quad n \in \mathbb{N} \tag{2.70}$$

It is important to note that we exclude A, C and E to be equal to zero since it gives the trivial solution $u_z(x, y, z, t) = 0$. The functions $X_l(x), Y_m(y)$ and $Z_n(z)$ associated with respectively k_x, k_y and k_z then are:

$$X_l(x) = A_l \cos\left(\frac{l\pi}{a}x\right), \quad l \in \mathbb{N} \tag{2.71}$$

$$Y_m(y) = C_m \cos\left(\frac{m\pi}{b}y\right), \quad m \in \mathbb{N} \tag{2.72}$$

$$Z_n(z) = E_n \cos\left(\frac{n\pi}{d}z\right), \quad n \in \mathbb{N} \tag{2.73}$$

The solution of equation (2.63) is therefore given by:

$$T_{lmn}(t) = G_{lmn}\cos(\omega_{lmn}t) + H_{lmn}\sin(\omega_{lmn}t) \tag{2.74}$$

where

$$\omega_{lmn}^2 = c^2\left[\left(\frac{l\pi}{a}\right)^2 + \left(\frac{m\pi}{b}\right)^2 + \left(\frac{n\pi}{d}\right)^2\right] \tag{2.75}$$

and G_{lmn} and H_{lmn} are constants.

Combining the results obtained for $X_l(x), Y_m(y), Z_n(z)$ and $T_{lmn}(t)$ we obtain the infinite sequence of product functions that satisfy the partial differential equation (2.54) and the boundary conditions (2.55) to (2.57):

$$\begin{aligned} u_{z_{lmn}} = &\cos\left(\frac{l\pi}{a}x\right)\cos\left(\frac{m\pi}{b}y\right)\cos\left(\frac{n\pi}{d}z\right) \\ &\times\left(\widetilde{G}_{lmn}\cos(\omega_{lmn}t) + \widetilde{H}_{lmn}\sin(\omega_{lmn}t)\right) \end{aligned} \tag{2.76}$$

where $\widetilde{G}_{lmn}$ and $\widetilde{H}_{lmn}$ are new constants. For every l, m and n, we obtain a solution which can be regarded as the (l, m, n) normal mode. This solution can then be considered a standing wave or eigenmode solution of the three-dimensional wave equation for a rectangular domain. In other words, this solution provides waves that are fixed in space and that oscillate for infinite time. The frequency f_{lmn} at which an eigenmode occurs is called the eigenfrequency or resonance frequency and is given by:

$$f_{lmn} = \frac{\omega_{lmn}}{2\pi} = c\sqrt{\left(\frac{l}{2a}\right)^2 + \left(\frac{m}{2b}\right)^2 + \left(\frac{n}{2d}\right)^2} \tag{2.77}$$

According to this equation, the eigenfrequency depends on three integers l, m and n. As a result, it may happen that there are several different modes having the same frequency. These modes are called degenerate modes. Any combination of these degenerate modes gives another vibration pattern with the same frequency. Once a standing wave is formed, some points in the medium appear to be standing still (nodes), while other points of the system are moving sinusoidally with the same frequency. On opposite sides of any nodal line or nodal surface, the displacements have opposite sign and are thus moving in opposite directions. The points in the medium moving with maximum amplitude are called the anti-nodes. A few normal modes are shown in figure 2.18. High displacement amplitudes (i.e. positive values) are shown in white, while low displacement amplitudes (i.e. negative values) are shown in black. In between the black and white regions, the nodal surfaces are clearly visible.

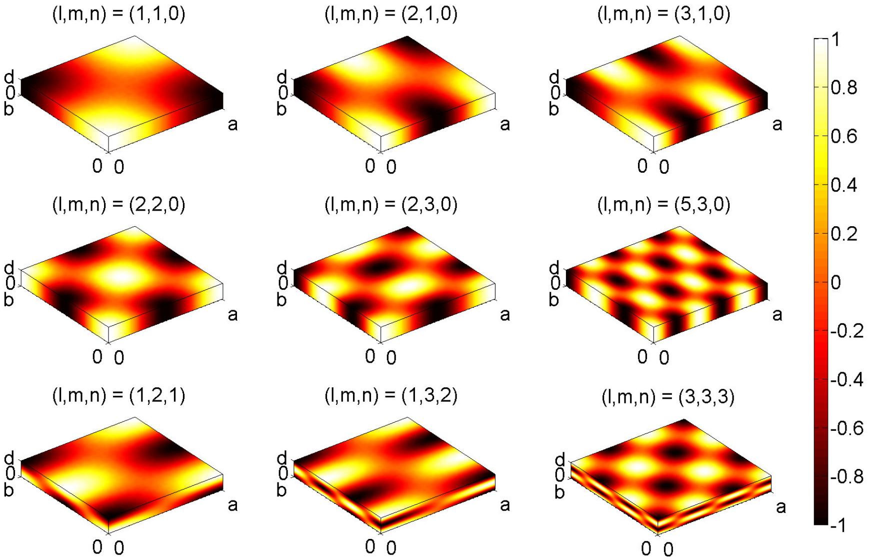

Figure 2.18: Normalized displacements of a few normal modes of a three-dimensional rectangular domain. The colour scale goes from white (for the largest values) to black (for the lowest values). In between the white and black zones, nodal surfaces are visible.

Equation (2.76) is only one solution of an infinite set of solutions. Any combination of l, m and n will provide valid solutions. Using the superposition principle we can formulate the most general solution of (2.58) in the following form:

$$\begin{aligned} u_z(x,y,z,t) = \sum_{l,m,n=0}^{\infty} & \cos\left(\frac{l\pi}{a}x\right)\cos\left(\frac{m\pi}{b}y\right)\cos\left(\frac{n\pi}{d}z\right) \\ & \times\left(\widetilde{G}_{lmn}\cos(\omega_{lmn}t) + \widetilde{H}_{lmn}\sin(\omega_{lmn}t)\right) \end{aligned} \tag{2.78}$$

The constants $\widetilde{G}_{lmn}$ and $\widetilde{H}_{lmn}$ can be determined by applying given initial conditions. Suppose that the initial position is given by:

$$u_z(x,y,z,0) = f(x,y,z) \tag{2.79}$$

and the initial velocity by:

$$\frac{\partial u_z}{\partial t}(x,y,z,0) = g(x,y,z) \tag{2.80}$$

Using the initial condition (2.79) into equation (2.78) we find:

$$\sum_{l,m,n=0}^{\infty} \widetilde{G}_{lmn} \cos\left(\frac{l\pi}{a}x\right) \cos\left(\frac{m\pi}{b}y\right) \cos\left(\frac{n\pi}{d}z\right) = f(x,y,z) \tag{2.81}$$

implying that the constants $\widetilde{G}_{lmn}$ can be determined in this case by using the Fourier coefficients given by the formula:

$$\widetilde{G}_{lmn} = \frac{8}{abd} \iiint_V f(x,y,z) \cos\left(\frac{l\pi}{a}x\right) \cos\left(\frac{m\pi}{b}y\right) \cos\left(\frac{n\pi}{d}z\right) dV \tag{2.82}$$

where V is the volume of the rectangular plate. Using the initial condition (2.80) into the derivative of equation (2.78), we get:

$$\sum_{l,m,n=0}^{\infty} \widetilde{H}_{lmn}\omega_{lmn} \cos\left(\frac{l\pi}{a}x\right) \cos\left(\frac{m\pi}{b}y\right) \cos\left(\frac{n\pi}{d}z\right) = g(x,y,z) \tag{2.83}$$

so that the constants $\widetilde{H}_{lmn}$ can be determined by the Fourier coefficients given by:

$$\widetilde{H}_{lmn} = \frac{8}{\omega_{lmn}abd} \iiint_V g(x,y,z) \cos\left(\frac{l\pi}{a}x\right) \cos\left(\frac{m\pi}{b}y\right) \cos\left(\frac{n\pi}{d}z\right) dV \tag{2.84}$$

Having determined the coefficients $\widetilde{G}_{lmn}$ and $\widetilde{H}_{lmn}$, the unique solution $u_z(x,y,z,t)$ of the initial boundary value problem follows immediately upon substituting (2.82) and (2.84) into equation (2.78).

In this section, we analytically determined the eigenmodes and eigenfrequencies of a three-dimensional rectangular domain with wave propagation velocity c. However, if one also would like to determine the resonance frequencies and the different vibrating modes of more irregularly shaped objects and solids, only numerical simulations turn out to be practical. Most finite element software packages, such as for instance Comsol Multiphysics [1], consist of an eigenfrequency solver that directly outputs the eigenfrequencies and the shape of the corresponding eigenmodes for any object and material under study.

2.4 Conclusion

In this chapter, the basic concepts of ultrasonic guided waves (Rayleigh waves and Lamb waves) and standing waves are introduced. All of these waves can be used in non-destructive testing and evaluation (NDT&E) applications. Rayleigh waves travel along the surface of a relatively thick solid material penetrating to a depth of about one wavelength. Therefore, they are very sensitive to surface defects and other surface features. Lamb waves are similar to surface waves, but they produce stresses throughout the whole thickness of the solid material. They can propagate in elastic structures for relatively long distances and are scattered by defects along this path. Consequently, they are very useful to scan plates, wires and tubes. Finally, for the inspection of materials confined in space standing waves can be used to diagnose and locate possible imperfections. Typical examples of NDT&E techniques in which these waves are used are considered in the following chapters.

Bibliography

[1] *COMSOL Multiphysics User's Guide, Version 3.3*, 2006.

[2] Achenbach, J. *Wave propagation in elastic solids.* North-Holland publishing company - Amsterdam; American Elsevier publishing company - New York, 1973.

[3] Gercek, H. Poisson's ratio values of rocks. *Int. J. Rock Mech. Min. 44* (2007), 1–13.

[4] Victorov, I. *Rayleigh and Lamb Waves.* Plenum Press New York, 1967.

Chapter 3

Finite element method

In the previous chapter we have seen that the physics behind wave propagation in materials can be translated into partial differential equations (PDEs). In order to gain more information about the propagation process itself, those equations need to be solved. Solving these equations by classical analytical methods for arbitrary shaped objects and/or heterogeneous distribution of elasticity is impossible, and therefore, dedicated numerical methods have been constructed. One of the most widely used numerical methods to solve PDEs is the finite element method, a numerical approach by which the PDEs can be solved approximately.

In this chapter, a short introduction to the finite element method is given. Since many millions of engineers and scientists are using the finite element method routinely, lots of books have been published on this subject [3–5]. Some of these books focus on the fundamental approach, others rather deal with a more applied point of view. In this thesis, we will not go into detail on the theory behind the finite element method, but, for completeness, we still want to give the basic concepts of the method. We also discuss the software package COMSOL Multiphysics, which is a commercially available finite element based program for simulating multi-physics and single-physics applications. Since COMSOL is used in the following chapters for the simulation of experimental techniques for ultrasonic non-destructive testing, the COMSOL libraries used in the developed models are also briefly discussed. For a detailed description of the software we refer to the COMSOL Multiphysics user's guide [2].

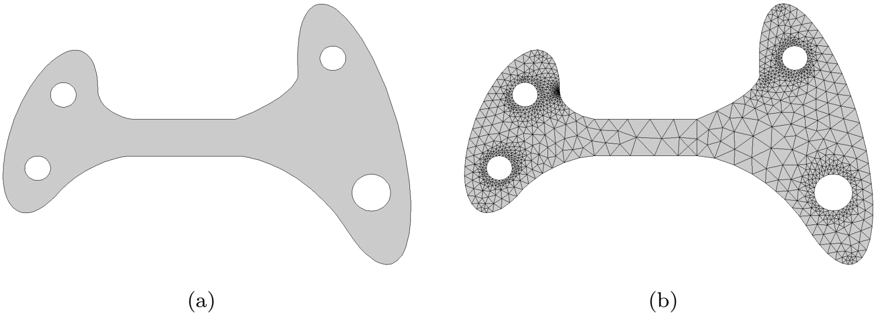
(a)

(b)

Figure 3.1: Finite element discretization: (a) Two-dimensional computational domain, (b) discretization of the domain into finite elements.

3.1 Basic concepts of the finite element method

The finite element method (FEM) is a numerical analysis technique for obtaining approximate solutions to a wide variety of physics and engineering problems. To explain the basic approach of FEM, consider an arbitrary two-dimensional medium, as shown in figure 3.1(a), and suppose we want to determine the displacements caused by a wave propagating in this medium. In principle, the displacement variables (u_x and u_y in this 2D example) possess infinitely many values because they are functions of each point in the medium. Consequently, the problem has an infinite number of unknowns. By using FEM, the problem will be reduced to a finite number of unknowns by dividing the domain under study into a finite number of finite elements, connected by nodes. The unknown displacements can then be expressed in terms of assumed interpolation functions within each element. Popular finite elements are triangular elements for two-dimensional simulations and tetrahedral elements for three-dimensional simulations. A typical example of a discretization for the two-dimensional medium shown in figure 3.1(a) into triangular elements is shown in figure 3.1(b). It is obvious that essentially any geometry can be easily represented by a union of such elements.

Instead of determining the displacements at every point in the domain, the displacements are only determined at a finite number of points, the nodes of the finite elements. These nodes usually lie on the element boundaries, where adjacent elements are connected. However, an element may also have a few interior nodes. The nodal values of each displacement variable and the interpolation functions for the elements completely define the behaviour of the variable within the elements. Once the displacements are determined in the node points, the interpolation functions completely define the displacements throughout the assemblage of elements.

In general, the solution of a problem by the finite element method always follows an orderly step-by-step process:

1. *Discretize the computational domain:* The first step is to divide the computational region into an equivalent system of finite elements with associated nodes. The number of elements used and their variation in size and type depends on the problem that needs to be solved. The elements must be made small enough to obtain a reasonably accurate solution and large enough to reduce computational effort. Small elements are used in regions with large gradients, whereas large elements can be used in regions where the results are relatively constant. Also, different element shapes and sizes can be used in the same solution region. For example, when analysing a wave travelling through different types of material, it is desirable to use different element sizes which depend on the wavelengths in the different materials.
2. *Select interpolation functions:* In the FEM, the field quantities at any point inside the domain other than the nodes are found by interpolation between the nodal values. The interpolation functions are selected on a local basis, meaning that the function is defined within the element using only the nodal values of the element itself. Often, polynomials are selected as interpolation functions for the field variable, because they are easy to integrate and differentiate. Depending on the degree of the polynomials, the interpolation is referred to as linear, quadratic, cubic, etc. Using these interpolation functions, a continuous quantity is approximated by a discrete model composed of a set of piecewise-continuous functions defined within each finite domain or finite element. The interpolation functions are chosen such that the approximated FEM solution becomes infinitely close to the exact solution as the finite element size goes to zero.
3. *Compute the element matrices:* Once the finite elements and their interpolation functions have been selected, we are ready to determine the matrix equations expressing the properties of the individual elements. This is done by first transforming the original partial or ordinary differential equation (strong formulation) to the so-called weak formulation. This weak formulation is obtained from the strong formulation by multiplication by a set of weighting functions and integration over the volume (in 3D problems), the area (in 2D problems) or the length (in 1D problems). After discretization, the approximated field quantities can be substituted into the weak formulation of the governing differential equation. The

volume and surface integrals over the entire domain/surface are then divided into sub-integrals over each finite element, each constituting an element matrix or element vector.

4. *Assemble the element matrices to obtain a global system of equations:* After the matrices for the individual elements have been computed, they are assembled into a global system of equations to find the properties of the overall system. In other words, the matrix equations expressing the behaviour of the finite elements are combined, forming the matrix equations expressing the behaviour of the entire system. The matrix equations for the entire system have the same form as the equations for an individual element except that they contain many more terms. The global matrix equations are generated by summing node-by-node the matrix equations derived for a single element.

5. *Introduce boundary conditions:* Once the element equations are assembled, they need to be modified to account for the boundary conditions of the entire domain. These boundary conditions are introduced via nodal forces or known nodal values. In addition, external sources can be introduced at this point using the same technique of specifying the forces/displacements at particular nodal points.

6. *Solve the global system of equations:* Finally, the assembly process results in a set of simultaneous algebraic equations that can be solved to obtain the unknown nodal values of the problem. To obtain an accurate solution, many nodes are usually needed. Consequently, computers are essential in solving these equations. Generally, the accuracy of the solution improves as the number of elements (nodes) increases, but also the computing time increases. The system of equations can be solved either by using Gaussian elimination or by using an iterative method. The first method requires less tuning and is often faster for 1-2D problems than the iterative method. However, the problem with this method is that the elimination process often requires large memory resources and long computing times, especially for 3D models. The iterative methods generally use less memory and are often faster in 3D.

7. *Interpret the results:* After the computer program calculated the nodal values, interior values of the field quantity can be found inside each element by interpolation. Often, the solution of the system of equations is used to calculate other important parameters (e.g. stress and strain can be calculated from the displacements). The final goal is to interpret and analyse the results. Usually, the results are presented as computer visualizations, such as contour plots, or selected results are printed.

Compared to the finite difference method, which is an alternative way of approximating solutions of PDEs, the most attractive feature of the finite element method is that it is particularly well suited for problems with complex geometries. In the finite difference method a rectangular grid is used, meaning that the grid would reasonably cover the solution region, but the boundaries must be approximated by a series of horizontal and vertical lines (i.e. staircase approximation). In the finite element method, a solution region can be analytically modelled or approximated by replacing it with an assemblage of discrete elements. Since these elements can be put together in a variety of ways, they can be used to represent exceedingly complex shapes. Also, a better approximation of the boundaries is possible since curved boundaries can be represented by straight lines of any inclination.

3.2 COMSOL Multiphysics

The large set of equations to be solved with the finite element method makes it impossible to obtain the results by hand. Luckily, computers nowadays are capable to solve this problem with high speed and high accuracy. For that reason, many software packages based on the finite element method have been developed recently. One of these software packages is Comsol Multiphysics, a powerful interactive environment for modelling and solving various kinds of scientific and engineering problems based on partial differential equations. When solving the PDEs, Comsol Multiphysics uses the above described finite element method.

Solving PDEs generally means one must take the time to set up the underlying equations, material properties, and boundary conditions for a given problem. However, thanks to a number of predefined modelling interfaces (physics modes) it is possible to build models by defining the relevant physical quantities, such as material properties, loads, constraints, sources and fluxes, rather than by defining the underlying equations. Comsol Multiphysics then automatically forms one or several PDEs and boundary conditions from these settings. If one cannot find a suitable physics mode or if one want to specify his own PDEs, one can use the PDE modes. With these modes the problem can be defined in terms of mathematical expressions and coefficients. The physics modes and the PDE modes can also be combined for multiphysics modelling.

While setting up a finite element model in Comsol Multiphysics, an analogue step-by-step procedure as specified above for a general FEM implementation is required. First the geometry of the structure to be analysed needs to be defined. This can be done in a very simple way as the simulation environment contains a graphical user interface that allows the user to create the desired geometry by simply clicking predefined buttons in the draw menu. It is also possible to import geometries constructed with other software packages. Next, one needs to specify the particular descriptions and settings for the underlying physics and equations in the model. For this, the built-in physics modes or PDE modes can be used. Then, the structure should be discretized into small elements. This subdivision into elements is called meshing. The simplest way to do this is by using the built-in mesh generator which automatically generates a standard mesh. Typical mesh parameters determining the element size and element distribution can be manually specified/adjusted in the mesh menu. The model is now ready to solve. For this, different solvers (stationary, time-dependent, eigenfrequency, parametric, etc.) included in COMSOL Multiphysics can be used. Once a model has been solved it is possible to visualize the obtained solution and if necessary use the post-processing tools for further analysis of the data. It is also possible to export a COMSOL simulation into the MATLAB environment or save it as a model M-file script. In this way one can run or manipulate COMSOL simulations in MATLAB.

In the following chapters COMSOL Multiphysics will be used for the simulation of experimental techniques for ultrasonic non-destructive testing. For those simulations we have used several predefined modes in COMSOL. The application specific modes used are the PDE modes in chapters 4 and 5 and the structural mechanics module in chapter 6, which we will both briefly discuss in the following sections.

3.2.1 PDE modes

In COMSOL Multiphysics one can specify nearly any type of PDEs using the PDE modes in the following way. Consider a computation domain Ω with domain boundary $\partial\Omega$ and a vector $\mathbf{u}$ containing the dependent variables $u_1, u_2, \ldots, u_N$, which are unknown functions on the computational domain. These variables can be determined by solving a specific PDE problem. In the general equation system form, the PDEs are written in the following form (for a stationary problem):

$$\sum_j \frac{\partial \mathit{\Gamma}_{lj}}{\partial j} = F_l \quad \text{in} \quad \Omega \tag{3.1}$$

with boundary conditions:

$$\sum_j -n_j \mathit{\Gamma}_{lj} = G_l + \sum_m \frac{\partial R_m}{\partial u_l} \mu_m \quad \text{on} \quad \partial\Omega \tag{3.2}$$

and

$$0 = R_m \quad \text{on} \quad \partial\Omega \tag{3.3}$$

where the equation index l ranges from 1 to N, the constraint index m ranges from 1 to the total number of constraints M, the index j runs over the spatial coordinates, n_j are the components of the outward unit normal vector $\mathbf{n}$ on $\partial\Omega$ and μ_m are Lagrange multipliers.

The first equation in the list above is the PDE, which must be satisfied in Ω. The second equation is a generalized Neumann boundary condition, whereas the third equation is a Dirichlet boundary condition. The coefficients $\mathit{\Gamma}_{lj}, F_l, G_l$ and R_m can be functions of the spatial coordinates, the dependent variables or the space derivatives of the dependent variables. F_l, G_l and R_m are scalars, whereas $\boldsymbol{\mathit{\Gamma}}_l$ is a vector with components $\mathit{\Gamma}_{lj}$. Many PDEs can be rewritten in the general from (3.1) and therefore, they can be solved using COMSOL Multiphysics. In chapters 4 and 5, this type of equations will be used for the simulation of respectively air-coupled ultrasonic non-destructive testing experiments and experiments using time reversal techniques.

3.2.2 Structural mechanics module

The structural mechanics module is an optional package that extends the structural mechanics application mode of COMSOL Multiphysics [1]. The module was specially developed to solve problems in the field of structural and solid mechanics. The module analysis capabilities include static, eigenfrequency, transient, frequency response, and parametric analysis. The eigenfrequency analysis, to find the undamped eigenfrequencies and mode shapes of a model, and the transient analysis, to find the transient response for a time-dependent model, will be used in chapter 6.

The structural mechanics module offers 14 different application modes. In chapter 6 we will use the Solid, Stress-Strain application mode to analyse 3D solids. The dependent variables in this application mode are the displacements u_x, u_y and u_z in respectively x-, y- and z-directions. These variables are used to formulate the governing equations based on the strain-displacement relationship (2.1) and the stress-strain relationship (2.2), which for linear conditions can be written as:

$$\boldsymbol{\tau} = D\boldsymbol{\varepsilon} \tag{3.4}$$

where D is the 6×6 elasticity matrix, and the stress and strain components are described in vector form with six stress and strain components in column vectors defined as:

$$\boldsymbol{\tau} = \begin{bmatrix} \tau_{xx} \\ \tau_{yy} \\ \tau_{zz} \\ \tau_{xy} \\ \tau_{yz} \\ \tau_{xz} \end{bmatrix}, \quad \boldsymbol{\varepsilon} = \begin{bmatrix} \varepsilon_{xx} \\ \varepsilon_{yy} \\ \varepsilon_{zz} \\ \varepsilon_{xy} \\ \varepsilon_{yz} \\ \varepsilon_{xz} \end{bmatrix} \tag{3.5}$$

The material models in the structural mechanics module of COMSOL can be either isotropic, orthotropic or fully anisotropic, each defining a different elasticity matrix D. For an isotropic material, the stress-strain relationship was given by equation (2.3). Replacing Lamé's parameters λ and μ by Young's modulus E and Poisson's ratio ν using equations (2.5), the elasticity matrix looks like:

$$D = \frac{E}{(1+\nu)(1-2\nu)} \begin{bmatrix} 1-\nu & \nu & \nu & 0 & 0 & 0 \\ \nu & 1-\nu & \nu & 0 & 0 & 0 \\ \nu & \nu & 1-\nu & 0 & 0 & 0 \\ 0 & 0 & 0 & 1-2\nu & 0 & 0 \\ 0 & 0 & 0 & 0 & 1-2\nu & 0 \\ 0 & 0 & 0 & 0 & 0 & 1-2\nu \end{bmatrix} \tag{3.6}$$

Consequently, in case of an isotropic fluid, only the values of E and ν need to be entered in COMSOL. For an orthotropic material, the elastic parameters are different in different orthogonal directions and the above described elasticity matrix can no longer be used. In stead, the orthotropic elasticity matrix is defined as:

$$D = \begin{bmatrix} D_{11} & D_{12} & D_{13} & 0 & 0 & 0 \\ D_{12} & D_{22} & D_{23} & 0 & 0 & 0 \\ D_{13} & D_{23} & D_{33} & 0 & 0 & 0 \\ 0 & 0 & 0 & D_{44} & 0 & 0 \\ 0 & 0 & 0 & 0 & D_{55} & 0 \\ 0 & 0 & 0 & 0 & 0 & D_{66} \end{bmatrix} \tag{3.7}$$

where the components are given by:

$$D_{11} = \frac{E_{xx}^2(E_{yy} - E_{zz}\nu_{yz}^2)}{D_{denom}} \tag{3.8}$$

$$D_{12} = \frac{E_{xx}E_{yy}(E_{yy}\nu_{xy} + E_{zz}\nu_{yz}\nu_{xz})}{D_{denom}} \tag{3.9}$$

$$D_{13} = \frac{E_{xx}E_{yy}E_{zz}(\nu_{xz} + \nu_{xy}\nu_{yz})}{D_{denom}} \tag{3.10}$$

$$D_{22} = \frac{E_{yy}^2(E_{xx} - E_{zz}\nu_{xz}^2)}{D_{denom}} \tag{3.11}$$

$$D_{23} = \frac{E_{yy}E_{zz}(E_{xx}\nu_{yz} + E_{yy}\nu_{xy}\nu_{xz})}{D_{denom}} \tag{3.12}$$

$$D_{33} = \frac{E_{yy}E_{zz}(E_{xx} - E_{yy}\nu_{xy}^2)}{D_{denom}} \tag{3.13}$$

$$D_{44} = 2G_{xy} \tag{3.14}$$

$$D_{55} = 2G_{yz} \tag{3.15}$$

$$D_{66} = 2G_{xz} \tag{3.16}$$

where

$$\begin{aligned} D_{denom} =& E_{xx}E_{yy} - E_{yy}^2\nu_{xy}^2 - E_{yy}E_{zz}\nu_{xz}^2 \\ & - E_{xx}E_{zz}\nu_{yz}^2 - 2E_{yy}E_{zz}\nu_{xy}\nu_{yz}\nu_{xz} \end{aligned} \tag{3.17}$$

In this case, the Young's moduli E_{xx}, E_{yy} and E_{zz}, the Poisson's ratios ν_{xy}, ν_{yz} and ν_{xz} and the shear moduli G_{xy}, G_{yz} and G_{xz} all depend on the axis orientation. In the orthotropic case, the values of these nine components need to be entered in designated edit fields in the user interface of COMSOL. Finally, for a general anisotropic material, all 21 components of the symmetric elasticity matrix D need to be entered. Besides entering the values of the elastic constants in each of these cases, the density ρ of the material under study is required as an additional input parameter.

Once the material properties are defined, we need to specify the boundary conditions. In the structural mechanics module, we can choose from a list of predefined boundary conditions, such as a free boundary, a fixed boundary, a prescribed displacement, a symmetry plane, a load, etc. After all boundary conditions are set, the model is ready to solve. Depending on the type of analysis, a different equation is solved. In case of a transient analysis, Newton's second law is considered. In case of an eigenfrequency analysis, the eigenfrequency equation is derived assuming a harmonic displacement field.

3.3 Conclusion

In this chapter, we first provided a compact introduction of the finite element method, focusing on the basic steps we need to follow while solving a problem by the finite element method. Next, we briefly discussed COMSOL Multiphysics, a commercially available software package based on the finite element method. COMSOL contains a number of built-in application modes, making it very easy in building models for different types of physics problems. Two of the application modes, the PDE modes and the structural mechanics application mode, will be used in the following chapters.

Bibliography

[1] *COMSOL Multiphysics, Structural Mechanics Module, User's Guide, Version 3.3*, 2006.

[2] *COMSOL Multiphysics User's Guide, Version 3.3*, 2006.

[3] Huebner, K., Dewhirst, D., Smith, D., and Byrom, T. *The finite element method for engineers*, 4 ed. John Wiley & Sons, 2001.

[4] Lakshminarayana, H. *Finite element analysis: Procedures in engineering.* Universities Press, 2004.

[5] Logan, D. *A first course in the finite element method*, 4 ed. Thomson Learning, 2007.

Chapter 4

Air-coupled ultrasonic non-destructive testing

Air-coupled ultrasonic non-destructive testing of materials is a non-contact technique which has become increasingly common. Moreover, air-coupled ultrasonic inspection of materials using single-sided access offers interesting possibilities for the development of in-line NDT systems. This chapter reports observations and simulations obtained from a single-sided air-coupled pitch-catch configuration. The pitch-catch technique involves a setup in which transmitter and receiver are located at the same side of the test object. Sound waves, reflected once or multiple times from the back-wall of the object or refracted by a discontinuity, are recorded and analysed for visualization. The feasibility of the technique is demonstrated, experimentally, in the case of artificial defects in aluminium samples. Depending on the configuration one or more ultrasonic images of the defect can be observed, their number and relative position containing information about the location of the defect. The experiments are simulated using two distinctive methods. The first simulation is based on a ray tracing (shadow) method approach, the second method uses a spectral solution implemented within Comsol Multiphysics. Both simulation methods allow simple prediction of the response images in experimental conditions with supplementary levels of complexity, which will assist the development and optimization of in-line inspection techniques [26].

In the first section, an introduction to air-coupled ultrasonic testing is given. Then, an experiment using an air-coupled ultrasonic single-sided pitch-catch technique on an aluminium bar with a borehole is discussed. The experiment is then simulated using the shadow method and the finite element method.

Information on both simulation methods is provided in the third section. In the fourth section experimental observations and simulations are compared. We shall see that there is a good qualitative agreement between both. In the last part of this chapter, the developed finite element method is used for simulations of experimental conditions with supplementary levels of complexity, as for example plates with a section of varying thickness and LED-rail profiles.

4.1 Air-coupled ultrasound

Ultrasonic immersion testing and ultrasonic contact methods are popular NDT techniques for the characterization and state investigation of materials. However, the use of coupling media such as water, glue or grease may not always be desirable depending on the inspection conditions. Honeycomb structures cannot be tested by immersion, as water fills the discontinuities and echoes will be subdued. Other objects, such as aeroplanes, are too large for inspection in water baths. An additional limitation concerns the instability of coupling media when testing moving or rotating parts. For all of the above reasons, and many more, there has been an increased interest in testing methods which can overcome the limitations of traditional sensor coupling.

One way of eliminating liquid coupling media is to transfer ultrasonic waves from the transducer to the material through a layer of air. Today's research in air-coupled ultrasound (ACU) is focused on three main topics: (1) the design of ACU sensors, (2) the simulation of the propagation of ultrasonic waves in homogeneous and heterogeneous media taking into account the air-coupled origin of the waves, and (3) the development of NDT&E methods on the basis of full ACU or hybrid (ACU in combination with a laser vibrometer) systems with regard to a large variety of materials and quality aspects.

With respect to the ACU sensors, it should be noted that the generation of ultrasound in air at frequencies higher than 250 kHz is challenging because of the strong absorption of the acoustic energy in the air, and the high acoustic impedance mismatch at air-solid interfaces. Hence a great part of the present technological research in the field of ACU deals with modelling and the design of air-coupled transducers which are capable to overcome the acoustic impedance gap with air as good as possible. This search has led to piezoelectric transducers with one or more ideal coupling layers [30, 32, 40, 61] and to micro-machined electrostatic transducers [49, 54], which are basically capacitive devices in general characterized by a large bandwidth. The efficiency of air-coupled transducers has improved significantly over the years. Slowly but surely, air-coupled ultrasound has been able to overcome many limitations of the conventional ultrasonic techniques, and, because of its non-contact nature, it offers new possibilities e.g. for in-line inspection of materials.

Parallel with the challenging ACU technology, simulation studies are being performed to optimize the performance of the measurement methods and to create efficient tools for data handling [28]. Models are being developed to describe (linear) wave propagation in complex 3D-media, to predict and benefit from the enhancement of ultrasonic energy transfer using mode conversion or special configurations based on a focused transmission mode [57], to evaluate pulse compression techniques [28], to support air-coupled mapping of viscoelastic stiffness and elastic anisotropy in modern materials [19, 55], to study guided waves propagating in plates, composite materials and sandwich structures [21, 34, 38], to simulate the interaction between Lamb modes with discontinuities in plates and composite materials [17–20, 37, 39], to investigate non-linear ACU effects [3], and to assess the near and far field of ACU transducers [32].

Finally, the development of practical applications dealing with non-contact ultrasound is undoubtedly a fast growing field of interest, especially in the single-sided configuration. More and more non-contact methods are applied to inspect industrial samples in off- or in-line mode [10, 11, 56, 58, 59]. Among others, we mention applications such as the examination of composite components and multi-layered materials by either linear, nonlinear, full or hybrid air-coupled ultrasound techniques [35, 48, 51], the ACU imaging of concrete slabs mapping out interior characteristics of the concrete such as crack planes, gravel nests and boreholes [9], the non-contact defect characterization of welded joints and spot welds [2, 10, 11, 50], the in-line monitoring of variations in the weight of a coating on a textile carrier [14], the in-line characterization and control of paper quality [46], the inspection of wood and art work for restoration purposes [31], the air-coupled detection of disbonds in adhesive joints [53], the investigation of honeycomb structures, the ACU measurements in food [27, 29, 43, 47], etc. In all of the above studied applications the availability of theoretical and/or simulation models is crucial to have a good understanding of the observed ultrasonic effects.

4.2 Air-coupled ultrasonic single-sided pitch-catch technique

As in conventional ultrasonic testing techniques, air-coupled transducers can be aligned in several ways: transmission or reflection, normal or oblique incidence. In many situations, a normal incidence through-transmission setup may not be achievable, for example, when the inspected material is only accessible from one

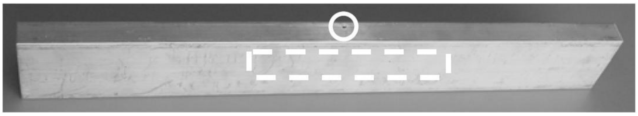

Figure 4.1: Rectangular aluminium bar with ∅ 2 mm borehole close to the top-side of the sample. The white circle indicates the borehole. The white rectangle indicates the *C*-scan area.

side. The single-sided pitch-catch technique then offers a valuable alternative. In this setup, transmitter and receiver are both positioned at oblique angles at the same side of the test object. An ultrasonic wave generated by the transmitter, enters the test object, reflects one or more times from the back-wall and is finally captured by the receiver. If the information carrying signal is influenced by the specular reflection, a sound absorbing material can be placed between transmitter and receiver.

An experimental setup for the air-coupled pitch-catch technique has recently been implemented at the laboratory for non-contact ultrasound (lab NCU) of KATHO. As part of the first test, the basic principles of the technique have been demonstrated with respect to well defined aluminium test samples with well defined artificial defects [12, 13]. The test sample used in the experiments is a rectangular bar of aluminium (density $\rho = 2700$ kg/m^3, longitudinal velocity $v_L = 6320$ m/s and shear velocity $v_T = 3130$ m/s) with dimensions 440 mm × 60 mm × 20 mm. Perpendicular to the lengthwise and thickness direction of the bar, and 4 mm outside the centre line, a 50 mm deep hole was drilled, with a diameter ∅ of 2 mm (see figure 4.1). This preparation allows to consider two experimental arrangements: one case in which the centre of the hole is located 6 mm from the top-side of the bar, and a second case in which, by rotating the bar 180°, the borehole is at 14 mm from the top-side.

The experiments are performed using an air-coupled pitch-catch configuration in which two transducers are positioned at oblique angles at the same side of the test sample at 15 mm from the top-side. Both transducers have a diameter ∅ of 12 mm. When the transmitted longitudinal wave in air reaches the surface of the aluminium sample, part of the wave is reflected while the other part of the wave is transmitted partially as a refracted longitudinal wave and partially as a mode converted shear wave in the solid, as shown in figure 4.2. The angles of reflection and/or refraction by mode conversion can be calculated from Snell's law:

$$\frac{\sin\theta}{v_{air}} = \frac{\sin\theta_L}{v_L} = \frac{\sin\theta_T}{v_T} \tag{4.1}$$

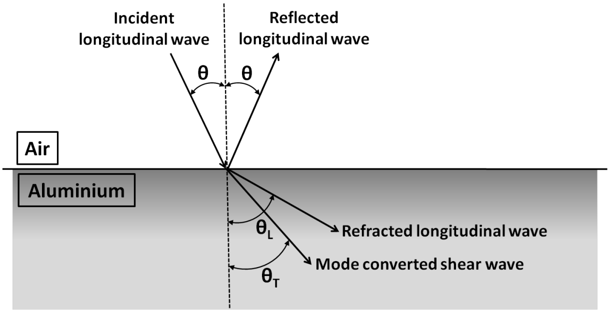

Figure 4.2: A longitudinal wave incident on an interface between air and aluminium is partially reflected as a longitudinal wave and partially transmitted in the solid as a refracted longitudinal wave and a mode converted shear wave.

where θ is the angle of incidence of the transmitted sound field in air with respect to the normal, θ_L is the angle of the refracted longitudinal wave in the aluminium bar with respect to the normal, θ_T is the angle of the mode converted shear wave in the aluminium bar with respect to the normal, v_{air} is the wave velocity of sound in air and v_L and v_T are respectively the longitudinal and shear wave velocity in aluminium. Since the longitudinal wave velocity v_L is always larger than the shear wave velocity v_T, the angle θ_L of the refracted longitudinal wave is always larger than the angle θ_T of the mode converted shear wave. The angle of incidence θ which makes the angle of the refracted longitudinal wave 90°, is known as the first critical angle. At this critical angle, all of the energy from the refracted longitudinal wave is converted to a surface following longitudinal wave. Beyond the first critical angle, only the shear wave propagates into the material. There is also an angle of incidence that makes the angle of the mode converted shear wave 90°. This angle is known as the second critical angle and all of the wave energy is now converted into a surface following shear wave. Any increase in angle of incidence beyond the second critical angle leaves no sound in the material at all, there is total internal reflection in air. In the experiments, the angle of incidence of the transmitted sound field in air is set to 4.5° with respect to the normal. Since this angle lies between the first (3.1°) and second (6.2°) critical angle, only shear waves are generated in the aluminium test sample. The receiving transducer makes the same angle of 4.5° with the normal, though in negative orientation.

The generated sound signal is a chirp signal (signal in which the frequency increases with time) with a Gaussian envelope represented as follows:

$$S(t) = \sin\left[2\pi\left(f_c - \frac{B}{2} + \frac{Bt}{2T}\right)t\right]\exp\left[-\frac{1}{2}\left(\frac{t-t_c}{\sigma}\right)^2\right] \tag{4.2}$$

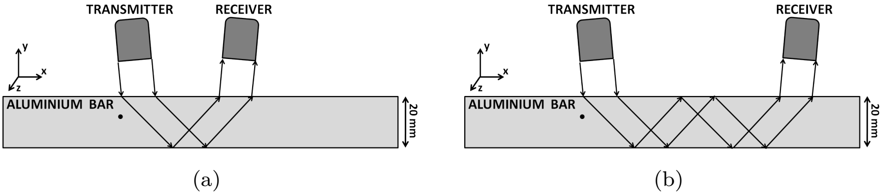

Figure 4.3: Simplified scheme of the air-coupled pitch-catch technique. Both transmitter and receiver are positioned along the same side of the test sample. The transmitted sound field is captured by the receiver which is positioned in (a) the first reflection maximum, or (b) the second reflection maximum.

with pulse duration $T = 50$ μs, central frequency $f_c = 750$ kHz, bandwidth $B = 250$ kHz (the chirp thus extends over the $625 - 875$ kHz frequency range), central time $t_c = T/2$ and standard deviation σ, which was chosen such that the amplitude of the Gaussian envelope at times $t = 0$ and $t = T$ equals one percent of the amplitude at time $t = t_c$. The chirp signal travels through the air to the test sample as a longitudinal wave, converts at the surface to a transverse signal propagating at a different angle further in the test sample, reflects once or several times from the bottom- and top-wall of the sample, and leaks each time from the sample as a longitudinal wave at an angle of 4.5°. The receiver captures the longitudinal wave at a fixed position along the sample surface, 15 mm above the top-wall. When the received sound field is due to a single reflection from the bottom-wall, we say that the receiver is positioned in the first reflection maximum of the back-reflected sound field. When the sound field has reflected twice from the back-wall before reaching the receiver, the receiver is said to be positioned in the second reflection maximum. Figure 4.3 shows a simplified scheme of both setups.

In the laboratory setup, the test sample is attached to a motorized xz-stage, while the transducers have fixed positions. This allows to make a two-dimensional scan in which the received signal strengths at the x- and z-positions of the sample are measured. Examples will be discussed in section 4.4. More information about the experiments can be found in Refs. [12, 13].

4.3 Numerical simulations

For the analysis of pitch-catch experiments, the availability of simulation models is crucial to a good understanding of the observed ultrasonic effects. We present here two such simulation methods which allow elementary predictions of some

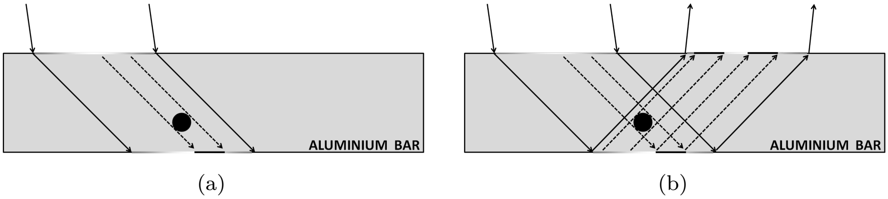

(a) (b)

Figure 4.4: Illustration of the shadow method for the aluminium bar with circular borehole. A Gaussian light beam is partially obscured by a small obstacle. This results in a decrease of the total strength of the signal: (a) part of the incident beam is obscured by the obstacle, (b) depending on the size and the location of the obstacle, part of the reflected beam may also be obscured.

basic experimental results. The first method is based on a mere geometric model in which the sound wave propagation through the defect is replaced by a Gaussian and non-diverging light beam obscured by an optically opaque obstacle. This model is also known as the shadow method [41]. The second simulation is performed using a numerical spectral solution code implemented in COMSOL [1]. Both models are used to simulate the air-coupled pitch-catch experiments, discussed in section 4.2, allowing a straight comparison between the experimental observations and the simulations.

4.3.1 Shadow method

The shadow method is also called the intensity-measurement or through-transmission method. It is a bare geometric model in which the sound wave and the artificial defect are replaced by a circular light beam with Gaussian cross-section and an opaque object with the same dimensions as the defect. At each instance when the light beam encounters the opaque object, the beam's energy is reduced by the size of the shadow.

An illustration of the shadow method for the aluminium bar with circular borehole can be found in figure 4.4. The beam impinges on the surface of the aluminium bar at an angle of 4.5°. Using Snell's law, we can calculate the propagation angle of the beam in the aluminium bar. The beam propagates further to the back-wall of the bar and is partly obscured by the defect, modelled as a geometrical object blocking the sound without scattering. This results in a reduced intensity of the incident beam, represented by the dark zone at the bottom-wall of the sample in figure 4.4(a). Depending on the relative location of beam and object, the intensity of the beam can be decreased several times. This is shown in figure 4.4(b), where part of the reflected beam is also obscured by the circular object. The integrated signal strength at the surface of the aluminium bar can be used as an indicator for the strength of the sound field that is captured by the receiver. For the signal strength at the second reflection maximum, another reflection between front and back side of the sample is taken into account.

It should be mentioned that the shadow method entails serious simplifications, since divergence, diffraction, scattering and any other frequency dependent effects are not taken into account. Therefore, the schematic representation of the ray paths as in figure 4.4 can not be compared with the actual propagation of ultrasonic waves. The presentation of the rays based on geometric-optical concepts of light and shadow is only valid in the extreme case of wavelengths which are very short compared to the dimensions of the transducers and the defects. These conditions are usually not fulfilled in practice or are only used as a rough approximation. Nevertheless, for the pitch-catch experiments discussed in section 4.2, the shadow method leads to a good qualitative interpretation of the experimental results.

4.3.2 Finite element method

The second method aims to be much closer to a description of the reality. In this simulation, the geometry includes the transmitter-receiver pair, their orientation and position, the layer of air, the leakage after each reflection, mode conversion, etc. In addition, frequency effects matter. The implementation is based on a finite element simulation using Comsol, and contains the following steps. First, we set up the geometry of the problem. We consider here a two-dimensional representation of the experimental setup, subdivided into several subdomains. For every subdomain, the governing equations have to be defined. To limit the computational domain, reflections at the edges should be eliminated. This is done by adding absorbing layers adjacent to the edges of the computational region, which basically implies an adaptation of the fundamental equations. Finally, we specify the boundary conditions between different subdomains and determine the mesh size for the finite element model in order to get an accurate solution.

Geometry

The 2D geometry is subdivided into six subdomains as illustrated in figure 4.5. The main rectangular domain in the centre represents the aluminium bar. On top of this domain we consider two domains of air separated by a sound absorbing material. The air domain on the left contains the transmitter, the one

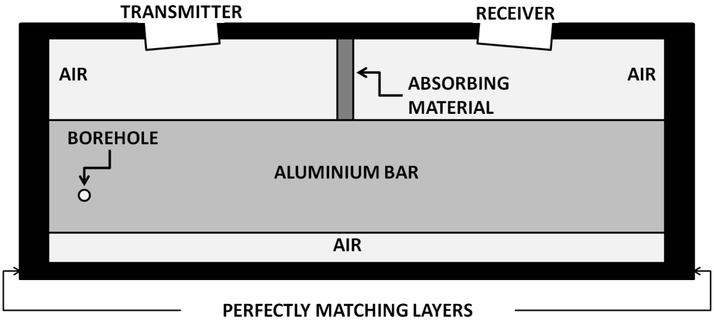

Figure 4.5: Illustration of the geometry of an aluminium bar with borehole used in the COMSOL simulation. The model contains 6 different domains: the aluminium test sample, 3 air domains (two on top, one at the bottom), a borehole filled with air and a sound absorbing material between transmitter and receiver. Perfectly matching layers (absorbing regions) are added to the computational region to eliminate unwanted reflections.

on the right accommodates the receiver. The sound absorbing material between transmitter and receiver is necessary to suppress the signal coming from the specular reflection at the air-aluminium surface. This specular reflection is usually several orders of magnitude stronger than the useful signal which is transmitted into the solid. Below the aluminium section we consider another layer of air. Finally, a circular domain is included inside the aluminium bar representing the air-filled borehole.

Governing equations

For the simulation of elastic waves in solids, we can start from the equations of motion (2.6). In two dimensions, the two basic equations are:

$$\frac{\partial^2 u_x}{\partial t^2} = \frac{1}{\rho_{solid}} \left(\frac{\partial \tau_{xx}}{\partial x} + \frac{\partial \tau_{xy}}{\partial y} \right) \tag{4.3}$$

$$\frac{\partial^2 u_y}{\partial t^2} = \frac{1}{\rho_{solid}} \left(\frac{\partial \tau_{xy}}{\partial x} + \frac{\partial \tau_{yy}}{\partial y} \right) \tag{4.4}$$

with ρ_{solid} the mass density of the solid material, u_i the (in-plane) components of the particle displacement and τ_{ij} the components of the stress tensor $(i, j \in \{x, y\})$. For isotropic materials, Hooke's law (2.3) can be used to relate stress and strain. In two dimensions, this leads to the following three relations:

$$\tau_{xx} = (\lambda + 2\mu)\frac{\partial u_x}{\partial x} + \lambda\frac{\partial u_y}{\partial y} \tag{4.5}$$

$$\tau_{yy} = \lambda\frac{\partial u_x}{\partial x} + (\lambda + 2\mu)\frac{\partial u_y}{\partial y} \tag{4.6}$$

$$\tau_{xy} = \mu\left(\frac{\partial u_x}{\partial y} + \frac{\partial u_y}{\partial x}\right) \tag{4.7}$$

with λ and μ Lamé's constants.

The propagation of sound waves in air can be modelled by an equation of motion for the two displacement components (conservation of momentum) and a single equation of continuity (conservation of mass). With some simplifications, in particular constant density, the equation of motion in two dimensions is given by:

$$\frac{\partial^2 u_x}{\partial t^2} = -\frac{1}{\rho_{air}}\frac{\partial p}{\partial x} \tag{4.8}$$

$$\frac{\partial^2 u_y}{\partial t^2} = -\frac{1}{\rho_{air}}\frac{\partial p}{\partial y} \tag{4.9}$$

where ρ_{air} is the mass density of air, p is the acoustic pressure in air and u_i are the (in-plane) components of the particle displacement ($i \in \{x, y\}$). The equation of continuity in two dimensions is given by:

$$\frac{\partial p}{\partial t} + \kappa\left(\frac{\partial v_x}{\partial x} + \frac{\partial v_y}{\partial y}\right) = 0 \tag{4.10}$$

where v_i are the (in-plane) components of the particle velocities and κ the bulk modulus of the medium. The bulk modulus can be expressed in terms of density and the speed of sound v_{air} in the medium as:

$$\kappa = \rho_{air} v_{air}^2 \tag{4.11}$$

Using this relation and taking the derivative of equation (4.10) with respect to t, we finally get:

$$\frac{\partial^2 p}{\partial t^2} = -\rho_{air} v_{air}^2\left(\frac{\partial a_x}{\partial x} + \frac{\partial a_y}{\partial y}\right) \tag{4.12}$$

with a_i the (in-plane) components of the particle acceleration.

In our model, we want to take into account the attenuation of sound in air. For plane waves, attenuation can be introduced by the addition of an imaginary part in the expression of the wave number. The complex wave number $\widetilde{k}$ then becomes:

$$\widetilde{k} = k - i\gamma \tag{4.13}$$

which, when substituted for example into the equation of a plane wave propagating in the positive x-direction, yields:

$$p = Ae^{-\gamma x}e^{-i(kx-\omega t)} \tag{4.14}$$

with a new exponentially decaying term $e^{-\gamma x}$ which resulted from the use of the complex wave number $\widetilde{k}$. γ is known as the absorption coefficient with units of nepers per unit distance and k is the real wave number. Bass et al. [4, 5] derived a formula for the atmospheric absorption as a function of frequency, relative humidity and atmospheric pressure. In figure 4.6, the atmospheric absorption was calculated as a function of angular frequency using this formula. It is obvious that the absorption coefficient is frequency dependent. In general, the absorption coefficient is proportional to the square of the frequency of sound. For the atmospheric absorption the proportionality is given by:

$$\gamma = 4.68 \times 10^{-13}\omega^2 \tag{4.15}$$

as illustrated by the quadratic fit in figure 4.6.

The complex wave number $\widetilde{k}$ is related to the velocity of sound by the following equation:

$$\widetilde{k} = \frac{\omega}{v_{air}} \tag{4.16}$$

where v_{air} should also be complex. Using equation (4.13) and neglecting the higher order terms, we find that:

$$\gamma = \omega\frac{\Im(v_{air})}{\Re(v_{air})^2} \tag{4.17}$$

where $\Im(v_{air})$ and $\Re(v_{air})$ are respectively the imaginary and real part of the sound velocity in air. Combining equations (4.15) and (4.17), the sound velocity

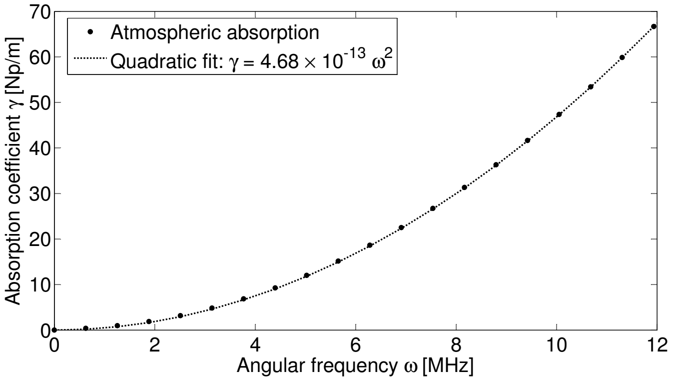

Figure 4.6: Atmospheric absorption γ as a function of angular frequency ω. The dots mark the atmospheric absorption values calculated with the formula derived by Bass et al. [4, 5]. The dashed line is a quadratic fit through these calculated values.

used in the model is $v_{air} = 340 + i\omega(5.41 \cdot 10^{-8})$ m/s. The imaginary part allows for a realistic representation of attenuation in air that depends on the angular frequency ω.

Perfectly matching layers

The above described (finite) geometry is only a good representation of an infinite aluminium bar surrounded by infinite domains of air if we are able to eliminate all unwanted reflections from the edges. Therefore, an absorbing boundary is required that will delete somehow waves that strike it, without reflecting them, and without requiring infeasible resolution.

In 1994, Bérenger introduced the perfectly matching layer (PML) for electromagnetic waves [6]. A PML is an absorbing boundary layer of artificial absorbing material that is placed adjacent to the edges of the computational model. When a wave enters a PML, it is highly attenuated by the internal absorption within the layer where it decays exponentially, without reflections from the edges of the absorber. Although PMLs were originally derived for Maxwell's equations and thus very useful for electromagnetic simulations [22, 24, 36, 60], the same ideas are immediately applicable to acoustic [45] and elastic waves in isotropic [23, 33] and anisotropic materials [25].

The PML, introduced by Bérenger, has the advantage of having a null reflection coefficient at all angles of incidence and at all frequencies before discretization by a numerical scheme. However, in actual computations with discrete methods, an amount of numerical reflection always occurs, especially in the case of evanescent waves [7]. A more efficient implementation of Bérenger's PML, called the convolutional PML (CPML), was introduced in 2000 by Roden and Gedney [52]. This technique is based on the complex stretched-coordinate formulation [42] which is found to be highly effective at absorbing evanescent waves [8] and thus improves the behaviour of the discrete PML. The method was originally developed in first-order formulation for electromagnetism and was used in simulations of elastic wave propagation [16]. Later, the method was extended to the second-order system describing elastic waves in terms of displacements, which is, in frequency domain, very easy to implement in Comsol [15, 44]. Therefore, we opted to use this formulation to add PMLs in our model.

In figure 4.5, the added PMLs are illustrated by the thick black regions. These PMLs are added to the model by simply adapting the basic equations (4.3) to (4.7) for solids and (4.8), (4.9) and (4.12) for air as described in refs. [15, 44]. First, we rewrite the system in the frequency domain and use the following complex coordinates transformation [22]:

$$\widetilde{x} = \int_{0}^{x} s_x(x')dx' \tag{4.18}$$

and

$$\widetilde{y} = \int_{0}^{y} s_y(y')dy' \tag{4.19}$$

where s_x and s_y are the complex stretched-coordinate metrics proposed by Kuzuoglu and Mittra [42]:

$$s_x(x) = \kappa_x(x) + \frac{\sigma_x(x)}{\alpha_x(x) + i\omega} \tag{4.20}$$

$$s_y(y) = \kappa_y(y) + \frac{\sigma_y(y)}{\alpha_y(y) + i\omega} \tag{4.21}$$

where, $\sigma_x, \sigma_y, \alpha_x$ and α_y are assumed to be positive and real, and κ_x and κ_y are real and greater than or equal to one. The terms σ_x and σ_y are the attenuation factors that cause the amplitude of the propagating wave to be reduced exponentially inside the PML layer, κ_x and κ_y are scaling factors that will accelerate the decay of evanescent waves and α_x and α_y are frequency-shifted factors that make the attenuation frequency dependent. The main idea behind this approach is that any coordinate transformation of the governing equations in the solids and in air is equivalent to expressing them in traditional Cartesian coordinates with transformed materials that do not necessarily exist in the physical world. However, such materials are still useful in computer simulations for the absorption of outgoing energy. The spatial coordinate dependence of the discussed parameters in the x-direction is given by [44]:

$$\kappa_x(x) = 1 + \kappa_{max} \left(\frac{x - x_0}{d_x} \right)^{n_1} \tag{4.22}$$

$$\sigma_x(x) = \sigma_{max} \left(\frac{x - x_0}{d_x} \right)^{n_1 + n_2} \tag{4.23}$$

$$\alpha_x(x) = \alpha_{max} \left(\frac{d_x - x + x_0}{d_x} \right)^{n_3} \tag{4.24}$$

where x_0 and d_x are respectively the starting position and the thickness of the PML layer in the x-direction. Similar expressions can be given for the parameters κ_y, σ_y and α_y. In our implementation κ_{max} and α_{max} are set equal to zero, as in the classical PML case, and σ_{max} is defined as in Li et al. [44]:

$$\sigma_{max} = \frac{(1 + n_1 + n_2) v_L \log\left(\frac{1}{R_0}\right)}{2 d_x} \tag{4.25}$$

where v_L is the longitudinal wave velocity in the material under study and R_0 is the maximum value for the reflection coefficient we tolerate from the CPML. In the present model, $R_0 = 10^{-6}, n_1 = 3$ and $n_2 = 0$ has been chosen. The thickness parameters d_x and d_y of the PML-layers in x- and y-direction are set equal to respectively 3 mm and 0.9 mm.

Replacing x and y by the complex coordinates $\widetilde{x}$ and $\widetilde{y}$ in the basic equations (4.3) to (4.7) for solids and noting that:

$$\frac{\partial}{\partial \widetilde{x}} = \frac{1}{s_x} \frac{\partial}{\partial x} \tag{4.26}$$

$$\frac{\partial}{\partial \widetilde{y}} = \frac{1}{s_y} \frac{\partial}{\partial y} \tag{4.27}$$

we obtain the following frequency domain equations:

$$-\omega^2 \rho_{solid} \hat{u}_x = \frac{1}{s_x}\frac{\partial \hat{\tau}_{xx}}{\partial x} + \frac{1}{s_y}\frac{\partial \hat{\tau}_{xy}}{\partial y} \tag{4.28}$$

$$-\omega^2 \rho_{solid} \hat{u}_y = \frac{1}{s_x}\frac{\partial \hat{\tau}_{xy}}{\partial x} + \frac{1}{s_y}\frac{\partial \hat{\tau}_{yy}}{\partial y} \tag{4.29}$$

$$\hat{\tau}_{xx} = \frac{\lambda + 2\mu}{s_x}\frac{\partial \hat{u}_x}{\partial x} + \frac{\lambda}{s_y}\frac{\partial \hat{u}_y}{\partial y} \tag{4.30}$$

$$\hat{\tau}_{yy} = \frac{\lambda}{s_x}\frac{\partial \hat{u}_x}{\partial x} + \frac{\lambda + 2\mu}{s_y}\frac{\partial \hat{u}_y}{\partial y} \tag{4.31}$$

$$\hat{\tau}_{xy} = \mu\left(\frac{1}{s_y}\frac{\partial \hat{u}_x}{\partial y} + \frac{1}{s_x}\frac{\partial \hat{u}_y}{\partial x}\right) \tag{4.32}$$

where $\hat{u}_i$ and $\hat{\tau}_{ij}$ are the Fourier transforms of respectively the (in-plane) components of the particle displacement and the components of the stress tensor $(i, j \in \{x, y\})$. In order to facilitate the implementation of the resulting second-order CPML wave equations in Comsol, we introduce a new density ρ'_{solid} equal to $\rho_{solid} s_x s_y$ and a new set of stress variables $\hat{\tau}'_{ij}$ $(i, j \in \{x, y\})$, defined as:

$$\hat{\tau}'_{xx} = \hat{\tau}_{xx} s_y = (\lambda + 2\mu)\frac{s_y}{s_x}\frac{\partial \hat{u}_x}{\partial x} + \lambda\frac{\partial \hat{u}_y}{\partial y} \tag{4.33}$$

$$\hat{\tau}'_{yy} = \hat{\tau}_{yy} s_x = \lambda\frac{\partial \hat{u}_x}{\partial x} + (\lambda + 2\mu)\frac{s_x}{s_y}\frac{\partial \hat{u}_y}{\partial y} \tag{4.34}$$

$$\hat{\tau}'_{xy} = \hat{\tau}_{xy} s_x = \mu\left(\frac{s_x}{s_y}\frac{\partial \hat{u}_x}{\partial y} + \frac{\partial \hat{u}_y}{\partial x}\right) \tag{4.35}$$

$$\hat{\tau}'_{yx} = \hat{\tau}_{xy} s_y = \mu\left(\frac{\partial \hat{u}_x}{\partial y} + \frac{s_y}{s_x}\frac{\partial \hat{u}_y}{\partial x}\right) \tag{4.36}$$

Multiplying equations (4.28) and (4.29) by $s_x s_y$, we can reconstruct the equations of motion and rewrite them in the following form:

$$-\omega^2 \rho'_{solid} \hat{u}_x = \frac{\partial \hat{\tau}'_{xx}}{\partial x} + \frac{\partial \hat{\tau}'_{xy}}{\partial y} \tag{4.37}$$

$$-\omega^2 \rho'_{solid} \hat{u}_y = \frac{\partial \hat{\tau}'_{yx}}{\partial x} + \frac{\partial \hat{\tau}'_{yy}}{\partial y} \tag{4.38}$$

In matrix form, this can be written as:

$$\nabla \cdot \begin{pmatrix} \hat{\tau}'_{xx} & \hat{\tau}'_{yx} \\ \hat{\tau}'_{xy} & \hat{\tau}'_{yy} \end{pmatrix} = \begin{pmatrix} -\omega^2 \rho'_{solid} \hat{u}_x \\ -\omega^2 \rho'_{solid} \hat{u}_y \end{pmatrix} \tag{4.39}$$

corresponding to the general form (3.1) of the PDE modes in COMSOL.

The same can be done for the equations in air. Taking the Fourier transform of the equations of motion (4.8) and (4.9) and the continuity equation (4.12) and using the complex coordinate transformation and stretched-coordinate metrics as for the solids, we obtain the following frequency domain equations:

$$\hat{a}_x = -\frac{1}{\rho_{air}} \frac{1}{s_x} \frac{\partial \hat{p}}{\partial x} \tag{4.40}$$

$$\hat{a}_y = -\frac{1}{\rho_{air}} \frac{1}{s_y} \frac{\partial \hat{p}}{\partial y} \tag{4.41}$$

$$\frac{\omega^2}{\rho_{air} v_{air}^2} \hat{p} = \frac{1}{s_x} \frac{\partial \hat{a}_x}{\partial x} + \frac{1}{s_y} \frac{\partial \hat{a}_y}{\partial y} \tag{4.42}$$

where $\hat{p}$ and $\hat{a}_i$ are the Fourier transforms of respectively the pressure in air and the (in-plane) components of the particle acceleration ($i \in \{x, y\}$). As for the solids, new variables are introduced for an easy implementation in COMSOL. The new components of the particle acceleration $\hat{a}'_i$ ($i \in \{x, y\}$) are defined as:

$$\hat{a}'_x = \hat{a}_x s_y = -\frac{1}{\rho_{air}} \frac{s_y}{s_x} \frac{\partial \hat{p}}{\partial x} \tag{4.43}$$

$$\hat{a}'_y = \hat{a}_y s_x = -\frac{1}{\rho_{air}} \frac{s_x}{s_y} \frac{\partial \hat{p}}{\partial y} \tag{4.44}$$

Finally, multiplying equation (4.42) by $s_x s_y$, we get:

$$\frac{\partial \hat{a}'_x}{\partial x} + \frac{\partial \hat{a}'_y}{\partial y} = \frac{\omega^2 s_x s_y}{\rho_{air} v_{air}^2} \hat{p} \tag{4.45}$$

which, in matrix form, can be written as:

$$\nabla \cdot \begin{pmatrix} \hat{a}'_x \\ \hat{a}'_y \end{pmatrix} = \frac{\omega^2 s_x s_y}{\rho_{air} v_{air}^2} \hat{p} \tag{4.46}$$

which is also corresponding to the general form (3.1) of the PDE modes in Comsol. Both equations (4.39) and (4.46) will be solved with Comsol in frequency domain.

Boundary conditions

The boundary conditions that need to be implemented at the interface between the solid sections and the ambient air represent continuity of the normal displacements, continuity of the normal stress components and zero tangential stress. Between the aluminium test sample and the sound absorbing material continuity of normal and tangential displacements and continuity of normal and tangential stress components is assumed. For all other boundaries, except at the active surface of the transmitter, we use stress-free conditions.

At the transmitter, the normal acceleration component (expressed in frequency space) is set to a frequency dependent amplitude multiplied by a generalized Gaussian function spatially distributed over the length of the transmitter's surface. The multiplication with a generalized Gaussian function is used to avoid numerical problems. The Gaussian function establishes a smooth transition between values at the edge of the boundary. The frequency dependence of the source allows to simulate the generation and response for different signals by solving the equations in frequency domain for a discrete representation of the spectral content of the signals. For example, the chirp signal (4.2) used in the pitch-catch experiments is first Fourier transformed. The temporal evolution and the amplitude of the Fourier transform of the chirp signal are shown in figure 4.7. Then, a selection of discrete frequencies within this spectrum, starting from 610 kHz to 890 kHz, separated by 5 kHz, is used as a parametric input for the boundary condition at the source. To get the time domain result, an inverse Fourier transform can be done using the Matlab software.

Meshing and solving

In order to obtain an accurate solution within an acceptable computation time, we choose a subdomain dependent triangular mesh in which the maximum element size in the aluminium bar is larger than the maximum element size in air, because of the larger wavelength in aluminium. The mesh size is chosen to be fine enough (i.e. less than 1/5th of the minimal wavelength) for an accurate solution at all frequencies of interest.

Once the mesh is defined, the model is solved using second-order Lagrange elements. Several calculations are performed, using a discrete sweep over the

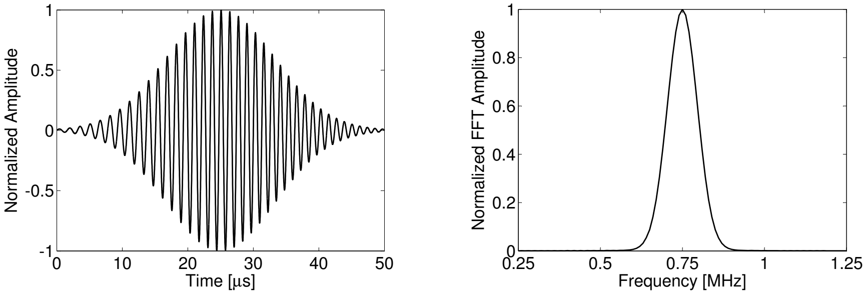

(a) (b)

Figure 4.7: Temporal evolution (a) and Fourier transform (b) of the chirp signal (4.2) used for the pitch-catch experiments. The frequency dependent amplitude is used as input for the source function in the finite element simulation.

relevant range of source frequencies. For every value of the source frequency, the solution is determined within Comsol. The result obtained for a continuous wave (CW) excitation at 750 kHz, corresponding to a snapshot in time, is shown in figure 4.8. The (real part of the) pressure field inside the air domains and the vertical stress component $-\tau_{yy}$ inside the solid domains are shown. We clearly see how the sound signal, generated by the transmitter at an angle of incidence of 4.5°, propagates through air, enters the aluminium test sample at a different angle, reflects from the bottom-wall of the test sample and is finally captured by the receiver in the first reflection maximum. Of course, the receiver can equally be placed in the second reflection maximum. Note also the strong interference of up- and down-going waves in the air near the transmitter, and the relatively tiny amount of energy (almost invisible) going to the receiver. The bottom figure shows a zoom of the top figure. In this figure the triangular mesh and the wavelengths in air and aluminium are indicated. We clearly see that the mesh is subdomain dependent and that the maximum mesh size is less than 1/5th of the wavelength in each subdomain.

In the experimental setup of the aluminium bar with a borehole, the received signals are recorded while the aluminium test sample is progressively moving in the x- and z-direction. In this simulation, the surface scanning is replaced by moving the position of the borehole in the horizontal direction (the z-direction movement is irrelevant for the 2D simulation), and by subsequently recording the signal and analysing its strength at the receiver for every position of the borehole. For the signal strength calculation we apply the following formula

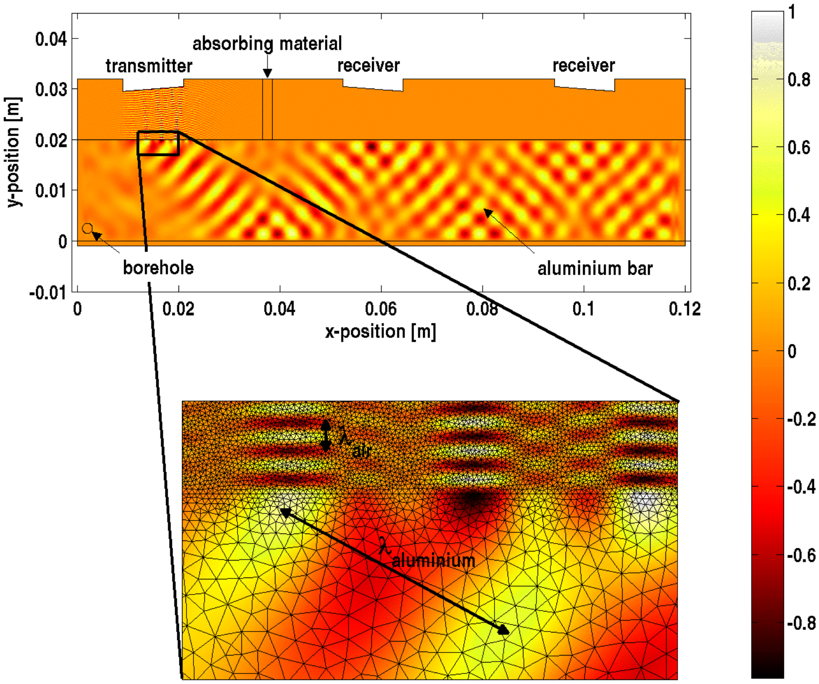

Figure 4.8: Visualization of the real part of the pressure field p in air and the vertical stress component $-\tau_{yy}$ in the solids simulated by the finite element simulation in Comsol. The solution is obtained for a continuous wave (CW) excitation at 750 kHz. The bottom figure shows a zoom of the top figure. In this figure, the triangular mesh and the wavelengths in air and aluminium are indicated. The colour scale is normalized according to its maximum value.

which represents the integrated response using Parceval's identity:

$$IR = \sum_f \left(\int_x \mid a_\perp(f,x) \mid^2 dx \right) \tag{4.47}$$

where $a_\perp(f,x)$ denotes the normal component of the particle acceleration at point x on the receiver's surface obtained as the response of a CW signal with excitation frequency f. The integral in the above equation runs over all points of the receiver, while the sum is taken over the relevant source frequencies used in the simulation.

In figure 4.9(a), we plotted the simulated integrated response measured by a receiver moving parallel to the aluminium bar, in the absence of a borehole. The

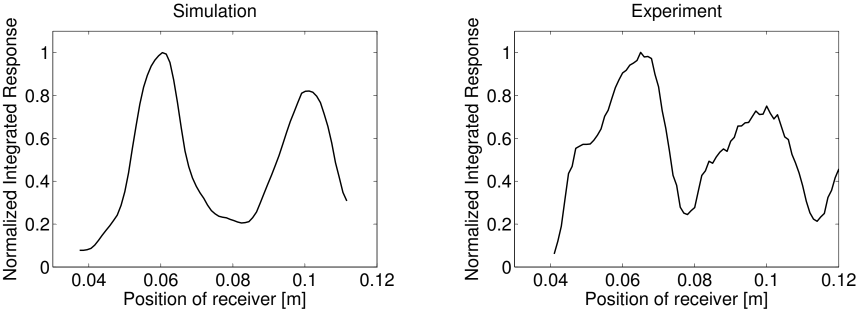

(a) (b)

Figure 4.9: Simulated (a) and experimentally measured (b) integrated response as a function of the position of a receiver moving parallel to the aluminium bar. The results are obtained for a chirp excitation with central frequency $f_c = 750$ kHz, bandwidth $B = 250$ kHz and pulse duration $T = 50$ μs, transmitted by a transducer fixed in space and positioned at the same side of the aluminium bar as the receiver. Maximum responses are measured in the first and second reflection maximum.

results are obtained for a chirp signal with Gaussian envelope, pulse duration $T = 50$ μs, central frequency $f_c = 750$ kHz and bandwidth $B = 250$ kHz, transmitted by a transducer fixed in space and positioned at the same side of the aluminium bar as the receiver. The simulated results can be compared to the experimentally measured integrated response, shown in figure 4.9(b). In both cases, the positions where the maximum responses are measured correspond to the theoretical determined positions of respectively the first and second reflection maximum.

4.4 Comparison between simulations and observations

Both simulation methods are verified by comparing the model predictions with the basic observations from the air-coupled pitch-catch experiments. The input parameters for the models match as close as possible the experimental material parameters discussed in section 4.2. As we will show, the qualitative agreement between observations and simulations is good, which provides potential for both simulation methods to be used in further analysis and interpretation of this relatively simple case, and for the consideration of more complicated cases.

4.4.1 Measurements in first and second reflection maximum

Figure 4.10 shows results from the first experimental setup where the borehole in the aluminium bar is positioned at 6 mm from the top-side and the receiver is positioned in the first reflection maximum (figure 4.10(a)). While the bar is moving in the x-direction, the borehole passes first through the incident beam and subsequently through the reflected beam. The two passages of the borehole through the sound field cause two well-separated scanning zones of reduced intensity in the measurements of the integrated response, plotted in figure 4.10(b). From the experiments, it was clear that the movement in the z-direction does not influence the scan-result [12, 13], which implies that a 2D representation/simulation is quite acceptable. Figures 4.10(c) and 4.10(d) display the results of the 1D line-scan for the 2D simulations of this experiment. For both the shadow method and the COMSOL simulation the measured response is plotted against the x-position of the borehole. Both simulations show two well-separated zones of intensity reduction at the receiver, in good agreement with the experimental observations. The differences in the positions of the minima in the experimental and simulation results can be attributed to small differences in the sound beam width and/or the borehole position between the experiment and the simulation.

In figure 4.11(a) we consider the same experimental setup as above, only the receiver is now positioned in the second reflection maximum. In this case, the borehole passes the sound field four times, with a large overlap between the second and the third passage. Three well-separated instances of reduced intensity are visible in the response plot in figure 4.11(b), with the middle zone exhibiting a larger width due to the overlap. The corresponding simulation results in figures 4.11(c) and 4.11(d) show the same three well-separated reductions of intensity. The small peak in the middle of the second intensity minimum for the shadow method simulation is due to the Gaussian nature of the beam. Since the borehole passes the sound field at the edge of the intersecting beams where the energy of both the incoming and reflected signal is diminished, the diminution will be reduced, producing a small interspersed peak. The interspersed peak is less obvious in the COMSOL simulation because of diffraction effects which are automatically accounted for.

In figure 4.12(a) the aluminium test sample is flipped upside-down, and the borehole is now at 14 mm from the top-side of the sample. As in figure 4.10(a) the receiver is positioned in the first reflection maximum. While the bar is moving, the borehole passes the sound field twice, with a large overlap between the incoming and the reflected beam. This results in the observation of a single broad zone of enhanced intensity reduction in the response plot in figure 4.12(b). The corresponding simulation results in figures 4.12(c) and 4.12(d) are in good

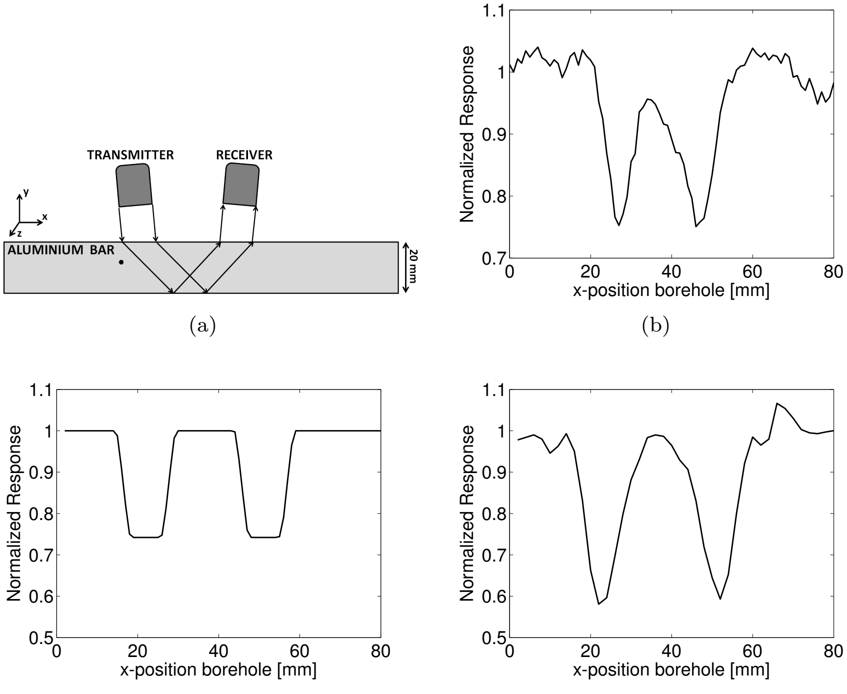

(a) (b)

(c) (d)

Figure 4.10: (a) Experimental setup: aluminium bar with borehole at 6 mm from the top-side. The receiver is positioned in the first reflection maximum. (b) Measured integrated response averaged over all z-positions. (c) Simulated integrated response calculated with the shadow method. (d) Simulated integrated response calculated with the finite element method implemented in COMSOL.

agreement with the observations. In both simulations we obtain one relatively broad minimum, with a peak in the middle caused by the partial overlap.

Finally, in figure 4.13(a), we moved the receiver to the second reflection maximum. The borehole is still at 14 mm from the top-side of the sample. Upon moving the bar in the x-direction, the hole again passes the beam four times, however, due to the overlap only two minima can be observed in the response plot in figure 4.13(b). Figures 4.13(c) and 4.13(d) again show a relatively good agreement between observations and simulations. In both simulations two well-separated zones of intensity reduction can be identified, with interspersed peaks in the middle of each minimum.

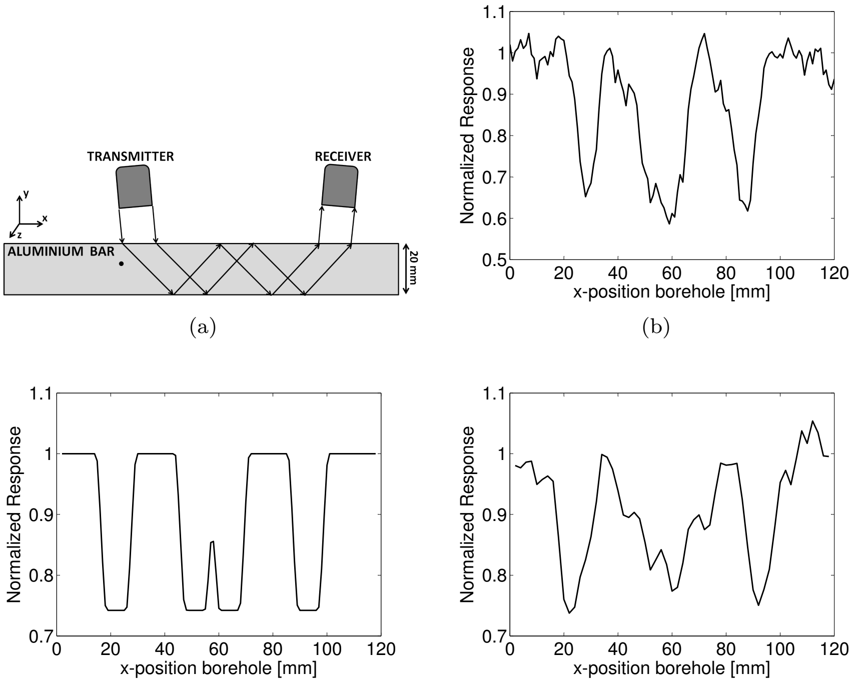

(a) (b)

(c) (d)

Figure 4.11: (a) Experimental setup: aluminium bar with borehole at 6 mm from the top-side. The receiver is positioned in the second reflection maximum. (b) Measured integrated response averaged over all z-positions. (c) Simulated integrated response calculated with the shadow method. (d) Simulated integrated response calculated with the finite element method implemented in COMSOL.

In order to show that the interspersed peaks occurring in the COMSOL simulated integrated responses from figures 4.12(d) and 4.13(d) are indeed due to the Gaussian nature of the beam, we calculated the integrated response in the case of a borehole at 15 mm from the top-side of the aluminium bar. Since the borehole is now one millimetre closer to the back-wall of the sample, it passes the intersecting beams of the sound field at a position where the energy of the incoming and reflected signal is less diminished than in the previous case. Therefore, we expect the interspersed peaks to be less obvious than in the case of a borehole at 14 mm from the top-side of the sample. In figure 4.14, the simulation results for the integrated response in the first and second reflection maximum are plotted. In the response measured at the first reflection maximum, the interspersed peak is still quite obvious, however, comparing this result with

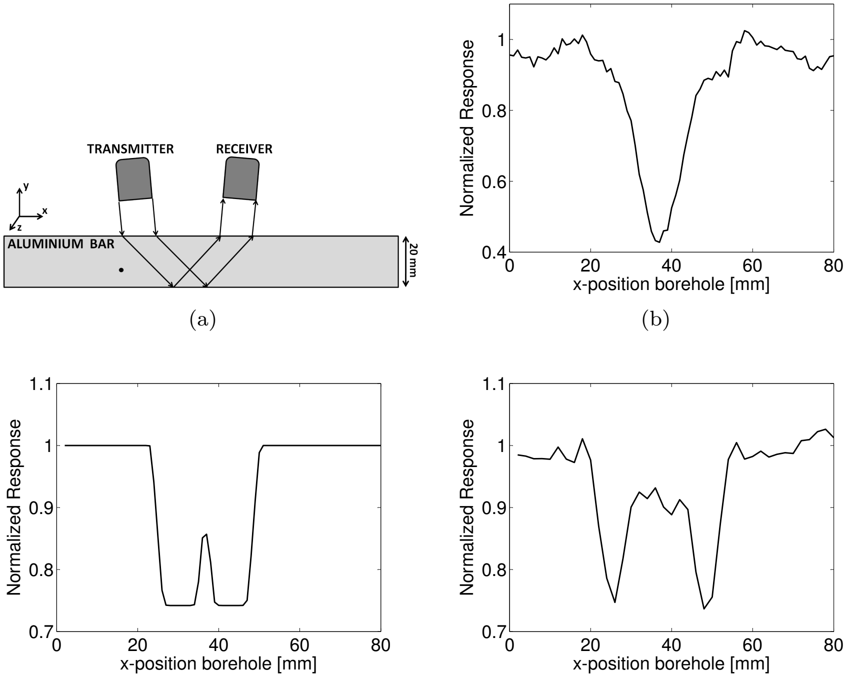

(a) (b)

(c) (d)

Figure 4.12: (a) Experimental setup: aluminium bar with borehole at 14 mm from the top-side. The receiver is positioned in the first reflection maximum. (b) Measured integrated response averaged over all z-positions. (c) Simulated integrated response calculated with the shadow method. (d) Simulated integrated response calculated with the finite element method implemented in COMSOL.

the one from figure 4.12(d), we see that the zone where the interspersed peak occurs has become smaller. In the response measured at the second reflection maximum, the interspersed peaks have almost totally disappeared.

In all four basic cases considered above, we found a good qualitative agreement between observations and simulations. The further the receiver is positioned from the transmitter, the more ultrasonic images of the defect can be observed, since the defect then passes the sound field multiple times. If the defect passes the sound field at positions where two beams intersect, the zone of reduced intensity becomes broader. Using this scanning technique, we are able to determine the actual location of the defect, i.e. close to the top-side of the sample or close to the bottom-side of the sample.

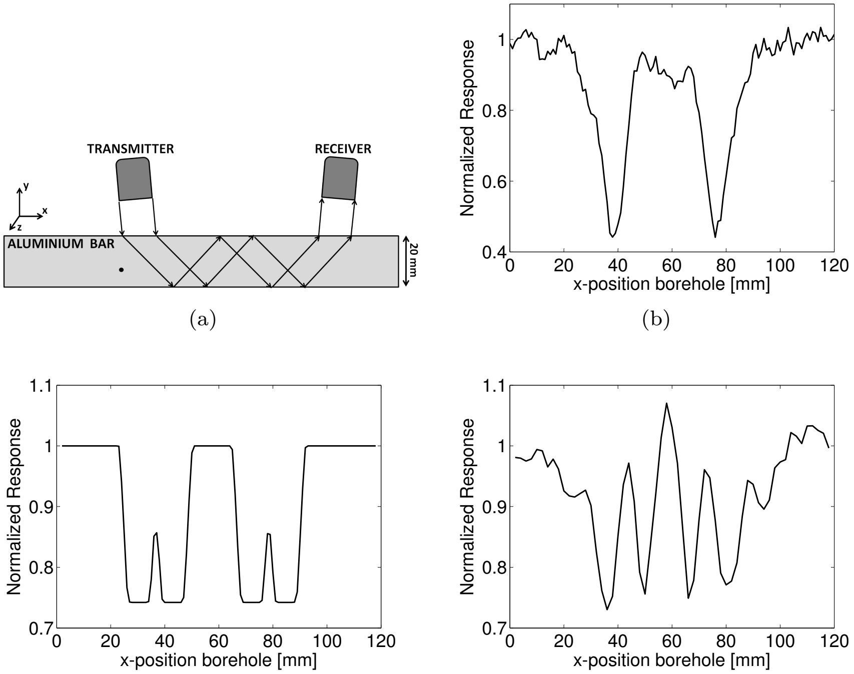

(a) (b)

(c) (d)

Figure 4.13: (a) Experimental setup: aluminium bar with borehole at 14 mm from the top-side. The receiver is positioned in the second reflection maximum. (b) Measured integrated response averaged over all z-positions. (c) Simulated integrated response calculated with the shadow method. (d) Simulated integrated response calculated with the finite element method implemented in COMSOL.

Both simulation methods can now be exploited to help interpret experimental results in more complex conditions, and/or to make simple predictions about such results. However, for a simulation closely linked to reality, we prefer to work with the COMSOL simulation instead of the shadow method because less simplifications have been introduced in former method. Therefore, in the next subsections we only use the COMSOL simulation to predict the influence of the vertical position of the borehole and to link these observations to the sound field inside the aluminium bar. In the last subsection, both simulation methods will be used to investigate the asymmetry effects due to a rectangular inclusion.

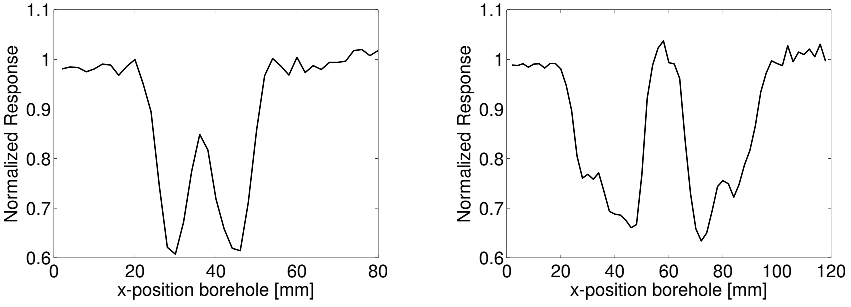

(a)

(b)

Figure 4.14: Simulated integrated response for an aluminium bar with borehole at 15 mm from the top-side and receiver in (a) the first reflection maximum and (b) the second reflection maximum. The simulation method is the finite element method implemented in COMSOL.

4.4.2 Effects of the borehole's vertical position

In the previous experiments and simulations the borehole was positioned either at 6 mm or at 14 mm from the top-side of the aluminium test sample and its location with respect to the emitter and receiver was only changed in the horizontal direction (x-direction). With the developed simulation tool, we are perfectly able to simulate additional subtle effects occurring when the borehole's position is altered in vertical direction (y-direction).

To investigate these effects, we calculated the integrated response using the COMSOL simulation for any arbitrary position (x, y) of the borehole in the aluminium bar, with the y-position running from 2.5 mm to 17.5 mm from the bottom-wall. The results representing the IR as a function of the borehole position can be visualized in a colour coded image as in figure 4.15. Each horizontal line in the colour coded image represents a horizontal scan of the IR for a particular depth of the borehole indicated on the vertical scale. Here, the response measurements in the first and the second reflection maximum are shown for a CW excitation at 750 kHz. High responses are shown in white, low responses are shown in black. These figures allow to interpret and appreciate the results discussed in the previous section in a more general sense. For receiver measurements in the first reflection maximum (figure 4.15(a)), two minima in the integrated response are visible if the borehole is close to the top-wall. As the borehole is located deeper into the aluminium bar, both reductions will occur more quickly after each other. Eventually, only one enlarged zone of reduced intensity is visible if the borehole is close to the bottom-wall. The slight increase

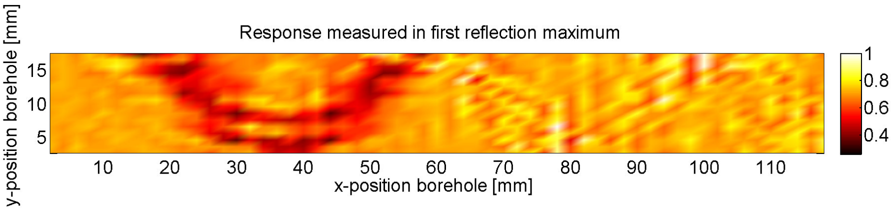

(a)

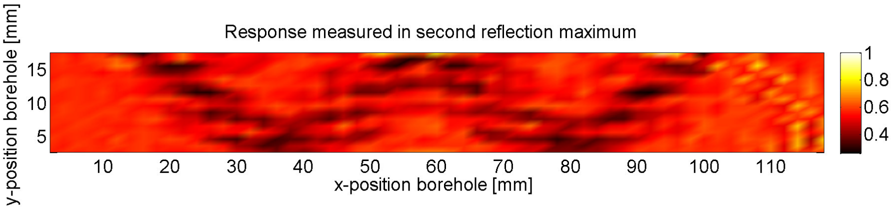

(b)

Figure 4.15: Integrated response as a function of the (x, y)-position of the borehole, calculated in (a) the first reflection maximum and (b) the second reflection maximum. The results are obtained for a CW excitation at 750 kHz. The lowest responses are shown in black. The colour scales are normalized according to the maximum response measured in the first reflection maximum.

of intensity for x greater than 60 mm is due to backscattering of the sound wave from the borehole. For measurements in the second reflection maximum (figure 4.15(b)), four reductions in the integrated response are visible if the borehole is located in the middle of the bar. For higher positions (near the top-wall of the bar) this reduces to three zones of reduced intensity with the middle zone exhibiting a larger width. For lower positions (near the bottom-wall of the bar) only two enlarged zones of reduced intensity are visible.

4.4.3 Link with Lamb mode generation

A close look at the above mentioned colour coded images reveals that regions with high intensity reduction alternate regions with practically no diminution, creating a wavy pattern in the response plot. We can appreciate this wave behaviour by comparing the images with the patterns of the horizontal (u_x) and vertical (u_y) displacement inside the aluminium test sample. This is done for a 750 kHz CW excitation in figure 4.16. Note that the displacement patterns display a strikingly similar structure as the wavy pattern in the response plots. Moreover, the displacement patterns resemble that of a typical Lamb wave.

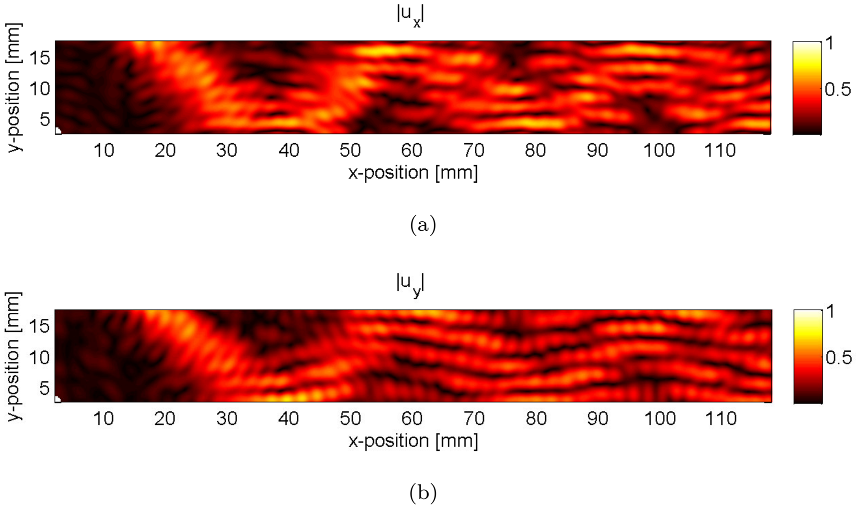

Figure 4.16: Amplitude of (a) the simulated horizontal displacement u_x and (b) the vertical displacement u_y inside the aluminium test sample in the case of a CW excitation at 750 kHz with a finite size transducer. The colour scale in each figure is normalized according to its maximum value. Low amplitudes are shown in black.

From the zigzagging wave model discussed in section 2.2.3, we concluded that a broad beam was needed to efficiently create a Lamb wave. However, in our simulation, as well as in the experiment, the transmitter is too small in order to create a true Lamb wave pattern. As can be appreciated from figure 4.16, the overlap of up- and down-going waves inside the solid medium is not complete, and consequently, the interference is not optimal.

Suppose, however, that we would redo the same experiment using a relatively large transmitter emitting a CW at 678687 Hz. In that case, we would create a particular situation in which a pure A_3 Lamb mode is generated in the aluminium bar (see dispersion curves in figure 2.5). Figures 4.17(a) and 4.17(b) show the corresponding cross-sectional distribution of the horizontal and vertical displacements in the aluminium plate. After a certain distance a steady pattern is established. Figure 4.17(c) represents the calculations of the integrated response when a borehole is moved in horizontal and vertical direction within the rectangle indicated in the top figures. As in the previous example (for 750 kHz signal generated by a small transducer) both images display similar patterns.

Hence, when performing experiments, the observed response plot will highly depend on the generated Lamb wave inside the solid. Depending on the position

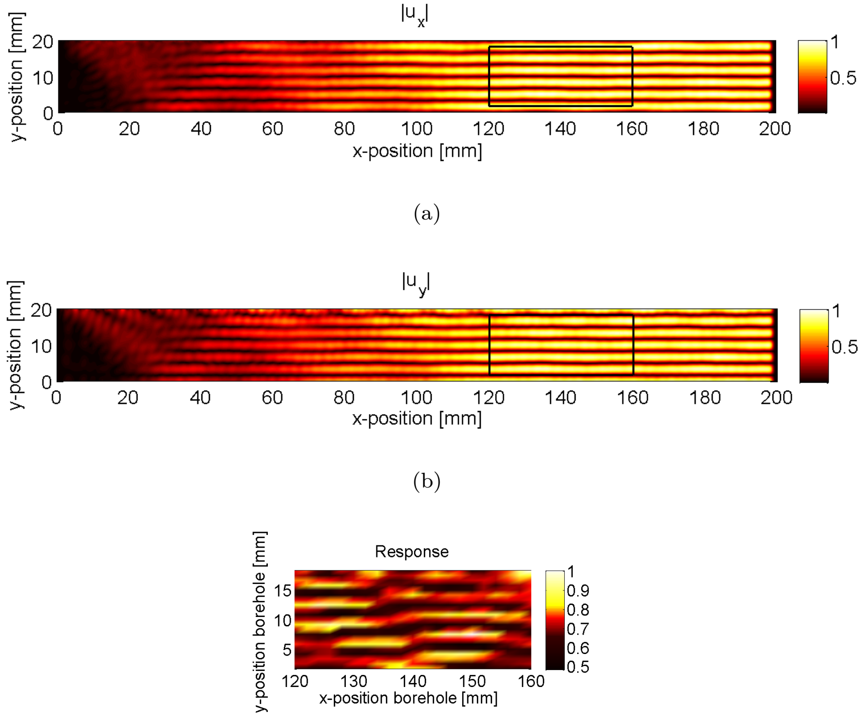

(a)

(b)

(c)

Figure 4.17: Amplitude of (a) the simulated horizontal displacement u_x and (b) the vertical displacement u_y inside the aluminium test sample in the case of a CW excitation at 678687 Hz (A_3 Lamb mode) for a large aperture transducer. The colour scale in each figure is normalized according to its maximum value. Low amplitudes are shown in black. (c) The integrated response measured for this A_3 Lamb mode as a function of the (x, y) position of the borehole. The lowest responses are shown in black. The possible positions of the borehole are indicated by the rectangle in the top figures.

of the borehole or defect, it may be located in a node line of the Lamb wave and therefore cannot be detected. For example in figure 4.17(c), a borehole that is exactly centred in the aluminium bar cannot be detected with the anti-symmetric A_3 Lamb wave since it is positioned in a node point of the generated Lamb wave and therefore no decrease in the response will be measured. The use of swept signals can avoid this problem as in that case, multiple Lamb modes are generated in the sample. It is worth noting that it is absolutely impossible to attain a similar interpretation of these results based on the shadow method.

4.4.4 Rectangular inclusion

The above results indicate that the finite element model is a beneficial tool for the interpretation of experimental observations. Hence, the method can also be used to make simple predictions of experimental results. An example is considered in this subsection.

Suppose the circular inclusion in the aluminium bar is replaced by a 5 cm deep drilled rectangular inclusion of dimensions 2 mm × 1 mm. Using both the shadow method and the COMSOL simulation, we can investigate the scanned response when the rectangular inclusion is displaced. In addition, we have studied the influence of its inclination. Three cases are considered: (1) the inclusion stands horizontally, with the 2 mm side parallel to the top-wall of the aluminium bar (figures 4.18 and 4.19); (2) the inclusion is rotated by $-46.24°$, which corresponds to the angle of the incident (down-going) sound beam inside the aluminium sample with respect to the normal (figures 4.20 and 4.21); and (3) the inclusion is rotated by $46.24°$, which corresponds to the angle the reflected (up-going) sound beam makes inside the sample with respect to the normal (figures 4.22 and 4.23). An obvious difference in the response plots between the three results can be observed.

Figures 4.18 and 4.19 show the results for a rectangular inclusion standing horizontally at 6 mm or 14 mm from the top-side. In figure 4.18 the receiver is positioned in the first reflection maximum, while in figure 4.19 the receiver is positioned in the second reflection maximum. As for the circular borehole, ultrasonic images of the defect can be observed if the defect passes the sound field. For a horizontal rectangular inclusion, the intensity reduction is independent whether the rectangular inclusion passes the incident beam or the reflected beam. The obstruction is identical for the incident and the reflected beam, since the projection of the object on the wave front is the same. This results in a fairly symmetric result in all response plots.

Figures 4.20 and 4.21 show the results for a rectangular inclusion inclined at $-46.24°$ and positioned at 6 mm or 14 mm from the top-side of the sample. In figure 4.20, the integrated response was measured by a receiver in the first reflection maximum, while in figure 4.21 the receiver was positioned in the second reflection maximum. In figure 4.20, we see that the passage of the inclusion through the incident beam causes less diminution than when the inclusion passes the reflected beam. The explanation for this difference is obviously found in the orientation of the inclusion. The incident wave front is blocked by the small side of the rectangular inclusion, while the reflected beam is blocked by the long side of the rectangular inclusion, resulting in asymmetric response plots. The same behaviour is found when the receiver is moved to the

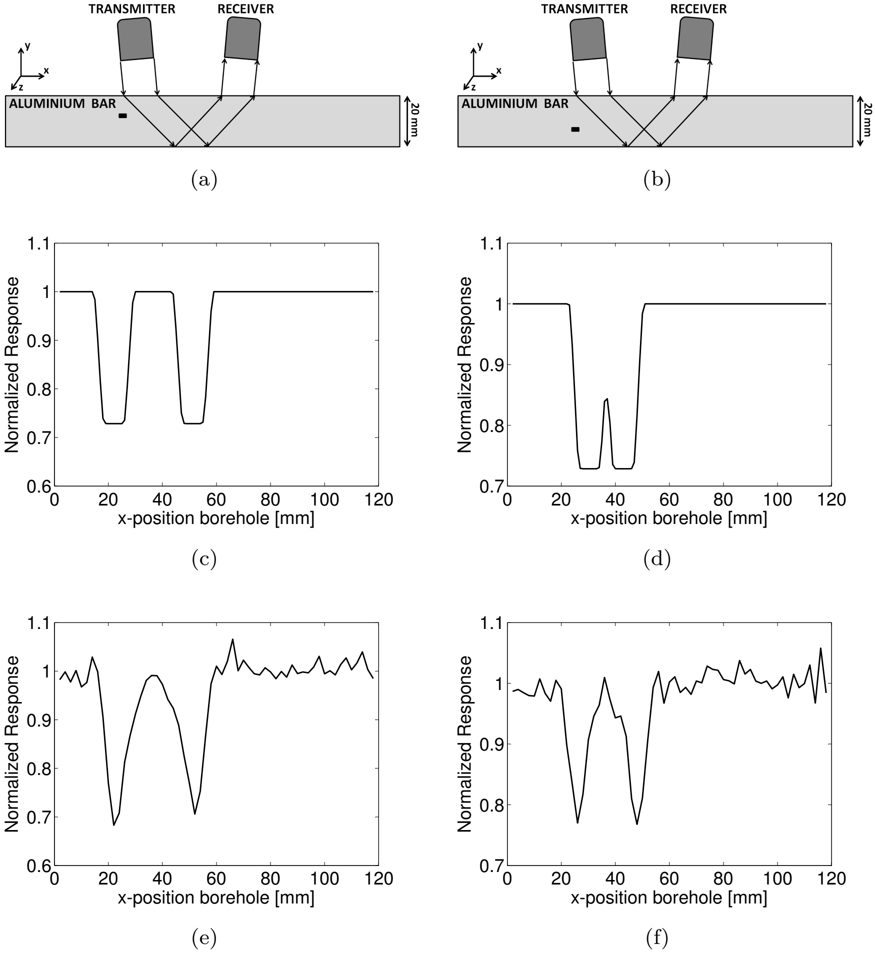

Figure 4.18: (a-b) Experimental setup: aluminium bar with rectangular inclusion at respectively 6 mm and 14 mm from the top-side and parallel to the top-wall. The receiver is positioned in the first reflection maximum. (c-d) Simulated integrated response for a rectangular inclusion at respectively 6 mm and 14 mm from the top-side calculated with the shadow method. (e-f) Simulated integrated response for a rectangular inclusion at respectively 6 mm and 14 mm from the top-side calculated with the finite element method implemented in COMSOL.

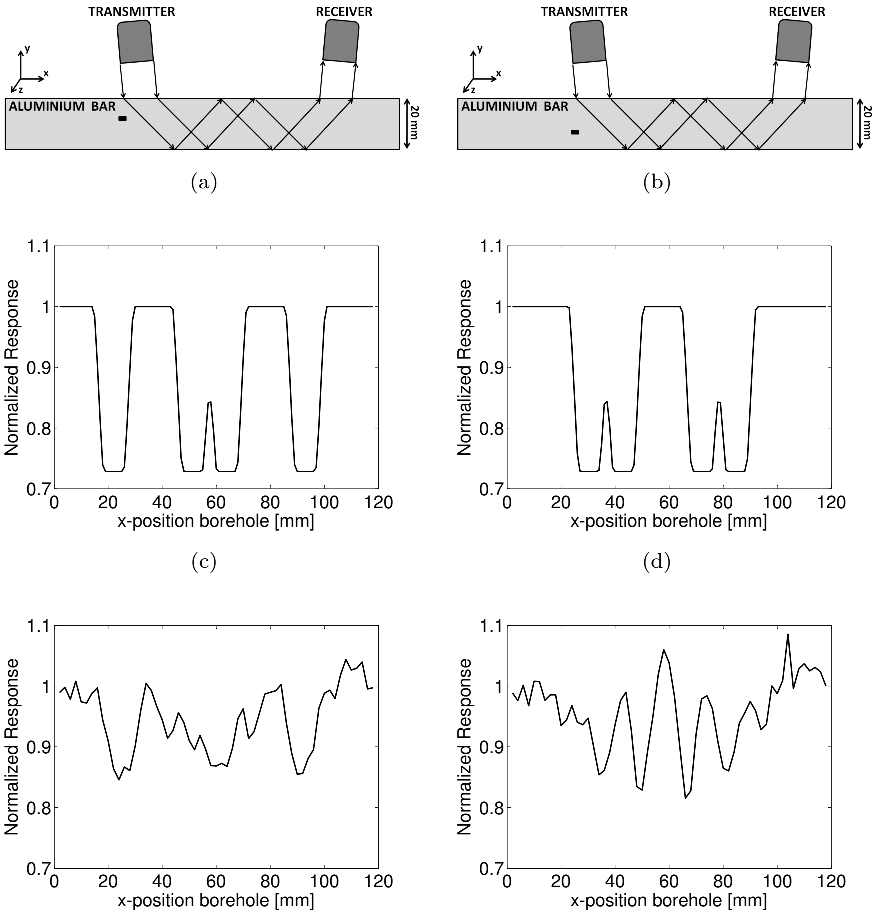

(a) (b) (c) (d) (e) (f)

Figure 4.19: (a-b) Experimental setup: aluminium bar with rectangular inclusion at respectively 6 mm and 14 mm from the top-side and parallel to the top-wall. The receiver is positioned in the second reflection maximum. (c-d) Simulated integrated response for a rectangular inclusion at respectively 6 mm and 14 mm from the top-side calculated with the shadow method. (e-f) Simulated integrated response for a rectangular inclusion at respectively 6 mm and 14 mm from the top-side calculated with the finite element method implemented in COMSOL.

second reflection maximum in figure 4.21. The diminution due to the beams blocked by the long side of the rectangular inclusion is much larger than the reduction caused by the beams blocked by the small side of the inclusion.

Finally, figures 4.22 and 4.23 show the results for a rectangular inclusion inclined at 46.24° and positioned at 6 mm or 14 mm from the top-side of the sample. The integrated response was again measured in the first (figure 4.22) and second (figure 4.23) reflection maximum. In figure 4.22, the opposite of figure 4.20 is observed. A passage of the inclusion through the reflected beam causes less diminution than a passage through the incident beam, since the reflected beam is blocked by the small side and the incident beam is blocked by the long side of the inclusion. Also in figure 4.23, where the response was measured in the second reflection maximum, the same behaviour was observed.

Experimental verification of the observed asymmetries is shown in figure 4.24. Figure 4.24(a) illustrates the line scan results obtained for the aluminium sample in which the rectangular inclusion stands horizontally, at 6 mm from the top surface of the sample. The response was measured in the first reflection maximum. This case corresponds to the simulations from figures 4.18(c) and 4.18(e). Two well-separated zones of increased intensity reduction are clearly visible, caused by two passages of the inclusion through the sound field, while the bar is moving. As predicted by the models, there is no difference between both reductions. Figures 4.24(b) and 4.24(c) on the other hand, show the experimental line scan observations for the samples with a rectangular inclusion drilled at an angle of respectively $-46.24°$ and 46.24°. Again, two zones of increased intensity reduction are visible, corresponding to the two passages of the inclusion through the sound field. The predicted asymmetry between both intensity reductions can be clearly seen. In figure 4.24(b), the first reduction is caused by the obstruction of the incident beam by the small side of the inclusion, while the second reduction is caused by the obstruction of the reflected beam by the long side of the rectangular inclusion. In figure 4.24(c), the opposite is observed. The first reduction is caused by the obstruction of the incident beam by the long side of the inclusion, while the second reduction is caused by the obstruction of the reflected beam by the small side of the rectangular inclusion. The finite element model is thus a valuable tool for the prediction of experimental results. We conclude that it must be possible to empirically infer the orientation of a rectangular inclusion just by measuring the response in one of the reflection maxima by means of an air-coupled pitch-catch configuration.

Using the COMSOL simulation, we can investigate the scanned response when the rectangular inclusion is displaced not only in the horizontal but also in the vertical direction. In figure 4.25, the integrated response is plotted as a function of the (x, y)-position for respectively a rectangular inclusion that stands horizontally, a rectangular inclusion inclined at $-46.24°$ and a rectangular

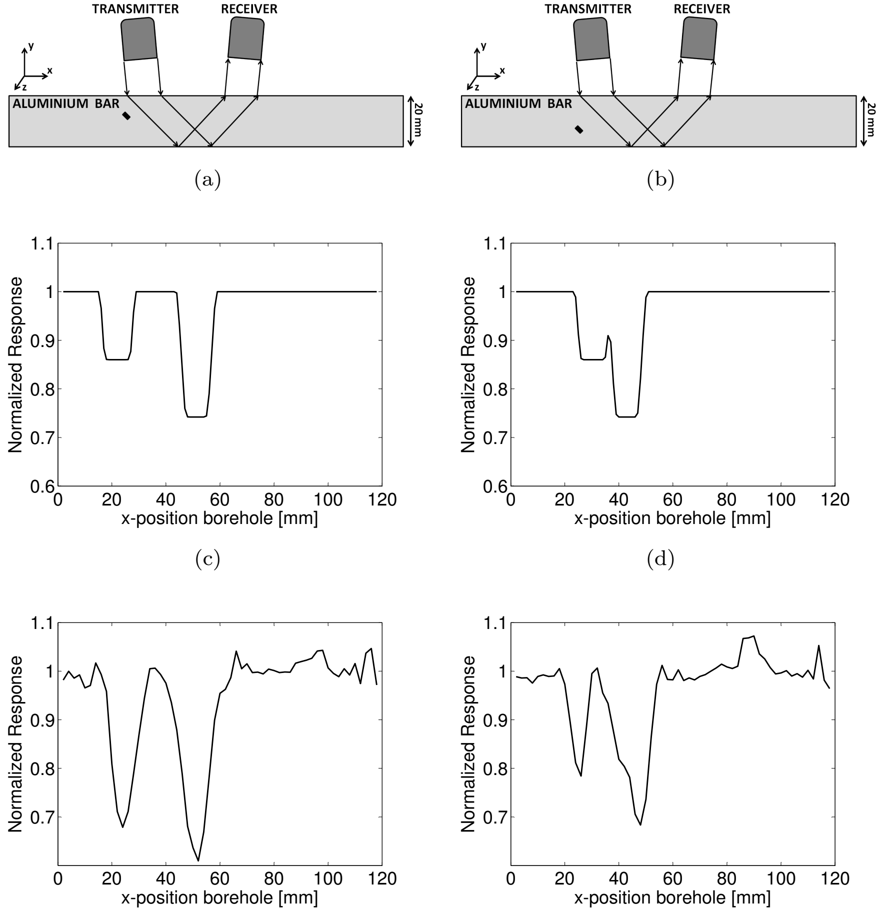

(a) (b)

(c) (d)

(e) (f)

Figure 4.20: (a-b) Experimental setup: aluminium bar with rectangular inclusion, inclined at −46.24°, at respectively 6 mm and 14 mm from the top-side. The receiver is positioned in the first reflection maximum. (c-d) Simulated integrated response for a rectangular inclusion at respectively 6 mm and 14 mm from the top-side calculated with the shadow method. (e-f) Simulated integrated response for a rectangular inclusion at respectively 6 mm and 14 mm from the top-side calculated with the finite element method implemented in COMSOL.

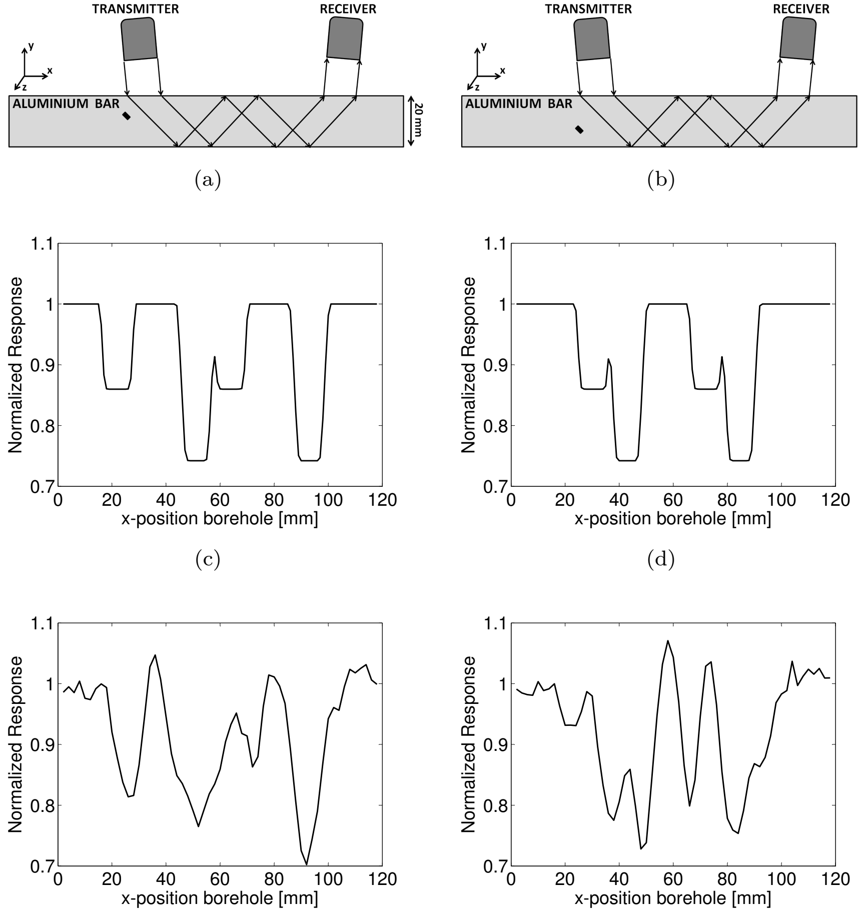

(a) (b)

(c) (d)

(e) (f)

Figure 4.21: (a-b) Experimental setup: aluminium bar with rectangular inclusion, inclined at −46.24°, at respectively 6 mm and 14 mm from the top-side. The receiver is positioned in the second reflection maximum. (c-d) Simulated integrated response for a rectangular inclusion at respectively 6 mm and 14 mm from the top-side calculated with the shadow method. (e-f) Simulated integrated response for a rectangular inclusion at respectively 6 mm and 14 mm from the top-side calculated with the finite element method implemented in COMSOL.

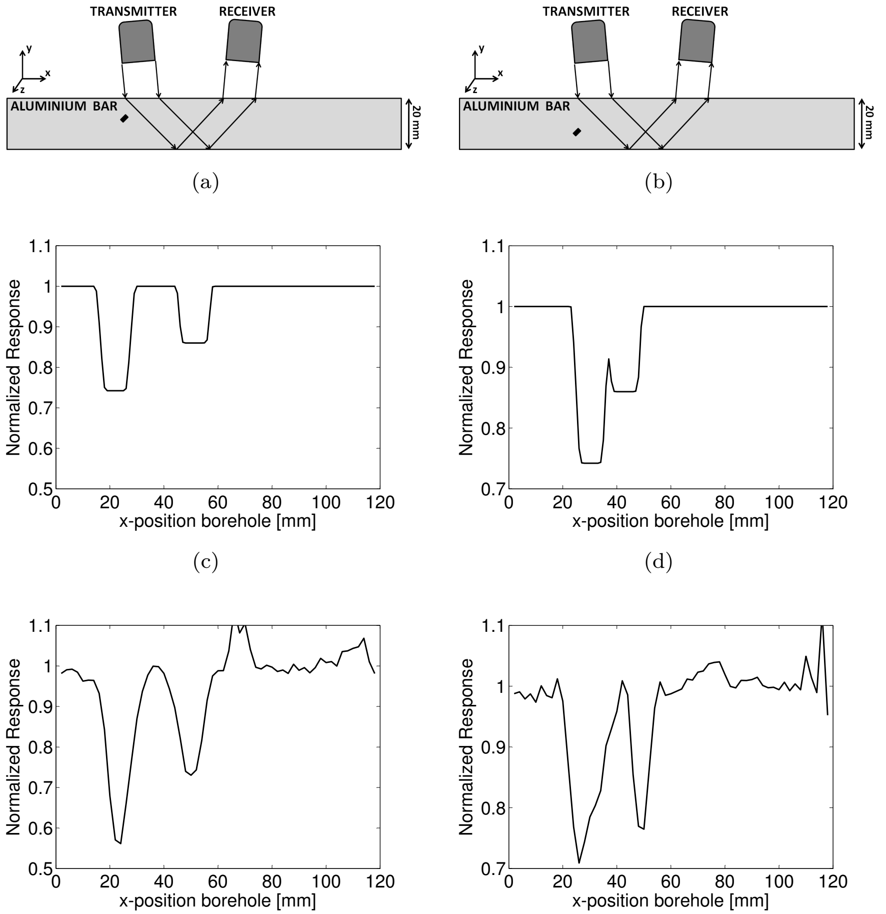

(a) (b) (c) (d) (e) (f)

Figure 4.22: (a-b) Experimental setup: aluminium bar with rectangular inclusion, inclined at 46.24°, at respectively 6 mm and 14 mm from the top-side. The receiver is positioned in the first reflection maximum. (c-d) Simulated integrated response for a rectangular inclusion at respectively 6 mm and 14 mm from the top-side calculated with the shadow method. (e-f) Simulated integrated response for a rectangular inclusion at respectively 6 mm and 14 mm from the top-side calculated with the finite element method implemented in COMSOL.

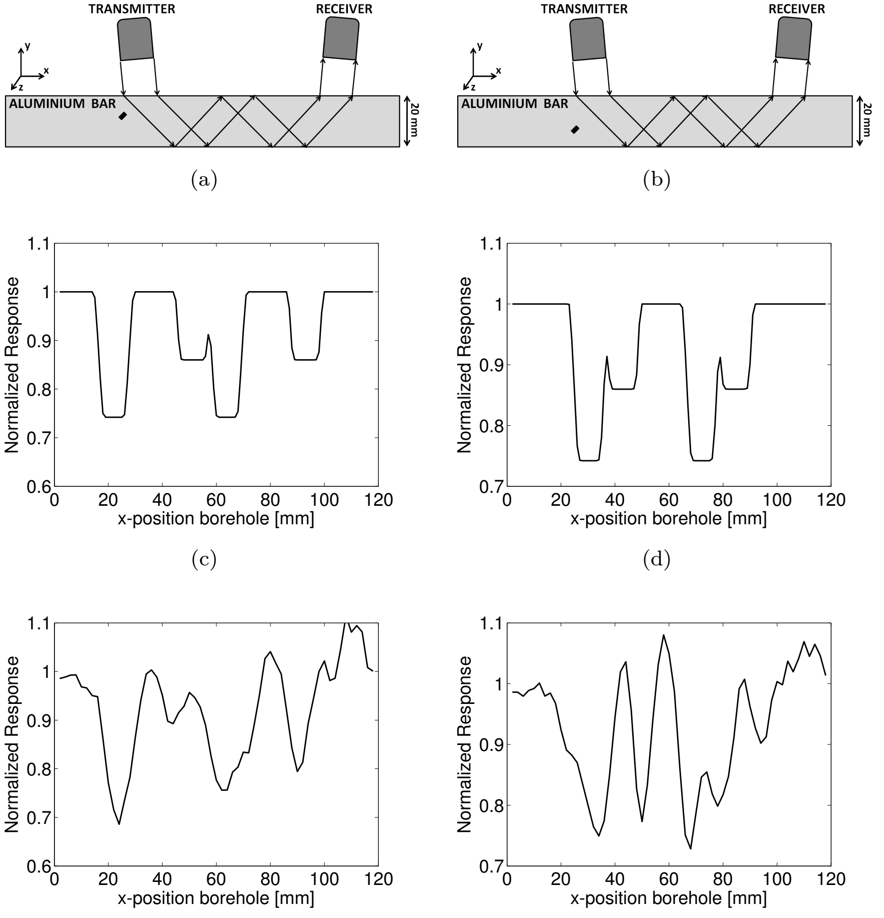

(a) (b)

(c) (d)

(e) (f)

Figure 4.23: (a-b) Experimental setup: aluminium bar with rectangular inclusion, inclined at 46.24°, at respectively 6 mm and 14 mm from the top-side. The receiver is positioned in the second reflection maximum. (c-d) Simulated integrated response for a rectangular inclusion at respectively 6 mm and 14 mm from the top-side calculated with the shadow method. (e-f) Simulated integrated response for a rectangular inclusion at respectively 6 mm and 14 mm from the top-side calculated with the finite element method implemented in COMSOL.

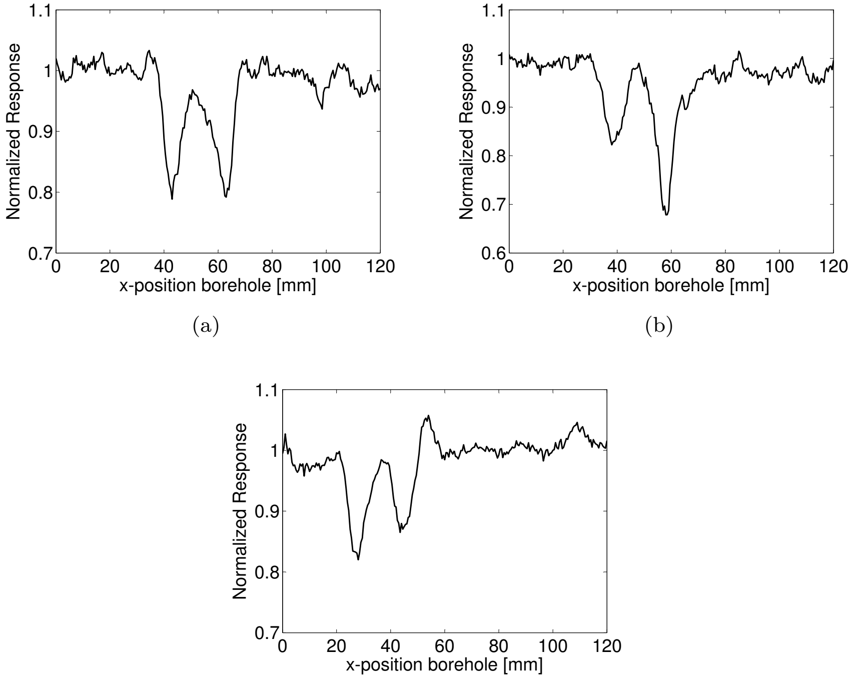

(a) (b)

(c)

Figure 4.24: Experimental observations of a setup with a rectangular inclusion positioned at 6 mm from the top-side of the aluminium sample and receiver positioned in the first reflection maximum. The measured integrated response was averaged over all z-positions and calculated for (a) a rectangular inclusion that stands horizontally, (b) a rectangular inclusion inclined $-46.24°$ and (c) a rectangular inclusion inclined at $46.24°$.

inclusion inclined at 46.24°. The response was each time measured in the first reflection maximum and the results are shown for a CW excitation at 750 kHz. High responses are shown in white, low responses are shown in black. In these figures, the same results as for the line scans can be observed. In figure 4.25(a), the intensity reduction is independent whether the rectangular inclusion passes the incident beam or the reflected beam. A fairly symmetric result is obtained. In figure 4.25(b), the passage of the inclusion through the incident beam causes less diminution than when the inclusion passes the reflected beam. In figure 4.25(c), the opposite is observed. Cases 2 and 3 yield asymmetric results. The observed wave pattern in the response plots is similar to the pattern observed in the case of a circular borehole, described in section 4.4.3.

The asymmetry is expressed more clearly in figure 4.26. These plots are obtained by (left-right) flipping of the response plots in figure 4.25 and subtracting this result from the original response image. The subtraction process accentuates the difference between the intensity reduction caused by the passage of the inclusion through the incident beam and the diminution caused by the passage through the reflected beam. In case 1, there is almost no difference between both reductions. In case 2 the diminution caused by the passage through the reflected beam is much larger than the reduction caused by the incident beam, and in case 3 we observe the opposite effect.

In the previous simulations, we considered three different orientations of the rectangular inclusion, either horizontally, with the long side parallel to the top-side of the aluminium sample, or inclined at −46.24° or 46.24°. However, using the COMSOL simulation, we can also investigate the influence of a variable inclination of the rectangular inclusion, starting from the horizontal position. The generated sound field is a continuous wave at 750 kHz. The rectangular inclusion has the same dimensions (1 mm × 2 mm) as in the above simulations, with its (central) y-position exactly at the centreline of the aluminium bar used in the pitch-catch experiments. The x-position of the centre of the inclusion coincides with the middle of the incident beam. In the simulations, the centre is kept fixed and the inclusion is rotated clockwise in steps of 1°, over 180°. For every orientation of the rectangular inclusion the response is measured in the first reflection maximum.

Figure 4.27 displays the results of this simulation which clearly illustrate that the response highly depends on the orientation of the inclusion. A relative maximum can be observed at approximately 136°, corresponding to the situation where the incident beam is obstructed by the small side of the rectangular inclusion. When the inclusion is inclined at approximately 20°, the incident beam is obstructed by a zone with length equal to the length of a diagonal of the rectangular inclusion. This is the largest possible obstruction and thus a minimum in the response is observed. We would expect another such minimum at approximately

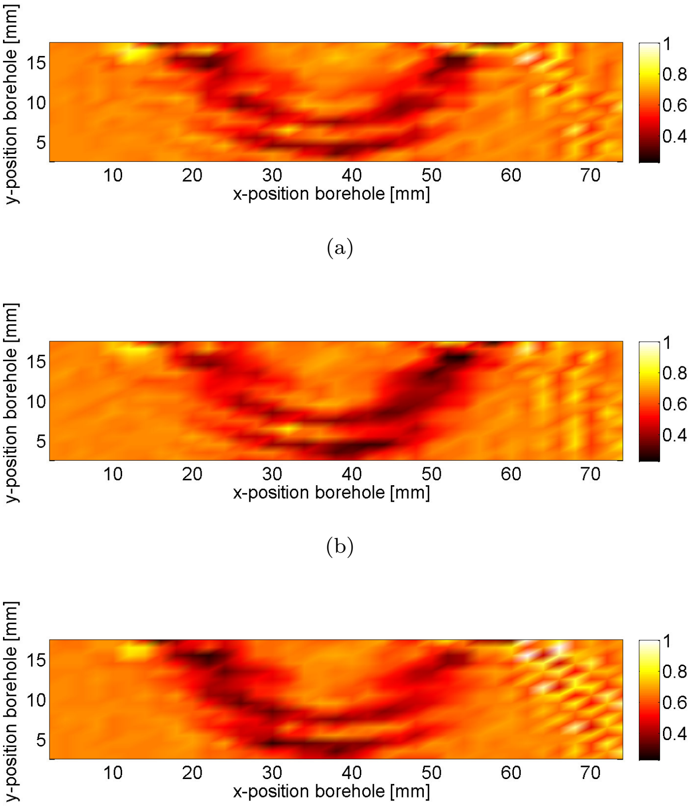

(a)

(b)

(c)

Figure 4.25: Integrated response as a function of the (x, y)-position of (a) a rectangular inclusion parallel to the top-wall, (b) a rectangular inclusion, inclined at $-46.24°$ and (c) a rectangular inclusion, inclined at $46.24°$. The response was each time measured in the first reflection maximum for a CW excitation at 750 kHz. Low responses are shown in black. The colour scale is the same in all three figures.

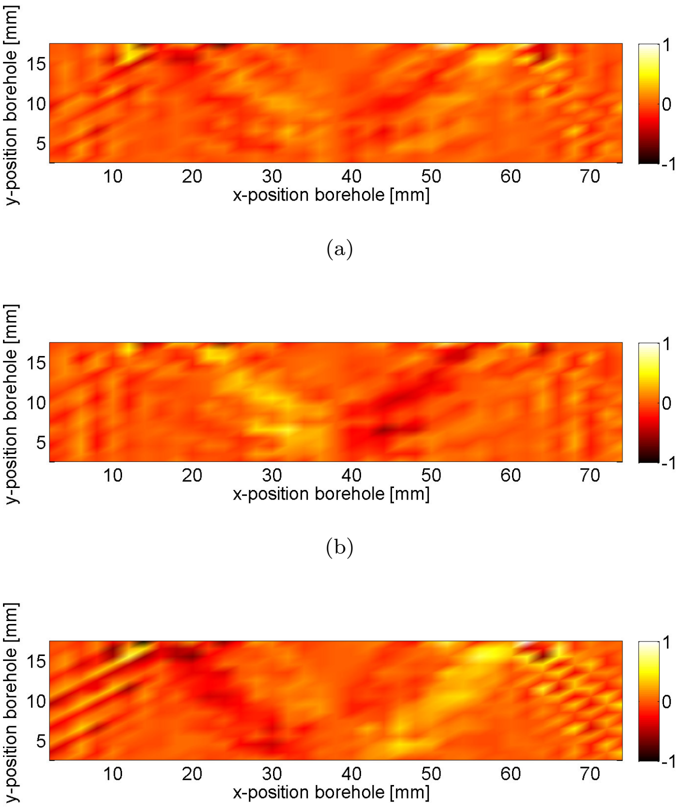

(a)

(b)

(c)

Figure 4.26: Difference between the intensity reductions caused by the passage of a rectangular inclusion through the incident beam and through the reflected beam. The results are shown for (a) a horizontal inclusion, (b) an inclusion inclined at −46.24° and (c) an inclusion inclined at 46.24°. The results are obtained for a CW excitation at 750 kHz. High values are shown in white, low values are shown in black. The colour scale is the same in all three figures.

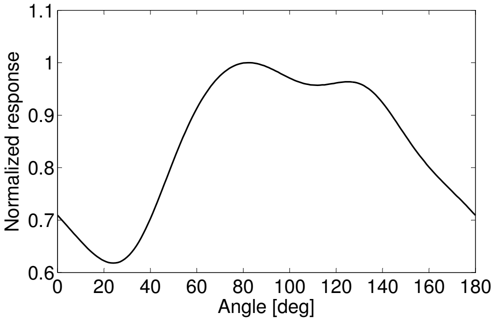

Figure 4.27: COMSOL simulation of a rotating rectangular inclusion in an aluminium bar. The response measured in the first reflection maximum for a CW excitation at 750 kHz depends highly on the orientation of the inclusion.

72°, when the sound field is obstructed by the second diagonal. However, a maximum is observed. A possible explanation for this maximum could be found in the reflections of the sound field on the inclusion, which are also captured by the receiver, resulting in a higher response.

4.5 Finite element simulation of more complex problems

The developed finite element model can be used in a variety of studies with the aim to determine the best parameters to be used in air-coupled experiments. The results of a parametric study may help in guiding and optimizing air-coupled techniques for typical applications in non-destructive testing. In this section we will focus on two particular examples: the ultrasonic testing of an aluminium plate with a section of varying thickness and a LED-rail.

In the first subsection, we will describe the propagation of Lamb waves through an aluminium plate with varying section, as can be found in welds for instance. We will show that several mode conversions of the generated Lamb wave can occur as a result of the variation in thickness. These mode conversions depend on the maximum thickness reached and on the total length of the area of the varying section. In the second subsection, we will discuss the ultrasonic testing of a LED-rail profile. We will show that the wave pattern observed in the air surrounding the LED-rail is strongly dependent on the frequency of the generated ultrasonic wave and on the presence of different electronic elements or air-bubbles inside the LED-rail. Based on the simulation results, we will

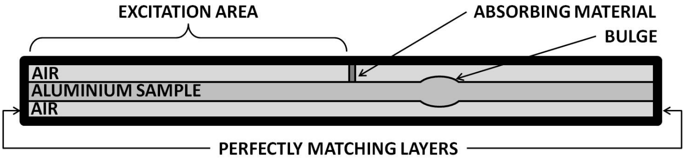

Figure 4.28: Illustration of the geometry of an aluminium plate with varying section used in the COMSOL simulation. The plate has a section of varying thickness, located between two areas of constant thickness $d = 2$ cm. PMLs were added to the computational region to eliminate unwanted reflections.

propose techniques for the ultrasonic testing of both the aluminium plate with varying section and the LED-rail.

4.5.1 Aluminium plate with varying section

In the previous sections, we studied simulations and observations of the air-coupled ultrasonic inspection of an aluminium plate of constant thickness with an air-filled inclusion. Suppose now, however, that the aluminium plate under study has a section of varying thickness, located between two areas of constant thickness, as for instance a bulge in the case of a two-sided weld. This varying section will make it difficult to detect the presence of possible inclusions, especially when they are located inside the varying section domain. It is therefore important to gain -as a start- information about the wave propagation inside a sample without inclusion, since this would make it easier to analyse the measured signals diffracted by inclusions. Indeed, if the waves propagating in an intact sample are totally known, we can assign any change in the received signals to defects in the sample.

In this section we will focus on the propagation of Lamb waves in a 2 cm thick aluminium plate with a bulge. The actual implementation of the bulge in COMSOL was done by means of quadratic Bézier curves. To suppress the signal coming from the specular reflection at the air-aluminium interface a sound absorbing material was added on top of the aluminium sample. PMLs were introduced to eliminate reflections at the edges of the computational region. An illustration of the implemented geometry is shown in figure 4.28. The aim of the study is to understand the behaviour of the Lamb waves generated in the excitation area and propagating in and through the varying section.

For the generation of Lamb waves, a CW excitation at 500 kHz by means of a large aperture transducer (diameter of approximately 3 cm) was considered. Different Lamb modes can be generated by changing the inclination angle of

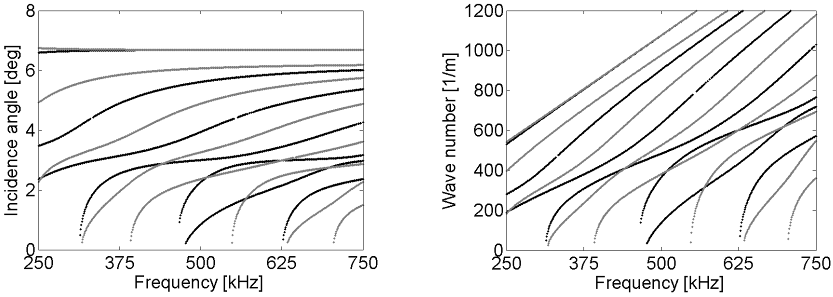

(a) (b)

Figure 4.29: Dispersion curves for a 2 cm aluminium plate. Anti-symmetric plate modes are plotted in grey, symmetric plate modes are plotted in black. (a) Angle of incidence as a function of frequency, (b) Lamb wave number as a function of frequency.

Lamb mode	θ [deg]	k_{Lamb} [1/m]
A_0/S_0	6.7	1076
A_1	6.1	977
S_1	5.6	904
A_2	4.9	787
S_2	3.9	635
A_3	3.3	526
S_3	3.0	484
A_4	2.4	381
S_4	2.3	365
S_5	0.8	137

Table 4.1: Symmetric and anti-symmetric Lamb modes with their corresponding incidence angle θ and wave number k_{Lamb} for an excitation frequency of 500 kHz.

the transducer. Typical dispersion curves for a 2 cm thick aluminium plate are plotted in figure 4.29. In figure 4.29(a), the vertical axis represents the inclination angle of the transducer and the horizontal one the excitation frequency. In figure 4.29(b) the Lamb wave number is given as a function of the excitation frequency. In both figures, anti-symmetric Lamb modes are plotted in grey, symmetric modes are plotted in black. It is clear that for a fixed frequency, changing the inclination angle results in the generation of a different Lamb mode with different wave number. In table 4.1, all symmetric and anti-symmetric Lamb modes that can occur at a frequency of 500 kHz are given with their corresponding incidence angle θ and wave number k_{Lamb}.

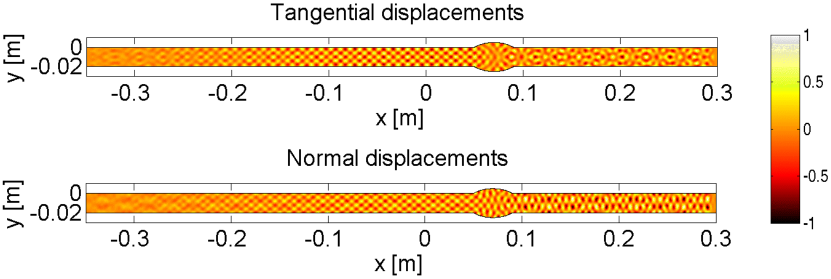

Figure 4.30: Snapshots of the simulated tangential and normal displacements in a 2 cm aluminium plate with a bulge of total width 4 cm and maximum thickness of approximately 3 cm for a CW excitation at 500 kHz. A symmetric S_2 Lamb mode is generated in the left part of the plate and is propagating until it reaches the bulge, where it is disturbed. The colour scale is normalized according to the maximum value of the displacements.

To illustrate the behaviour of a Lamb wave propagating in a sample with varying thickness, we first study the results of one particular aluminium plate in which the bulge has a total width of 4 cm and the maximum thickness reached is approximately 3 cm. The Lamb mode generated in the sample is a symmetric S_2 Lamb mode. From table 4.1 it follows that the angle of incidence needs to be equal to 3.9°. In figure 4.30 snapshots of the simulated tangential (u_x) and normal (u_y) displacements in the plate are displayed. In the left part of the plate regular wave patterns are observed for both the tangential and normal displacements, corresponding to the patterns of the symmetric S_2 Lamb mode generated in the plate. This Lamb mode propagates further in the plate until it reaches the bulge. In the bulge, the symmetric S_2 Lamb mode is converted and the converted Lamb wave propagates then further in the right part of the aluminium plate.

To obtain the essential qualitative information on the mode conversion and on the wave number variation in the wave guide a spatial Fourier transform of the tangential and normal displacement at the top surface of the plate can be performed. Figures 4.31(a) and 4.32(a) show respectively a snapshot of the tangential and normal displacements at the top surface of the aluminium plate and at the right hand side of the bulge ($0.1 \text{ m} \leq x \leq 0.25 \text{ m}$). Wave number domain spectra obtained by spatially Fourier transforming both displacements are plotted in figures 4.31(b) and 4.32(b). In both wave number domain spectra, peaks are found at specific wave numbers, corresponding to several symmetric Lamb modes (see table 4.1). From these figures, it seems that the initially generated symmetric S_2 Lamb mode is converted in the bulge into

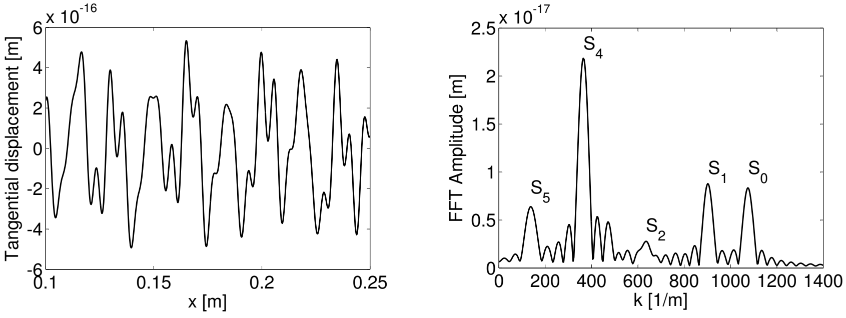

(a) (b)

Figure 4.31: (a) Snapshot of the tangential displacements at the top surface of a 2 cm aluminium plate with a bulge of total width 4 cm and maximum thickness of approximately 3 cm for a CW excitation at 500 kHz. The displacements are measured at the right hand side of the bulge. (b) Wave number domain spectrum obtained by spatially Fourier transforming the tangential displacements. The peaks give an indication of the Lamb modes propagating in the plate.

the symmetric Lamb modes S_0, S_1, S_2, S_4 and S_5, with some of them being more dominant than others. The reason why the initially generated symmetric mode is only converted into other symmetric modes is because of the symmetry of the aluminium sample. For asymmetric samples, symmetric modes can be converted into anti-symmetric modes and vice versa.

Typical displacement fields of the different Lamb modes inside the aluminium plate and on the right hand side of the varying section domain can be discerned by spatially Fourier transforming the tangential and normal displacements inside the plate (at various depths) with respect to the x-coordinate, filtering the results in the wave number domain around the specific Lamb wave numbers and inverse Fourier transforming the filtered results to obtain the displacements in space domain again. The wave number domain spectra for the tangential and normal displacements inside the aluminium plate are shown in figure 4.33. In both figures, the highest amplitudes are found at the wave numbers of the symmetric Lamb modes S_0, S_1, S_2, S_4 and S_5 (see table 4.1), corresponding to the results in figures 4.31 and 4.32. If we now, for example, filter these spectra around the wave number $k = 1076$ m^{-1} of the symmetric S_0 Lamb mode and then, inverse Fourier transform the filtered signals, we obtain a snapshot of the displacement fields of the symmetric S_0 mode contribution in the plate. In figure 4.34 these simulated displacement fields are plotted and compared with the theoretical displacement fields for the S_0 Lamb mode obtained using equations (2.51) and (2.52) (where the coordinate z is to be identified with y in

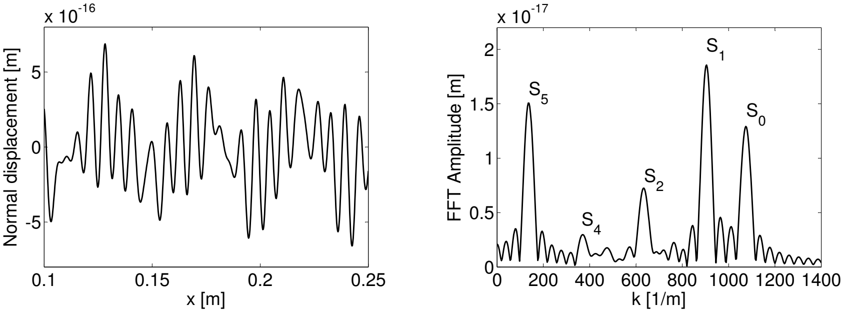

(a) (b)

Figure 4.32: (a) Snapshot of the normal displacements at the top surface of a 2 cm aluminium plate with a bulge of total width 4 cm and maximum thickness of approximately 3 cm for a CW excitation at 500 kHz. The displacements are measured at the right hand side of the bulge. (b) Wave number domain spectrum obtained by spatially Fourier transforming the normal displacements. The peaks give an indication of the Lamb modes propagating in the plate.

this case), showing that the simulated displacement fields indeed correspond to those of the symmetric S_0 mode. The same procedure can now be repeated for the other Lamb modes (S_1, S_2, S_4 and S_5), filtering the wave number domain spectra around the wave numbers of these modes (see table 4.1). The simulated and theoretically determined displacement fields for these Lamb modes are shown in figures 4.35 to 4.38.

To demonstrate that the disturbed wave patterns at the right hand side of the bulge in figure 4.30 are indeed caused by interference of the Lamb modes S_0, S_1, S_2, S_4 and S_5, we can compare these displacement fields to the displacement fields composed of the sum of the displacement fields of the individual Lamb waves in the plate (figures 4.34(a) to 4.38(a)). In figure 4.39(a), the displacement fields for the tangential and normal displacement obtained by summing the displacement fields of the different symmetric Lamb waves are shown. In figure 4.39(b), a zoom of the displacement fields from figure 4.30 is shown to compare them with the summed displacement fields. As expected, there is a good correspondence between all displacement fields. The only difference between the two figures is the decreasing amplitudes in the summed displacement fields for x approaching 0.1 or 0.25 m. This, however, has no physical meaning and is totally attributed to the filtering process.

Using the finite element simulation we showed that a symmetric S_2 Lamb wave propagating in a 2 cm aluminium plate with a bulge of total width 4 cm

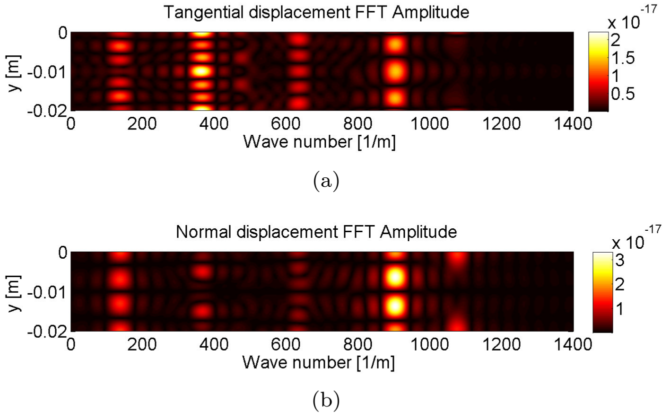

Figure 4.33: Wave number domain spectra as a function of depth in a colour coded representation. The spectra are obtained by spatially Fourier transforming the tangential (a) and normal (b) displacements at each depth with respect to the x-coordinate inside a 2 cm aluminium plate with a bulge of total width 4 cm and maximum thickness of approximately 3 cm for a CW excitation at 500 kHz. Maximum amplitudes are shown in white and are occurring at wave numbers corresponding to the expected Lamb waves (see table 4.1).

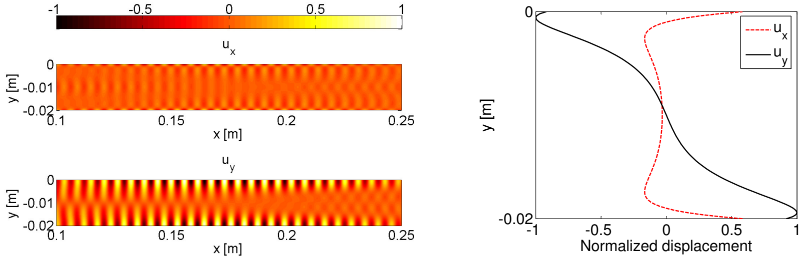

(a) (b)

Figure 4.34: Displacement fields for the symmetric S_0 mode converted contribution after propagation of a symmetric S_2 mode in a 2 cm aluminium plate with a bulge of total width 4 cm and maximum thickness of approximately 3 cm for a CW excitation at 500 kHz. (a) Snapshots of the simulated displacement fields obtained by spatially Fourier transforming the tangential and normal displacements inside the aluminium plate with respect to the x-coordinate, filtering the results around $k = 1076 \text{ m}^{-1}$ and inverse Fourier transforming the filtered signals. (b) Theoretically determined displacement amplitudes as a function of depth. The displacements in (a) and (b) are normalized according to the maximum of the absolute value of the tangential and normal displacement amplitudes.

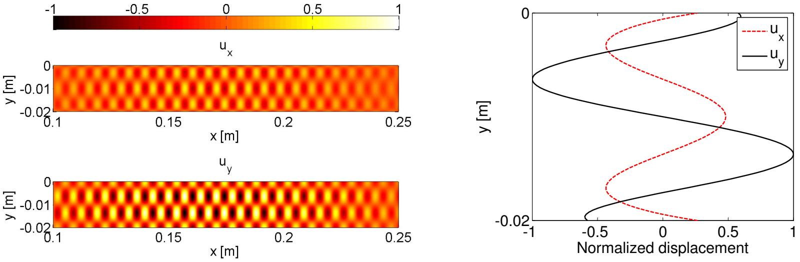

(a) (b)

Figure 4.35: Displacement fields for the symmetric S_1 mode converted contribution after propagation of a symmetric S_2 mode in a 2 cm aluminium plate with a bulge of total width 4 cm and maximum thickness of approximately 3 cm for a CW excitation at 500 kHz. (a) Snapshot of the simulated displacement fields obtained by spatially Fourier transforming the tangential and normal displacements inside the aluminium plate with respect to the x-coordinate, filtering the results around $k = 904\ \mathrm{m}^{-1}$ and inverse Fourier transforming the filtered signals. (b) Theoretically determined displacement amplitudes as a function of depth. The displacements in (a) and (b) are normalized according to the maximum of the absolute value of the tangential and normal displacement amplitudes.

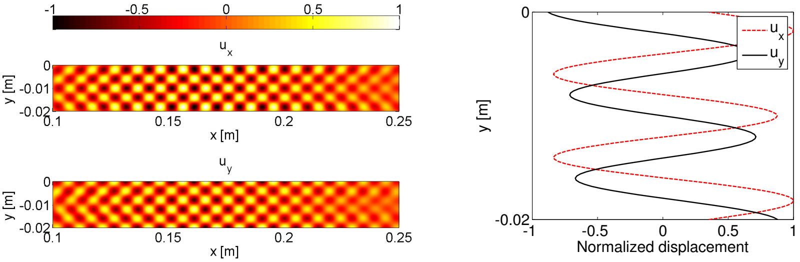

(a) (b)

Figure 4.36: Displacement fields for the symmetric S_2 mode converted contribution after propagation of a symmetric S_2 mode in a 2 cm aluminium plate with a bulge of total width 4 cm and maximum thickness of approximately 3 cm for a CW excitation at 500 kHz. (a) Snapshot of the simulated displacement fields obtained by spatially Fourier transforming the tangential and normal displacements inside the aluminium plate with respect to the x-coordinate, filtering the results around $k = 635\ \mathrm{m}^{-1}$ and inverse Fourier transforming the filtered signals. (b) Theoretically determined displacement amplitudes as a function of depth. The displacements in (a) and (b) are normalized according to the maximum of the absolute value of the tangential and normal displacement amplitudes.

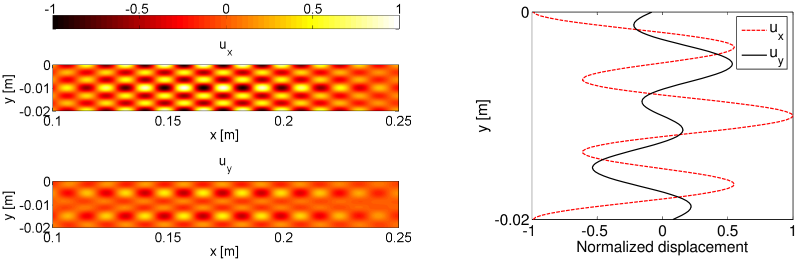

(a) (b)

Figure 4.37: Displacement fields for the symmetric S_4 mode converted contribution after propagation of a symmetric S_2 mode in a 2 cm aluminium plate with a bulge of total width 4 cm and maximum thickness of approximately 3 cm for a CW excitation at 500 kHz. (a) Snapshot of the simulated displacement fields obtained by spatially Fourier transforming the tangential and normal displacements inside the aluminium plate with respect to the x-coordinate, filtering the results around $k = 365$ m^{-1} and inverse Fourier transforming the filtered signals. (b) Theoretically determined displacement amplitudes as a function of depth. The displacements in (a) and (b) are normalized according to the maximum of the absolute value of the tangential and normal displacement amplitudes.

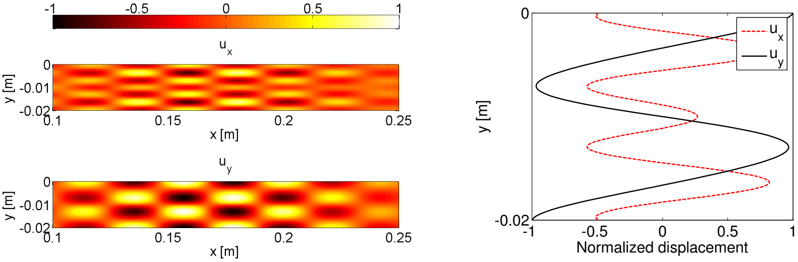

(a) (b)

Figure 4.38: Displacement fields for the symmetric S_5 mode converted contribution after propagation of a symmetric S_2 mode in a 2 cm aluminium plate with a bulge of total width 4 cm and maximum thickness of approximately 3 cm for a CW excitation at 500 kHz. (a) Snapshot of the simulated displacement fields obtained by spatially Fourier transforming the tangential and normal displacements inside the aluminium plate with respect to the x-coordinate, filtering the results around $k = 137$ m^{-1} and inverse Fourier transforming the filtered signals. (b) Theoretically determined displacement amplitudes as a function of depth. The displacements in (a) and (b) are normalized according to the maximum of the absolute value of the tangential and normal displacement amplitudes.

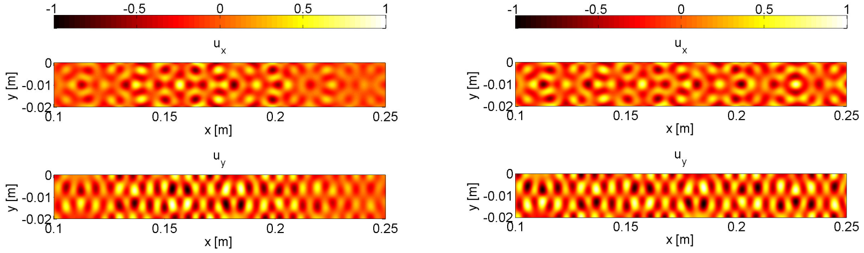

(a) (b)

Figure 4.39: Displacement fields after propagation of a symmetric S_2 mode in a 2 cm aluminium plate with a bulge of total width 4 cm and maximum thickness of approximately 3 cm for a CW excitation at 500 kHz. (a) Snapshot of the simulated displacement fields obtained by spatially Fourier transforming the tangential and normal displacements inside the aluminium plate with respect to the x-coordinate, filtering the results around the wave numbers of the Lamb modes S_0, S_1, S_2, S_4 and S_5, inverse Fourier transforming the filtered signals and summing all the results. (b) Snapshot of the simulated displacement fields obtained with the COMSOL finite element simulation. In fact this is a zoom from the displacement fields plotted in figure 4.30. The displacements in (a) and (b) are normalized according to the maximum of the absolute value of the tangential and normal displacement amplitudes.

and a maximum thickness of approximately 3 cm is converted into five other symmetric Lamb modes inside the varying section domain, each of them with a different amplitude. This results in typical wave number domain spectra at the top surface of the sample, at the right hand side of the bulge (figures 4.31(b) and 4.32(b)). Taking these results as a reference, any new change in the wave number domain spectra can now be assigned to defects in the sample. Suppose, for example, that an air-filled circular inclusion of radius 2.5 mm is located right in the centre of the bulge. Determining the tangential and normal displacements at the top surface of the plate (at the right hand side of the bulge) and spatially Fourier transforming these displacements, we obtain the wave number domain spectra for this aluminium sample. In figure 4.40, the calculated wave number domain spectra for the aluminium sample with inclusion (dotted line) are compared to the spectra from figures 4.31(b) and 4.32(b) for the sample without inclusion (full line). In both samples the initially generated symmetric S_2 Lamb mode was converted into the same five symmetric Lamb modes. However, clear differences in both figures can be observed. The presence of the circular inclusion in the centre of the bulge causes the fundamental mode S_0 and the second order mode S_2 to become more dominant, while the first order mode S_1 and the fourth order mode S_4 become less dominant.

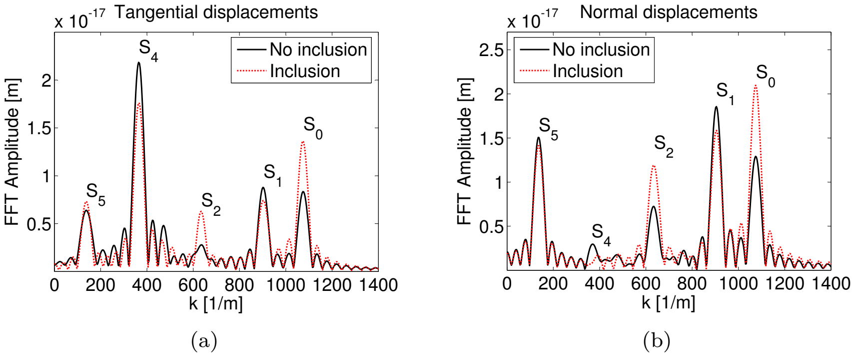

(a) (b)

Figure 4.40: Wave number domain spectra obtained by spatially Fourier transforming the tangential (a) and normal (b) displacements at the top surface of a 2 cm aluminium plate with a bulge of total width 4 cm and maximum thickness of approximately 3 cm for a CW excitation at 500 kHz. The full lines represent the results for an intact aluminium plate, the dotted lines represent the results for an aluminium plate containing an air-filled circular inclusion of radius 2.5 mm in the centre of the bulge.

Based on the simulation results, an air-coupled ultrasonic technique for the detection of a defect in an aluminium plate with a section of varying thickness can be proposed. A schematic representation of the experimental setup is shown in figure 4.41. An air-coupled ultrasonic transducer is positioned above the left part of the plate. As a result of a continuous wave signal excitation at a specific angle of incidence, a Lamb wave is generated in the plate. The Lamb wave propagates further in the plate until it reaches the bulge, where mode conversion of the Lamb wave in one or several other Lamb waves occurs. A disturbed wave, formed by interference of the different Lamb modes, is then propagating further in the right part of the plate. At the top surface of this part of the plate, a laser Doppler vibrometer can be used to measure the displacements along a line in the x-direction. Spatially Fourier transforming these displacements, a wave number domain spectrum for this line is obtained. Then, the transducer and the laser Doppler vibrometer are moved in small steps in the z-direction and the same procedure is followed for every z-position of transducer and vibrometer until the whole scanning area is covered. This results in a set of wave number domain spectra, with each spectrum corresponding to one z-position. Finally, or -in a more advanced version- while making the scan, all spectra are compared with another and changes in the characteristics can then be assigned to defects inside the bulge. This technique thus allows to detect a defect and to get an idea of the exact location of the defect.

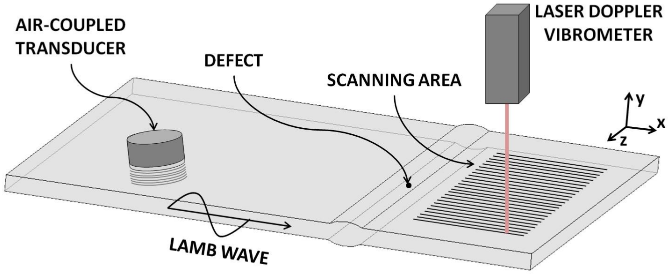

Figure 4.41: Schematic representation of the experimental setup for the air-coupled ultrasonic testing of an aluminium plate with a section of varying thickness. A defect inside the bulge can be detected by generating a Lamb wave in the left part of the plate and measuring the displacements in a scanning area at the top surface of the right part of the plate. Spatially Fourier transforming the displacements, wave number domain spectra are obtained which can be studied to detect the defect.

Until now, we only discussed the results for the generation of a symmetric S_2 Lamb mode in a 2 cm aluminium plate with a bulge of total width 4 cm and maximum thickness of approximately 3 cm. Obviously the wave number domain spectra will change with generated Lamb wave, bulge width and bulge thickness. In figure 4.42, the wave number domain spectra of the normal displacements at the top surface of the aluminium sample (at the right hand side of the bulge), obtained for a CW excitation at 500 kHz are plotted for different generated Lamb modes and different bulge widths. The initially generated Lamb wave in the left part of the plate is indicated in the box to the right of each figure. Wave numbers of specific Lamb modes are indicated in each figure by a white line. In each figure, several mode conversions are visible. However, these mode conversions strongly depend on the initially generated Lamb wave and on the bulge width. Moreover, for this aluminium sample, when the initially generated Lamb mode is symmetric, it is only converted in other symmetric modes. When the initially generated mode is anti-symmetric, it is only converted in anti-symmetric modes. In figure 4.43, the wave number domain spectra of the normal displacements at the top surface of the sample (at the right hand side of the bulge) are plotted for different generated Lamb modes and different maximum bulge thicknesses, showing that the spectra also strongly depend on the bulge thickness. Also in this case, symmetric modes are converted into symmetric modes, while anti-symmetric modes are converted into anti-symmetric modes. From these results it follows that every situation has its own specific wave number domain spectrum, which needs to be determined before the above described ultrasonic air-coupled NDT technique can be used for the detection of possible defects in the material.

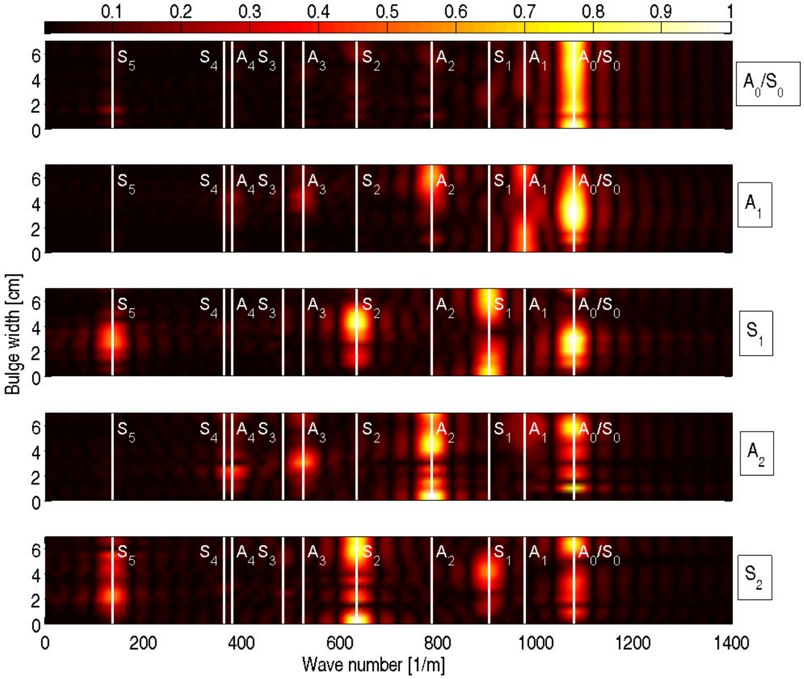

Figure 4.42: Wave number domain spectra of the normal displacements at the top surface of a 2 cm aluminium plate with a bulge for a CW excitation at 500 kHz. The results are obtained for different bulge widths and different generated Lamb modes. The maximum thickness of the bulge is fixed to approximately 3 cm. The initially generated Lamb mode is indicated in the box at the right hand side of each figure. Wave numbers of different Lamb modes are indicated in each figure by the white lines. The colour scale in each figure is normalized according to its maximum value.

A future step in this study should contain an experimental verification of the simulation results presented here and a dedicated test of the proposed ultrasonic air-coupled technique for the detection of defects inside a section of varying thickness. In a first attempt, the technique needs to be tested on well defined aluminium test samples with well defined artificial defects, such as air-filled inclusions. Later, the technique can then be used for the non-destructive testing of more complex materials, e.g. the air-coupled non-destructive inspection of welding joints.

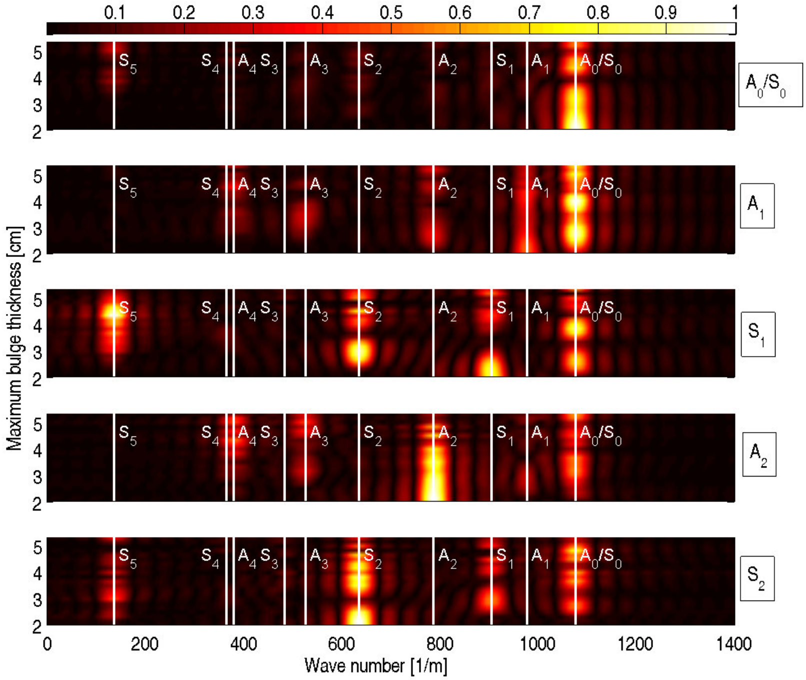

Figure 4.43: Wave number domain spectra of the normal displacements at the top surface of a 2 cm aluminium plate with a bulge for a CW excitation at 500 kHz. The results are obtained for different bulge thicknesses and different generated Lamb modes. The total width of the bulge is fixed to 4 cm. The initially generated Lamb mode is indicated in the box at the right hand side of each figure. Wave numbers of different Lamb modes are indicated in each figure by the white lines. The colour scale in each figure is normalized according to its maximum value.

4.5.2 Ultrasonic testing of a LED-rail

Until now, the finite element model was only used for the simulation of plate-like structures surrounded by air. However, the developed model can also be used for the simulation of more complex shaped samples composed of multiple materials. To illustrate this, we implemented a LED-rail into the model.

A typical example of a LED-rail is shown in figure 4.44. Different coloured LEDs, embedded in resin and placed within an aluminium profile are clearly visible. The interior of the LED-rail is shown in figure 4.45 by means of a Röntgen scan. The black zone in the centre of the LED-rail is the printed circuit

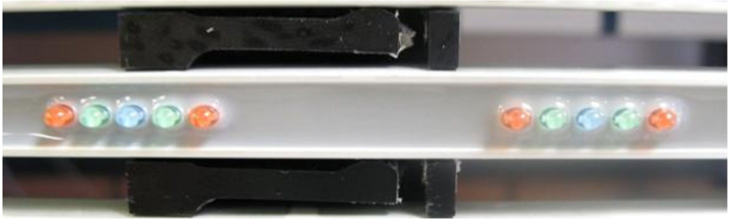

Figure 4.44: Top-view of a LED-rail. The LEDs are embedded in a resin inside a U-shaped aluminium profile.

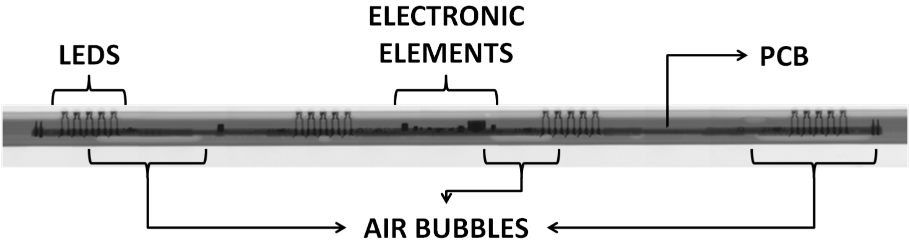

Figure 4.45: Röntgen scan of a LED-rail. The LEDs and several electronic elements are mounted on a PCB. In the surrounding resin, air bubbles can be found.

board (PCB). On top of this PCB the LEDs and several electronic elements are mounted. The dark grey zone is the resin in which the PCB, the LEDs and the electronic elements are embedded. Underneath the PCB, some light grey zones are found, corresponding to air bubbles. The ultimate goal would be to guide the design, develop and optimize a detection technique based on air-coupled (non-contact) ultrasound to localize these air gaps.

To get a better idea of how a LED-rail is manufactured, we can look at different cross-sections of the rail, schematically represented in figure 4.46. The total width of the rail is 12 mm and the total height is 13 mm. The bottom part of the rail has a circular shape with radius 6 mm. The rail consists of a U-shaped aluminium profile with a thickness 1.2 mm (black region). On the inside surface of this aluminium profile there are a few small protrusions on which a PCB (dark grey region) rests. The PCB has a thickness of 1.5 mm and consists of glass fiber reinforced epoxy (GFRE). On top of the PCB the LED (figure 4.46(b)) and other electronic elements are mounted. The aluminium profile is filled with a resin (light grey region).

The 2D geometry of cross-sections of the LED-rail, implemented in the finite element model in COMSOL, may be subdivided into seven subdomains, as

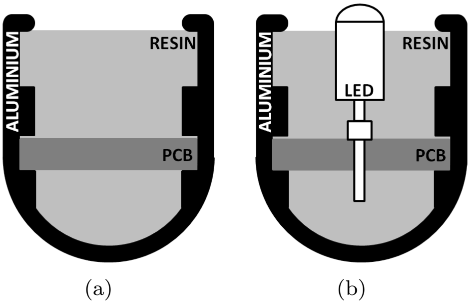

(a) (b)

Figure 4.46: Schematic representation of a few cross-sections of a LED-rail: (a) LED-rail consisting of a U-shaped aluminium profile filled with a resin. A PCB is resting on small protrusions on the inside surface of the aluminium profile, (b) LED-rail with LED mounted on the PCB.

Material	ρ [kg/m^3]	v_L [m/s]	v_T [m/s]
Aluminium	2700	6320	3130
GFRE	1850	2874	1100
Resin	1250	969	/
Electronic element	8000	5000	3000
Air	1.22	340	/

Table 4.2: Material parameters used for the finite element simulation of a LED-rail profile.

illustrated in figure 4.47. The black U-shaped domain represents the aluminium profile of the rail. For simplicity, the protrusions on the inside of the aluminium profile, on which the PCB rests, are not considered. Inside the aluminium profile, we consider three domains. In the middle, a rectangular domain was implemented, representing the PCB and consisting of GFRE. Above and below this domain we have two domains representing the resin. On top of the PCB domain, possible electronic elements are implemented as squares. At the bottom of the PCB, a circular domain representing an air bubble can be added. The aluminium rail cover and its interior are surrounded by a rectangular domain with width 2 cm and height 2.5 cm. This domain represents the air surrounding the rail. Finally, PMLs were added to the edges of the computational region to eliminate unwanted reflections. The material parameters used in the different domains are depicted in table 4.2.

The goal of this study is to provide guidance for the design of an air-coupled NDT technique for the detection of air bubbles and/or electronic elements inside

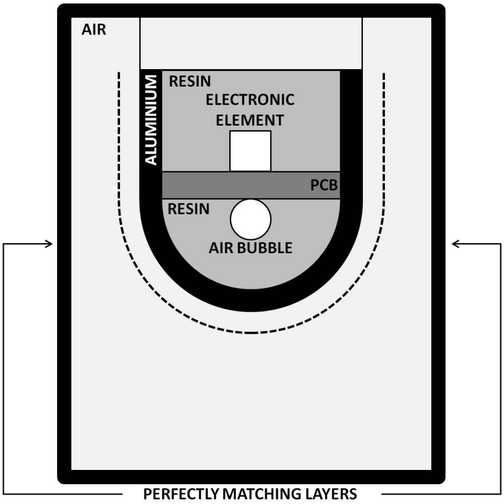

Figure 4.47: Illustration of the geometry of a LED-rail used in the COMSOL simulation. The geometry is subdivided into seven subdomains: a U-shaped aluminium domain, two domains of resin, a rectangular domain representing the PCB, a square domain representing an electronic element, a circle representing an air bubble and a rectangular domain for the surrounding air. Centrally located above the LED-rail, a 6 mm diameter air-coupled ultrasonic transducer is implemented. To eliminate unwanted reflections of the sound field, PMLs are added to the edges of the computational region. The dotted line will be used for post-processing of the simulation results.

the LED-rail. Using our COMSOL simulation model with appropriate source excitation and boundary conditions between the elements, it is possible to gain more information on the pressure field in the air surrounding the LED-rail in the absence of these components. In figure 4.48, a snapshot of the pressure field in the surrounding air is plotted for a 500 kHz CW excitation by an air-coupled transducer of 6 mm diameter centrally located above the LED-rail. Since the LED-rail is fully symmetric, a symmetric wave pattern is observed around the rail. A close look at the pressure field reveals that regions with high pressure alternate with low pressure zones. This is also observed in figure 4.49, where the normalized amplitude of the pressure in air was measured on a line surrounding the LED-rail (see dotted line in figure 4.47 and full line in figure 4.48). The vertical axis in figure 4.49 represents the normalized pressure amplitude and the horizontal axis represents the distance along the line, with distance 0 corresponding to the centre of the line.

The above discussed line scan can now be used to study the changes in the pressure field in different circumstances. First, we will study the influence of

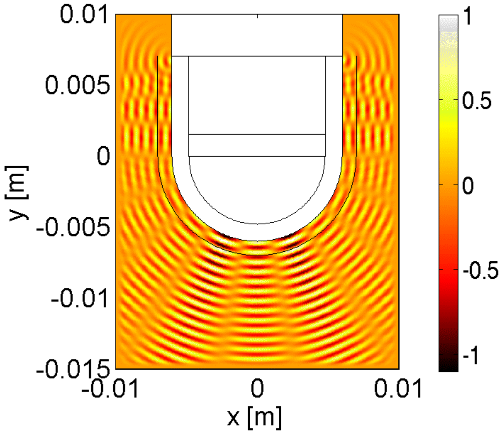

Figure 4.48: Snapshot of the pressure field in the air surrounding a LED-rail for a CW excitation at 500 kHz by means of a 6 mm diameter air-coupled ultrasonic transducer centrally located above the LED-rail. The line surrounding the LED-rail is used for post-processing of the simulation results. The colour scale is normalized according to its maximum value.

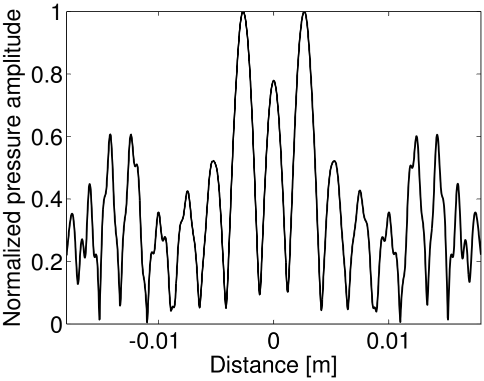

Figure 4.49: Line scan of the simulated normalized pressure amplitude on a line surrounding the LED-rail for a CW excitation at 500 kHz.

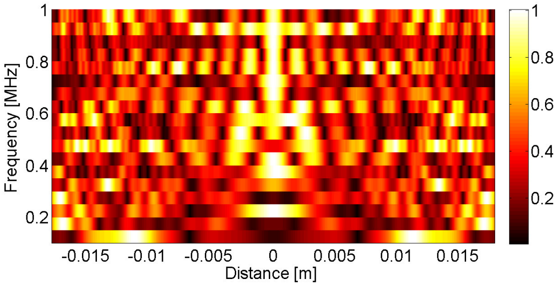

Figure 4.50: Line scans of the simulated normalized pressure amplitude on a line surrounding the LED-rail for a CW excitation at different frequencies. Every line scan is normalized according to its maximum value. The simulated pressure amplitudes strongly depend on the excitation frequency (i.e. different maxima, different number of maxima, more or less extended regions of maximum pressure).

the frequency of a CW excitation on the simulated pressure field. Therefore, we performed several simulations in which continuous waves were excited with each time a different excitation frequency, starting from 100 kHz to 1 MHz in steps of 50 kHz. For every frequency we determined the normalized pressure amplitude on the virtual line surrounding the LED-rail. Finally, the simulated line scan for each frequency is plotted as part of a colour coded image in figure 4.50. It is clear that, for every frequency, the observed pressure field in air is symmetric. Furthermore, for every CW excitation, regions of high pressure alternate regions of low pressure, as in the case of a 500 kHz CW excitation. However, there are quite large differences to be found in the simulated pressure amplitudes at different frequencies. Depending on the frequency, the different maxima in the pressure field are redistributed. The maximum pressure is not always found right under the LED-rail (distance 0), but can also be found to the left/right of the rail. In addition, regions of maximum pressure can be more or less extended and the number of maxima can be different. From these results, it appears that the observed wave pattern around a LED-rail strongly depends on the frequency of the generated ultrasonic wave.

Choosing now a fixed frequency for the CW excitation, e.g. 500 kHz, we can study the influence of the presence of an electronic element or an air bubble on the pressure field. Therefore, we determined the normalized pressure amplitudes along the line surrounding the LED-rail for different sized electronic elements or air bubbles. In figure 4.51, the normalized pressure amplitudes are plotted in case of different square-shaped electronic elements. The vertical axis represents the side length of the electronic elements, starting from 0 mm (no electronic element) to 5 mm in steps of 0.5 mm. The horizontal axis represents the distance

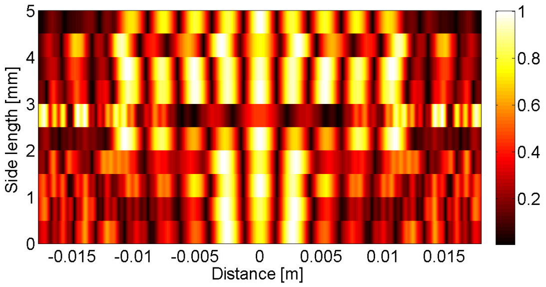

Figure 4.51: Line scans of the simulated normalized pressure amplitude on a line surrounding the LED-rail for a CW excitation at 500 kHz. Inside the LED-rail square-shaped electronic elements with different side lengths are inserted. Every line scan is normalized according to its maximum value. The simulated pressure amplitudes strongly depend on the size of the electronic elements (i.e. different maxima, different number of maxima, more or less extended regions of maximum pressure).

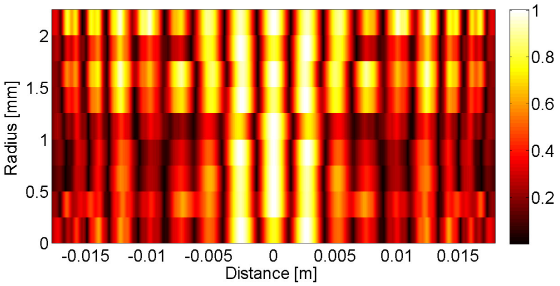

Figure 4.52: Line scans of the simulated normalized pressure amplitude on a line surrounding the LED-rail for a CW excitation at 500 kHz. Inside the LED-rail circular air bubbles with different radii are inserted. Every line scan is normalized according to its maximum value. The simulated pressure amplitudes strongly depend on the size of the air bubbles (i.e. different maxima, different number of maxima, more or less extended regions of maximum pressure).

along the line. Figure 4.52 shows the normalized pressure amplitudes in case of different circular air bubbles. In this figure, the vertical axis represents the radius of the circular air bubble, starting from 0 mm (no air bubble) to 2.25 mm in steps of 0.25 mm. In both figures, the simulated pressure amplitudes strongly depend on the size of the electronic element or the air bubble.

Based on the simulation results, an air-coupled ultrasonic technique for the inspection of a LED-rail could be proposed. A schematic representation of

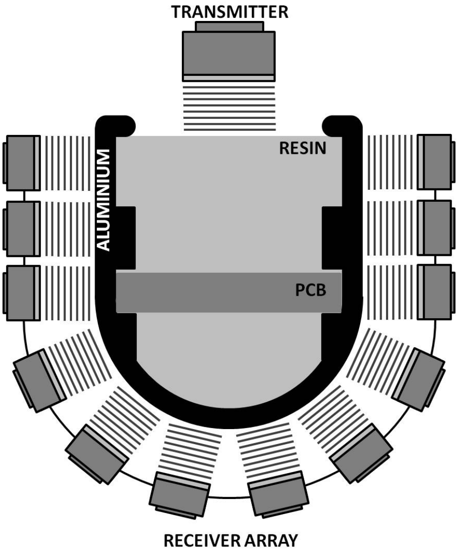

Figure 4.53: Schematic representation of the experimental setup for the air-coupled ultrasonic inspection of a LED-rail. An ultrasonic CW signal is transmitted by a transmitter centrally located above the LED-rail. The pressure field in the air surrounding the LED-rail is measured by means of a receiver array.

the technique is shown in figure 4.53. An air-coupled ultrasonic transducer is centrally located above the LED-rail, emitting a CW signal at a certain frequency. The emitted ultrasonic wave then propagates further in air, until it reaches the rail. Inside the rail, the signal is reflected and/or refracted along multiple paths before it is finally transmitted on the other side of the LED-rail. Upon leaving the aluminium rail, the transmitted signal is captured by a receiver array surrounding the rail. Using the various received signals, an image of the transmitted sound field can be formed. Moving the transmitter and the receiver array along the LED-rail, the whole rail can be scanned. Since the sound field around the LED-rail is highly influenced by the presence of electronic elements and/or air bubbles inside the rail, changes in the produced images are found at positions where the electronic elements and/or air bubbles are located.

At the laboratory for non-contact ultrasound of KATHO, a simple experiment to test the proposed technique was recently performed, using a single receiver instead of an array of receivers. The receiver was initially positioned right under the LED-rail and was then rotated starting from 0 degrees to 22 degrees in steps of 2 degrees. At every position of the receiver, the response was measured for a 50 μs tone-burst excitation at respectively 850, 900 and 950 kHz. The first experimental results clearly showed the large frequency dependence and the typical sound field patterns with regions of maximum intensity alternating regions with almost no intensity could be observed. Also, significant changes in the measured responses were found at positions where electronic elements or air bubbles are present in the LED-rail, confirming the simulation results and proving the potential of the proposed air-coupled ultrasonic NDT technique for the inspection of LED-rails. The numerical model presented here can now be used to further guide the design and development of an in-line inspection tool.

4.6 Conclusion

Comsol PDE modes with addition of CPML layers have been used for the simulation of various cases of air-coupled pitch-catch inspection of materials. The simplest test case consists of an aluminium plate containing a borehole. Subsequently, an aluminium plate with varying thickness transition was considered, and finally a quite complicated composition of a LED-rail was studied.

Regarding the aluminium bar with a circular borehole, two different simulation models, a simple geometric model and a finite element based model, have been developed and tested by comparing the predictions with basic observational results. We have shown that the simulation results are in qualitative good agreement with the observations implying that both simulation methods can be beneficial for the interpretation of air-coupled experiments. However, for a more realistic account of the experimental conditions and a better interpretation of the results, the finite element simulation is more appropriate.

Apart from the pure comparison of measurements and simulations, we also performed numerical experiments using the finite element simulation method to predict the effect of experimental parameters which are hard to vary in real conditions, such as the vertical position of a defect in a solid plate, and we elaborated on the danger of using pure (mono-frequency) Lamb waves for the detection of a defect by linking the predictions at the receiver to the displacement field inside the solid. Defects that appear in nodes of Lamb waves will have little or no influence on the received intensity. The use of swept signals can be considered to avoid this problem.

In addition, the simulation methods have been applied to predict the influence of a rectangular inclusion on the response plots. The simulations showed the possibility to determine the orientation of a rectangular inclusion simply by performing a single-sided air-coupled pitch-catch experiment and measuring the response in the first or second reflection maximum.

The finite element model has also been used for the implementation of more complex models, and was illustrated for two particular examples: an aluminium plate with a section of varying thickness and a LED-rail. Based on the simulation results, two air-coupled ultrasonic techniques for the non-destructive testing of the samples were proposed. For the locally bulged aluminium plate, the technique is based on the detection of mode conversions in the sample caused by the passage of a Lamb wave through the varying section domain. For the inspection of a LED-rail, we proposed a technique using an array of receivers surrounding the rail. Simulation tools have been prepared and made available to provide guidance in the design, further development and optimization of these inspection methods.

Indeed, the models described here can be used in a variety of studies with the aim to determine the best parameters to be used in a particular experiment. Parameters that can be investigated concern for example the position and distance between transmitter and receiver, the array configuration, the angle of incidence, the frequency spectrum of excitation, etc. The goal of these studies is to help optimizing air-coupled techniques for applications in non-destructive testing such as the inspection of welding joints, detection of air bubbles in LED-rail profiles, etc.

Bibliography

[1] *COMSOL Multiphysics User's Guide, Version 3.3*, 2006.

[2] Arone, M., Cerniglia, D., and Nigrelli, V. Defect characterization in Al welded joints by non-contact Lamb wave technique. *J. Mater. Process. Tech. 176* (2006), 95–101.

[3] Ballad, E., Vezirov, S., Pfleiderer, K., Solodov, I., and Busse, G. Nonlinear modulation technique for NDE with air-coupled ultrasound. *Ultrasonics 42* (2004), 1031–1036.

[4] Bass, H., Sutherland, L., Zuckerwar, A., Blackstock, D., and Hester, D. Atmospheric absorption of sound: Further developments. *J. Acoust. Soc. Am. 97* (1995), 680–683.

[5] Bass, H., Sutherland, L., Zuckerwar, A., Blackstock, D., and Hester, D. Erratum: Atmospheric absorption of sound: Further developments. *J. Acoust. Soc. Am. 99* (1996), 1259.

[6] Bérenger, J. A perfectly matched layer for the absorption of electromagnetic waves. *J. Comput. Phys. 114* (1994), 185–200.

[7] Bérenger, J. Evanscent waves in PML's: origin of the numerical reflection in wave-structure interaction problems. *Transactions on Antennas and Propagation 47* (1999), 1497–1503.

[8] Bérenger, J. Numerical reflection from FDTD-PMLs: a comparison of the split PML with the unsplit and CFS PMLs. *Transactions on Antennas and Propagation 50* (2002), 258–265.

[9] Berriman, J., Purnell, P., Hutchins, D., and Neild, A. Humidity and aggregate content correction factors for air-coupled ultrasonic evaluation of concrete. *Ultrasonics 43* (2005), 211–217.

[10] Blomme, E., Bulcaen, D., and Declercq, F. Air-coupled ultrasonic NDE: experiments in the frequency range 750 kHz - 2 MHz. *NDT&E Int. 35* (2002), 417–426.

[11] Blomme, E., Bulcaen, D., and Declercq, F. Recent observations with air-coupled NDE in the frequency range of 650 kHz to 1.2 MHz. *Ultrasonics 40* (2002), 153–157.

[12] Blomme, E., Bulcaen, D., Declercq, F., Deveugele, J., and Lust, P. Single-sided air-coupled ultrasonic inspection of thick plate materials. In *Proceedings of the International Congress on Ultrasonics* (Vienna, April 2007).

[13] Blomme, E., Bulcaen, D., Declercq, F., Deveugele, J., and Lust, P. Air-coupled ultrasonic pitch-catch method for material inspection. In *Emerging technologies in non-destructive testing* (Stuttgart, April 2008), G. Busse, G. Busse, D. Van Hemelrijck, and I. Solodov, Eds., pp. 137–143.

[14] Blomme, E., Bulcaen, D., Declercq, F., and Lust, P. Air-coupled ultrasonic evaluation of coated textiles. *Ultrason* (2002), 757–760.

[15] Bou Matar, O., Galopin, E., Li, Y., and Ducloux, O. An optimized convolution-perfectly matched layer (C-PML) absorbing boundary condition for the second-order elastic wave equation - Application to surface and Lamb waves propagation. In *Proceedings of the COMSOL users Conference* (Grenoble, October 2007).

[16] Bou Matar, O., Preobrazhensky, V., and Pernod, P. Two-dimensional axisymmetric numerical simulation of supercritical phase conjugation of ultrasound in active solid media. *J. Acoust. Soc. Am. 118* (2005), 2880–2890.

[17] Castaings, M., and Cawley, P. The generation, propagation, and detection of Lamb waves in plates using air-coupled ultrasonic transducers. *J. Acoust. Soc. Am. 100* (1996), 3070–3077.

[18] Castaings, M., Cawley, P., Farlow, R., and Hayward, G. Single sided inspection of composite materials using air coupled ultrasound. *J. Nondestruct. Eval. 17* (1998), 37–45.

[19] Castaings, M., and Hosten, B. Air-coupled measurement of plane wave, ultrasonic plate transmission for characterising anisotropic, viscoelastic materials. *Ultrasonics 38* (2000), 781–786.

[20] Castaings, M., and Hosten, B. Lamb and SH waves generated and detected by air-coupled ultrasonic transducers in composite material plates. *NDT&E Int. 34* (2001), 249–258.

[21] Castaings, M., and Hosten, B. Guided waves propgating in sandwich structures made of anisotropic, viscoelastic, composite materials. *J. Acoust. Soc. Am. 113* (2003), 2622–2634.

[22] Chew, W., Jin, J., and Michielssen, E. Complex coordinate stretching as a generalized absorbing boundary condition. *Microw. Opt. Techn. Let. 15* (1997), 363–369.

[23] Chew, W., and Liu, Q. Perfectly matched layers for elastodynamics: A new absorbing boundary condition. *Journal of Computational Mechanics 4* (1996), 341–359.

[24] Chew, W., and Weedon, W. A 3D perfectly matched medium from modified Maxwells equations with stretched coordinates. *Microw. Opt. Techn. Let. 7* (1994), 599–604.

[25] Collino, F., and Tsogka, C. Application of the perfectly matched absorbing layer model to the linear elastodynamic problem in anisotropic heterogeneous media. *Geophysics 66* (2001), 294–307.

[26] Delrue, S., Van Den Abeele, K., Blomme, E., Deveugele, J., Lust, P., and Bou Matar, O. Two-dimensional simulation of the single-sided air-coupled ultrasonic pitch-catch technique for non-destructive testing. *Ultrasonics 50* (2010), 188–196.

[27] Gan, T., Hutchins, D., and Billson, D. Preliminary studies of a novel air-coupled ultrasonic inspection system for food containers. *J. Food Eng. 53* (2002), 315–323.

[28] Gan, T., Hutchins, D., Billson, D., and Schindel, D. The use of broadband acoustic transducers and pulse-compression techniques for air-coupled ultrasonic imaging. *Ultrasonics 39* (2001), 181–194.

[29] Gan, T., Pallav, P., and Hutchins, D. Non-contact ultrasonic quality measurements of food products. *J. Food Eng. 77* (2006), 239–247.

[30] Gomez, T. Acoustic impedance matching of piezoelectric transducers to the air. *IEEE T. Ultrason. Ferr. 51* (2004), 624–633.

[31] Grimberg, R., Savin, A., Steigmann, R., and Bruma, A. Ultrasound and visual examination of wood based products. In *Proceedings of the 8th International Conference of the Slovenian Society for Non-Destructive Testing* (Portoro, September 2005), pp. 109–115.

[32] Gudra, T., Pluta, M., and Kojro, Z. The measurement and numerical modelling of the diffraction field of a spherical ultrasonic transducer working in the air at the frequency of 1.3 MHz. *Ultrasonics 38* (2000), 794–798.

[33] Hastings, F., Schneider, J., and Broschat, S. Application of the perfectly matched layer (PML) absorbing boundary condition to elastic wave propagation. *J. Acoust. Soc. Am. 100* (1996), 3061–3069.

[34] Hosten, B., and Biateau, C. Finite element simulation of the generation and detection by air-coupled transducers of guided waves in viscoelastic and anisotropic materials. *J. Acoust. Soc. Am. 123* (2008), 1963–1971.

[35] Imielinska, K., Castaings, M., Wojtyra, R., Haras, J., Le Clezio, E., and Hosten, B. Air-coupled ultrasonic C-scan technique in impact

response testing of carbon fibre and hybrid: glass, carbon and kevlar/epoxy composites. *J. Mater. Process. Tech. 157* (2004), 513–522.

[36] Katz, D., Thiele, E., and Taflove, A. Validation and extension to three dimensions of the Berenger PML absorbing boundary condition for FD-TD meshes. *Microw. Opt. Techn. Let. 4* (1994), 268–270.

[37] Kazys, R., Demcenko, A., Mazeika, L., Sliteris, R., and Zukauskas, E. Investigation of mode conversion in ultrasonic air-coupled non-destructive testing. *Emerging Technologies in Non-Destructive Testing* (2008), 129–135.

[38] Kazys, R., Demcenko, A., Zukauskas, E., and Mazeika, L. Air-coupled ultrasonic investigation of multi-layered composite materials. *Ultrasonics 44* (2006), 819–822.

[39] Ke, W., Castaings, M., and Bacon, C. 3D finite element simulations of an air-coupled ultrasonic NDT system. *NDT&E Int. 42* (2009), 524–533.

[40] Kelly, S., Hayward, G., and Gomez, T. An air-coupled ultrasonic matching layer employing half wavelength cavity resonance. *Ultrason* (2001), 965–968.

[41] Krautkramer, J., and Krautkramer, H. *Ultrasonic testing of materials.* Springer, 1990.

[42] Kuzuoglu, M., and Mittra, R. Frequency dependence of the constitutive parameters of causal perfectly matched anisotropic absorbers. *Microwave and Guided Wave Letters 6* (1996), 447–449.

[43] Lagrain, B., Boeckx, L., Wilderjans, E., Delcour, J., and Lauriks, W. Non-contact ultrasound characterization of bread crumb: Application of the Biot-Allard model. *Food Res. Int. 39* (2006), 1067–1075.

[44] Li, Y., and Bou Matar, O. Convolutional perfectly matched layer for elastic second-order wave equation. *J. Acoust. Soc. Am. 127* (2010), 1318–1327.

[45] Liu, Q., and Tao, J. The perfectly matched layer for acoustic waves in absorptive media. *J. Acoust. Soc. Am. 102* (1997), 2072–2082.

[46] McIntyre, C., Hutchins, D., Billson, D., and Stor-Pellinen, J. The use of air-coupled ultrasound to test paper. *IEEE T. Ultrason. Ferr. 48* (2001), 717–727.

[47] Meyer, S., Hindle, S., Sandoz, J., Gan, T., and Hutchins, D. Non-contact evaluation of milk-based products using air-coupled ultrasound. *Meas. Sci. Technol. 17* (2006), 1838–1846.

[48] Park, W., Choi, S., Lee, J., Seo, K., and Byun, J. Laser-generated ultrasonic technique for inspecting delamination in CFRP. *Key Eng. Mat. 321-323* (2006), 968–971.

[49] Pizarro, L., Certon, D., Lethiecq, M., and Hosten, B. Airborne ultrasonic electrostatic transducers with conductive grooved backplates: tailoring their centre frequency, sensitivity and bandwidth. *Ultrasonics 37* (1999), 493–503.

[50] Potter, T., Ghaffari, B., and Mozurkewich, G. Sub-wavelength resolution in air-coupled ultrasound images of spot welds. *NDT&E Int. 38* (2005), 374–380.

[51] Riegert, G., Pfleiderer, K., Gerhard, H., Solodov, I., and Busse, G. Modern methods of NDT for inspection of aerospace structures. In *Proceedings of the European Conference on Non-Destructive Testing* (Berlin, September 2006).

[52] Roden, J., and Gedney, S. Convolution PML (CPML): an efficient FDTD implementation of the CFS-PML for arbitrary media. *Microw. Opt. Techn. Let. 27* (2000), 334–339.

[53] Schindel, D. Air-coupled ultrasonic measurements of adhesively bonded multi-layer structures. *Ultrasonics 37* (1999), 185–200.

[54] Schindel, D., Hutchins, D., Zou, L., and Sayer, M. The design and characterization of micromachined air-coupled capacitance transducers. *IEEE T. Ultrason. Ferr. 42* (1995), 42–50.

[55] Solodov, I., Döring, D., and Busse, G. Mapping of elastic anisotropy with air-coupled phonon-focusing of guided and surface waves. In *Proceedings of the European Conference on Non-Destructive Testing* (Berlin, September 2006).

[56] Solodov, I., Pfleiderer, K., Gerhard, H., Predak, S., and Busse, G. New opportunities for NDE with air-coupled ultrasound. *NDT&E Int. 39* (2006), 176–183.

[57] Solodov, I., Stoessel, R., and Busse, G. Material characterization and NDE using focused slanted transmission mode of air-coupled ultrasound. *Res. Nondestruct. Eval. 15* (2004), 65–85.

[58] Stoessel, R. *Air-coupled ultrasound inspection as a new non-destructive testing tool for quality assurance.* PhD thesis, University of Stuttgart, Germany, 2003.

[59] Stoessel, R., Krohn, N., Pfleiderer, K., and Busse, G. Air-coupled ultrasound inspection of various materials. *Ultrasonics 40* (2002), 159–163.

[60] Taflove, A., and Hagness, S. *Computation electrodynamics: Perfectly matched layer absorbing boundary conditions.* Artech House Publishers, 2005, ch. 7, pp. 273–328.

[61] Turo, A., Salazar, J., Chavez, J., Kichou, H., Gomez, T., Montero de Espinosa, F., and Garcia-Hernandez, M. Ultra-low noise front-end electronics for air-coupled ultrasonic non-destructive evaluation. *NDT&E Int. 36* (2003), 93–100.

Chapter 5

Time reversed acoustics

In acoustic and ultrasonic non-destructive testing techniques, it is sometimes beneficial to concentrate sound energy at a chosen location in space and at a specific instance in time, for example to improve the signal-to-noise ratio. Time reversal techniques, taking advantage of the reversible character of the wave equation, are particularly suited to focus ultrasonic waves in time and space. The quality of the energy focusing in solid media using principles of time reversed acoustics is highly influenced by the nature and dimensions of the medium, the number of transducers and the length of the received signals. Normally, a large number of transducers enclosing the domain of interest is needed to improve the quality of the focusing. However, in the case of highly reverberant media, the number of transducers can be reduced to only one (single-channel time reversal).

To demonstrate and give a better understanding of particular single-channel time reversal techniques, a numerical simulation study has been developed based on the finite element model discussed in the previous chapter. First, the model allows to simulate the single-channel reciprocal time reversal technique in a reverberant medium, in which the end result is a focus of energy at the original receiver location. Furthermore, we were able to demonstrate the possibility of selectively focusing energy along each of the spatial directions, either individually or collectively, and to focus on multiple locations simultaneously. For focusing in a non-reverberant medium, which is impossible when using only one source, an adaptation of the single-channel reciprocal time reversal procedure has been recently suggested by means of a chaotic cavity transducer (i.e. a transducer glued on a cavity of chaotic shape). Moreover, the chaotic cavity transducer can be used to create a virtual phased array, enabling energy focusing at an arbitrary point in the medium. Using the finite element model, both concepts of the chaotic cavity transducer were illustrated and confirmed.

In the first section, a brief introduction to time reversal techniques is given. Section 2 outlines the necessary adaptations of the 2D finite element model, developed in the previous chapter, for the simulation of time reversal experiments. Results of different finite element simulations of time reversal experiments are discussed in the third, fourth and fifth section. The third section covers results of simulations of time reversal experiments in a reverberant medium, focusing on single-channel reciprocal time reversal to focus high levels of acoustic energy at a certain position in the medium and illustrating the possibility to selectively focus each of the different vector components or to focus on multiple locations simultaneously. The fourth section covers results of simulations of a chaotic cavity transducer, demonstrating the possibility to focus energy in a non-reverberant sample using reciprocal single-channel time reversal. Finally, in the fifth section, the concept of a virtual phased array is illustrated.

5.1 Time reversal techniques

Time reversal (TR) techniques have become a hot topic of innovative research in ultrasonic applications [12–15]. The basic premise of time reversed acoustics (TRA) is that, if the wave field can be known as a function of time on some boundary surrounding a given region, then it can also be found at every point inside that region at previous times by using the wave equation with time running backwards. In other words, the result of a TR process is that the waves recorded on the boundary are focused back in space and time on the acoustic sources, or on the scattering targets inside the region which were acting as sources. Doing so, it enables us to locate strong scatterers (e.g. inclusions and interfaces with high impedance contrast) which are hidden inside a region. Applications of TRA can be found in seismology (earthquake localisation) [2, 21–23], diagnostic and therapeutic medicine [7, 17, 28, 38], and in non-destructive testing [18, 24, 34–36, 39–41].

In a classical TRA experiment, waves generated by an acoustic source are first measured by an array of piezoelectric transducers located around the source, and then time reversed and re-emitted by the same transducers array. The created time reversed wave then propagates back and eventually focuses on the location of the initial source, now remaining passive. The quality of the focusing can be improved if the transducers cover a closed surface around the medium in order to obtain information from all wave fronts propagating in all directions [5].

In practice, however, this is difficult to realize and the TR operation is usually performed on a limited angular area, limiting the reversal and focusing quality.

An important advantage of TRA for engineering materials is that it works extremely well in heterogeneous media (actually better than in homogeneous ones). Multiple scattering in transmission experiments [6] or multiple reflections in wave guides [19, 27, 32, 33] or inside chaotic cavities [8–10], instead of being a hindrance, actually improve the focusing. This reduces the number of receivers needed to obtain a good reversal quality. Draeger et al. [8–10] and Fink et al. [16] even proved the possibility of reducing the number of elements down to one by using multiple reflections inside a closed chaotic cavity. In addition, it was shown that the focusing quality can be increased by a longer recording of the time reversed signal [8]. However, for too long time windows, the focusing quality can no more be improved, since the essential signal information can no longer be discerned from noise due to attenuation in the material.

In standard single-channel TR experiments, a signal measured by the receiver is time reversed and subsequently re-emitted back into the medium by a transducer located at the same position of the receiver, focusing at the original source position [2]. Due to reciprocity in acoustic and elastic wave propagation, the back propagation of the time reversed signal can also take place from the position of the source to the position of the receiver, resulting in a focus of energy at the original receiver location [1]. This procedure is called reciprocal TR. Implementation of reciprocal TR thus allows to selectively focus acoustic/elastic energy at any position in a given medium, provided the direct received signal can be predicted or obtained at that position, for instance by an appropriate material model or -for surface locations- by recording the signal using a laser vibrometer or a non-contact transducer. The reciprocal TR technique can, for instance, be used to focus a large amount of energy at a certain position in order to trigger nonlinear features at that location [20, 40, 41].

In this chapter, we will concentrate on the numerical support of the single-channel reciprocal time reversal technique using the finite element model developed in the previous chapter and adapted for the simulation of time reversal techniques. Several virtual experiments will be performed, verifying important concepts of the single-channel reciprocal time reversal technique. In future, the models can then be modified and extended to help in the further development and optimization of the different TR techniques discussed here.

5.2 Time reversal finite element simulations

To demonstrate the feasibility and usefulness of single-channel reciprocal time reversal techniques, we will concentrate on the numerical support of these techniques. To this extend, a fully numerical approach is envisaged, that covers the emission of a virtual sound wave from the source location, the recording of the direct wave propagation signal (single or multiple components) at a particular location for the receiver position, the back propagation of the time reversed signal(s) from the original location of the emitter and the analysis of the energy focusing quality on the considered receiver location.

For the simulation of the numerical TR experiments, the model developed in the previous chapter and described in section 4.3.2 is used. For 2D simulations, equations (4.39) and (4.46), already adjusted for introducing PMLs and rewritten to facilitate the implementation in the PDE modes of Comsol, can be used for the implementation of respectively a solid material and a fluid. Both equations can easily be extended to 3D.

An acoustic/ultrasonic source can be introduced in the model by implementing it as a particular boundary condition. In traditional TR experiments, the source signal consists of a short pulse, which is applied to the transducer. To obtain spatial and temporal focusing, the impulse response of this signal, measured by the receiver, is time reversed and broadcasted back into the medium. It is shown, however, that the quality of the focusing can be improved by applying a pulse compression technique which requires a linear sweep signal as excitation signal instead of a short pulse [3, 4, 11]. The linear frequency sweep signal used in our simulation is the following:

$$S(t) = \sin\left[2\pi\left(f_c - \frac{B}{2} + \frac{Bt}{2T}\right)t\right]\exp\left[-\frac{1}{p}\left(\frac{t-t_c}{\sigma}\right)^p\right] \tag{5.1}$$

where f_c is the central frequency, B is the total bandwidth that is swept and T is the duration of the signal. In order to reduce time domain side lobes which may appear in the pulse compression process, the sweep signal was multiplied with a generalized Gaussian time window with exponent p, central time $t_c = T/2$ and standard deviation σ, chosen such that the amplitude of the Gaussian envelope at times $t = 0$ and $t = T$ equals one percent of the amplitude at time $t = t_c$. Broadcasting this sweep signal from the source location, the direct wave propagation signal $R(t)$ is detected at the receiver position. To augment the signal-to-noise ratio of the focusing after time reversal, pulse compression of the received signal is accomplished by first taking the cross-correlation of $R(t)$ with the input signal $S(t)$, resulting in a cross-correlated signal $C(t)$, given by:

$$C(t) = S(-t) * R(t) \tag{5.2}$$

where $*$ denotes the convolution. Finally, the cross-correlated signal is time reversed and broadcasted back from the source into the medium, resulting in a high quality focus of energy at the receiver location.

Since the simulations represent wave propagation phenomena in a supposedly linear medium, the finite element model used for the TR simulations is solved in the frequency domain, and we will work with the Fourier transforms of the different time signals, denoted with a hat ($\hat{}$). The initial forward propagation of the sweep signal from the source to the receiver is implemented as follows. First, the linear frequency sweep signal $S(t)$ is Fourier transformed, resulting in a frequency dependent function $\hat{S}(f)$. A selection of discrete frequencies within this spectrum is then used as a parametric input for the boundary condition at the source. For every frequency within this spectrum, a complex amplitude can be measured at the receiver location, resulting in a frequency dependent function $\hat{R}(f)$, corresponding to the Fourier transform of the time signal $R(t)$ detected by the receiver. For the back propagation step of the time reversal process, the Fourier transform of the cross-correlated signal $C(t)$ needs to be determined. At this point, we can take advantage of the convolution theorem, stating that the Fourier transform of a convolution is the point-wise product of Fourier transforms. In other words, convolution in time domain equals point-wise multiplication in frequency domain. For the cross-correlated signal $C(t)$, this means that the Fourier transform of this signal, i.e. $\hat{C}(f)$, equals the point-wise product of the Fourier transform of the time reversed input signal $S(-t)$ and the Fourier transform of the received signal $R(t)$. Since the Fourier transform of a time reversed signal equals the complex conjugate of the original signal spectrum, the Fourier transform of the cross-correlated signal can be calculated as follows:

$$\hat{C}(f) = \overline{\hat{S}(f)} \cdot \hat{R}(f) \tag{5.3}$$

where $\overline{\hat{S}(f)}$ denotes the complex conjugate of $\hat{S}(f)$. Finally, the complex conjugate of the spectrum $\hat{C}(f)$ of the cross-correlated signal (i.e. the Fourier transform of the time reversed cross-correlated signal) is used as a parametric input for the boundary condition at the source and for every frequency, a complex amplitude is measured at the receiver location, resulting in a frequency dependent complex-valued function, which corresponds to the Fourier transform of the focusing signal. In every step of the simulation, the time domain results can be obtained by performing an inverse Fourier transform of the data using the MATLAB software.

The above procedure can be economized as follows. Taking maximal advantage of the spectral method, one can obtain the exact same solution of the model without performing two separate simulations (i.e. one for the forward propagation and one for the back propagation phase). Therefore, the model first needs to be solved for a discrete number of frequencies using a constant amplitude equal to one as an input for the boundary condition at the source, instead of using the Fourier transform $\hat{S}(f)$ of the linear frequency sweep signal $S(t)$. For every frequency, the amplitudes calculated in each point of the model are then stored. The focusing signal can now be calculated as follows. First, the stored solution at the receiver location is multiplied -frequency by frequency- by the spectrum $\hat{S}(f)$ of the sweep signal, resulting in the frequency dependent function $\hat{R}(f)$. This signal is then used to determine the spectrum of the cross-correlated signal $\hat{C}(f)$, in accordance with equation (5.3). Finally, the original stored solution at the receiver location is multiplied -again frequency by frequency- by the complex conjugate of this spectrum to get the Fourier transform of the focusing signal. Finally, the time domain signal can be obtained by performing an inverse Fourier transform of the data using MATLAB. Using this method, the TR simulations become less time consuming. Moreover, if there are no changes in the geometry, the solutions for different parameters (e.g. different source signals, different focal points, etc.) can be determined using only the stored data from one simulation.

5.3 Time reversal in a reverberant medium

As mentioned in section 5.1, reciprocal time reversal provides the possibility to focus elastic waves in any particular point of a multi-reverberant sample using only one channel. In this section, this will be illustrated, studying the results of a numerical simulation of reciprocal single-channel time reversal in an odd shaped 2D aluminium sample.

The considered aluminium sample has a circular shape with two flat sides. The maximum height of the sample is 3 cm and the maximum width is 3.5 cm. An illustration of the geometry of the aluminium sample used in the COMSOL simulations is shown in figure 5.1. All boundaries of the sample, except the active surface of the transmitter (i.e. the flat side on top of the sample), are expected to be stress-free. At the transmitter, the normal stress component is set equal to the frequency dependent amplitude of the Fourier transform of the sweep signal, given in equation (5.1), with central frequency $f_c = 600$ kHz, bandwidth $B = 600$ kHz, duration $T = 100$ μs and $p = 20$. The temporal evolution and the Fourier transform of the sweep signal are both plotted in figure 5.2.

In the following subsections, we will first demonstrate the single-channel time reversal technique to focus energy at a point inside the aluminium sample. Then we will show that we are able to focus along each of the spatial directions, either

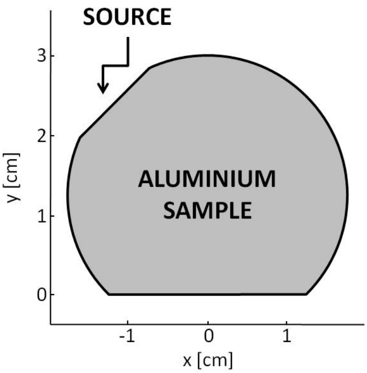

Figure 5.1: Illustration of the geometry of an aluminium multi-reverberant sample used in the COMSOL simulation. The sample has a maximum height of 3 cm and a maximum width of 3.5 cm. A sweep signal is emitted at the flat side on top of the aluminium sample.

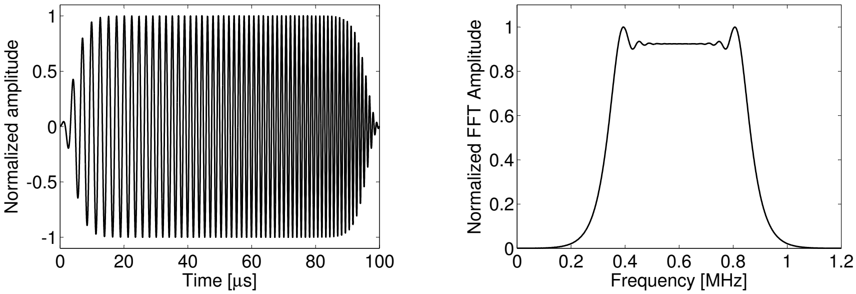

(a) (b)

Figure 5.2: Temporal evolution (a) and Fourier transform (b) of the sweep signal (5.1) used for the simulation of a reciprocal single-channel TR experiment in an aluminium multi-reverberant sample. The frequency dependent amplitude is used as input for the source function in the finite element simulation.

individually or collectively. Finally, it is shown that in a linear medium, signals measured at different locations can be added and time reversed, resulting in a focusing of the energy on all individual measurement locations.

5.3.1 Single-channel time reversal

In this simulation, the chosen focal point is located at $(0, 1.5)$ cm inside the aluminium medium. After the sweep signal is emitted from the source, the vertical displacement component u_y is calculated at the focal point for a total duration of 1 ms. The resulting time signal is plotted in figure 5.3(a). It is clear that the signal is composed of multiple reflections on the stress-free boundaries of the reverberant aluminium sample. The attenuation in the signal is due to damping introduced in the model. The direct wave recorded signal, calculated at the focal point, is then cross-correlated with the time reversed input signal and the obtained cross-correlated signal is time reversed and re-emitted from the source into the aluminium sample. Again, the vertical displacement component u_y can be measured at the focal position. The resulting focusing signal, this time calculated for a total duration of 2 ms, and a zoom of this signal around the focal time are displayed in figures 5.3(b) and 5.3(c), showing both a clear peak at the focal time $t = 0$.

To improve the quality of the focusing the inverse filtering (IF) method can be used rather than the classical TR method [37]. In our case, the IF method with a single transducer coupled to a chaotic cavity consists in the inversion of the eigenmode energy [30]. Fundamentally, the IF approach performs an inversion of the energy of the eigenmodes, and constructs the re-emitted signal as a linear combination of all the eigenmodes of the cavity, weighted by this inversion. Doing so, the focusing process takes advantage of all eigenmodes of the system including those with the weakest energy which are poorly exploited in the TR focusing process.

In figure 5.4(a), the spectral content of the direct wave recorded signal (figure 5.3(a)) is displayed, showing the different eigenmodes present in the aluminium multi-reverberant sample. In the classical TR method, this spectrum is used in the back propagation phase of the TR process. Multiplying the different eigenmodes with the inverse of their energy, provided their energy is larger than some threshold value to avoid division by zero, gives the spectral content plotted in figure 5.4(b). Using this spectrum in the back propagation phase of the TR process instead of the original one, it is clear that all modes, including those with the weakest energy, will now be exploited. The resulting focusing signal and a zoom of this signal around the focal time $t = 0$ are respectively displayed in figures 5.5(a) and 5.5(b). As predicted, an improvement of the focusing

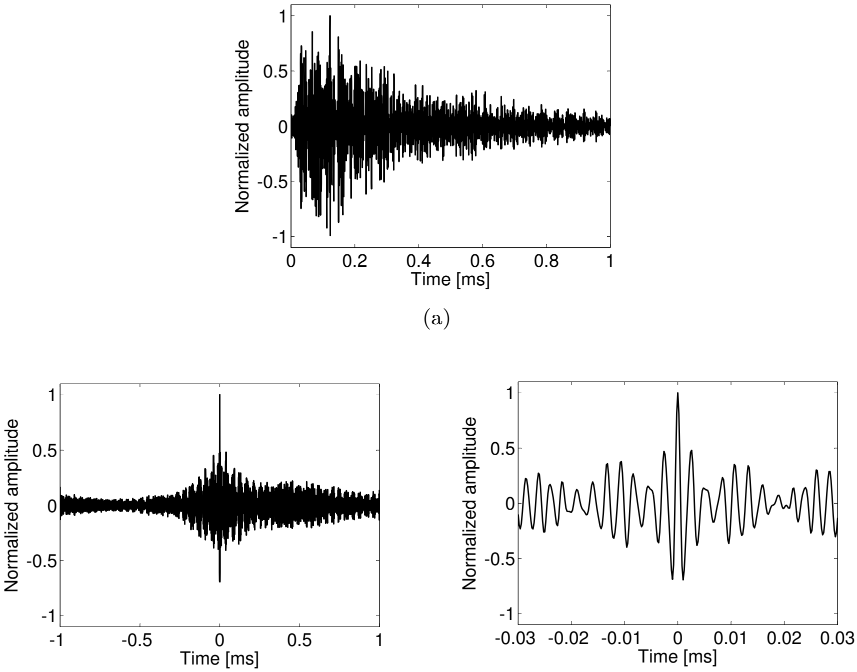

(a)

(b)

(c)

Figure 5.3: Illustration of the focusing in time in a single-channel reciprocal TR numerical experiment: (a) Direct wave recorded signal. (b) Focusing signal in a multi-reverberant aluminium sample for a linear sweep excitation. The Direct wave recorded signal is cross-correlated with the time reversed input signal. The time reversed cross-correlated signal is re-emitted by the source, resulting in the focusing signal. (c) Zoom of the focusing signal around the focal time.

quality can be observed using the IF technique compared to the classical TR method (figures 5.3(b) and 5.3(c)). This is linked, as expected, to the fact that the number of eigenmodes used with the IF method is higher than with the classical TR method. In the following, however, we will still use the classical TR method instead of the IF method. Even though the second method gives rise to a better focusing quality, the results obtained with the first method will prove to be sufficient to demonstrate and illustrate the different TR techniques discussed in this chapter.

The result of a single-channel reciprocal TR process is not only that the wave recorded by the receiver is focused back in time, but also that it is focused back

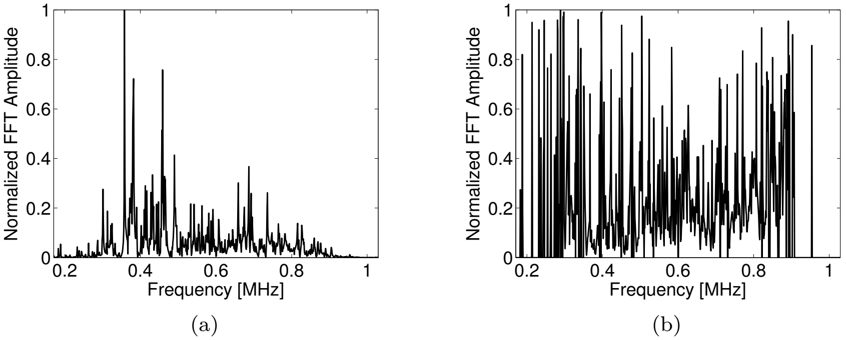

Figure 5.4: (a) Spectral content of the direct wave recorded signal (figure 5.3(a)). (b) Spectral content after IF. This spectrum is obtained by multiplying the different eigenmodes of the original spectrum with the inverse of their energy, provided their energy is larger than some threshold value to avoid division by zero.

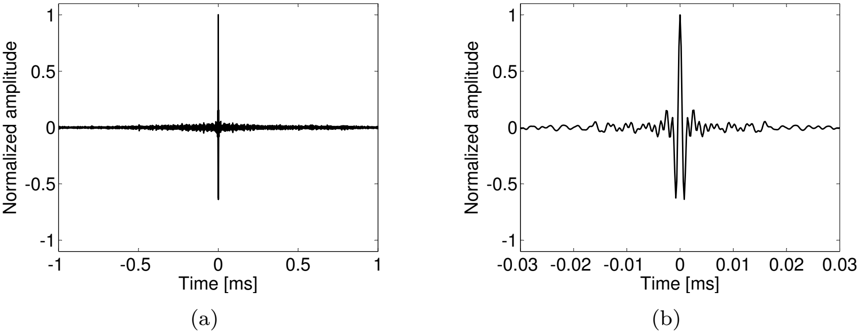

Figure 5.5: (a) Illustration of the focusing in time obtained with the IF method. (b) Zoom of the focusing signal around the focal time.

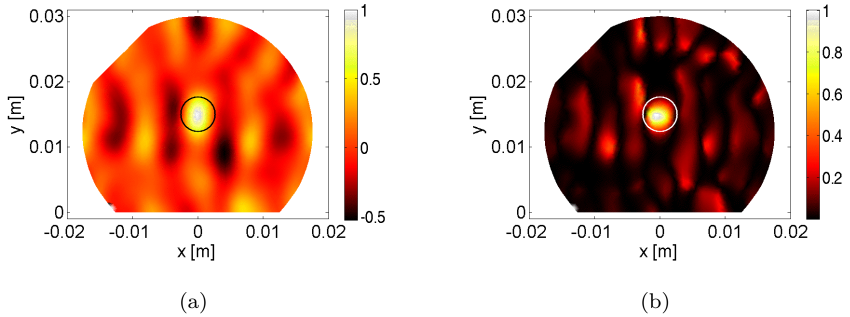

Figure 5.6: Illustration of the spatial focusing in a single-channel reciprocal TR numerical experiment. The focal point (encircled in the figure) is located at $(0, 1.5)$ cm. (a) Snapshot of the vertical displacement components u_y in a multi-reverberant aluminium sample at the focal time. The spatial focal point is at the position where the direct signal was received. (b) FNR (Focus-to-noise quality) plot of the vertical displacement components obtained using equation (5.4). In each figure, the colour scale is normalized according to its maximum value.

in space on the receiver location. In figure 5.6(a), a snapshot of the vertical displacement components in the multi-reverberant aluminium sample is shown at the focal time $t = 0$. High values are plotted in white, while low values are plotted in black. In the figure, the spatial focal point (encircled in the figure) is at the position where the direct signal was received, confirming that the single-channel reciprocal TR process indeed focuses back on the location of the receiver. An even more clear view of the focal spot is obtained by calculating, for every point in the sample, a "focus-to-noise ratio" (FNR) of the recorded time signals, defined as follows:

$$\mathrm{FNR}(x, y) = \frac{u_i(x, y, t_F)^2}{\mathrm{mean}\left[u_i(x, y, t \neq t_F)^2\right]} \tag{5.4}$$

where t_F is the focal time and $u_i(x, y, t)$ is the displacement of point (x, y) at time t ($i \in \{x, y\}$). The focus-to-noise ratio is thus equal to the ratio of the squared displacement amplitude at the focal time t_F to the mean of the squared displacement amplitudes at all other times. In figure 5.6(b), the vertical displacement components were used to calculate the focus-to-noise ratios $\mathrm{FNR}(x, y)$ in every point of the aluminium sample, resulting in a FNR plot. High FNR values are shown in white and low FNR values are shown in black. It is obvious that the highest FNR values are observed at the position of the focal point.

5.3.2 Multi-component time reversal

The simulation results already confirmed the possibility to focus high levels of acoustic energy at an arbitrary location using single-channel reciprocal TR. With the developed model, however, we can also verify the possibility to selectively focus energy along each of the two spatial coordinates individually or collectively, as demonstrated by Ulrich et al. [42]. Ulrich and co-workers showed that, using reciprocal TR, the vector nature of the focus (x and y displacement components) is maintained. If both displacement components are measured at a particular location in a medium and the sum of those signals is broadcasted back into the medium after time reversal and in scalar form (i.e. in one direction), then, the medium will ensure a simultaneously focusing of energy in both directions. If, however, only the x-component (y-component) is broadcasted back into the medium, then there will only be a focusing in the x-direction (y-direction) and not in the y-direction (x-direction).

In the previous simulations, we calculated the vertical displacement component at a particular location in the sample and the final result, after the TR procedure, was a focusing of energy, both in time and space, along the vertical displacement component on that location (see figure 5.3(b) and figure 5.6). According to the above reasoning, there should be no focusing along the other spatial coordinate. This is indeed confirmed in figures 5.7(a) and 5.7(b), where the time signals at the focal position for respectively the horizontal and vertical displacement component after TR of the direct recorded vertical displacement component are plotted. In the time signal for the vertical displacement component a clear focusing peak is found, while no peak is observed in the time signal for the horizontal displacement. Furthermore, looking at the FNR plots of respectively the horizontal and vertical displacement components in figures 5.7(c) and 5.7(d), we see that high FNR values at the focal position (encircled in the figures) are only found in the results for the vertical displacements.

A similar behaviour is observed when only the direct recorded horizontal displacement component u_x is considered in the time reversed signal. In figure 5.8, temporal and spatial simulation results after TR of the direct recorded horizontal displacement component u_x are visualized. As expected, evidences of a focusing of energy at the focal position (encircled in the bottom figures) are found only in the time signal of the simulated horizontal displacement measured at the focal position (figure 5.8(a)) and in the FNR plot of the horizontal displacement (figure 5.8(c)). No focusing of energy is observed in the results for the vertical displacement component (figures 5.8(b) and 5.8(d)).

Finally, the situation where both the horizontal and vertical displacement component are measured at the desired focal point, and returned simultaneously

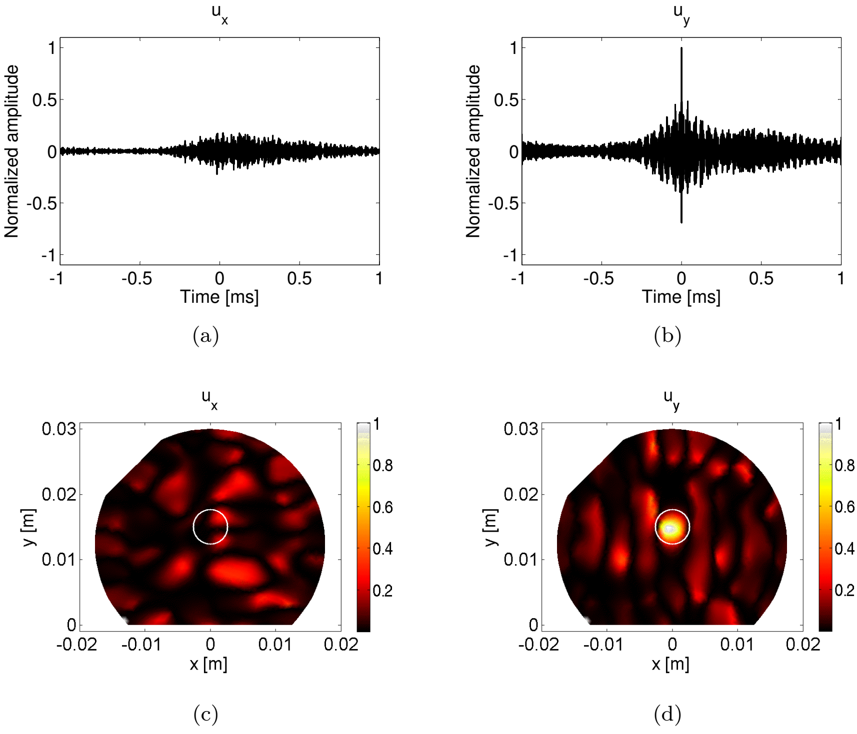

Figure 5.7: Simulated displacements in a multi-reverberant aluminium sample after reciprocal TR of the direct recorded vertical displacement component u_y. The focal position is located at $(0, 1.5)$ cm and is encircled in the bottom figures. (a) Simulated horizontal displacement measured at the focal position, (b) simulated vertical displacement measured at the focal position, (c-d) FNR plots of respectively the horizontal and vertical displacement component obtained using equation (5.4). The colour scales are normalized according to the maximum value of the vertical displacement component.

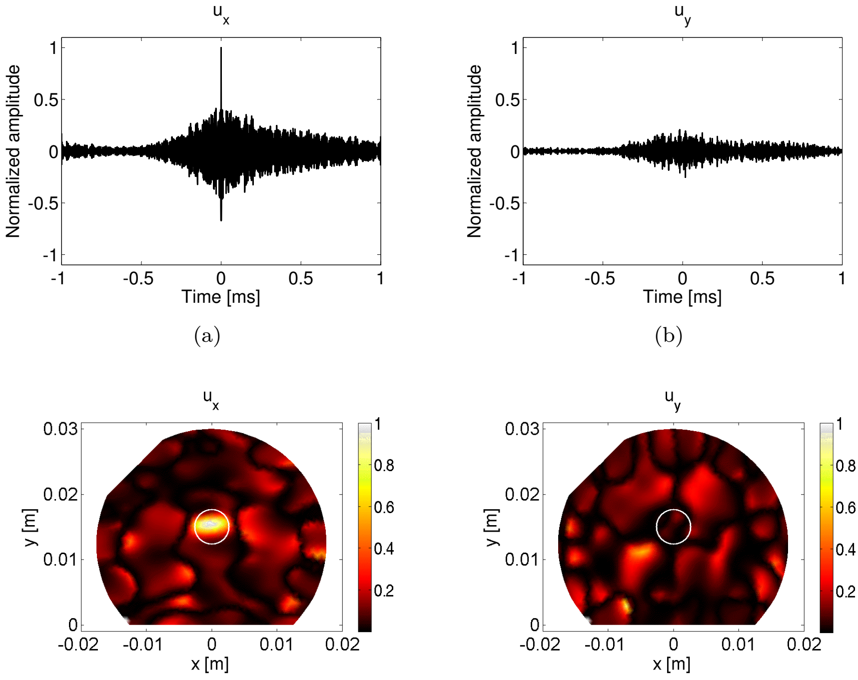

(a) (b)

(c) (d)

Figure 5.8: Simulated displacements in a multi-reverberant aluminium sample after reciprocal TR of the direct recorded horizontal displacement component u_x. The focal position is located at $(0, 1.5)$ cm and is encircled in the bottom figures. (a) Simulated horizontal displacement measured at the focal position, (b) simulated vertical displacement measured at the focal position, (c-d) FNR plots of respectively the horizontal and vertical displacement component obtained using equation (5.4). The colour scales are normalized according to the maximum value of the horizontal displacement component.

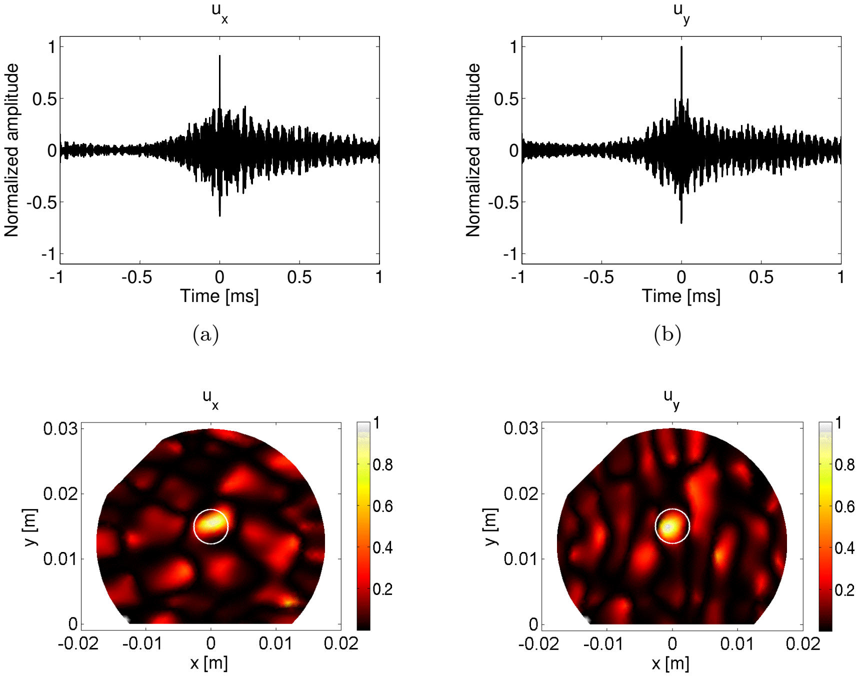

(a) (b)

(c) (d)

Figure 5.9: Simulated displacements in a multi-reverberant aluminium sample after reciprocal TR of the sum of the direct recorded horizontal and vertical displacement components u_x and u_y. The focal position is located at $(0, 1.5)$ cm and is encircled in the bottom figures. (a) Simulated horizontal displacement measured at the focal position, (b) simulated vertical displacement measured at the focal position, (c-d) FNR plots of respectively the horizontal and vertical displacement component obtained using equation (5.4). The colour scales are normalized according to the maximum value of the vertical displacement component.

after TR, is simulated. In this case, the simple scalar summation of both signals is broadcasted back into the aluminium sample after reciprocal TR. The results of this simulation are plotted in figure 5.9. The horizontal and vertical displacement components at the focal position are displayed in figures 5.9(a) and figures 5.9(b), showing both a temporal focusing of energy at the focal time. Apart from the focusing in time, the TR also focuses the energy spatially in both spatial directions. This can be observed in figures 5.9(c) and 5.9(d), where FNR plots of respectively the horizontal and vertical displacement components are plotted.

The above results demonstrated and confirmed the procedure for selectively focusing elastic energy along each of the spatial coordinates, either individually or collectively, using a scalar source, for a 2D multi-reverberant aluminium sample. With the developed finite element model, however, it is also possible to simulate the 3D case. This is illustrated considering the 3D version of the multi-reverberant aluminium sample used in the 2D simulations. The sample has the same width and height as the 2D sample, but now has a thickness of 1 cm. The source is located on the flat left hand side surface near the top of the sample. After emitting the same sweep signal as before, the normal displacement component u_z is measured in a point with coordinates $(0, 0, 1)$ cm, located at the front surface of the aluminium sample. The recorded signal is then used as a new input signal in the back propagation phase of the TR process. Finally, the three displacement components are measured at the focal position and are displayed in figures 5.10(a) to 5.10(c). Similar to the 2D case, there is only a focusing peak to be found in the normal displacement component, since this component was used in the TR procedure. In figure 5.10(d), the spatial focusing of the reciprocal TR experiment is illustrated by means of a snapshot of the normal displacement component in the 3D aluminium sample at the focal time. It is obvious that the highest displacement amplitudes (white colour) are found at the position of the focal point.

The above results illustrate the potential to model numerical reciprocal TR experiments both in 2D and 3D, using the developed finite element model. However, since the calculations in 3D are very time consuming and computationally intensive, most of the simulations in this chapter are performed in 2D.

5.3.3 Time reversal in multiple points

The previous simulations showed the ability of single-channel reciprocal TR to selectively or collectively focus elastic energy in any arbitrary location along each of the spatial directions. To collectively focus the individual components of motion, combinations of the time signals for the displacement components at the receiver location are considered in the rebroadcast signal. For instance, when $u_x + u_y$ was considered as input signal, the time reversed signal redistributed and focused the energy in both x- and y-direction. A similar approach can be followed to focus energy in multiple points. Re-emitting a combination of the time signals measured at the different locations, the energy will focus on all individual measurement locations.

To illustrate this, we discuss the results of simulations of time reversal in the 2D multi-reverberant aluminium sample, used in the previous sections. Suppose that

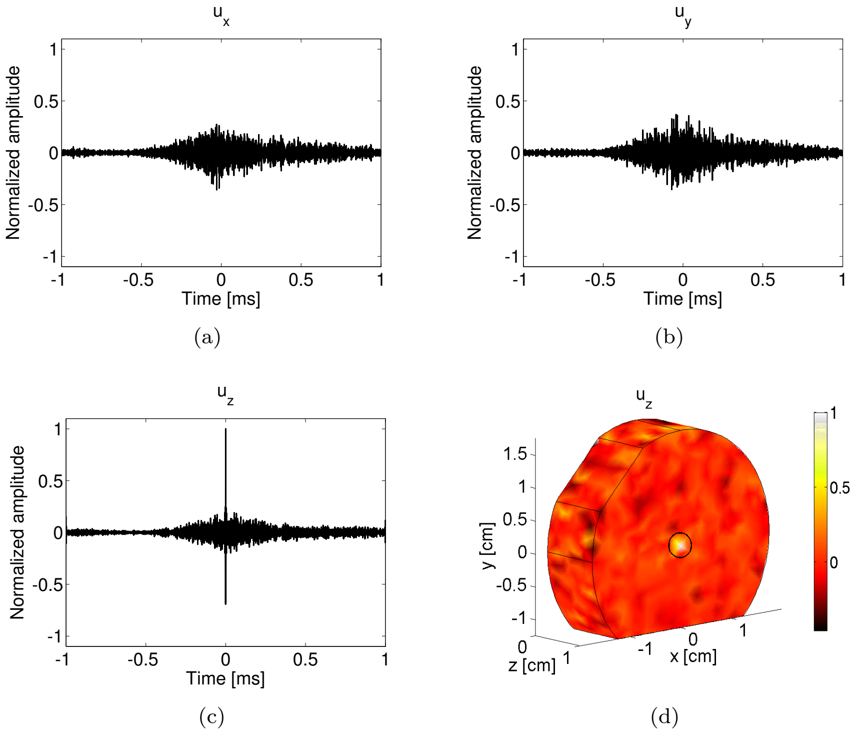

Figure 5.10: (a-b-c) Simulated displacement components at the focal position in a 3D multi-reverberant aluminium sample after reciprocal TR of the direct recorded normal displacement component u_z. (d) Snapshot of the normal displacement component u_z in a 3D multi-reverberant aluminium sample at the focal time. The results were obtained for a reciprocal TR of the direct recorded normal displacement component u_z. The focal position is located at $(0, 0, 1)$ cm and is encircled in the figure. The colour scale is normalized according to the maximum value of the normal displacement component.

the vertical displacement components are measured at two different locations in the sample, e.g. point 1 located at $(0, 1.5)$ cm and point 2 located at $(-0.5, 1)$ cm. Both measured signals are now added and the sum signal is used in the TR process. After TR, the horizontal and vertical displacement components are measured at both locations. Since the sum signal was used, we expect to see a focusing in time and space at both locations. Moreover, since only the vertical displacement components are considered in the time reversed signal, the focus may only occur in the time signals for the vertical displacement components and not in those for the horizontal displacement components. The focusing of

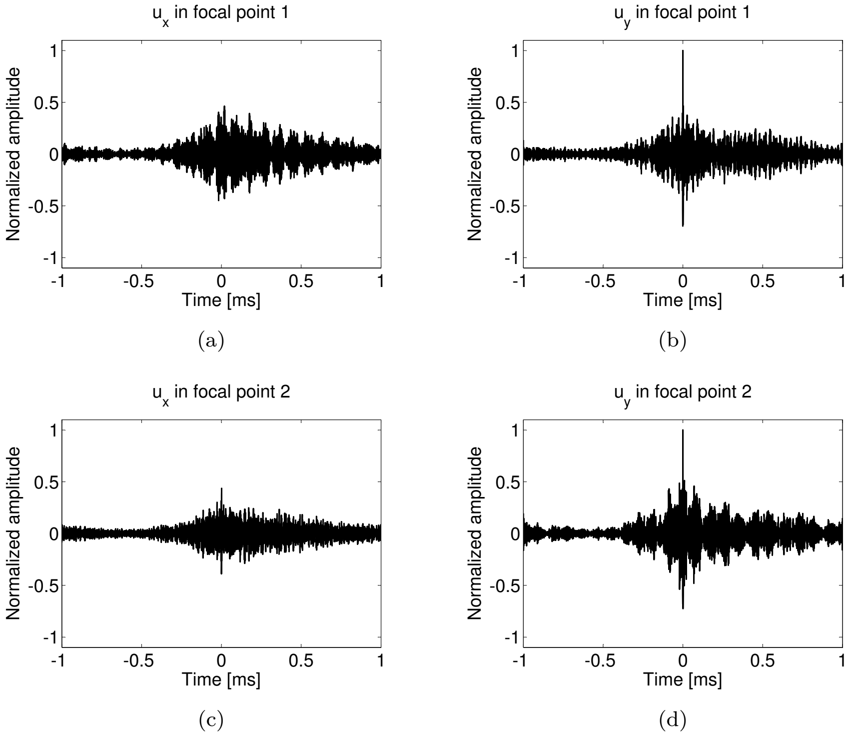

Figure 5.11: Simulated horizontal and vertical displacements measured at two different locations (point 1 at $(0, 1.5)$ cm and point 2 at $(-0.5, 1)$ cm) in a multi-reverberant aluminium sample after TR of the sum signal of the direct recorded vertical displacements in both locations.

the vertical displacement component in time is observed in figure 5.11, where the simulated horizontal and vertical displacements at the two measurement locations are displayed. Clear focus peaks are found in the vertical displacement components and not in the horizontal displacement components. The focusing in space is observed in figure 5.12, where FNR plots of the horizontal and vertical displacement components after TR of the sum signal of the direct recorded vertical displacement components at the two different positions are displayed. As expected, high FNR values at the focal positions are only observed in the FNR plot for the vertical displacement components.

Extending the above described methods for multi-component TR and TR in multiple points, we should also be able to focus in two different points, with the energy in the first point focused along the vertical direction and the energy in

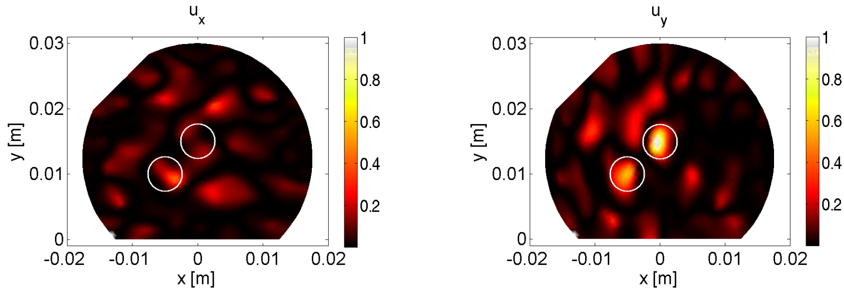

(a) (b)

Figure 5.12: FNR plots of the horizontal and vertical displacement components measured in a multi-reverberant aluminium sample after TR of the sum signal of the direct recorded vertical displacements at two different locations (point 1 at $(0, 1.5)$ cm and point 2 at $(-0.5, 1)$ cm). The two focal points are encircled in the figures. The colour scales are normalized according to the maximum value of the vertical displacement component.

the second point focused along the horizontal direction. To illustrate this, we determined, in the forward propagation phase of the TR process, the vertical displacement component u_y in one point located at $(0, 1.5)$ cm and the horizontal displacement component u_x in a second point located at $(-0.5, 1)$ cm. For the back propagation phase of the reciprocal TR procedure, we again re-emitted the simple scalar sum of both calculated signals in the sample. As confirmed in figure 5.13 (temporal focusing) and figure 5.14 (spatial focusing), this leads to focusing of energy in both points. In the first point, the focusing will be along the y-direction, in the second point, the focusing will be in the x-direction.

Until now, we managed to illustrate the simultaneous focus of various displacement components at different points by simply adding the direct recorded signals and sending them back into the sample. Along the same reasoning, non-simultaneous focusing can be realized when relative delays are introduced before summing the signals. This, again, can be illustrated in the 2D aluminium test sample. After excitation of the sweep signal, the vertical displacement time signals were measured at two different points located at respectively $(0, 1.5)$ cm and $(-0.5, 1)$ cm. Subsequently, a time shift of 0.1 ms is introduced in the time signal for point 2. In the frequency domain, this can be realized by just multiplying the received complex signal with a factor $\exp(2\pi i f t)$, where f is the frequency and t is the time delay. After the time shifting, the different signals are added and re-emitted. The time signals of the vertical displacement components at the expected focal points are shown in figure 5.15. From the

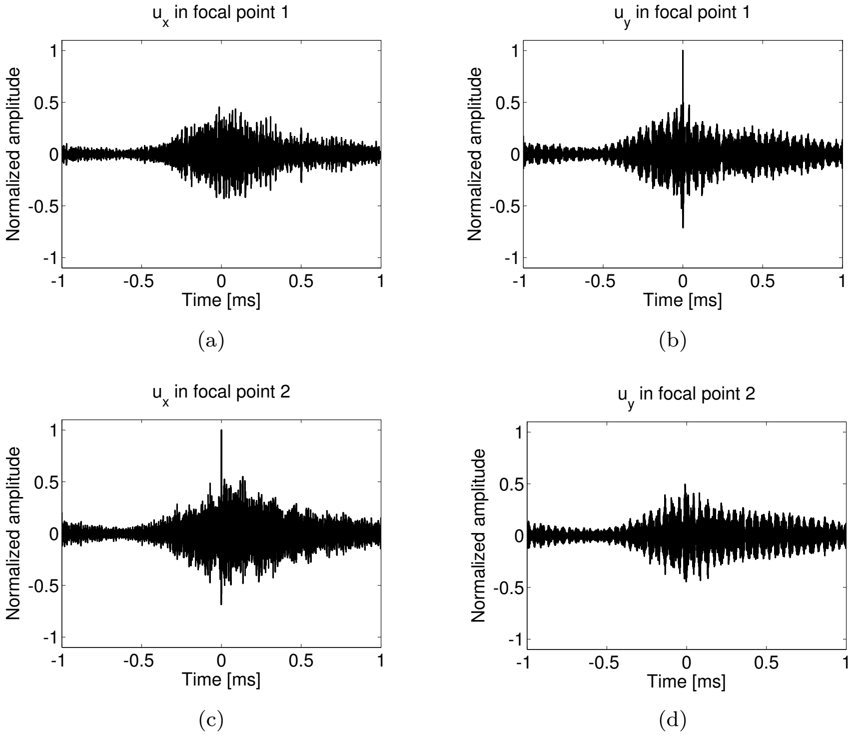

Figure 5.13: Simulated horizontal and vertical displacements measured at two different locations (point 1 at $(0, 1.5)$ cm and point 2 at $(-0.5, 1)$ cm) in a multi-reverberant aluminium sample after TR of the sum signal of the direct recorded vertical displacement in point 1 and the direct recorded horizontal displacement in point 2.

figures, it is clear that the elastic energy focuses in the first point at the focal time $t_F = 0$, while the energy in the second point focuses 0.1 ms later. This time shifting of the recorded signals will be used later (in section 5.5) to create a virtual phased array configuration using reciprocal TR.

5.4 Chaotic cavity transducer

In the previous section, simulation results of single-channel reciprocal TR in a reverberant medium were discussed. With the developed finite element model, we were able to demonstrate the use of single-channel reciprocal TR to focus

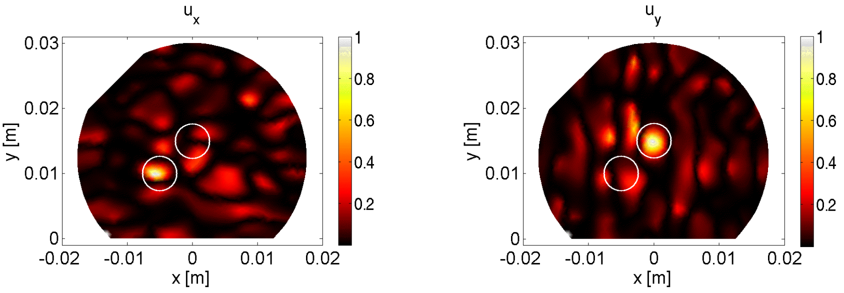

(a) (b)

Figure 5.14: FNR plots of the horizontal and vertical displacement components measured in a multi-reverberant aluminium sample after TR of the sum signal of the direct recorded vertical displacement in point 1 located at $(0, 1.5)$ cm and the direct recorded horizontal displacement in point 2 located at $(-0.5, 1)$ cm. The two focal points are encircled in the figures. The colour scales are normalized according to the maximum value of the vertical displacement component.

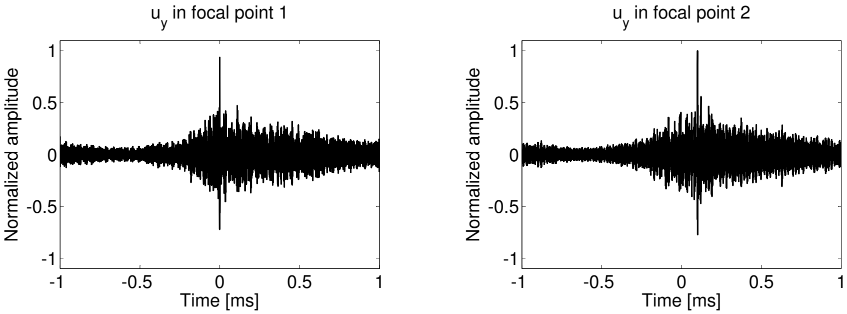

(a) (b)

Figure 5.15: Simulated vertical displacements measured at two different locations (point 1 at $(0, 1.5)$ cm and point 2 at $(-0.5, 1)$ cm) in a multi-reverberant aluminium sample after TR of the sum signal of the direct recorded vertical displacement in point 1 and the time shifted direct recorded vertical displacement in point 2. Due to the time shift, the focal time t_F in every point is different: $t_F = 0$ in point 1 and $t_F = 0.1$ ms in point 2.

energy in one or multiple points and along one or multiple spatial directions. Due to the high number of reflections inside the reverberant medium, we each time observed a clear TR focusing both in time and in space.

In case of a non-reverberant sample, the described TR technique cannot be used anymore, since the absence of reflections implies that the only information path between the source and the receiver is the direct path. For an accurate re-focusing of the energy multiple information paths coming from different directions (i.e. originating at different virtual source locations) are required. In this section, a solution for this problem is proposed using a chaotic cavity transducer, consisting of a transducer glued to a cavity of chaotic shape, which, on his turn, is glued to the non-reverberant sample. The principle of a chaotic cavity transducer was originally introduced for 3D imaging in fluids [25, 26, 29–31]. Here, we extend the concept of the chaotic cavity transducer to applications dealing with elastic waves in solids.

For the actual implementation in Comsol, an aluminium chaotic cavity is used. The shape of this chaotic cavity is similar to the aluminium sample used in the previous section to demonstrate single-channel reciprocal TR in a reverberant sample. The chaotic cavity is placed on top of a non-reverberant sample. In the simulations, the non-reverberant medium is modelled as a finite size rectangular medium with perfectly matching layers on three of its boundaries, thus mimicking a semi-infinite sample. At the fourth boundary, stress-free boundary conditions are implemented, except at the interface between the cavity and the non-reverberant sample, where continuity has been assumed. The rest of the fourth boundary is implemented as a stress-free boundary. The density of the non-reverberant medium is considered to be equal to 1000 kg/m^3 and the longitudinal and shear velocities are respectively 3000 m/s and 1500 m/s. An illustration of the geometry is displayed in figure 5.16.

To demonstrate the single-channel reciprocal TR method in the non-reverberant sample, we use the same TR procedure as before. First, a sweep signal (the same as in section 5.3) is generated at the active surface of the transmitter (i.e. the flat side on top of the chaotic cavity). When the emitted signal reaches the interface between the cavity and the non-reverberant sample, part of the signal is reflected and keeps propagating in the cavity, while the other part is transmitted into the non-reverberant sample. This process keeps going on till no more energy is trapped in the cavity. During the process part of the transmitted energy enters the semi-infinite medium with irregular time delays, and propagates in different directions towards the receiver location. The signal measured at the receiver location is then recorded and used as a new input signal in the back propagation step of the TR process. Finally, the zone around the receiver location is analysed, and evidences of TR focusing can be observed both in time and space. This TR focusing is fully caused by the reflections

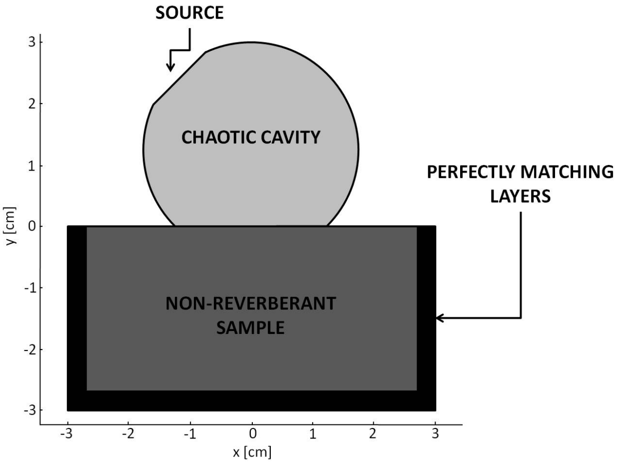

Figure 5.16: Illustration of the geometry of a chaotic cavity transducer on top of a non-reverberant sample used in the Comsol simulation. The chaotic cavity transducer has a maximum height of 3 cm and a maximum width of 3.5 cm. The non-reverberant sample has a height of 3 cm and a width of 6 cm and is modelled using perfectly matching layers (thick black regions at the boundaries).

inside the chaotic cavity. The non-reverberant medium itself is not responsible for the focusing due to a lack of reflections.

Using the single-channel reciprocal TR in combination with a chaotic cavity, we are able to focus energy at any position in a non-reverberant medium. Moreover, similar to the reciprocal TR in a reverberant medium, we are able to selectively or collectively focus energy along any or all spatial directions. This is demonstrated in figures 5.17, 5.18 and 5.19, where each of the different vector components were focused, either selectively or collectively, at the focal position $(0, -2)$ cm (encircled in the figures, inside the non-reverberant sample). In each figure, we displayed the simulated time signals of both displacement components at the focal position (illustrating the focusing in time) and the FNR plots of the simulated displacement components in the non-reverberant solid material (illustrating the focusing in space). In figure 5.17, the direct recorded horizontal displacement component u_x was used as an input signal in the back propagation step of the reciprocal TR. This results in a selectively TR focusing in time and space along the horizontal displacement component. In figure 5.18, the direct recorded vertical displacement component u_y was used, resulting in a selectively TR focusing in time and space along the vertical displacement component. In figure 5.19, the sum of both displacement components was used as a new input signal, yielding a TR focusing in both spatial directions.

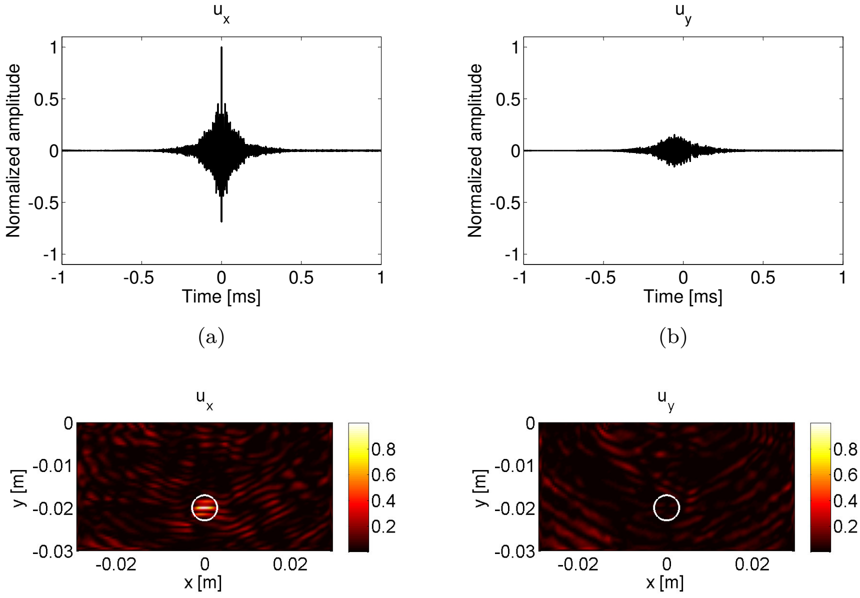

(a) (b)

(c) (d)

Figure 5.17: Simulated displacements in a non-reverberant solid material after reciprocal TR of the direct recorded horizontal displacement component u_x. The focal position is located at $(0, -2)$ cm and is encircled in the bottom figures. (a) Simulated horizontal displacement measured at the focal position, (b) simulated vertical displacement measured at the focal position, (c-d) FNR plots of respectively the horizontal and vertical displacement component obtained using equation (5.4). The colour scales are normalized according to the maximum value of the horizontal displacement component.

The application of single-channel reciprocal TR in a reverberant medium enabled us not only to focus along multiple spatial directions, but also -simultaneously or with a well defined delay- in multiple points. This is also possible in a non-reverberant medium when using reciprocal TR in combination with a chaotic cavity. To illustrate this, we apply the chaotic cavity transducer TR focusing procedure on the direct recorded horizontal displacement components u_x at two different positions, located at respectively $(-1, -2)$ cm and $(1, -2)$ cm in the non-reverberant solid material. Figure 5.20 shows the results in time and space for this simulation, obtained after re-emitting the time reversed sum signal through the chaotic cavity transducer. Looking at the time signals for the horizontal displacement components at the two different positions (figures 5.20(a)

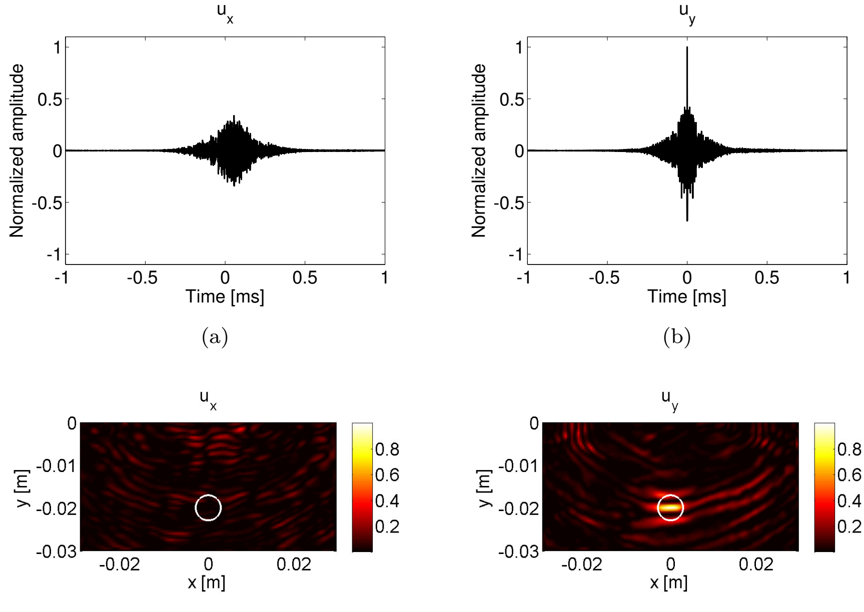

(a) (b)

(c) (d)

Figure 5.18: Simulated displacements in a non-reverberant solid material after reciprocal TR of the direct recorded vertical displacement component u_y. The focal position is located at $(0, -2)$ cm and is encircled in the bottom figures. (a) Simulated horizontal displacement measured at the focal position, (b) simulated vertical displacement measured at the focal position, (c-d) FNR plots of respectively the horizontal and vertical displacement component obtained using equation (5.4). The colour scales are normalized according to the maximum value of the vertical displacement component.

and 5.20(b)), we clearly see that energy is focused in time in both positions. The TR focusing in space is observed in the FNR plot of the simulated horizontal displacement in the solid material (figure 5.20(c)), where high FNR values (white colour) occur at both focal positions (encircled in the figure).

5.5 Virtual phased array configuration

In the previous section, we showed the potential of a chaotic cavity transducer to focus energy in multiple points inside a non-reverberating medium. Using this result and the principle of Huygens, we can now use the chaotic cavity

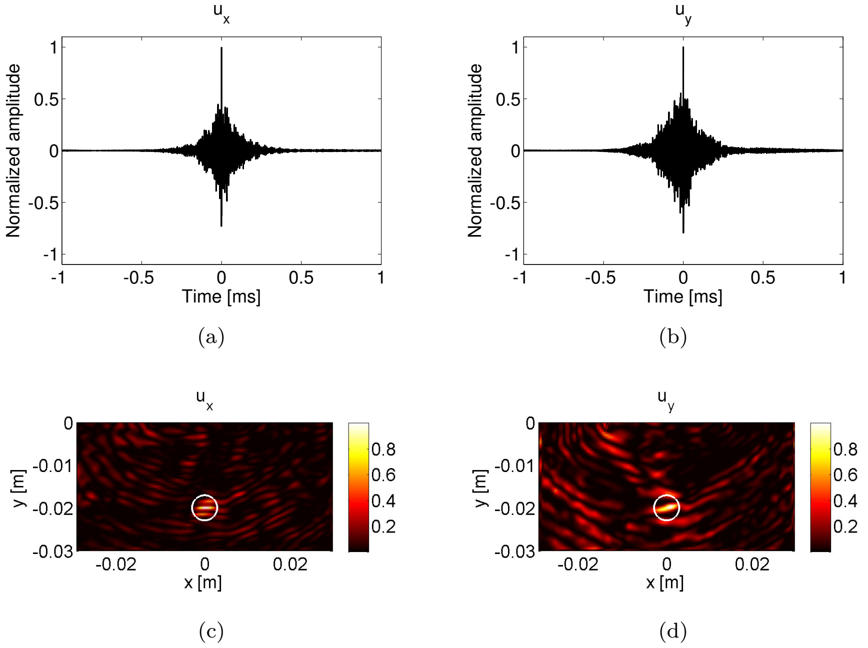

Figure 5.19: Simulated displacements in a non-reverberant solid material after reciprocal TR of the sum of the direct recorded horizontal displacement component u_x and the direct recorded vertical displacement component u_y. The focal position is located at $(0, -2)$ cm and is encircled in the bottom figures. (a) Simulated horizontal displacement measured at the focal position, (b) simulated vertical displacement measured at the focal position, (c-d) FNR plots of respectively the horizontal and vertical displacement component obtained using equation (5.4). The colour scales are normalized according to the maximum value of the displacement components.

transducer to create a virtual phased array, enabling the focusing of energy in any arbitrary position in both reverberant and non-reverberant media. Phased array probes are composed of multiple ultrasonic elements that can transmit waves independently at different times. They can be used to focus ultrasonic beams, applying time delays to the elements to create constructive interference of the wave fronts, allowing the energy to be focused at any position in the medium. The principle behind phased arrays is based on the Huygens principle and is illustrated in figure 5.21, where delay laws have been computed to focus the acoustic beam at a specified position. As shown in the figure, each element radiates a spherical wave at a specified time. The superposition of these wavelets results in a curved wave front that focuses at the desired location.

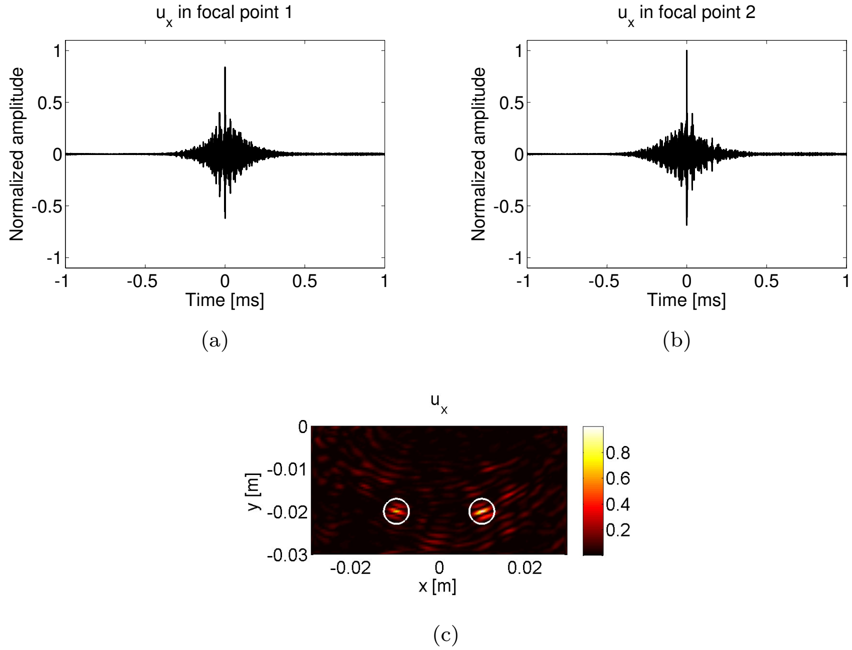

(a)

(b)

(c)

Figure 5.20: Simulated displacements in a non-reverberant solid material after reciprocal TR of the sum of the direct recorded horizontal displacement components u_x at two different positions, located at respectively $(-1, -2)$ cm and $(1, -2)$ cm. Both positions are encircled in the bottom figure. (a) Simulated horizontal displacement measured at the first focal position, (b) simulated horizontal displacement measured at the second focal position, (c) FNR plot of the horizontal displacement component obtained using equation (5.4). The colour scale is normalized according to the maximum value of the horizontal displacement component.

In order to transform a chaotic cavity transducer into a phased array, a well-defined sequence of preparatory steps needs to be followed. As in the previous examples, we start with the excitation of a sweep signal. Subsequently, the response signals are measured in a series of points located on a line parallel to the interface between the cavity and the sample in which we intend to focus the energy. Then, a combination of these direct recorded signals is formed, depending on the location of the desired focal point. The resulting signal is cross-correlated with the original input signal and time reversed. This TR signal is finally used as a new input signal in the back propagation step of the reciprocal TR.

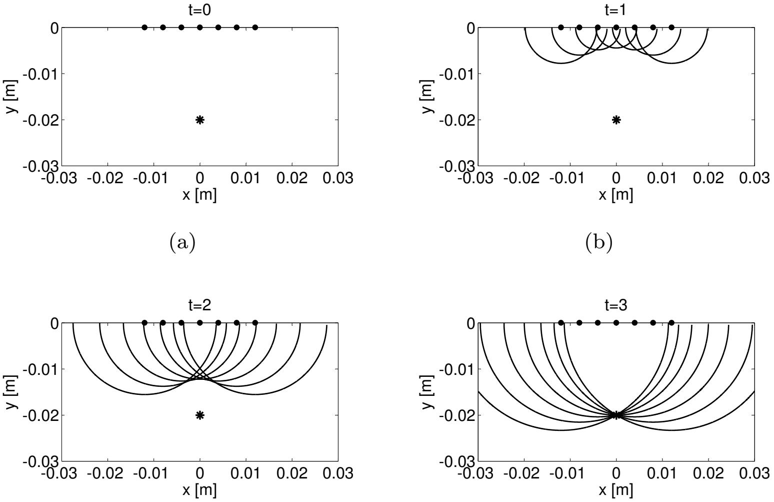

(a) (b)

(c) (d)

Figure 5.21: Illustration of the phased array principle to focus waves at a fixed point. The figures are given for four consecutive time steps. The black dots indicate the positions of the elements radiating a spherical wave at a specified time. The position of the different wave fronts in each time step is illustrated by the full lines. The asterisk denotes the location of the focusing.

As discussed earlier, simply adding the direct recorded signals and re-emitting the sum signal will result in a simultaneous focusing of energy in all considered recording positions. At that particular focusing instance, every “recording” point may be considered as a source of secondary wavelets that spread out in all directions. In case of the simultaneous energy focusing, a plane wave is created propagating in the direction perpendicular to the recording line. However, when relative time delays are introduced before summing the signals, the focal time in every point will be different (as demonstrated in section 5.3.3). Consequently, the “recording” points radiate secondary waves at different times, similar to the illustration shown in figure 5.21. Thus, choosing and applying appropriate time delays we should be able to focus energy in an arbitrary point. The required time delays can be calculated by determining the distances between the recording points and the intended focal point and dividing these distances by the wave propagation speed in the considered medium. The direct recorded signals are then time shifted such that the energy is last focused in the recording points closest to the intended focal point.

To successfully create a virtual phased array in a medium, the wave speed distribution in the medium needs to be known in order to determine the appropriate time delays of the different recording signals. For a chaotic cavity connected to a fluid, the technique works very well, since waves can only propagate with the longitudinal wave velocity [29–31]. In a solid material, however, the focusing using a virtual phased array becomes less straightforward, since waves can propagate inside the material either with the longitudinal wave velocity or with the transversal wave velocity. Moreover, in semi-infinite half-spaces and in plates, the Rayleigh and Lamb waves even can play an important role. And finally, anisotropy and heterogeneity can make the picture even more complicated.

To obtain a better understanding of the concept of the virtual phased array in solids, we first study the 2D configuration of an aluminium chaotic cavity on top of a non-reverberant solid material ($\rho = 1000$ kg/m^3, $v_L = 3000$ m/s and $v_T = 1500$ m/s), as illustrated in figure 5.16. After emitting a sweep signal (similar to the sweep signal used before), the response signals (i.e. horizontal and vertical displacement components) are measured in 25 recording points located 2 mm under the interface between the cavity and the solid material and with x-coordinates starting from -1.2 cm to 1.2 cm in steps of 1 mm. The positions of the recording points are indicated by black dots in the subsequent figures. Our goal is to successfully focus energy along one or both spatial directions at an arbitrary point in the non-reverberant solid material using the virtual phased array concept.

Before focusing at an arbitrary point in the medium using appropriate time delays, we first study the generation of plane waves created by simultaneously focusing the energy selectively along the horizontal and vertical displacement component in all 25 recording points. In the first simulation, we re-emitted the sum signal of the direct recorded horizontal displacement components at the recording positions, resulting in a simultaneous focusing of energy along the horizontal displacement component in all recording points. This is illustrated in figure 5.22, where the horizontal and vertical displacement fields inside the solid material are shown at the time corresponding to the “line focusing time”. In the plot for the horizontal displacement field, we clearly observe a TR focusing at the recording points (black dots), represented by a zone of high energy (brighter colours). There is no evidence of constructive focusing in the vertical displacement component.

The simultaneous focusing of the horizontal component will create secondary waves from horizontally oriented dipoles with energy propagating with both the longitudinal and transversal wave velocity. The part with the longitudinal wave velocity will mainly propagate in the horizontal direction, while the part with the transversal wave velocity will primarily propagate in the vertical direction.

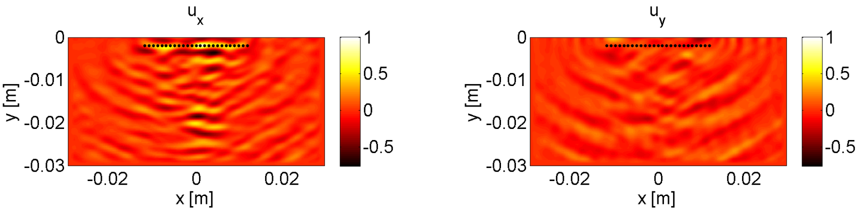

(a) (b)

Figure 5.22: Simulated displacements in a non-reverberant solid material after reciprocal TR of the sum of the direct recorded horizontal displacement components u_x in 25 recording points, indicated by black dots. (a) Horizontal displacement component at the focal time, (b) vertical displacement component at the focal time. The colour scales are normalized according to the maximum value of the horizontal displacement component.

Since the only constructive interference will occur in the vertical direction, a plane wave will be created preferentially propagating with the transversal wave velocity in the direction normal to the recording line. To verify this, we determined the time it takes for the plane wave to travel from the recording points to an arbitrary point in the medium. In figure 5.23(a), the simulated horizontal displacement at a point located at $(0, -2)$ cm inside the solid material, is displayed. A zoom (figure 5.23(b)) around the time of arrival of the plane wave reveals that the plane wave peak takes 12 microseconds to travel a distance of 1.8 cm from the recording points to the considered point. Dividing this distance by the travel time, we indeed find the shear wave velocity ($v_T = 1500$ m/s).

A similar study can be performed for a simultaneous TR focusing of the vertical displacement component in all 25 recording points. In figure 5.24, the displacement fields at the "line focusing time" inside the solid material are shown. A simultaneous focusing of energy in the vertical displacement component at the recording points is clearly observed. Again, this focusing creates a plane wave propagating in the negative y-direction. However, in this case, the simultaneous focusing of the vertical component will create secondary waves from vertically oriented dipoles with the part with the longitudinal wave velocity mainly propagating in the vertical direction and the part with the transversal wave velocity mainly propagating in the horizontal direction. Consequently, the created plane wave will preferentially propagate with the longitudinal wave velocity in the direction normal to the recording line. This is again verified by analysing the simulated vertical displacement at a point located at $(0, -2)$ cm inside the solid material (see figures 5.25(a) and 5.25(b)). The plane wave travels a distance of 1.8 cm from the recording points to the

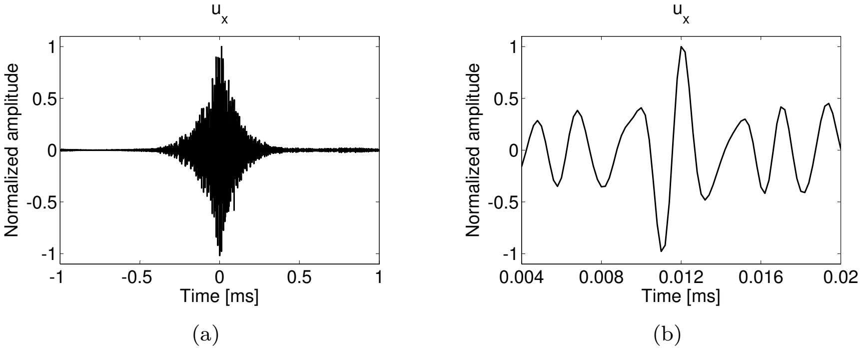

Figure 5.23: (a) Simulated horizontal displacement at $(0, -2)$ cm inside a non-reverberant solid material after reciprocal TR of the sum of the direct recorded horizontal displacement components u_x in 25 recording points. (b) Zoom of the simulated horizontal displacement around the time of arrival of the plane wave.

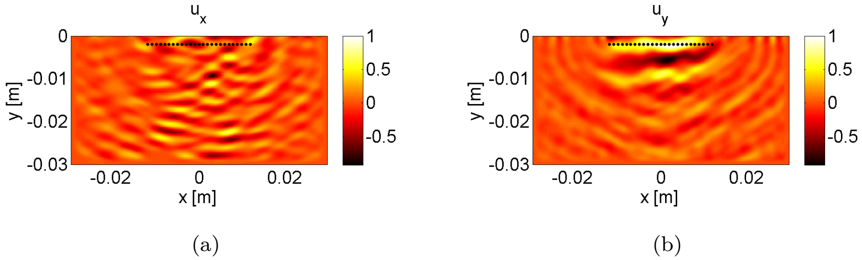

Figure 5.24: Simulated displacements in a non-reverberant solid material after reciprocal TR of the sum of the direct recorded vertical displacement components u_y in 25 recording points, indicated by black dots. (a) Horizontal displacement component at the focal time, (b) vertical displacement component at the focal time. The colour scales are normalized according to the maximum value of the vertical displacement component.

considered point in 6 microseconds yielding a wave propagation velocity equal to the longitudinal velocity ($v_L = 3000$ m/s).

From the above discussed results, it follows that TR focusing of the horizontal (vertical) displacement components in the recording points results in the creation of secondary waves, originating at the recording points and generating a plane wave propagating perpendicularly to the recording line with the transversal (longitudinal) velocity. With this knowledge, we are now able to calculate the

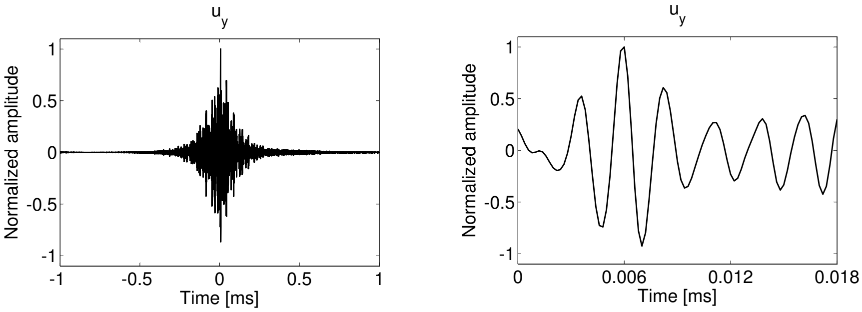

(a) (b)

Figure 5.25: (a) Simulated vertical displacement at $(0, -2)$ cm inside a non-reverberant solid material after reciprocal TR of the sum of the direct recorded vertical displacement components u_y in 25 recording points. (b) Zoom of the simulated vertical displacement around the time of arrival of the plane wave.

appropriate time delays of the different recording signals, in order to selectively or collectively focus along each spatial direction at an arbitrary point in the medium using the virtual phased array.

To focus the horizontal displacement component at an arbitrary position, we first need to focus the horizontal displacement components at the recording positions, with appropriate time delays. Since this focusing will create secondary waves (from horizontally oriented dipoles) preferentially propagating with the transversal wave velocity in the direction perpendicular to the recording line, the time delays can be calculated by determining the distance of the recording points to the intended focal point divided by this velocity. For a focal point located at $(0, -2)$ cm inside the non-reverberant material, the time shifts are represented by the full line in figure 5.26. The calculations reveal that, in order to focus the horizontal displacement component at the focal time $t = 0$ in point $(0, -2)$ cm, the focusing in the recording points needs to be 12 μs (for the middle recording position) to 14.4 μs (for the left- and rightmost recording positions) earlier, i.e., a time difference of 1.44 periods (for a central frequency of 600 kHz).

This is illustrated in figure 5.27, where snapshots of the horizontal displacement field inside the non-reverberant solid material are displayed for four different times. The 25 recording positions are indicated by black dots and the intended focal position is encircled. At $t = -12$ μs, we see that the energy is indeed focused at the middle recording points, while the focus in the leftmost and rightmost points has already passed. The TR focusing in the recording points

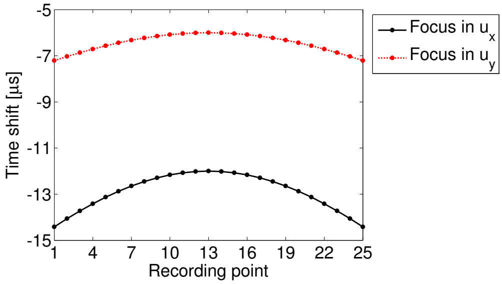

Figure 5.26: Time shifts of the different recording signals for a focus at $(0, -2)$ cm inside a non-reverberant solid material ($\rho = 1000$ kg/m^3, $v_L = 3000$ m/s and $v_T = 1500$ m/s) using the virtual phased array. The full line represents the time shifts needed to focus the horizontal displacement component, the dotted line represents the time shifts needed to focus the vertical displacement component. Recording point 1 corresponds to the leftmost point, recording point 25 corresponds to the rightmost point.

creates a wave front (indicated by an arrow) which propagates in the negative y-direction. Finally, at $t = 0$, the secondary waves radiated by the recording positions constructively interfere with each other, resulting in a clear TR focusing at the intended focal position. Figure 5.28 confirms that the focusing only occurs in the horizontal displacement component. The top figures represent the simulated time signals for the horizontal and vertical displacement component at the focal position. The bottom figures represent FNR plots of the horizontal and vertical displacement fields. TR focusing in time and space is only observable in the left figures for the horizontal displacement component.

A similar procedure can be followed to focus the vertical displacement component at $(0, -2)$ cm inside the non-reverberant material. In this case, we first focus the vertical displacement components, with appropriate time shifts, at the 25 recording positions. This will create secondary waves (dipoles with energy in the vertical direction) preferentially propagating with the longitudinal wave velocity. The time delays should therefore be calculated using the distance of the recording points to the focal point divided by the longitudinal wave velocity. The calculated time shifts are represented by the dotted line in figure 5.26, showing that the TR focusing in the recording points needs to be 6 μs (for the middle recording position) to approximately 7 μs (for the left- and rightmost recording positions) earlier than the focusing in the focal point at $t = 0$. Figure 5.29 illustrates the focusing process by means of snapshots of the simulated vertical displacement field inside the non-reverberant solid material. The recording points are indicated by black dots and the focal point is encircled.

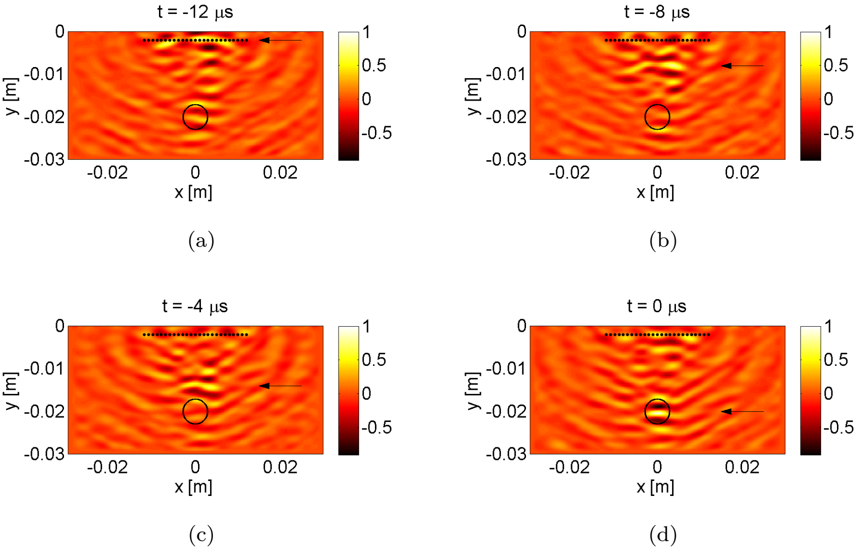

(a) (b)

(c) (d)

Figure 5.27: Snapshots of the simulated horizontal displacement field inside a non-reverberant solid material for TR focusing using a virtual phased array. The results are displayed for four different times. The 25 recording positions of the virtual phased array are indicated by the black dots. The intended focal point is encircled. The arrow marks the position of the wave front that was created by time shifted TR focusing in the recording points. The colour scales are normalized according to the maximum value of the horizontal displacement component measured at the focal time.

At $t = -6$ μs, we clearly see that energy is focused around the recording points. Due to the time delays, a curved wave front is created that propagates in the negative y-direction until it finally focuses at the intended focal point at $t = 0$. In this case, focusing is only observed for the vertical displacement component, as confirmed by figure 5.30. The two top figures represent the time signals of the simulated horizontal and vertical displacements at the focal point, showing a clear focusing in time only in the y-component of the displacement. The bottom figures represent FNR plots of the horizontal and vertical displacement in the sample, illustrating the focusing in space of the y-component of the displacement.

To focus collectively both displacement components at the same time and the same location we just need to sum the properly time shifted direct recorded horizontal displacements and the time shifted direct recorded vertical displacements and use this signal as a new input signal. This will result in a

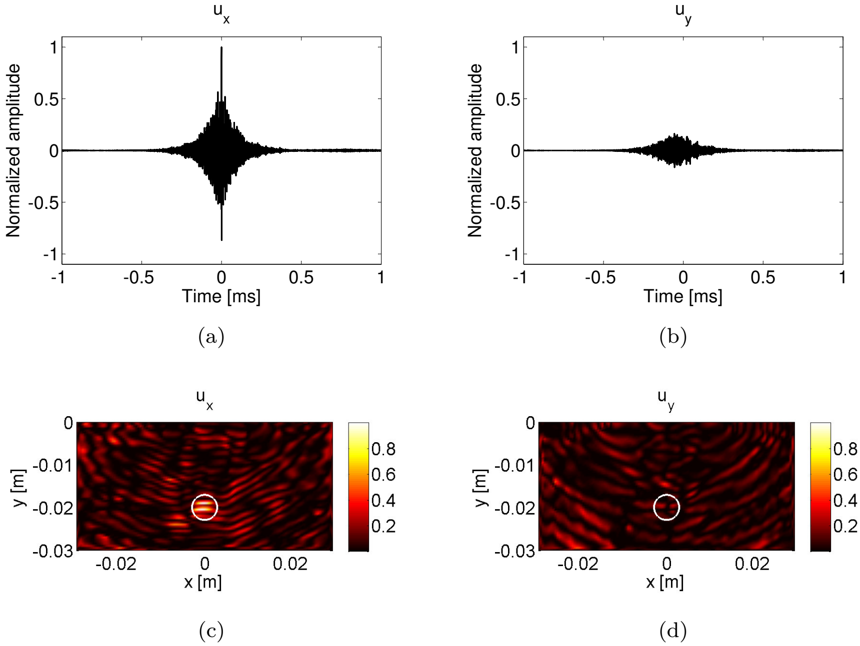

(a) (b)

(c) (d)

Figure 5.28: Simulated displacements in a non-reverberant solid material for TR focusing of the horizontal displacement component u_x using a virtual phased array. The focal position is located at $(0, -2)$ cm and is encircled in the bottom figures. (a) Simulated horizontal displacement measured at the focal position, (b) simulated vertical displacement measured at the focal position, (c-d) FNR plots of respectively the horizontal and vertical displacement component obtained using equation (5.4). The colour scales are normalized according to the maximum value of the horizontal displacement component.

focusing of both displacement components at the recording positions. Note, however, that the focusing of both displacement components in one recording point will occur at different times, due to the different time shifts used in both cases. The horizontal displacement components will first focus in the recording points, creating a wave front with particle displacements in the horizontal direction and preferentially propagating away from the recording points with the transversal velocity. A few microseconds later, the vertical displacement components will focus in the recording points and create a wave front with particle displacements in the vertical direction and preferentially propagating away from the recording points with the longitudinal velocity. Both wave fronts will reach the focal point at the same time, resulting in a TR focusing along

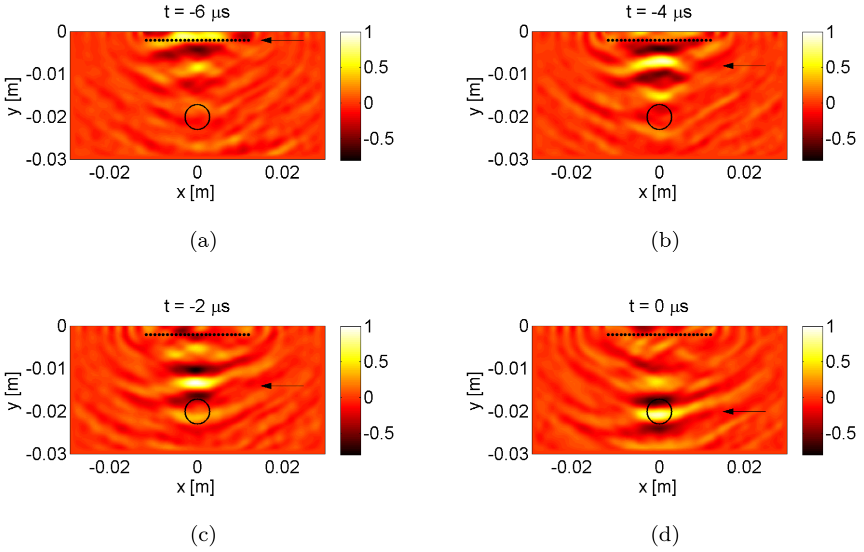

Figure 5.29: Snapshots of the simulated vertical displacement field inside a non-reverberant solid material for TR focusing using a virtual phased array. The results are displayed for four different times. The 25 recording positions of the virtual phased array are indicated by the black dots. The intended focal point is encircled. The arrow marks the position of the wave front that was created by time shifted TR focusing in the recording points. The colour scales are normalized according to the maximum value of the vertical displacement component measured at the focal time.

both displacement components. In figure 5.31 the focusing in time and in space of both displacement components is shown. The top figures represent the time signals of the simulated displacement components at the focal point. The bottom figures represent FNR plots of the displacement components in the non-reverberant medium.

Comparing the results displayed in figures 5.28, 5.30 and 5.31, obtained using a virtual phased array, with the results for a direct TR displayed in figures 5.17, 5.18 and 5.19, we clearly see that the use of a virtual phased array hardly affects the quality of the focusing, both in time and in space. Moreover, the use of a virtual phased array has a great advantage over the direct TR method. To focus energy at an arbitrary point (x_1, y_1) inside a medium using the direct TR method, the direct response signal needs to be known at that point inside the medium. For a focusing at (x_2, y_2) one needs again the direct response at that point, etc... A full scan of a zone of the medium using direct TR

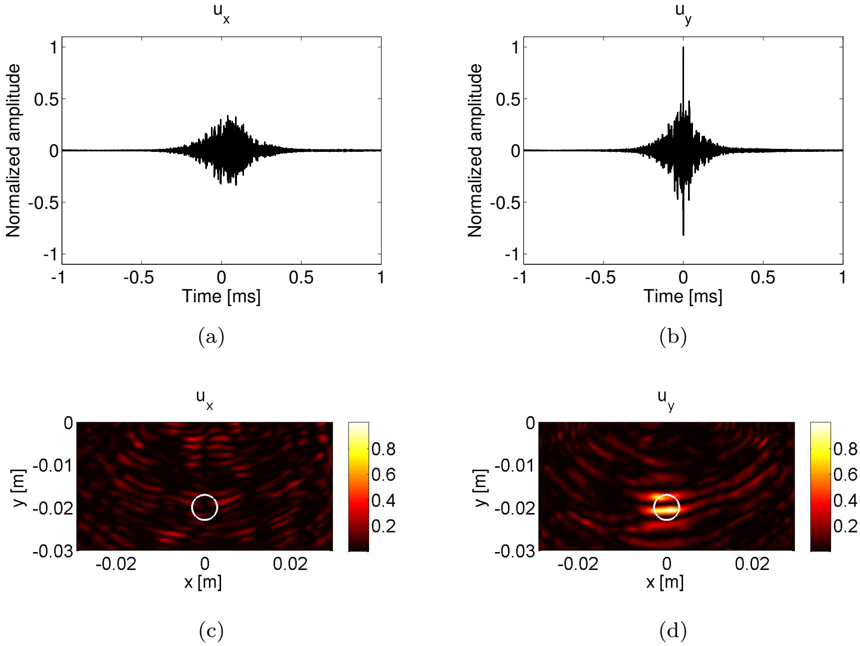

(a) (b)

(c) (d)

Figure 5.30: Simulated displacements in a non-reverberant solid material for TR focusing of the vertical displacement component u_y using a virtual phased array. The focal position is located at $(0, -2)$ cm and is encircled in the bottom figures. (a) Simulated horizontal displacement measured at the focal position, (b) simulated vertical displacement measured at the focal position, (c-d) FNR plots of respectively the horizontal and vertical displacement component obtained using equation (5.4). The colour scales are normalized according to the maximum value of the vertical displacement component.

focusing thus requires to know the direct response signals at any point within the zone of interest. With the virtual phased array, however, only the response signals in a limited number of recording points are required (these points can even be outside the zone of interest). Changing the time shifts of the different recording signals we are able to focus in any point of the inspection zone. Results of this procedure are illustrated in figures 5.32 and 5.33. In figure 5.32 we display the calculated time shifts of the recording signals, necessary to focus the vertical displacement component in a point located at $(1, -1.5)$ cm inside the non-reverberant solid material. In figure 5.33, the simulated results for this TR focusing are displayed. The top figures represent the simulated time signals of the horizontal and vertical displacement component at the focal point, showing

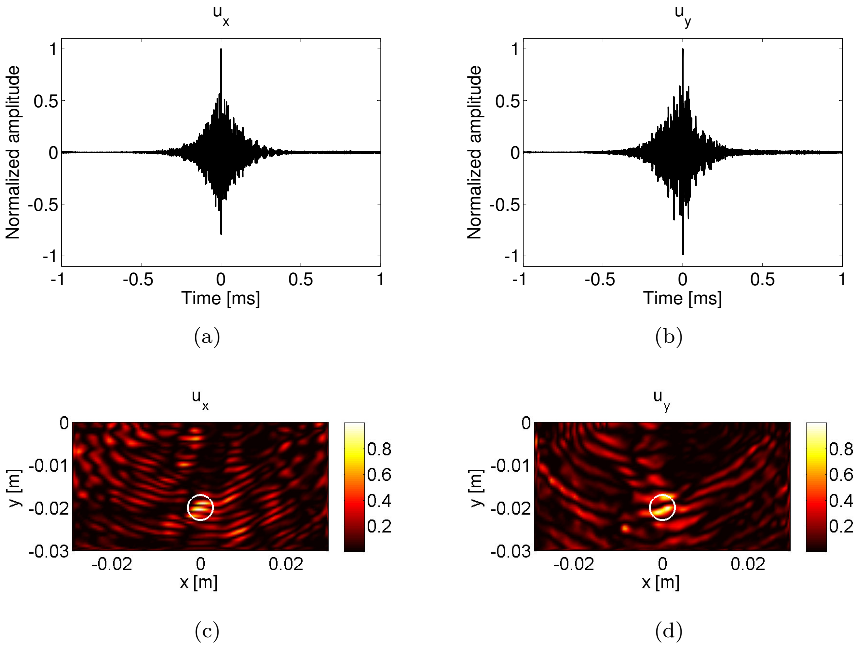

(a) (b)

(c) (d)

Figure 5.31: Simulated displacements in a non-reverberant solid material for TR focusing of both displacement components using a virtual phased array. The focal position is located at $(0, -2)$ cm and is encircled in the bottom figures. (a) Simulated horizontal displacement measured at the focal position, (b) simulated vertical displacement measured at the focal position, (c-d) FNR plots of respectively the horizontal and vertical displacement component obtained using equation (5.4). The colour scales are normalized according to the maximum value of the displacement components.

a clear focusing of the vertical component in time. The bottom figures show FNR plots of both displacement components, illustrating the focusing in space of the vertical component.

Another advancement worth mentioning, is that the electronics and software for the control of a virtual phased array system based on the chaotic cavity transducer are far more simpler than the electronics and software required for a commercial phased array device. Instead of 128 or more signals, amplifiers and receivers it suffices to work with a single transducer, amplifier and receiver system, thereby reducing the application costs efficiently.

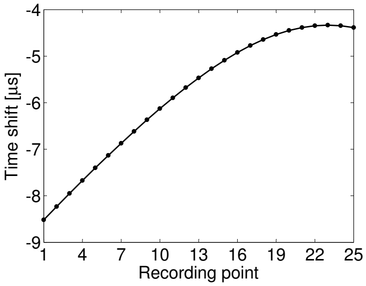

Figure 5.32: Time shifts of the different recording signals for a focusing of the vertical displacement component in a point located at $(1, -1.5)$ cm inside a non-reverberant solid material ($\rho = 1000$ kg/m^3, $v_L = 3000$ m/s and $v_T = 1500$ m/s) using the virtual phased array. Recording point 1 corresponds to the leftmost point, recording point 25 corresponds to the rightmost point.

Since the focus obtained with a virtual phased array is created by constructive interference of wave fronts originating from the recording points, we expect the focusing quality to be dependent on the number of recording points. Therefore, we analysed the results of TR focusing of the vertical displacement component at the focal position $(0, -2)$ cm using a virtual phased array with an increasing number of recording points, starting from two to 21 points with the leftmost and rightmost point at a fixed position. In figure 5.34, the time signals of the vertical displacement component at the focal position are displayed for a different number of recording points. It is obvious that the higher the number of recording points used in the virtual phased array, the better the focusing quality will be. However, this quality improvement is less obvious for a high number of recording points. In the figure, for instance, almost no difference in focusing quality is observed between ten or twelve recording points. The same behaviour is observed when we study the FNR plots of the vertical displacement component in the sample, displayed in figure 5.35. In the figure, the recording positions are indicated by white dots and the focal position is encircled. Using only two recording points in the virtual phased array, the constructive interference of the wave fronts originating from the recording positions is not large enough to get a spatial focusing. Using more than two recording points, a focal spot appears and the quality of the focal spot improves as the number of recording points increases, reaching a maximum at a certain number of points.

To determine the number of recording points at which the focusing quality starts saturating, we calculated the FNR value, which is a quantitative measure of the focusing quality, at the focal position and plotted the values as a function of the distance between the recording points in figure 5.36. From the figure,

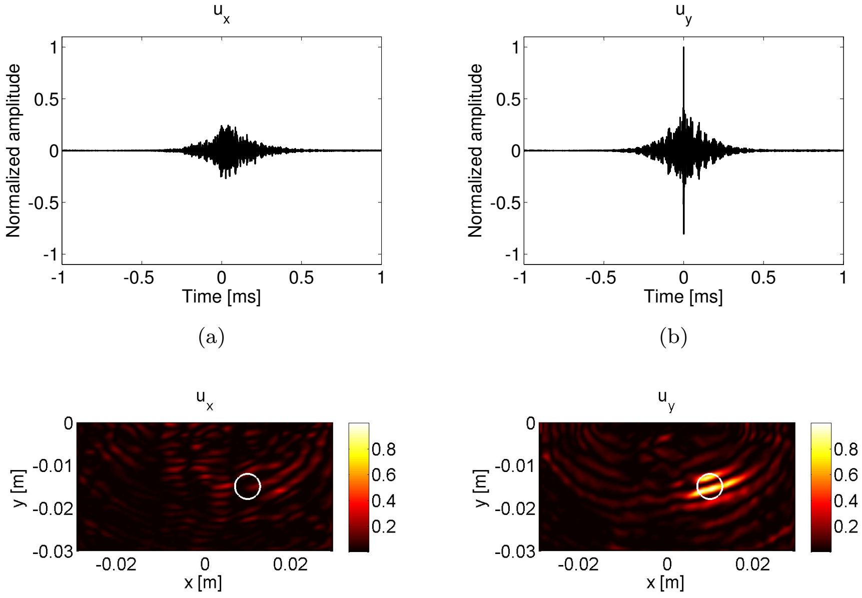

(a) (b)

(c) (d)

Figure 5.33: Simulated displacements in a non-reverberant solid material for TR focusing of the vertical displacement component u_y using a virtual phased array. The focal position is located at $(1, -1.5)$ cm and is encircled in the bottom figures. (a) Simulated horizontal displacement measured at the focal position, (b) simulated vertical displacement measured at the focal position, (c-d) FNR plots of respectively the horizontal and vertical displacement component obtained using equation (5.4). The colour scales are normalized according to the maximum value of the vertical displacement component.

it is clear that the FNR value increases with decreasing distance between the recording points, and thus with increasing number of points. At a distance of approximately half the wavelength of the longitudinal wave (for a central frequency of 600 kHz) the FNR value starts saturating, meaning that the best focusing quality is reached if the recording points are at a distance of approximately half that wavelength. Smaller distances will not further improve the quality significantly. The wavelength of the longitudinal wave is to be used here, since longitudinal waves play an important role in TR focusing of the vertical displacement components, as demonstrated in the above results. For TR focusing of the horizontal displacement components, the wavelength of the shear wave should be used.

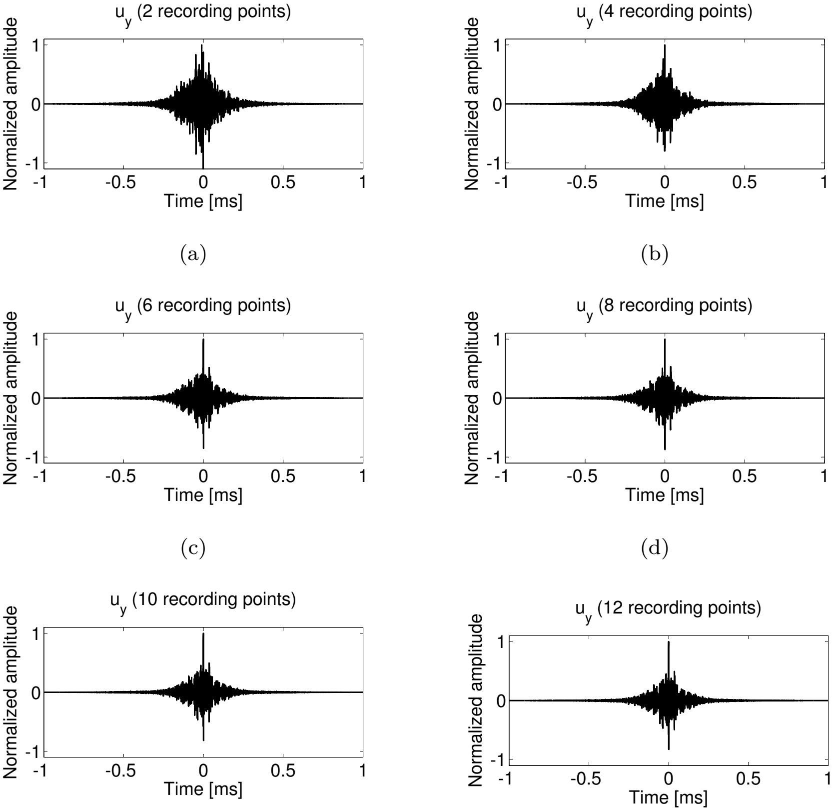

(a) (b)

(c) (d)

(e) (f)

Figure 5.34: Simulated vertical displacement component measured at the focal position in a non-reverberant solid material for TR focusing of the vertical displacement component u_y using a virtual phased array with a different number of recording points: (a) 2 recording points, (b) 4 recording points, (c) 6 recording points, (d) 8 recording points, (e) 10 recording points and (f) 12 recording points.

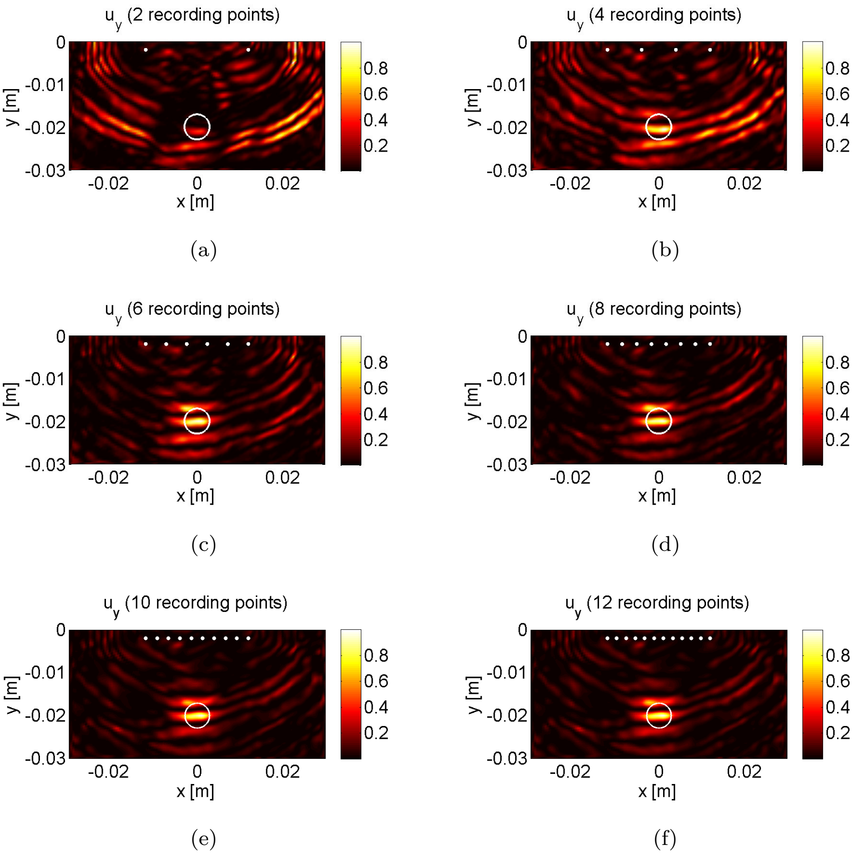

Figure 5.35: FNR plots of the vertical displacement component measured in a non-reverberant solid material for TR focusing of the vertical displacement component u_y using a virtual phased array with a different number of recording points: (a) 2 recording points, (b) 4 recording points, (c) 6 recording points, (d) 8 recording points, (e) 10 recording points and (f) 12 recording points. The focal position is located at $(0, -2)$ cm and is encircled in the figures. The white dots mark the positions of the recording points. The colour scale in each figure is normalized according to its maximum value.

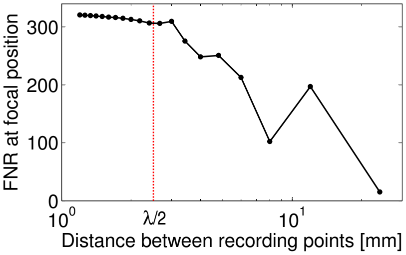

Figure 5.36: FNR values at the focal position as a function of the distance between the recording points for TR focusing of the vertical displacement component u_y using a virtual phased array. The dotted line indicates a distance of half a wavelength of the longitudinal wave (for a central frequency of 600 kHz). The FNR value, a quantitative measure for the focusing quality, starts saturating at a recording point distance of approximately half a wavelength.

The critical distance of approximately half a wavelength can be explained by noticing that in a TR experiment the focal spot size cannot be smaller than half a wavelength [5]. Therefore, if two recording points are separated by less than half a wavelength, their focal spots will partly overlap and they will contribute to the virtual phased array as if they were only one element. More generally, a group of recording points within half a wavelength acts as one recording point and as a consequence, the focusing quality at the intended focal point will not further improve.

To close this section, we present the first results of a 3D simulation of a TR experiment using a virtual phased array. The model consists of an aluminium chaotic cavity on top of a semi-infinite steel sample and is illustrated in figure 5.37. The semi-infinite steel sample is modelled using perfectly matching layers on five of its boundaries. At the sixth boundary, stress-free boundary conditions are implemented, except at the interface between the cavity and the steel sample, where continuity has been assumed. The rest of the sixth boundary is implemented as a stress-free boundary. In front of the cavity a set of 16 recording points is considered to create a virtual phased array that will be used to focus the out-of-plane displacement component in a point located on the top surface of the steel sample. The procedure is the same as before, with some modification in the details. First, a sweep signal is emitted and the out-of-plane displacement components are calculated/stored at the recording positions. These signals are time shifted (using appropriate time delays, see later), and summed. The resulting signal is re-emitted in a time reversed fashion into the chaotic cavity, and gives rise to TR focusing of the out-of-plane components at the recording positions. Every recording point may now be considered as the

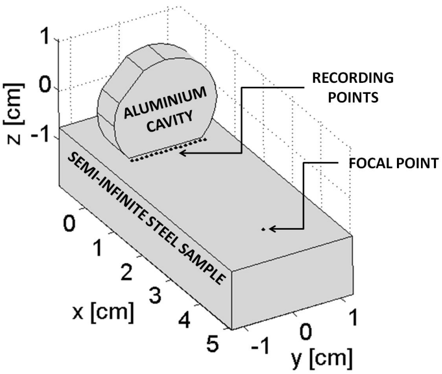

Figure 5.37: Illustration of the geometry of a 3D aluminium chaotic cavity on top of a semi-infinite steel sample used in the COMSOL simulation. The semi-infinite steel sample is modelled using perfectly matching layers on five of its six boundaries. In front of the cavity, on the top surface of the steel sample, 16 recording points are considered. These points are used to create a virtual phased array to focus energy in the focal point.

surface source of secondary spherical waves travelling inside the steel sample. With the right time delays, all secondary waves will constructively interfere at the intended focal spot. To calculate the time delays, we determine the distance from the recording positions to the intended focal position divided by an appropriate velocity. Since the secondary sources originate from the top surface and radiate their energy most efficiently into a Rayleigh wave along the top surface, the Rayleigh wave velocity can be suggested as a good choice for the time delay calculation. Figure 5.38(a) shows the simulated out-of-plane displacement signal calculated at the focal position based on the Rayleigh wave velocity for the calculation of the time delays. The clear temporal focal peak indeed validates the choice of the Rayleigh wave velocity for the time delay calculations in this simulation. The low signal-to-noise ratio in the figure was due the fact that we used a small time window in this simulation, to reduce the computational time of the 3D simulation. Figure 5.38(b) shows a FNR plot of the out-of-plane displacement component at the top surface of the sample, illustrating the focusing in space. The focal position is encircled in the figure.

In future, the concept of a virtual phased array needs to be tested on more 3D samples. As one of the tasks, it will be necessary to develop a suitable method to determine the wave distribution in the samples, in order to calculate the time delays of the different recording signals. Doing so, the basic concept that is illustrated in this section can hopefully be extended and further optimized

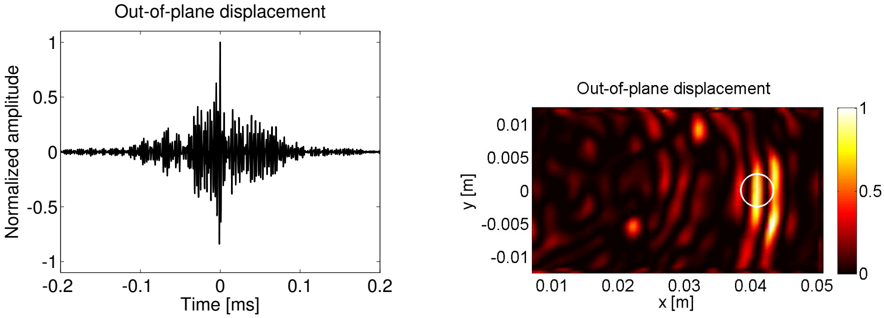

(a) (b)

Figure 5.38: Simulated out-of-plane displacements in a 3D semi-infinite steel sample after TR focusing using a virtual phased array. The time delays of the different recording signals are calculated using the Rayleigh wave velocity. (a) Simulated out-of-plane displacement measured at the focal position on the top surface of the sample, (b) FNR plot of the out-of-plane displacement component at the top surface of the steel sample obtained using equation (5.4). The focal position is encircled in the figure.

for more complex situations, as for instance in anisotropic materials where the wave speed distribution is highly dependent on the direction.

5.6 Conclusion

In this chapter, the finite element model, initially developed in the previous chapter for the implementation of air-coupled NDT experiments, was adapted for the implementation of time reversal experiments.

First, we provided numerical supporting evidence of the ability of TR to focus energy in a multi-reverberant sample using only one channel. We demonstrated the single-channel reciprocal TR to simultaneously focus in multiple points and to selectively or collectively focus the individual displacement components (multi-component TR). This has important implications for the use of TR in NDT. Indeed, some defects will not respond to a compression, but only to a shearing, or vice versa. With the knowledge we have now, it is possible to focus energy with a certain ‘polarization’ to selectively identify defects.

Apart from the use of TR in reverberant media, we proposed a handy technique to apply TR in non-reverberant media using a chaotic cavity transducer. The principle of a chaotic cavity transducer was originally introduced for 3D imaging in fluids, but we extended the principle to applications dealing with elastic waves in solids. Our numerical simulations confirmed that with the use of a chaotic cavity, we are able to focus energy in a non-reverberant solid medium.

In the last part of this chapter, the chaotic cavity transducer was used to create a virtual phased array with only one transducer. The virtual phased array allows to focus energy in any arbitrary point in a medium, simply by focusing, at different times, in different points on a predefined line. With the developed finite element model, we were able to verify the basic concepts of the virtual phased array. We illustrated multi-component TR in a non-reverberant solid using the virtual phased array. In the considered 2D configuration, it was shown that TR focusing along the horizontal displacement component could be achieved if the transversal wave velocity was used to determine appropriate time shifts, while the longitudinal wave velocity needs to be used for TR focusing along the vertical displacement component. We also demonstrated that the best focusing quality is obtained if the distance between the recording points is approximately half the wavelength of the longitudinal wave for TR focusing of the vertical displacement components and half the wavelength of the shear wave for TR focusing of the horizontal displacement components. For smaller distances, the quality is not further improved.

Future work will consist in studying more complex 3D configurations. A suitable technique to determine the wave speed distribution inside materials needs to be developed, especially in the case of anisotropic materials. Another interesting problem would be to study the behaviour of a chaotic cavity transducer embedded in a solid material. Industrial components designed with such embedded chaotic cavity transducers could then be used as self-sensing devices, with obvious applications in aeronautics, automotive, construction engineering, etc. The ultimate goal of the simulations is to optimize the technique for such practical uses.

Bibliography

[1] Achenbach, J. *Reciprocity in elastodynamics.* Cambridge University Press, 2003.

[2] Anderson, B., Griffa, M., Larmat, C., Ulrich, T., and Johnson, P. Time reversal. *Acoustics Today 4* (2008), 5–16.

[3] Bou Matar, O., Li, Y., Delrue, S., and Van Den Abeele, K. Optimization of chaotic cavity transducers to nonlinear elastic imaging. In *Proceedings of the 10th French Congress on Acoustics* (Lyon, April 2010).

[4] Bou Matar, O., Li, Y., and Van Den Abeele, K. On the use of a chaotic cavity transducer in nonlinear elastic imaging. *Appl. Phys. Lett. 95* (2009), 141913.

[5] Cassereau, D., and Fink, M. Time-reversal of ultrasonic fields - Part 3: Theory of the closed time-reversal cavity. *IEEE T. Ultrason. Ferr. 39* (1992), 579–592.

[6] Derode, A., Roux, P., and Fink, M. Robust acoustic time reversal with high-order multiple scattering. *Phys. Rev. Lett. 75* (1995), 4206–4209.

[7] Dos Santos, S., Domenjoud, M., and Prevororsky, Z. Ultrasonic imaging of human tooth using chirp-coded nonlinear time reversal acoustics. *Physics Prodecia 3* (2010), 913–918.

[8] Draeger, C., Aime, J., and Fink, M. One-channel time-reversal in chaotic cavities: Experimental results. *J. Acoust. Soc. Am. 105* (1999), 618–625.

[9] Draeger, C., and Fink, M. One-channel time-reversal of elastic waves in a chaotic 2D-silicon cavity. *Phys. Rev. Lett. 79* (1997), 407–410.

[10] Draeger, C., and Fink, M. One-channel time-reversal in chaotic cavities: Theoretical limits. *J. Acoust. Soc. Am. 105* (1999), 611–617.

[11] Fillinger, L., Sutin, A., and Sarvazyan, A. Time reversal focusing of short pulses. *Ultrason* (2007), 220–223.

[12] Fink, M. Time reversal of ultrasonic fields - Part 1: Basic principles. *IEEE T. Ultrason. Ferr. 39* (1992), 555–566.

[13] Fink, M. Time reversed acoustics. *Phys. Today 50* (1997), 34–40.

[14] Fink, M. Time-reversed acoustics. *Sci. Am. 281* (1999), 91–97.

[15] Fink, M., Cassereau, D., Derode, A., Prada, C., Roux, P., Tanter, M., Thomas, J., and Wu, F. Time-reversed acoustics. *Rep. Prog. Phys. 63* (2000), 1933–1995.

[16] Fink, M., and de Rosny, J. Time-reversed acoustics in random media and in chaotic cavities. *Nonlinearity 15* (2002), R1–R18.

[17] Fink, M., Montaldo, G., and Tanter, M. Time-reversal acoustics in biomedical engineering. *Annu. Rev. Biomed. Eng. 5* (2003), 465–497.

[18] Goursolle, T., Dos Santos, S., Bou Matar, O., and Callé, S. Nonlinear based time reversal acoustic applied to crack detection: Simulations and experiments. *Int. J. Nonlin. Mech. 43* (2008), 170–177.

[19] Ing, R., and Fink, M. Time-reversed Lamb waves. *IEEE T. Ultrason. Ferr. 45* (1998), 1032–1043.

[20] Janssen, E., and Van Den Abeele, K. Dual energy time reversed elastic wave propagation and nonlinear signal processing for localisation and depth-profiling of near-surface defects: A simulation study. *Ultrasonics 51* (2011), 1036–1043.

[21] Larmat, C., Guyer, R., and Johnson, P. Time-reversal methods in geophysics. *Phys. Today 63* (2010), 31–35.

[22] Larmat, C., Montagner, J., Fink, M., Capdeville, Y., Tourin, A., and Clevede, E. Time-reversal imaging of seismic sources and application to the great Sumatra earthquakes. *Geophys. Res. Lett. 33* (2006), 1–4.

[23] Larmat, C., Tromp, J., Liu, Q., and Montagner, J. Time reversal location of glacial earthquakes. *J. Geophys. Res.-Sol. Ea. 113* (2008), B09314.

[24] Le Bas, P., Van Den Abeele, K., Dos Santos, S., Goursolle, T., and Bou Matar, O. Experimental analysis for nonlinear time reversal imaging of damage materials. In *Proceedings of the European Conference on Non-Destructive Testing* (Berlin, September 2006).

[25] Montaldo, G., Palacio, D., Tanter, M., and Fink, M. Time reversal kaleidoscope: A smart transducer for three-dimensional ultrasonic imaging. *Appl. Phys. Lett. 84* (2004), 3879–3881.

[26] Montaldo, G., Palacio, D., Tanter, M., and Fink, M. Building three-dimensional images using a time-reversal chaotic cavity. *IEEE T. Ultrason. Ferr. 52* (2005), 1489–1497.

[27] Montaldo, G., Roux, P., Derode, A., Negreira, C., and Fink, M. Generation of very high pressure pulses with 1-bit time reversal in a solid waveguide. *J. Acoust. Soc. Am. 110* (2001), 2849–2857.

[28] Porter, M., Roux, P., Song, H., and Kuperman, W. Tumor treatment by time-reversal acoustics. In *Proceedings of the International Conference on Acoustics, Speech, and Signal Processing* (Phoenix, March 1999), pp. 2107–2110.

[29] Quieffin, N. *Etude du rayonnement acoustique de structures solides: vers un système d'imagerie haute résolution.* PhD thesis, Université Paris VI - Pierre et Marie CURIE, 2004.

[30] Quieffin, N., Catheline, S., Ing, R., and Fink, M. 2D pseudo-array using an ultrasonic one channel time-reversal mirror. *Ultrason* (2004), 801–804.

[31] Quieffin, N., Catheline, S., Ing, R., and Fink, M. Real-time focusing using an ultrasonic one channel time-reversal mirror coupled to a solid cavity. *J. Acoust. Soc. Am. 115* (2004), 1955–1960.

[32] Roux, P., and Fink, M. Time reversal in a waveguide: Study of the temporal and spatial focusing. *J. Acoust. Soc. Am. 107* (2000), 2418–2429.

[33] Roux, P., Roman, B., and Fink, M. Time-reversal in an ultrasonic waveguide. *Appl. Phys. Lett. 70* (1997), 1811–1813.

[34] Saenger, E., Kocur, G., Jud, R., and Torrilhon, M. Application of time reverse modeling on ultrasonic non-destructive testing of concrete. *Appl. Math. Model. 35* (2011), 807–816.

[35] Sutin, A., and Johnson, P. Nonlinear elastic wave NDE II: Nonlinear wave modulation spectroscopy and nonlinear time reversed acoustics. *Review of Quantitative Nondestructive Evaluation 24* (2005), 385–392.

[36] Sutin, A., Johnson, P., and TenCate, J. Development of nonlinear time reversed acoustics (NLTRA) for applications to crack detection in solids. In *Proceedings of the World Congress on Ultrasonics* (Paris, September 2003), pp. 155–158.

[37] Tanter, M., Aubry, J., Gerber, J., Thomas, J., and Fink, M. Optimal focusing by spatio-temporal inverse filter. I: Basic principles. *J. Acoust. Soc. Am. 110* (2001), 37–47.

[38] Trefna, H., Vrba, J., and Persson, M. Time-reversal focusing in microwave hyperthermia for deep-seated tumors. *Phys. Med. Biol. 55* (2010), 2167–2185.

[39] Ulrich, T., Johnson, P., and Sutin, A. Imaging nonlinear scatterers applying the time reversal mirror. *J. Acoust. Soc. Am. 119* (2006), 1514–1518.

[40] Ulrich, T., Sutin, A., Claytor, T., Papin, P., Le Bas, P., and TenCate, J. The time reversed elastic nonlinearity diagnostic applied to evaluation of diffusion bonds. *Appl. Phys. Lett. 93* (2008), 151914.

[41] Ulrich, T., Sutin, A., Guyer, R., and Johnson, P. Time reversal and non-linear elastic wave spectroscopy (TR NEWS) techniques. *Int. J. Nonlin. Mech. 43* (2008), 209–216.

[42] Ulrich, T., Van Den Abeele, K., Le Bas, P., Griffa, M., Anderson, B., and Guyer, R. Three component time reversal: Focusing vector components using a scalar source. *J. Appl. Phys. 106* (2009), 113504.

Chapter 6

Nonlinear ultrasonic spectroscopy of delaminations and cracks

Nonlinear acoustic techniques are becoming increasingly popular in the field of NDT. They provide extreme sensitivity in detecting incipient damage in the form of micro-cracks or delaminations. In this chapter, the main focus lies on the detection of closed delaminations in composite materials and surface breaking cracks in metals. Since early stage delaminations and cracks tend to be closed at rest, these defects can only be detected using nonlinear ultrasonic techniques. By applying a finite excitation amplitude that is able to overcome an activation threshold the contact can be opened or closed. This local contact phenomenon is called clapping and gives rise to a nonlinear stress-strain relation at the defect location.

In order to obtain a better understanding and analysis of the macroscopic nonlinear behaviour that can be observed at the component level, we developed and investigated the results of a finite element model for a composite material containing one or more delaminations. The model makes use of local node splitting and the nonlinear constitutive behaviour is implemented by means of spring-damper elements at the defect's interface. The results of an intensive parametric study allow a better insight in the behaviour of the excited defects in experimental conditions, including the appearance of subharmonics and harmonics of the excitation frequency generated by the clapping delamination. Based on the developed model it should be possible to determine position, shape, depth and orientation of one or multiple delaminations by studying the amplitude patterns of the generated subharmonic and harmonic frequencies in the surface scan response signals [9, 10].

In the first section, typical defects with imperfect adhesion, such as delaminations and cracks are discussed. These defects are often referred to as contact acoustic nonlinearities (CANs). Then, a three-dimensional finite element model for a composite material containing a single circular delamination is proposed. The following two sections cover the results of a parametric study in which the clapping effect, the generation of harmonics and subharmonics and the influence of the delamination shape, position, depth and orientation are illustrated and discussed. An extension to multiple delaminations is studied in section five. In the last part of this chapter, we adapted the model to the study of surface breaking cracks.

6.1 Contact acoustic nonlinearities

Metals and metal alloys are the most commonly used type of engineering materials, since they possess several attractive properties including their high structural strength per unit mass, their high resistance to shear, torque and deformation as well as many others. Nowadays, however, composite materials are increasingly being used in numerous industrial products, opening new markets and applications. Reinforcing fibers give composites the attributes of high strength and stiffness which translates to high performance. In addition, fiber/resin combinations have significantly lower weight densities when compared to steel and concrete. This means superb strength-to-weight and stiffness-to-weight ratios. On the other hand, one of the main disadvantages of composites is the fact that they are difficult to repair when damaged, since most of the composites use thermoset matrices that can't be reshaped. Once damaged, the presence of internal defects may significantly alter the stiffness and reduce the strength of the composites. As a result, there has been an increased interest in NDT methods for this type of materials.

Typical defects that can occur in layered composite materials and metals are respectively delaminations and surface breaking cracks. They can be induced as a result of manufacturing faults or due to subsequent operational effects, such as impact loads, fatigue, thermal loading, etc. Once initiated, they gradually grow within the material upon further loading and eventually lead to failure of the component. Therefore, the non-destructive evaluation of these defects is very important in both the manufacture and in-service sustainment of these materials. Delaminations and cracks can be detected by traditional linear ultrasonic techniques if they are open, since the ultrasound is then scattered, reflected or transmitted by the defect. However, early stage delaminations and cracks tend to be closed at rest. In a closed defect, the adhesion between two regions of the material is affected, but the two interfaces of the delamination are still in contact. By applying a finite excitation amplitude that is able to overcome the defects specific activation threshold, the contact can be opened or closed. This local contact behaviour (commonly referred to as breathing, kissing or clapping) gives rise to a nonlinear stress-strain relation at the defect location since the stress-strain response is different in tension than in compression (violation of the simple Hooke's law). Solid-to-solid interfaces with imperfect adhesion, such as delaminations and cracks, are often referred to as contact acoustic nonlinearities (CANs) [13, 27, 30].

CANs are among the most efficient mechanisms generating nonlinear features. When a sample, containing such a defect, is excited by a high amplitude single tone external excitation, e.g. a sinusoidal wave, the frequency spectrum of its nonlinear structural response is no longer dominated only by the frequency of the excitation signal. Higher order harmonics and subharmonics, whose frequencies have a prescribed relation with the excitation frequency, appear in the spectrum as a result of the nonlinearity [12, 13, 27, 30].

Typical nonlinear ultrasonic techniques that provide extreme sensitivity in detecting incipient damage in the form of cracks or delaminations are based on the investigation of the amplitude dependence on the spectral content of the sample's response. In particular, such techniques rely on the detection of harmonics $(2f_{exc}, 3f_{exc}, \ldots)$ and subharmonics $(f_{exc}/2, f_{exc}/3, \ldots)$ that were generated as a result of the clapping of the two interfaces of the defect excited at frequency f_{exc} and with an excitation amplitude high enough to initiate the clapping behaviour. These methods, in which the internal damage is measured directly through the instantaneous detection of nonlinearity parameters are part of a larger class of NDT techniques, called Nonlinear Elastic Wave Spectroscopy (NEWS) [11, 31, 32].

In the following, a three-dimensional finite element model of a sample containing a contact acoustic nonlinearity is developed. With this model, several nonlinear ultrasonic techniques for the detection of these types of defects can be simulated, illustrated and optimized. The model allows to support experimental techniques to detect defects and to identify the location of these defects by exploiting the specific information carried by the subharmonic and harmonic frequencies generated at the defect's interface.

6.2 3D finite element simulation

A vast amount of theoretical (semi-analytical) [25, 26] and experimental [16–21, 33, 34] research on the nonlinear behaviour of delaminations is available in literature. However, for a better understanding and a more in-depth analysis of the macroscopic nonlinear behaviour of excited delaminations, the development of numerical simulation models is crucial. Sarens et al. [21] simulated the nonlinear elastic behaviour of delaminations by a three-dimensional second-order, finite difference model. The most attractive feature of the finite difference method is that it is very easy to implement. The main drawback of this type of simulations is that finite difference models are restricted to handle rectangular shapes and simple alterations thereof, as already mentioned in chapter 3. To increase flexibility, we choose to base our investigations on a finite element method.

Standard procedures in finite element methods for contact modelling are based on Newton's law of impact or the penalty method [14, 15, 35]. In Newton's impact law, a relation is considered between the velocities of two bodies immediately after impact and at the moment of impact. A serious drawback of this method is that it does not allow the implementation of permanent contact of the two bodies, instead a sequence of impacts will occur. The penalty method defines a force proportional to the penetration depth of the two bodies in contact. When a penetration is found between two bodies the force is applied to resist, and ultimately eliminate, the penetration. In this section, a three-dimensional finite element model for a composite material containing a single circular delamination is proposed. The model makes use of local node splitting and the nonlinear constitutive behaviour is implemented by means of particular nonlinear spring-damper elements at the delamination interface. These spring-damper elements are only active when the two sides of the delamination tend to collapse. By doing this, we ensure that there will never be an overlap between the two interfaces of the delamination in contrast to the penalty method, where the restoring force is only used when there is already overlap. The three-dimensional finite element simulation is implemented in the structural mechanics module of Comsol, discussed in section 3.2.2. The main innovative contribution of this study is the implementation of the clapping effect.

6.2.1 Geometry and material parameters

The material under consideration is a composite plate containing a circular delamination, parallel to the surface. The composite plate has a length and a width of 40 mm, and a thickness of 2 mm. The delamination has a diameter of

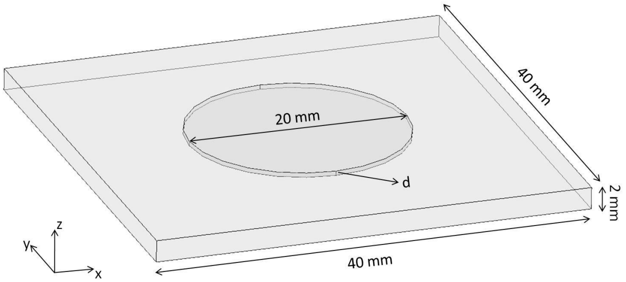

Figure 6.1: Illustration of the geometry used in the COMSOL simulation. The model contains a composite plate of dimensions 40 mm × 40 mm × 2 mm and a small cylinder made of the same composite material with a diameter of 20 mm and a height d ($d < 1$ mm). The bottom surface of the cylinder represents the delamination interface.

20 mm and is located near the centre of the plate at a depth d, with respect to the top surface of the plate. The actual implementation of the sample into COMSOL is done as follows. First, a rectangular domain with the dimensions of the composite plate is constructed. Then, a small cylinder with a diameter of 20 mm and height d is added, so that the top surface of the cylinder coincides with the top surface of the rectangular plate. Finally, two 'model' domains are created: domain 1 is formed by the subtraction of the cylinder from the rectangular plate and domain 2 is the cylinder itself. The bottom surface of the cylinder, which is then at a depth d with respect to the top surface of the plate, represents the delamination interface. The geometry is illustrated in figure 6.1.

The composite material used in our simulations is a unidirectional (anisotropic) carbon fiber composite with density $\rho = 1800$ kg/m^3. The anisotropy of the material is taken into account by working with the orthotropic material properties, as listed in table 6.1. As we can see, the elastic parameters largely depend on the fiber orientation. Along the fiber direction, the stiffness is generally much larger than perpendicular to the fibers. As discussed in section 3.2.2, the implementation of an orthotropic material in COMSOL is done by simply entering the values of these nine parameters in designated edit fields in the user interface.

A small amount of damping has been added to the model. One of the damping models in the structural mechanics module of COMSOL is the Rayleigh damping model [1], where the damping is assumed to be proportional to a linear combination of the stiffness and mass. In this study, we have set the mass damping parameter α_{dM} equal to zero, and the stiffness damping parameter

Young's modulus [GPa]	Shear modulus [GPa]	Poisson's ratio
$E_{xx} = 161.0$	$G_{xy} = 5.17$	$\nu_{xy} = 0.32$
$E_{yy} = 11.38$	$G_{yz} = 3.98$	$\nu_{yz} = 0.436$
$E_{zz} = 11.38$	$G_{xz} = 5.17$	$\nu_{xz} = 0.32$

Table 6.1: Orthotropic material constants for unidirectional carbon fiber composite [21].

was chosen as follows:

$$\beta_{dK} = \frac{1}{2\pi f_{exc} Q} \tag{6.1}$$

where f_{exc} is the excitation frequency and Q is the quality factor. The quality factor used in all simulations is $Q = 20$.

6.2.2 Boundary conditions and sources

Boundary conditions are required for both the interior and exterior boundaries of the geometry. At the outer edges of the simulated object, stress-free boundaries are implemented. All interior boundaries are split into two parts, one part belonging to the cylinder (domain 2) and one part belonging to the rectangular region (domain 1). This is done by using the assembly mode for those two domains in COMSOL [2]. At the shell of the cylinder, continuity should be assumed between the two domains and thus, the two parts need to be fully connected. In COMSOL this can be implemented by defining identity pairs which connect parts of an assembly [2]. The application modes in COMSOL use the pairs to put constraints on the equations such that the solution becomes continuous across the border between the parts.

The most challenging part of the model is the implementation of the boundary conditions at the delamination interface. As discussed earlier, delaminations that are dynamically excited can be opened or closed. Furthermore, this behaviour is local in the sense that some parts of the delamination can be opened, while other parts are closed at the same time. When the delamination is locally in an open state, it is obvious that stress-free boundary conditions have to be implemented at the local interface. When the delamination is locally closed, the material across the interface should appear to be continuous. In the latter case an extra constraint is required to ensure that there will be no overlap between the two interfaces of the delamination. In the model, this was implemented by introducing virtual spring-damper elements, which connect every two corresponding points of the top and bottom interface of

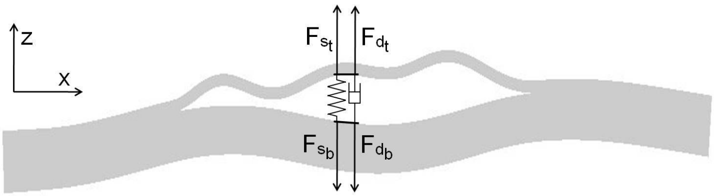

Figure 6.2: Illustration of the virtual spring-damper elements introduced for the implementation of the delamination boundary conditions. The spring-damper elements are implemented in COMSOL by defining four forces: F_{s_t}, F_{d_t}, F_{s_b} and F_{d_b} respectively acting on both the top (subscript t) and bottom (subscript b) interface of the delamination.

the delamination (see figure 6.2). The practical implementation of the spring-damper elements was realized by defining two spring forces F_{s_t} and F_{s_b} and two damping forces F_{d_t} and F_{d_b} respectively acting on both the top (subscript t) and bottom (subscript b) interface of the delamination.

Both spring forces are simple functions of the separation distance or gap Δz between two corresponding points at the delamination interface, defined as:

$$\Delta z = u_{z_t} - u_{z_b} \tag{6.2}$$

with u_{z_t} and u_{z_b} respectively the (time dependent) normal displacement in a point at the top and bottom interface of the delamination.

In order to investigate the effects of a realistic interaction between the delamination interfaces, we have chosen to implement spring forces that are based on the representation of the Lennard-Jones potential, from which the repulsive/adhesive contact forces acting between two points can be deduced. In our model, we used a quasi-linear approximation of the Lennard-Jones potential, as the implementation of the true Lennard-Jones potential within COMSOL results in stability problems when the potential goes to infinity for particle distances going to zero. The quasi-linear spring force F_{s_t} on the top interface used in the subsequent simulations is defined as:

$$F_{s_t} = \begin{cases} k_1(Z_0 - \Delta z) & \text{if} \quad \Delta z < Z_0 \\ k_2(Z_0 - \Delta z) & \text{if} \quad Z_0 \leq \Delta z < aZ_0 \\ k_3(bZ_0 - \Delta z) & \text{if} \quad aZ_0 \leq \Delta z < bZ_0 \\ 0 & \text{if} \quad \Delta z \geq bZ_0 \end{cases} \tag{6.3}$$

where Z_0 is a small characteristic distance between both interfaces at rest, a and b are free parameters used in the separation conditions with a larger than

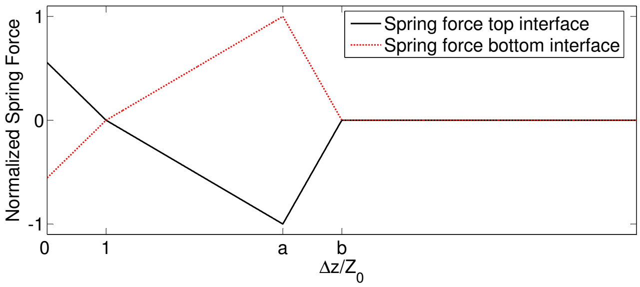

Figure 6.3: Spring forces F_{s_t} and F_{s_b} respectively acting on the top and bottom interface of the delamination as a function of the gap distance Δz.

unity and b larger than a, and k_1, k_2 and k_3 are virtual spring constants. The spring constant k_3 depends on the spring constant k_2 as follows:

$$k_3 = \frac{1-a}{b-a} k_2 \tag{6.4}$$

The spring force F_{s_b} on the bottom interface is equal but opposite to the spring force F_{s_t} on the top interface. Both spring forces are plotted in figure 6.3 as a function of the gap distance Δz.

In the case when the separation condition

$$\Delta z \geq b Z_0 \tag{6.5}$$

is satisfied, the delamination is open with a “large” gap between the top and bottom interface, meaning that there will be no interaction between both interfaces. Hence, the spring forces are zero and the interfaces are free to move as long as the interface gap stays large enough. Since the delamination is limited in size, the outer edges of the delamination are connected to the rest of the elastic material, which pulls back on the edges of the delamination. Therefore, the movement of the interfaces is restricted, and the restoring forces make it possible for the delamination to close again. If the gap falls below the threshold bZ_0, i.e. when

$$\Delta z < b Z_0 \tag{6.6}$$

is satisfied, nonzero forces are activated. These forces can either be positive or negative (repelling or restoring forces). At moments when both interfaces tend to overlap (i.e. the separation distance Δz becomes smaller than the characteristic length Z_0), the spring forces will counteract this movement by

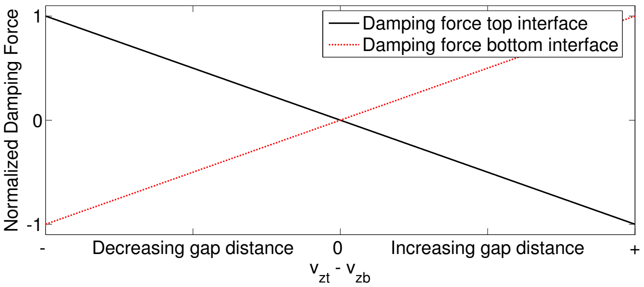

Figure 6.4: Damping forces F_{d_t} and F_{d_b} respectively acting on the top and bottom interface of the delamination as a function of the rate of change of the gap distance Δz, which is defined as the difference in particle velocity for a point at the top interface with respect to its corresponding point at the bottom interface.

pushing both sides of the delamination in the opposite direction ($F_{s_t} > 0$ and $F_{s_b} < 0$) and those repelling forces will prevent the overlap. For gaps between Z_0 and bZ_0 (the "non"-separation condition still being satisfied), restoring forces are considered that oppose the separation of the interface boundaries ($F_{s_t} < 0$ and $F_{s_b} > 0$). In this case the interfaces are still connected by a virtual spring and the material appears to be continuous. The restoring forces reach a maximum at a gap distance equal to aZ_0. For larger distances, the forces decrease until they are zero at a gap distance equal to bZ_0.

Apart from the spring forces, two damping forces were also implemented. Both damping forces are simple functions of the rate of change of the gap distance Δz, which is defined as the relative velocity of a point at the top interface with respect to the velocity of the corresponding point at the bottom interface. The damping force F_{d_t} on the top interface is then defined as:

$$F_{d_t} = \begin{cases} -\gamma(v_{z_t} - v_{z_b}) & \text{if} \quad \Delta z < bZ_0 \\ 0 & \text{if} \quad \Delta z \geq bZ_0 \end{cases} \tag{6.7}$$

with v_{z_t} and v_{z_b} respectively the (time dependent) normal velocity in a point at the top and bottom interface of the delamination and γ the damping coefficient. The damping force F_{d_b} on the bottom interface is equal but opposite to the damping force F_{d_t} on the top interface. Both damping forces are plotted in figure 6.4 as a function of the rate of change of the gap distance Δz.

As with the spring forces, the damping forces are equal to zero when the separation condition

$$\Delta z \geq bZ_0 \tag{6.8}$$

is satisfied. Both interfaces can move freely, without extra damping. Nonzero damping forces, either positive or negative, are activated when the separation condition

$$\Delta z < bZ_0 \tag{6.9}$$

is satisfied. A decreasing gap distance (i.e. when $v_{z_t} < v_{z_b}$) is counteracted by two damping forces reducing the rate at which the two surfaces move towards each other ($F_{d_t} > 0$ and $F_{d_b} < 0$). When the gap distance is increasing (i.e. when $v_{z_t} > v_{z_b}$), the damping forces reduce the rate at which the two surfaces move away from each other ($F_{d_t} < 0$ and $F_{d_b} > 0$).

For the numerical computations, six parameters need to be specified as input: Z_0, k_1, k_2, a, b and γ. Z_0 is the equilibrium distance between the top and bottom interface if the delamination is closed. As both interfaces should be in contact for a closed delamination, Z_0 is chosen very small (e.g. in the order of the inter-atomic distance). k_1 is the spring constant of the virtual spring for the repelling force used at the moment when both interfaces tend to overlap (i.e. the separation distance Δz becomes smaller than the characteristic length Z_0). Care should be taken in setting a value for this parameter. For too small spring constant values, the repelling forces that are activated when the interface gap vanishes will be too small and there will be an overlap between the two interfaces. For too high values of k_1, the repelling forces will be too large (i.e. physically impossible) and the stability of the code is not longer assured. k_2 is the spring constant of the virtual spring used to keep both interfaces connected when the delamination gap is between Z_0 and aZ_0. For too high values of k_2, the separation distance Δz will always remain smaller than aZ_0 and the interfaces will stay in contact during the entire simulation. For too small values of k_2, the restoring forces are too small to hold the interfaces together. The parameters a and b appear in the separation conditions. a is chosen larger than unity and b is chosen larger than a. The larger the values of a and b, the longer the interfaces are connected and the longer the material appears to be continuous. Finally, the parameter γ is the damping coefficient that appears in the damping forces. The larger the value of γ, the less chance of an overlap between the two interfaces of the delamination. For too high values of γ, the damping forces will be too strong and the gap distance will always remain smaller than bZ_0 and the material will appear to be continuous during the entire simulation. This way, we can easily see that high values for both k_2, a, b and γ will provide asymptotically the behaviour of a delamination that is very stiff and never opens. Numerical simulations have been performed to verify that under these conditions the material remains perfectly continuous and linear.

Finally, external acoustic/ultrasonic sources can be introduced in the model by implementing them as a particular boundary condition. In the following simulations, a localized excitation point source was considered at the top surface of the sample that continuously applied a sinusoidal out-of-plane (normal) displacement at frequency f_{exc} for the entire duration of the simulation. The source was positioned at the left lower corner on the top surface.

6.3 Circular delamination parallel to the surface

The numerical simulation model outlined in section 6.2 has been applied to a number of simple exemplary cases in order to get a better understanding of the typical nonlinear behaviour of delaminations under dynamic excitation. In the following, we will first validate the new implementation of the equation of state for a circular delamination parallel to the surface of a composite sample, as already discussed by Sarens et al. [21]. In particular, we will describe the clapping phenomenon that can be observed at the delamination interface, and we will demonstrate the generation of localized (sub)harmonics of the excitation frequency due to this clapping behaviour. It will be shown that the results from the finite element model for parallel delaminations are in good agreement with the results discussed by Sarens et al. [21]. Later, in section 6.4, the influence of the delamination shape, position and depth on the harmonic and subharmonic generation will be discussed. Most of the simulations were performed for a circular delamination parallel to the surface of the composite sample. To emphasize the flexibility of the finite element model, we included in the last part of section 6.4 some results in which the delamination was inclined with respect to the surface of the plate.

It should be mentioned that all discussed results have been simulated using the same parameters. The equilibrium distance Z_0 is set to 0.1 nm, which is in the order of the inter-atomic distance. The parameters a and b used in the separation condition are fixed at respectively 4 and 5. The actual implementation of the spring forces in COMSOL was done by introducing face loads on the delamination boundaries. These loads are defined as forces per unit area and therefore, two new constants k_1^* and k_2^*, which are respectively equal to the spring constants k_1 and k_2 divided by the unit area, are introduced. In the simulations, the constants k_1^* and k_2^* are respectively equal to $5 \cdot 10^{12}$ N/m^3 and $3 \cdot 10^{12}$ N/m^3, which are reasonable values in this analysis. As with the spring forces, a new constant γ^* equal to the damping coefficient γ divided by the unit area, needs to be introduced to implement the damping forces into COMSOL. In the model, the coefficient γ^* equals 10^6 Ns/m^3.

6.3.1 Clapping mechanism

The first simulations were performed using a circular delamination (diameter of 20 mm and centred on the plate), located at a depth of 0.4 mm. Using the eigenfrequency analysis tool of Comsol, we determined the eigenfrequencies and the corresponding eigenmode patterns of the composite plate. Since the eigenmode pattern corresponding to a frequency of 25250 Hz has an anti-node, and thus high displacement amplitudes, at the position of the delamination, we choose this frequency as the excitation frequency f_{exc}.

In order to illustrate the amplitude dependence of the delaminated sample, we first concentrate on the results obtained at two different excitation amplitudes. Figures 6.5 and 6.6 display snapshots of the simulated total displacements of the composite plate in case of a low and a high excitation amplitude. The results are displayed using deformed slice plots in x- and y-direction to have a clear picture of the displacements inside the composite plate, especially at the delamination interface. The deformation in each point is proportional to the total displacement in that point. Figure 6.5 concerns the results for a low excitation amplitude at five instances during one excitation period T. In this case, we can clearly observe the eigenmode pattern generated in the plate. Because of the low excitation amplitude, the delamination will stay closed during the entire simulation and thus, the delamination has no influence on the total displacements. Figure 6.6 represents the results for a high excitation amplitude at the same five instances. In this case, the excitation amplitude is large enough to overcome the activation threshold of the delamination and the contact is opened. The layer above the delamination is highly influenced by the nonlinear clapping and behaves like a membrane vibrating according to its own eigenmode pattern. Remark that the displacements above the delamination are much higher than the displacements elsewhere.

Since the delamination mainly influences the displacements of the layer above and below the delamination, we can also consider the normal displacements at the top surface of the sample instead of considering the total displacements within the entire composite plate. Figure 6.7 displays snapshots of the simulated normal displacements at the top surface of the composite sample in case of a low (figure 6.7(a)) and high (figure 6.7(b)) excitation amplitude at the same five instances during one excitation period. The colour scales for the top and bottom figures are normalized by the ratio of high to low excitation amplitude. In case of a low excitation amplitude, no influence of the delamination on the normal displacements is observed, since the delamination is not opened. In case of a high excitation amplitude, the normal displacements above the delamination are much higher than the displacements elsewhere as a result of the clapping of the delamination (most obvious at times t, $t + 0.5T$ and $t + T$).

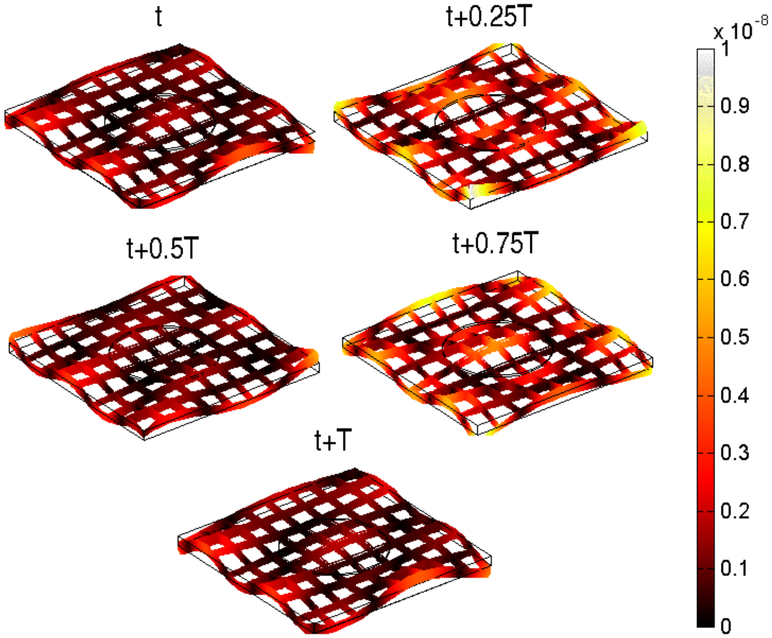

Figure 6.5: Simulated total displacements (in m) of a 40 mm × 40 mm × 2 mm composite plate with a 20 mm diameter delamination centred on the plate and located at a depth of 0.4 mm, at five instances during one full excitation period T, in case of a low excitation amplitude (0.01 μm). The displacements are plotted using deformed slice plots in x- and y-direction to have a clear picture of the displacements inside the plate, especially at the delamination interface. The deformation is proportional to the total displacement in each point. Here, no influence of the delamination on the displacements is observed.

6.3.2 Generation of harmonics and subharmonics

In order to gain further understanding of the behaviour of the delamination, we analysed the simulation results using similar representations as introduced by Sarens et al. [21]. First, we studied the time signals of the normal displacements just above and just below the delamination at five different positions at the delamination interface. These displacements are shown at the left hand side of figure 6.8. The full line represents the displacement of a point just above the delamination, the dotted line represents the displacement amplitude just below the delamination interface. In the centre column of figure 6.8, the normalized frequency spectra just above the delamination

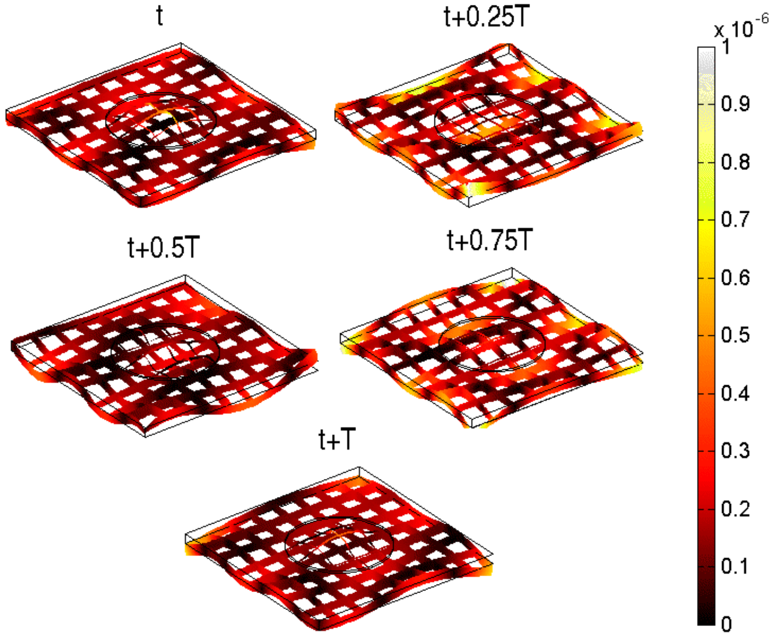

Figure 6.6: Simulated total displacements (in m) of a 40 mm × 40 mm × 2 mm composite plate with a 20 mm diameter delamination centred on the plate and located at a depth of 0.4 mm, at five instances during one full excitation period T, in case of a high excitation amplitude (1 μm). The displacements are plotted using deformed slice plots in x- and y-direction to have a clear picture of the displacements inside the plate, especially at the delamination interface. The deformation is proportional to the total displacement in each point. Here, higher displacement amplitudes can be found above the delamination, with the top layer being detached from the underlying material, causing the delamination to be opened.

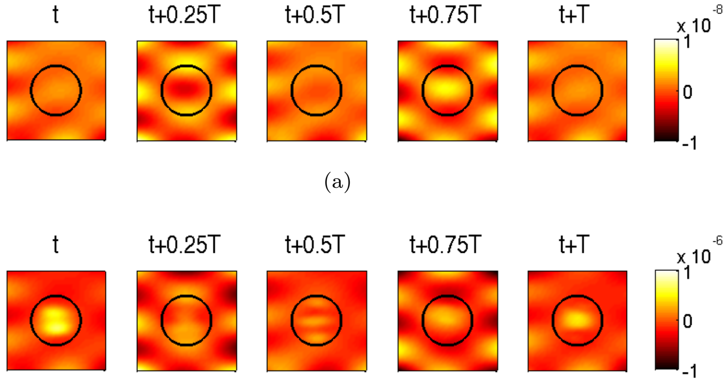

(a)

(b)

Figure 6.7: Simulated normal displacements (in m) at the top surface of a 40 mm × 40 mm × 2 mm composite plate with a 20 mm diameter delamination centred on the plate and located at a depth of 0.4 mm, at five instances during one full excitation period T, in case of (a) a low excitation amplitude (0.01 μm) and (b) a high excitation amplitude (1 μm). The circle indicates the position of the delamination.

for the same five positions are given. At the right hand side of figure 6.8, the actual position of the five measurement locations at the delamination is shown. Looking at the normal displacement signals, we notice that the two sides of the delamination periodically hit each other for a short duration, resulting in a clapping behaviour. The observed clapping events result in the creation of harmonics and subharmonics of the excitation frequency. At the five positions, the impact of the two sides of the delamination suffices to open the delamination during two excitation cycles, resulting in a subharmonic vibration of the membrane above the delamination. The subharmonic $f_{exc}/2$ can be clearly found in the Fourier spectrum calculated at those positions. Apart from the creation of the subharmonic $f_{exc}/2$, several harmonics of the excitation frequency ($2f_{exc}$, $3f_{exc}$, $\ldots$) are being generated and, even more, harmonics of the subharmonic ($3f_{exc}/2$, $5f_{exc}/2$, $\ldots$) can be identified.

The above study of the normal displacements and the corresponding displacement spectra of five different points showed that the clapping behaviour of a delamination results in the creation of harmonics and subharmonics. In order to obtain more information of the entire vibrating layer above the delamination, we temporally Fourier transformed the vibration pattern of each point at the top surface of the plate. This allows to make plots of the spatially distributed response filtered at a fixed response frequency f. For the high amplitude excitation simulation discussed above, figure 6.9 displays the calculated Fourier

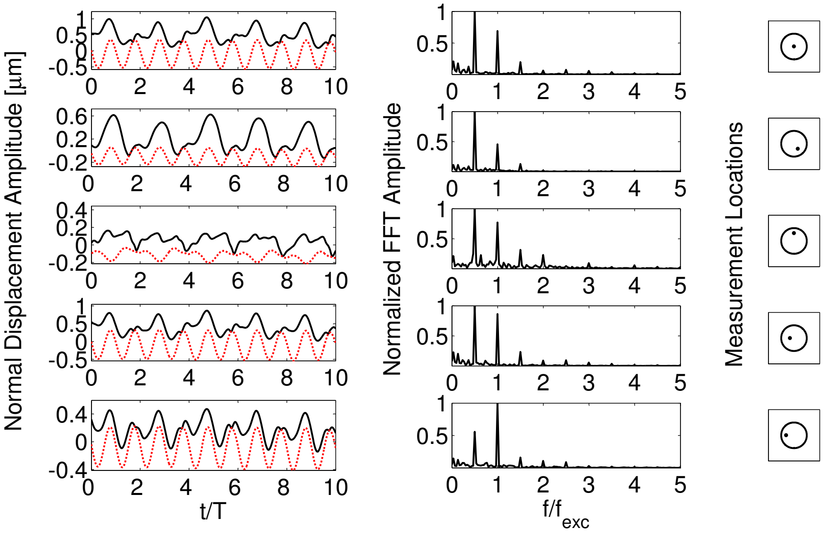

Figure 6.8: Simulation results for a 40 mm × 40 mm × 2 mm composite sample with a 20 mm diameter delamination centred on the plate and located at a depth of 0.4 mm. LEFT: Simulated normal displacement response signals at five different positions on the delamination interface. The full line represents the displacement just above the delamination interface, the dotted line is the displacement just below the delamination interface. MIDDLE: Simulated normalized displacement frequency spectra just above the delamination interface for the same five positions. RIGHT: The actual position of the five measurement locations at the delamination (= circle).

amplitude distribution for a number of response frequencies f. For each plot, the ratio f/f_{exc} is given as a header. Again, a clearly visible subharmonic at $f_{exc}/2$ can be distinguished. Also, the second harmonic ($2f_{exc}$) and the third harmonic of the subharmonic ($3f_{exc}/2$) are slightly visible.

Until now, the clapping behaviour of the delamination was studied by looking either at the Fourier spectrum for one position at the delamination interface (figure 6.8) or at the amplitude pattern of the entire top surface for a fixed response frequency (figure 6.9). Both methods have severe drawbacks. In the first method, the response is highly dependent on the position of the measurement. If the position under study is, for example, located at a node point of the generated mode pattern in the plate, no harmonics or subharmonics will be observed, and false conclusions can be drawn about the local state of the sample. Also points near the edges of the delamination are less useful, since the observed amplitudes there are smaller. In the second method, the

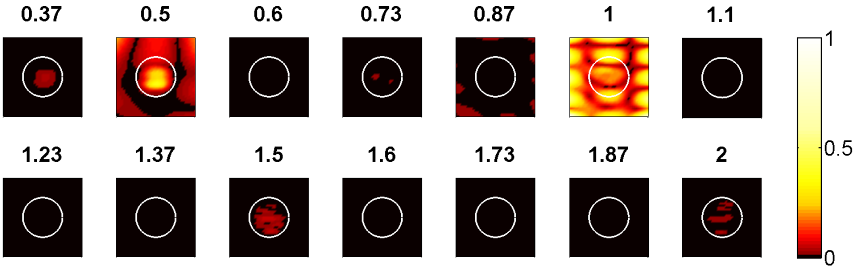

Figure 6.9: Simulated amplitude patterns for a 40 mm × 40 mm × 2 mm composite sample with a 20 mm diameter delamination centred on the plate and located at a depth of 0.4 mm obtained by Fourier transforming the temporal evolution of the normal displacement in each point at the top surface of the sample. The value above each figure represents the ratio f/f_{exc}. The circle indicates the position of the delamination. The colour scale is normalized according to the maximum value of the amplitudes. The lowest amplitudes are shown in black.

problem is situated in the frequency space. In order to search for an informative subharmonic or harmonic response at a frequency f, the amplitude pattern for f needs to be compared with the amplitude patterns for a number of frequencies around f. A subharmonic or harmonic is found if the amplitudes at f are higher with respect to the amplitudes at the surrounding frequencies. If the data is analysed and interpreted at the wrong response frequency, again false conclusions can be drawn about the state of the sample. However, if -as a start- only global information about (sub)harmonic generation in the sample is required (and no localization of the defect) it would be better to have all spatial and spectral information combined into one single analysis. To do this, we used the following approach which can be fully automated without end-user intervention once the signals have been recorded on the surface of the sample. We first temporally Fourier transform the vibration pattern of each point at the surface of the plate. Subsequently, we identify the maximum amplitude in the spatial 2D picture for each response frequency. Finally, the maximum amplitude is plotted against the response frequency. The difference with the above techniques is that the maxima are not linked to a specific location, but to the global maximum surface response at that frequency. The result of this procedure for the above discussed simulation is plotted in figure 6.10. We clearly see that maxima can be found at the same subharmonic ($f_{exc}/2$) and harmonic ($2f_{exc}$, $3f_{exc}$ and $4f_{exc}$) frequencies as discussed earlier. Also, the harmonics of the subharmonic ($3f_{exc}/2$, $5f_{exc}/2$, $7f_{exc}/2$ and $9f_{exc}/2$) are slightly visible. Localization can be obtained by narrowing down the zone of the surface used in the analysis.

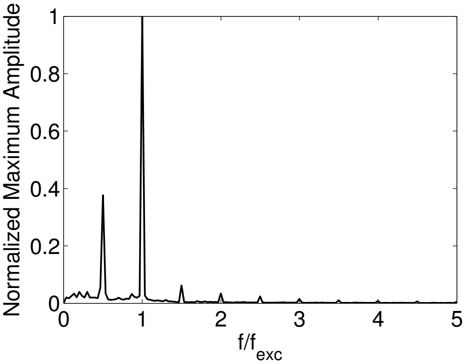

Figure 6.10: Normalized maximum amplitude response for a 40 mm × 40 mm × 2 mm composite sample with a 20 mm diameter delamination centred on the plate and located at a depth of 0.4 mm obtained by Fourier transforming the temporal evolution of the normal displacement in each point at the top surface of the sample and retaining only the maximum amplitude over the entire top surface at each frequency f.

Similar results of the creation of (sub)harmonics appeared in both experiments, as has been reported in several journal papers by the group of Solodov and Busse [12, 13, 27, 30], and simulations, as discussed by Sarens et al. [21], demonstrating that the dynamics of delaminations is well implemented in the finite element model. However, closer consideration of the finite difference simulation results by Sarens et al. [21] reveals that the finite element model turns out the be more stable (e.g. smoother simulated displacement time signals) and more flexible (e.g. possibility to implement more complex shapes and situations).

6.4 Different delamination parameters

In the previous section, the creation of subharmonics and harmonics was illustrated for a delamination at a fixed position (centred on the plate) and depth (0.4 mm) and with a fixed circular shape and a fixed orientation (parallel to the top surface of the composite plate). In this section, we will study the influence of those four parameters on the generated subharmonic and harmonic spectra and on the amplitude patterns at the top surface of the sample. We will show that the shape, position, depth and orientation of a delamination can be determined by studying the amplitude patterns of the excited subharmonic and harmonic frequencies.

6.4.1 Influence of delamination shape

Figures 6.6 and 6.7 revealed that mostly the normal displacement amplitudes above an unstable delamination are affected by the presence of the delamination. The displacement amplitudes elsewhere on the sample surface remain basically unaffected. In addition, the Fourier analysed amplitude patterns in figure 6.9 provide essential supplemental information to determine the shape of a delamination. Indeed, the amplitude patterns for the harmonic and subharmonic frequencies that were generated by the clapping delamination clearly show that the zones with the largest amplitudes follow the shape of the delamination. At subharmonic and harmonic frequencies (f/f_{exc} equal to 0.5, 1.5 and 2), the largest amplitudes can be found within the circle, which indicates the shape of the delamination.

Exploiting the flexibility of the finite element code, numerical simulations have also been performed for other shapes of the delamination. We report here the results for three different samples, each containing a delamination centred on the plate and located at a depth of 0.4 mm. The delamination in the first sample has an elliptical shape with semi-major axis length of 10 mm and semi-minor axis length of 5 mm. The semi-major axis is directed along the y-direction and the semi-minor axis is directed along the x-direction. The second delamination has a square shape with side length equal to 15 mm. The third delamination has a rectangular shape with length 20 mm and width 5 mm. This delamination is oriented along one of the diagonals of the top surface of the sample.

Figure 6.11 displays the normalized maximum amplitude response for the top surface of the three samples. For the elliptical delamination (figure 6.11(a)) and the rectangular delamination (figure 6.11(c)) only harmonics of the excitation frequency f_{exc} (which is still equal to 25250 Hz) are generated, while for the square-shaped delamination (figure 6.11(b)) also a subharmonic $f_{exc}/2$ and harmonics of this subharmonic are generated.

The amplitude patterns for the harmonic and subharmonic frequencies that were generated in each of the three samples by the clapping delamination are shown in figures 6.12, 6.13 and 6.14. The outer edges of the delamination are each time indicated on the figures to compare them with the displacement amplitudes. In all three cases, there is a large correspondence between the shape of the delamination and the positions of (sub)harmonic generation. Moreover, the higher the frequency of the generated (sub)harmonic, the more clearly the shape is distinguished. However, it is clear that some parts of the delaminations are more difficult to detect than other parts. First, there appears to be no contrast at the zones with sharp edges, e.g. the corners of the square-shaped and rectangular delaminations. This is explained by noticing that these regions

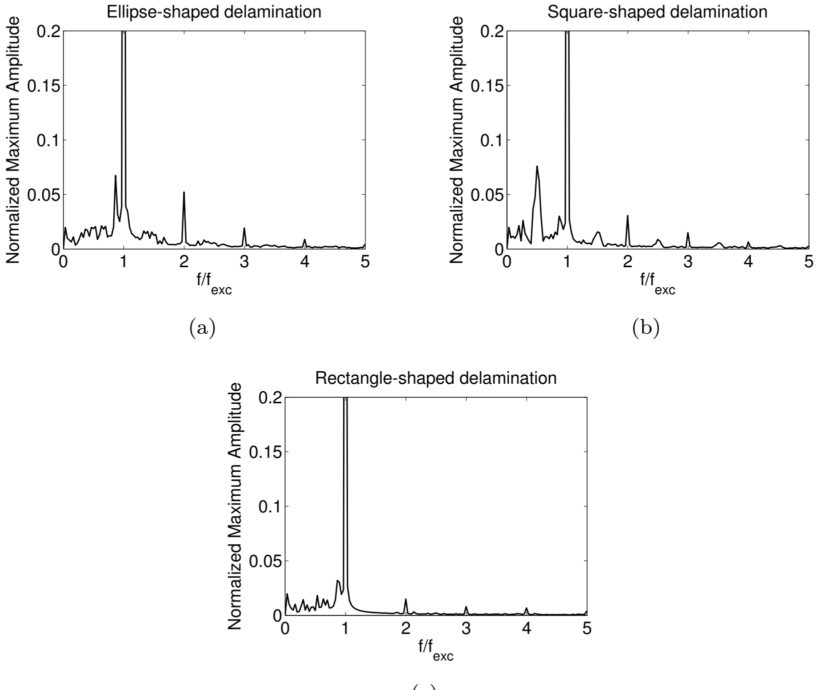

(a)

(b)

(c)

Figure 6.11: Normalized maximum amplitude response for the top surface of three different composite plates, containing each a different delamination. Each delamination is centred on the plate and located at a depth of 0.4 mm. The different shapes are: (a) an ellipse shape with semi-major axis length of 10 mm and semi-minor axis length of 5 mm, (b) a square shape with side length equal to 15 mm and (c) a rectangular shape with length 20 mm and width 5 mm. The rectangular delamination is oriented along one of the diagonals of the top surface of the sample.

are much smaller than the smallest wavelengths inside the sample and thus, they are insufficiently excited to be detected. In addition, the parts of a delamination positioned in a node line of the standing wave pattern that was created by exciting the composite plates with frequency $f_{exc} = 25250$ Hz are difficult to detect, e.g. the top and bottom zones of the elliptical and rectangular delaminations. The created standing wave pattern, with the nodes and anti-nodes, is clearly visible in the amplitude patterns for the fundamental frequency. Since the displacements in the vicinity of a node line are very small or even equal to zero, it is almost impossible to make the delamination clap at these positions.

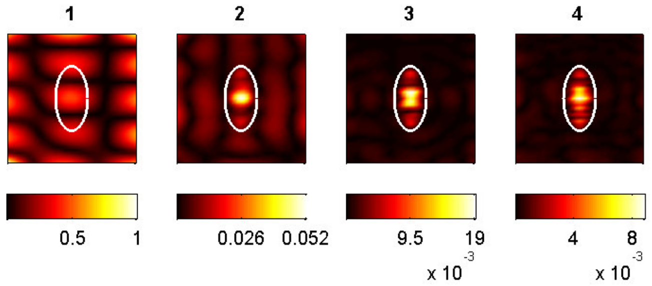

Figure 6.12: Simulated amplitude patterns for the fundamental frequency f_{exc} and the second, third and fourth harmonic of this frequency in a 40 mm × 40 mm × 2 mm composite sample with an elliptical delamination with semi-major axis length of 10 mm and semi-minor axis length of 5 mm. The delamination is centred on the plate and located at a depth of 0.4 mm. The value above each figure represents the ratio f/f_{exc}. The lowest amplitudes are shown in black. The ellipse indicates the position of the delamination.

A solution for the node line problem can be found in using a sweep signal instead of a single excitation frequency. In a sweep signal, the frequency increases or decreases with time. Consequently, different modes of the composite plate are excited. In general, a sweep signal can be represented as follows:

$$S(t) = A \sin\left(2\pi f_s t + \frac{\pi B t^2}{T}\right) \tag{6.10}$$

where A is the amplitude of the signal, f_s is the starting frequency of the sweep signal, B is the bandwidth determining the total range of frequencies present in the sweep signal and T is the duration of the signal. It is obvious that the frequency of the signal increases with time t. In the present simulations, we considered a sweep signal that extends over the $10 - 60$ kHz frequency range, meaning that $f_s = 10$ kHz and $B = 50$ kHz. The duration T of the signal was set equal to 40 periods of a sine wave with frequency equal to the maximum frequency present in the sweep signal. Figure 6.15(a) illustrates the sweep signal used in the simulations. Figure 6.15(b) shows the corresponding frequency spectrum obtained by taking the Fourier transform of the sweep signal. From the frequency spectrum, it can be seen that the lower and higher limits of the frequencies are respectively 10 kHz and 60 kHz.

Until now, we determined the shape of a delamination by looking at the amplitude patterns for the generated (sub)harmonic frequencies. However, when using a sweep signal this is not longer possible. Therefore, another method has to be used in order to determine the shape of a delamination. A

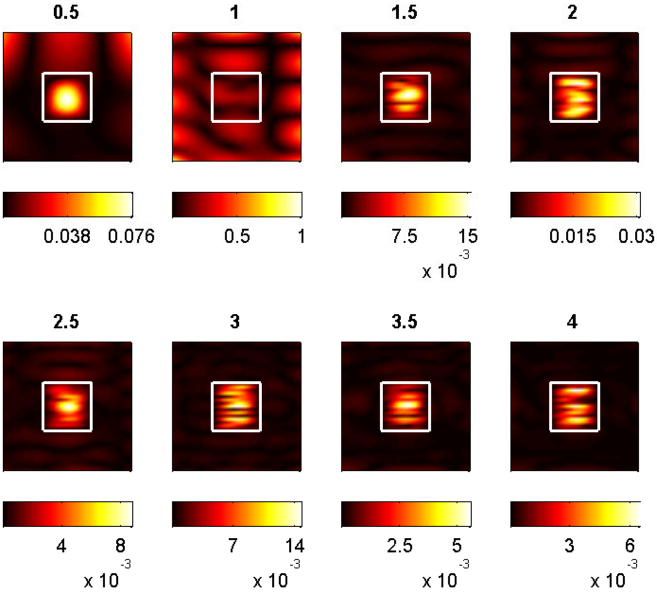

Figure 6.13: Simulated amplitude patterns for the fundamental frequency f_{exc}, the second, third and fourth harmonic of this frequency, the subharmonic frequency $f_{exc}/2$ and the third, fifth and seventh harmonic of this subharmonic frequency in a 40 mm × 40 mm × 2 mm composite sample with a square-shaped delamination with side length equal to 15 mm. The delamination is centred on the plate and located at a depth of 0.4 mm. The value above each figure represents the ratio f/f_{exc}. The lowest amplitudes are shown in black. The square indicates the position of the delamination.

common method used to extract nonlinear features from the elastic response of a sample insonified by an ultrasonic wave is the scaling subtraction method (SSM), first proposed by Scalerandi et al. [23]. The method consists of a simple difference between signals once a reference signal has been defined for the examined sample. In general, a very low amplitude excitation is used as a comparison signal which, linearly rescaled in amplitude, is subtracted from the signal recorded at larger excitation amplitudes to yield the nonlinear signature. Many experimental and numerical studies based on SSM can be found in literature [3–8, 22, 24].

Applying the concept of SSM to our simulations, we first excite the composite sample using the sweep signal (6.10) with a low excitation amplitude A_{low}, and we determine the normal displacements at the top surface of the sample. In this case, the excitation amplitude will be too low to excite the delamination and

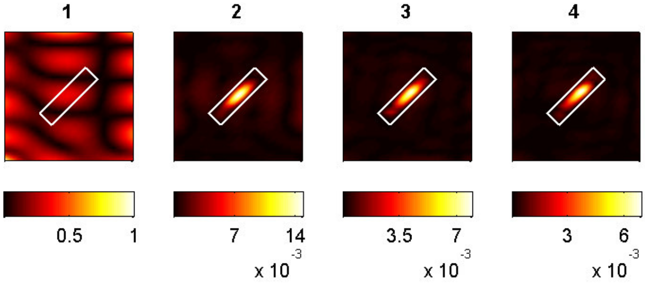

Figure 6.14: Simulated amplitude patterns for the fundamental frequency f_{exc} and the second, third and fourth harmonic of this frequency in a 40 mm × 40 mm × 2 mm composite sample with a rectangular delamination with length 20 mm and width 5 mm. The delamination is centred on the plate, located at a depth of 0.4 mm and oriented along one of the diagonals of the top surface of the sample. The value above each figure represents the ratio f/f_{exc}. The lowest amplitudes are shown in black. The rectangle indicates the position of the delamination.

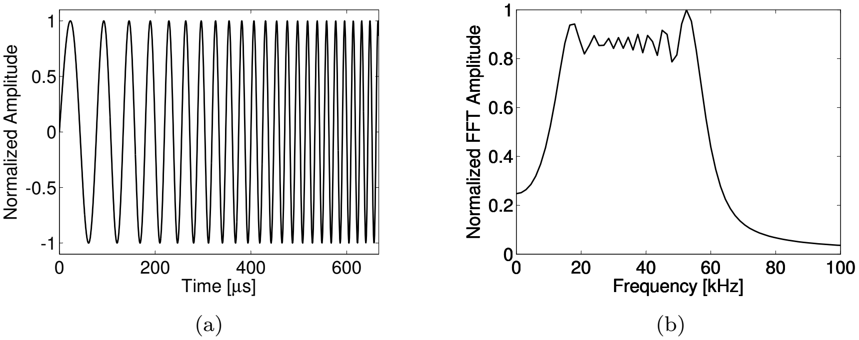

(a) (b)

Figure 6.15: Temporal evolution (a) and Fourier transform (b) of the sweep signal (6.10) used in the finite element simulations. The frequency spectrum clearly shows the frequency range of the sweep signal.

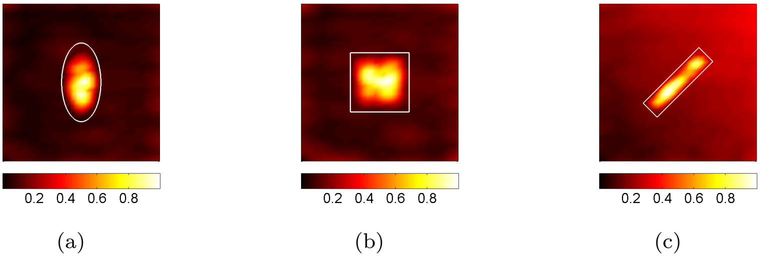

Figure 6.16: Maximum amplitude plots of the scaling subtracted normal displacements at the top surface of three composite samples with dimensions 40 mm × 40 mm × 2 mm and with each a different delamination centred on the plate and located at a depth of 0.4 mm. The different delamination shapes are: (a) an elliptical delamination with semi-major axis length of 10 mm and semi-minor axis length of 5 mm, (b) a square-shaped delamination with side length equal to 15 mm and (c) a rectangular delamination with length 20 mm and width 5 mm. The rectangular delamination is oriented along one of the diagonals of the top surface of the sample. The colour scale in each figure is normalized according to its maximum value.

the contact will stay closed. Consequently, the delamination has no influence on the determined normal displacements and these displacements can thus be used as a 'linear' reference signal. Then, the sample is excited using the same sweep signal, but now with a larger excitation amplitude A_{high} equal to nA_{low}. Again, the normal displacements are determined at the top surface of the sample. In this case, the excitation amplitude is high enough to excite the delamination and this will cause a nonlinear contribution to the normal displacements. If we then subtract the reference signal, multiplied by a factor n, from the normal displacements of the second simulation, the nonlinear contributions at the top surface of the sample are extracted from the signals. Based on the results for single frequency excitation of delaminations, we obviously expect these nonlinear contributions to be mainly localized above the delamination.

Figure 6.16 shows maximum amplitude plots of the subtracted signals at the top surface of the three composite samples with respectively an elliptical, a square-shaped and a rectangular delamination. The shape of the delamination is indicated in each plot. We clearly see that the maximum values of the subtracted signals follow the shape of the delaminations. As several modes were excited by the use of a sweep signal, the maximum amplitudes are also more globally distributed over the total delamination and we have no longer a problem with node lines, as was the case in figures 6.12, 6.13 and 6.14.

6.4.2 Influence of delamination position

In the previous subsection, we studied the amplitude patterns of the excited subharmonic and harmonic frequencies to determine the shape of a delamination centred on a composite plate and located at a depth of 0.4 mm. Apart from the shape of a delamination, it is also interesting to get an indication of the position of a delamination. Since the largest amplitudes can be found above the delamination position, the amplitude patterns can also be used to determine the position of the delamination, even if the delamination is not centred on the plate. To illustrate this, we discuss the results of simulations of four composite samples each containing a circular delamination with radius 5 mm, located at a depth of 0.4 mm. The (x, y)-coordinates of the centre of the delaminations are respectively $(0, 0), (-7, -4), (7, 4)$ and $(10, 6)$ mm. All samples were excited using a single excitation frequency $f_{exc} = 25250$ Hz.

Figure 6.17 displays the normalized maximum amplitude response at the top surface of the four samples. In the top right corner of every figure, the position of the circular delamination is illustrated. For the delamination centred on the plate we clearly see the existence of a subharmonic at $f_{exc}/2$, harmonics of this subharmonic and harmonics of the excitation frequency. In the other samples, only harmonics of the excitation frequency are generated. If we now just focus on the harmonics of the excitation frequency we see that these harmonics are most efficiently excited in the first sample, while the excitation of the harmonics is least efficient in the fourth sample. The results for the second and third sample look quite similar.

The simulated amplitude patterns for the fundamental frequency and the second, third and fourth harmonic of this frequency for the four samples are depicted in figure 6.18. In each graph the position of the delamination is indicated by the circle. The colour scales are normalized according to the maximum value of the amplitudes in all four samples at a certain frequency. In all four cases, the position of the delamination is clearly detected in the amplitude patterns for the harmonic frequencies. However, the detection is most clear in the first sample. This can be easily explained by looking at the position of the delaminations with respect to the standing wave pattern in the samples, which is clearly visible in the amplitude patterns for the fundamental frequency. In the first sample, the delamination is positioned in an anti-node of the standing wave pattern. Since the displacement amplitudes are maximal at that position, the delamination is easily opened and starts to clap, resulting in high amplitudes above the delamination in the amplitude patterns for harmonic frequencies. In the second and third sample, part of the delaminations is positioned in a node line while the other part is positioned close to an anti-node, making it more difficult to open the delamination and therefore, smaller amplitudes in

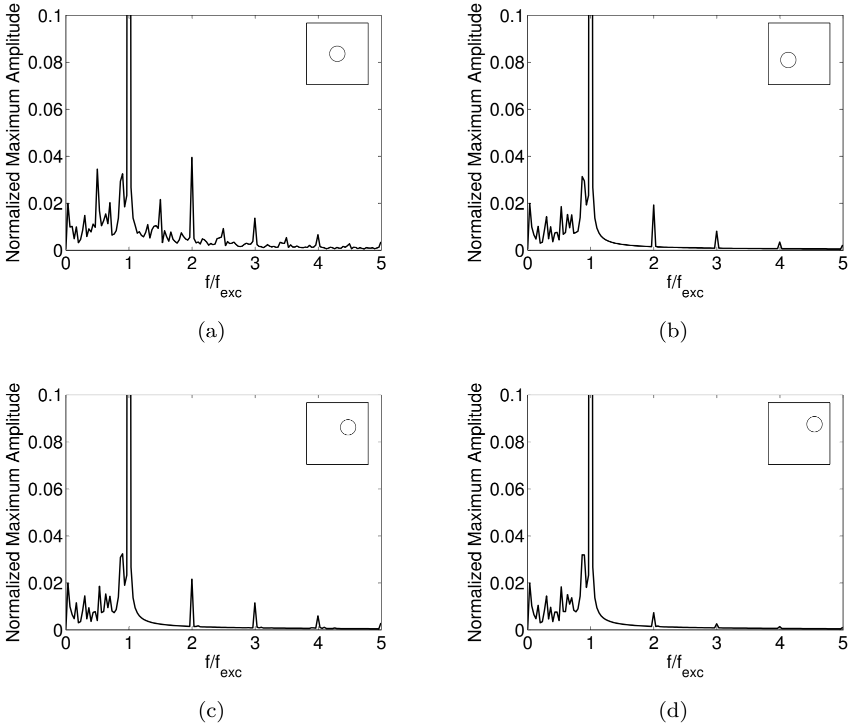

(a) (b)

(c) (d)

Figure 6.17: Normalized maximum amplitude response for the top surface of four different composite plates, containing each a small circular delamination with radius 5 mm. In each sample the delamination is located at a depth of 0.4 mm, but the (x, y)-coordinates of the centre of the delaminations are different: (a) centre coordinates $(0, 0)$ mm, (b) centre coordinates $(-7, -4)$ mm, (c) centre coordinates $(7, 4)$ mm and (d) centre coordinates $(10, 6)$ mm. The position of the delamination within the samples is illustrated in the top right corner of every figure.

the amplitude patterns are found compared to the first sample. Finally, in the fourth sample, the delamination is fully positioned in a node line of the standing wave pattern. Because of the very small displacements there, the delamination is less efficiently excited compared to the other samples, resulting in very small amplitudes in the amplitude patterns.

To ensure the detection of every possible delamination, even those positioned at a node line, it would be better to again use the sweep signal (6.10) in combination with SSM. In figure 6.19, the maximum amplitude plots of the scaling subtracted normal displacements at the top surface of the four composite samples are shown. The position of the delaminations is each time indicated by the white circle. The colour scale is normalized according to the maximum value of the subtracted signals in the four samples. Using SSM, we see that every delamination is detected almost equally well. This in contrast to the detection of the delaminations using the amplitude patterns for the generated (sub)harmonic frequencies (figure 6.18).

6.4.3 Influence of delamination depth

Obviously the nonlinearly generated subharmonic and harmonic spectra will change with delamination depth. In the following, we discuss and compare the results of simulations of a composite plate with a circular delamination with radius 10 mm close to the upper surface of the plate (depth 0.2 mm or 0.3 mm), or close to the centre of the plate (depth 0.7 mm, 0.8 mm or 1.0 mm).

The left hand side of figure 6.20 displays the normalized maximum amplitude response for delaminations close to the top surface of the sample. On the right hand side we have plotted the simulated normal displacements at the centre of the delamination. The two figures in the top row represent the results for a delamination at a depth of 0.2 mm. In the bottom row, the results are displayed for a 0.3 mm deep delamination. For the results at 0.2 mm depth, the normalized maximum amplitude plot clearly shows the existence of a subharmonic at approximately $f_{exc}/5$. This subharmonic behaviour is also recognizable in the normal displacement plot at the right, where we observe that the delamination most of the time remains open during five excitation cycles, resulting in a subharmonic vibration mode of the layer above the delamination. A similar result is found for a delamination at 0.3 mm (bottom figures of figure 6.20). Here, a significant subharmonic at $f_{exc}/3$ is observed. In this case, both sides of the delamination clap or impact each other every three periods. In addition, several harmonics of that subharmonic can be distinguished. Earlier we already showed that a subharmonic $f_{exc}/2$ (and its harmonics) was generated in the case of a delamination at a depth of 0.4 mm (see figure 6.10). In all cases,

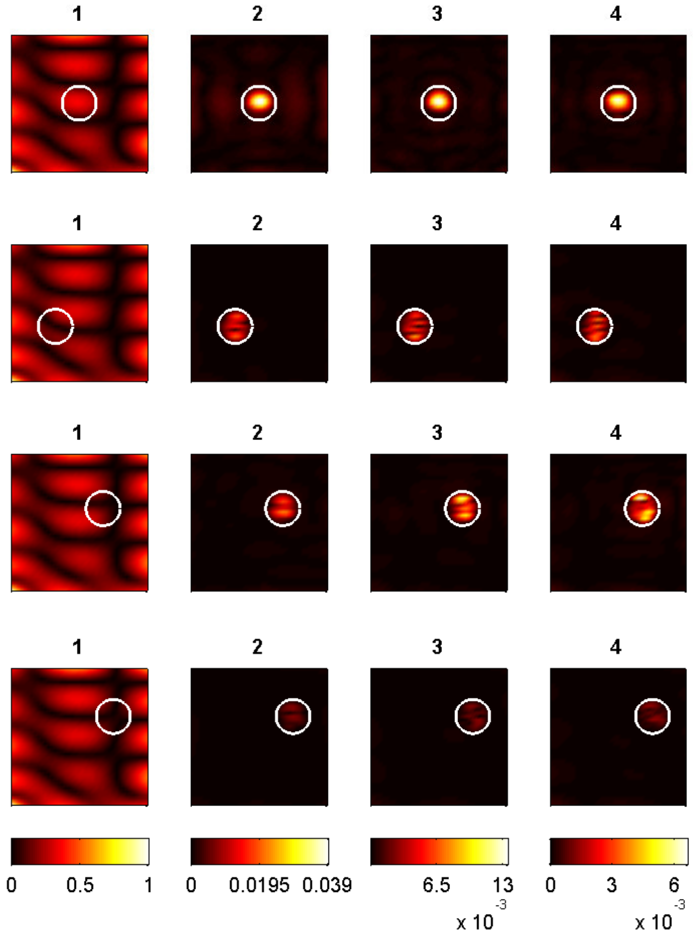

Figure 6.18: Simulated amplitude patterns for the fundamental frequency f_{exc} and the second, third and fourth harmonic of this frequency in four 40 mm × 40 mm × 2 mm composite samples with a small circular delamination with radius 5 mm. In each sample the delamination is located at a depth of 0.4 mm and the (x, y)-coordinates of the centre of the delaminations are respectively $(0, 0), (-7, -4), (7, 4)$ and $(10, 6)$ mm. The value above each figure represents the ratio f/f_{exc}. The lowest amplitudes are shown in black. The circles indicate the position of the delaminations. The same colour scale is used in all four samples at each frequency.

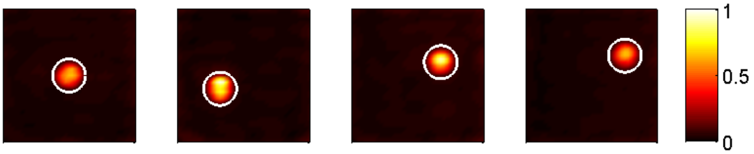

Figure 6.19: Maximum amplitude plots of the scaling subtracted normal displacements at the top surface of four composite samples with dimensions 40 mm × 40 mm × 2 mm and with each a small circular delamination with radius 5 mm. In each sample the delamination is located at a depth of 0.4 mm and the (x, y)-coordinates of the centre of the delaminations are respectively $(0, 0), (-7, -4), (7, 4)$ and $(10, 6)$ mm. The position of the delaminations is indicated by the circles. The colour scale is normalized according to the maximum value of the subtracted signals in the four samples. High values are shown in white, low values are shown in black.

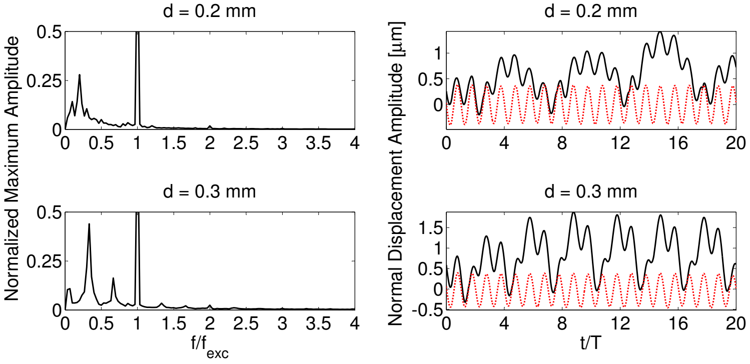

Figure 6.20: LEFT: Normalized maximum amplitude response for 2 mm thick composite samples with a delamination at different depths close to the top surface (d = 0.2, 0.3 mm), showing the existence of subharmonic behaviour in the surface response. RIGHT: Simulated normal displacement amplitudes at the centre of the delamination. The solid line represents the displacements of a point just above the delamination, the dotted line represents the displacements of a point just below the delamination.

the energy transfer to the harmonics of the excitation frequency (at $2f_{exc}$ and $3f_{exc}$) is noticeable but small.

Similar to the results discussed by Sarens et al. [21], it appears that the frequency ratio of the dominating subharmonic becomes smaller for delaminations located closer to the top surface of the sample. This can be easily explained as follows.

At instances when both interfaces of the delamination hit each other, the energy of the impact is utilized to open the delamination. The delamination opens again immediately. If the layer above the delamination is very thin, the energy suffices to open the delamination during multiple excitation cycles. The thicker the layer, and thus the deeper the delamination, the harder it is to open the delamination for a longer period. This "trampoline" effect evidently results in subharmonics with a higher frequency value. For delaminations that are located deep inside the sample, we expect that subharmonics will not longer be created. This is indeed shown in figure 6.21. On the left hand side, the normalized maximum amplitude plots are displayed for 2 mm thick composite samples with a delamination close to the centre of the plate, at depths $d = 0.7$, 0.8, and 1.0 mm (centre of the sample). In all three cases, there are no subharmonics to be discerned. For delamination depths 0.7 mm and 0.8 mm an indication of harmonics of the excitation frequency still exists. In the normal displacement responses (at the right hand side of figure 6.21) we notice that the typical nonlinear clapping effect, with very short times of impact/contact, has disappeared. Within each excitation period, the top and bottom interfaces of the delamination move along with each other for an extended period of time. During that time interval, the delamination remains locally closed. The impact at the time of closure is not high enough to generate a trampoline effect. In this particular example, the stresses and strains are equal to zero at $z = 1$ mm, therefore, if the delamination is exactly at the centre of the plate, the local nonlinear behaviour disappears entirely. Both interfaces are in contact during the entire simulation. As a consequence, no subharmonics and no harmonics are being generated.

In figure 6.22 the normalized maximum amplitude plots for different delamination depths (some of them were already separately shown in figure 6.10, and in the left hand side graphs of figures 6.20 and 6.21) are all plotted in a colour-coded "intensity" graph. High values are shown in white, low values are shown in black. The colour at the fundamental frequency is saturated to ensure good visibility of the generated subharmonics and harmonics. As discussed above, subharmonics (and harmonics of the generated subharmonic) are only generated if the delamination is close to the top surface of the composite sample. The lower the frequency value of the generated subharmonic, the smaller the delamination depth. Harmonics of the excitation frequency are generated at almost every delamination depth, however the closer the delamination is to the centre of the composite plate, the harder it becomes to generate harmonics. For a delamination exactly at the centre of the plate, no harmonics are being generated.

The above results imply that the nonlinearity contributions (harmonics and subharmonics of the excitation frequency) are less strong if the delamination is

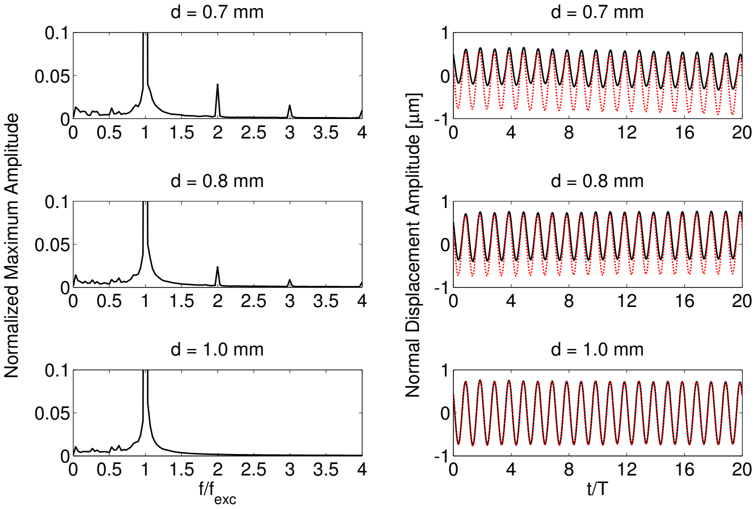

Figure 6.21: LEFT: Normalized maximum amplitude response for 2 mm thick composite samples with a delamination at different depths close to the centre of the sample ($d = 0.7$, 0.8, 1.0 mm). In all three cases, no subharmonics can be discerned. If the delamination is located in the centre of the plate, no harmonics are generated either. RIGHT: Simulated normal displacement amplitudes at the centre of the delamination. The solid line represents the displacements of a point just above the delamination, the dotted line represents the displacements of a point just below the delamination.

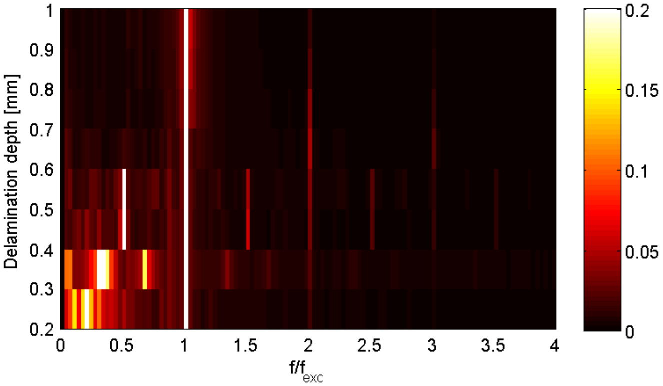

Figure 6.22: Normalized maximum amplitude response for 2 mm thick composite samples with a delamination at different depths. Low responses are shown in black, high responses are shown in white. The colour at the fundamental frequency is saturated to ensure good visibility of all generated harmonics and subharmonics.

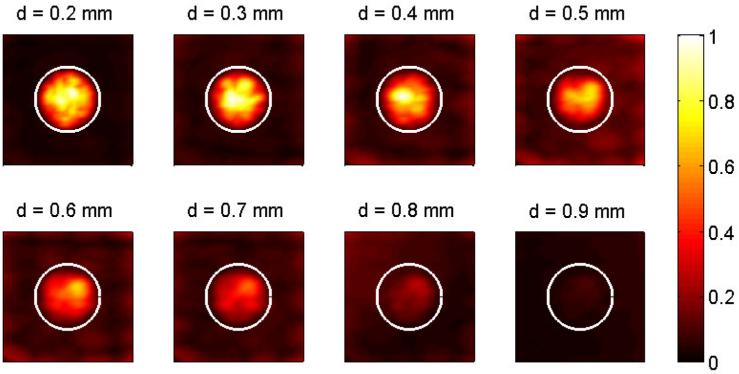

Figure 6.23: Maximum amplitude plots of the scaling subtracted normal displacements at the top surface of eight different composite samples with a circular delamination of radius 10 mm at different depths. The dimensions of the samples are 40 mm × 40 mm × 2 mm. The different delamination depths are each time indicated on top of each graph. The position of the delaminations is indicated by the circles. The colour scale is normalized according to the maximum value of the subtracted signals in all samples. High values are shown in white, low values are shown in black.

located deeper into the sample. Therefore, we expect delaminations close to the centre of the plate to be more difficult to detect using SSM. Figure 6.23 visualizes the maximum amplitude plots of the scaling subtracted normal displacements at the top surface of eight different composite samples with different delamination depths. The results were obtained using the sweep signal (6.10). The colour scale in the figures is normalized according to the maximum value of the subtracted signals in all samples. As expected, the amplitudes of the subtracted signals decrease with the delamination depth. The highest amplitudes (white colour) are found above the delamination at depth 0.2 mm, while the lowest values (black colour) are found above the 0.9 mm deep delamination. In figure 6.24, the same maximum amplitude plots are displayed for four of the eight samples, using, in this case, the full colour map in each figure (i.e. white colour represents the maximum value within each individual figure) instead of the normalized colour map used in figure 6.23. This allows to better appreciate the quality and contrast of the imaging of the delamination we might obtain from a single experiment. Note that even though the effects of (sub)harmonic generation become smaller with increasing delamination depth, the quality of the imaging of the delamination is still good enough to detect the delamination, even at large depths.

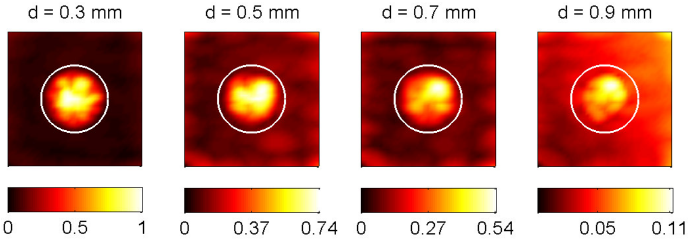

Figure 6.24: Maximum amplitude plots of the scaling subtracted normal displacements at the top surface of four different composite samples with a circular delamination of radius 10 mm at different depths. The dimensions of the samples are 40 mm × 40 mm × 2 mm. The different delamination depths are each time indicated on top of each graph. The position of the delaminations is indicated by the circles. In each figure, the colour scale goes from zero to its maximum value.

6.4.4 Influence of delamination orientation

It was shown in section 6.4.1 that the shape of a delamination can be determined by looking at the amplitude patterns. In addition, we also concluded from section 6.4.3 that the existence and level of subharmonics can be linked to the depth of the delamination. In this section, we investigate the influence of the inclination of a delamination on the amplitude patterns of the generated subharmonics.

For this part of the study, results from two different composite plates will be compared. In both plates, a circular delamination with radius 10 mm is located at a nominal depth of 0.4 mm. However, the delamination in the first plate is rotated by 1 degree about the in-plane y-axis, such that the left half of the delamination (smaller x-values) is closer to the top surface than the right half. In the second sample, the circular delamination is also rotated by 1 degree, but now in the opposite direction. In this sample, the right half of the delamination is the closest to the top surface of the sample. A schematic of the cross-section of both samples is shown in figure 6.25.

The normalized maximum amplitude responses for the top and bottom surface of both plates are visualized in figure 6.25. Since the maximum amplitude response is a global measure of the nonlinear spectrum over the entire surface, the results for a -1 or $+1$ degree inclination are very similar. Small differences are only due to the fact that the source was positioned at the left lower corner on the top surface. Evidences of a subharmonic at $f_{exc}/2$, higher harmonics at $2f_{exc}$ and $3f_{exc}$, and harmonics of the subharmonic at $3f_{exc}/2$ and $5f_{exc}/2$ are clearly visible in both samples. The observed peaks at the bottom surface

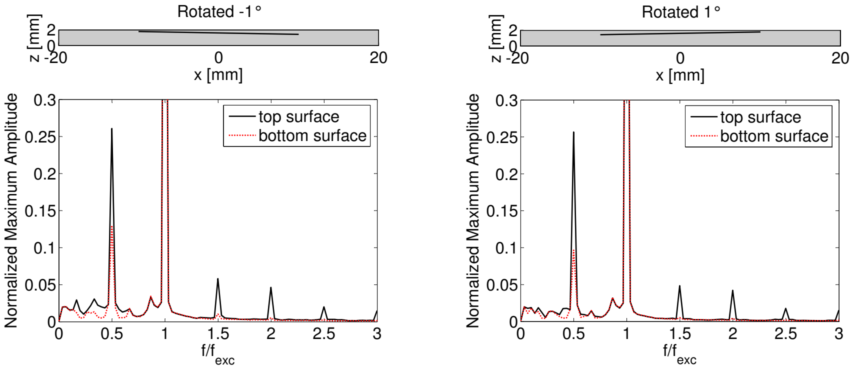

(a) (b)

Figure 6.25: Normalized maximum amplitude response for the top (solid line) and bottom (dotted line) surface of two different composite plates, containing a circular delamination centred on the plate and at a nominal depth of 0.4 mm. (a) The delamination was rotated by -1° about the in-plane y-axis, (b) the delamination was rotated by 1° around the y-axis. In both plates, a subharmonic $f_{exc}/2$, harmonics of this subharmonic and harmonics of the excitation frequency are generated.

(dotted lines) are less obvious suggesting that the delamination is positioned in the upper half of both plates.

Figure 6.26 visualizes the spatial amplitude response patterns at the subharmonic frequency $f_{exc}/2$, the third harmonic $3f_{exc}/2$ of this subharmonic and the second harmonic $2f_{exc}$ of the excitation frequency, calculated for both the top (figure 6.26(a)) and bottom (figure 6.26(b)) surface of the samples. The value above each figure represents the ratio f/f_{exc}. The top (bottom) figures represent the results for the plate in which the left (right) half of the delamination is closest to the upper surface of the plate. The delaminations are clearly visible in the amplitude patterns at the top surface, however, they cannot be detected in the amplitude patterns at the bottom surface of both samples. Consequently, these pictures confirm that the delamination in both samples must be located in the upper half of the plates. The peaks observed in the normalized maximal amplitude response for the bottom surface of both samples (figure 6.25) can be attributed to the fact that subharmonics and harmonics are not fully localized at the position of the clapping delamination, but also radiate energy in the rest of the sample (see 'non-zero' amplitudes outside the ellipses in figure 6.26). However, the observed displacement amplitudes at subharmonic and harmonic frequencies at the delamination position are much higher than the amplitudes observed elsewhere in the samples.

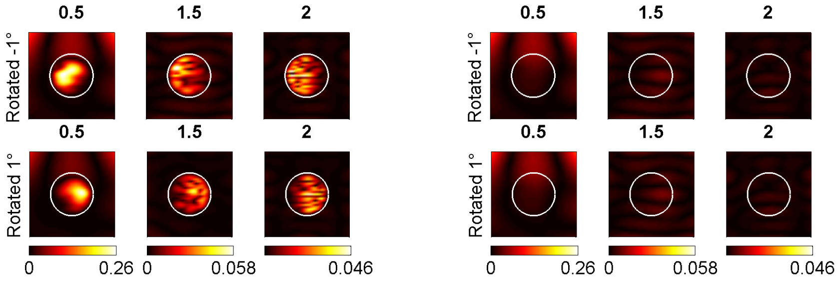

(a) (b)

Figure 6.26: Simulated amplitude patterns for the subharmonic frequency $f_{exc}/2$, the harmonic of the subharmonic $3f_{exc}/2$ and the second harmonic $2f_{exc}$ in two different composite samples containing a circular delamination at a depth of 0.4 mm. The results for a delamination inclined by $-1°$ about the in-plane y-axis are plotted in the six top figures. The results for a delamination inclined by $1°$ around the y-axis are plotted in the bottom figures. (a) Amplitude patterns obtained by Fourier transforming the temporal evolution of the normal displacement in each point at the top surface of the plates, and displaying the results at $f_{exc}/2$, $3f_{exc}/2$ and $2f_{exc}$. (b) Amplitude patterns obtained by using the normal displacements at the bottom surface of the plates. The value above each figure represents the ratio f/f_{exc}. The ellipse indicates the position of the inclined delamination. Low amplitudes are shown in black.

In both samples, the results at the top surface of the samples show large amplitudes above the delamination. In contrast to the results for a non-inclined delamination where the amplitudes are quasi-uniformly distributed over the delamination zone, we now observe that, in each case, the largest amplitudes are dominantly located in one particular half of the ellipse (which indicates the position of the inclined delamination). The reason for this is obviously found in the fact that subharmonics disappear gradually when the delamination is located deeper and deeper into the sample. In general, if the largest amplitude responses are found above one half of the delamination, the subharmonic must be generated most efficiently in that half and therefore, that part of the delamination must be closer to the top surface of the sample. For the first sample, the data tells us that the left half should be closer to the top surface, while for the second sample, the right half should be closer to the top surface. This is indeed in correspondence with the samples described earlier.

The use of a sweep signal in combination with SSM gives similar results. Figure 6.27 shows the maximum amplitude plots of the scaling subtracted

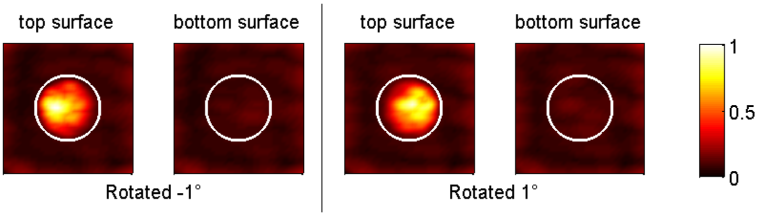

Figure 6.27: Maximum amplitude plots of the scaling subtracted normal displacements at the top and bottom surface of two different composite samples with an inclined circular delamination of radius 10 mm. The dimensions of the samples are 40 mm × 40 mm × 2 mm. In the first sample, the delamination was inclined by -1°. In the second sample, the delamination was inclined by 1°. The ellipses indicate the position of the inclined delaminations. The colour scales are normalized according to the maximum value of the subtracted signals in the four figures. High values are shown in white, low values are shown in black.

normal displacements at the top and bottom surface of the two samples. Large amplitudes above the delamination are only found in the results at the top surface and are dominantly located in one particular half of the ellipse indicating the position of the inclined delamination.

We have performed a similar analysis on a composite plate with a circular delamination located in the centre of the plate and rotated by -4 degrees about the in-plane y-axis, such that the left half of the delamination is closer to the top surface of the plate and the right half of the delamination is closer to the bottom surface of the plate. Figure 6.28 shows an illustration of a cross-section of this sample. The normalized maximum amplitude response in figure 6.28 shows that the level of subharmonics generated by the delamination is weak. This could be expected, as the delamination is located near the centre of the plate, where the trampoline effect responsible for the observation of subharmonics is not likely to occur. For this sample, we investigate the spatial amplitude patterns of the second harmonic $2f_{exc}$. The simulated amplitude patterns are shown for both the top and bottom surface of the sample in figure 6.29. In the previous example (figure 6.26) we attributed the large difference in magnitude of the spatial amplitude patterns at the top and bottom surface of the samples to the fact that the delamination was located in the upper half of the composite plate. Here, the centre of the delamination is located at the centre of the plate and therefore, the overall magnitude of the amplitudes at the top and bottom surface are expected to be equal. Moreover, since the delamination was rotated by -4 degrees, such that the left half was closer to the top surface and the right half closer to the bottom surface, we expect the second harmonic at the top surface to be most efficiently generated above the left hand side of the

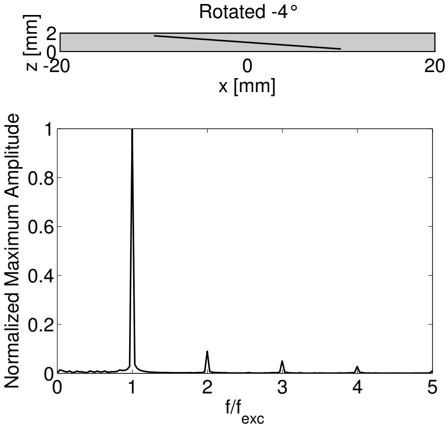

Figure 6.28: Normalized maximum amplitude response for the top surface of a composite plate with a delamination located in the centre of the plate. The delamination was rotated by $-4°$ around the y-axis.

delamination while the second harmonic at the bottom surface is expected to be predominantly generated under the right hand side of the delamination. These expectations are exactly confirmed in figure 6.29. At the top surface, the highest amplitudes are found in the left part of the ellipse, which indicates the position of the inclined delamination. At the bottom surface, the highest amplitudes are found in the right hand side of the ellipse. The clapping of the left and right part of the delamination also slightly affects the behaviour of the middle part of the delamination. Consequently, there is also an indication of the generation of a second harmonic in the middle part of the delamination. This is in contrast to the results for a non-inclined delamination, where no (sub)harmonics are generated over the entire length of the delamination if it is positioned in the centre of the plate.

6.5 Multiple delaminations in a composite plate

In the previous section we studied the possibility to determine the shape, position, depth and orientation of a single delamination in a composite plate. Applying the same technique, it should also be possible to detect multiple delaminations with one numerical experiment. To validate this, we investigate the response of a sample containing two circular delaminations with diameter 5 mm. In a first setup both delaminations are located at a depth of 0.4 mm.

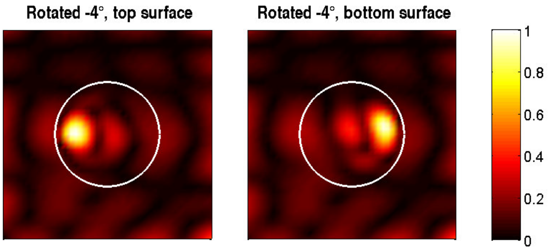

Figure 6.29: Simulated amplitude patterns for the second harmonic $2f_{exc}$ in a 2 mm thick composite plate with a delamination in the centre (nominal depth=1 mm). The delamination was rotated by $-4°$ about the in-plane y-axis. The amplitude pattern on the left is obtained by Fourier transforming the temporal evolution of the normal displacement in each point at the top surface of the plate, and displaying the results at $2f_{exc}$. The pattern on the right is obtained by using the normal displacements at the bottom surface of the plate. The ellipse indicates the position of the inclined delamination. The colour scales are normalized according to the maximum amplitude measured at the second harmonic. Low amplitudes are shown in black.

The first delamination is centred on the plate, while the centre of the second delamination has (x, y)-coordinates $(10, 6)$ mm.

The normalized maximum amplitude response for the top surface of the sample is displayed in figure 6.30. The position of the two delaminations is illustrated in the top right corner of the figure. We clearly observe the generation of a subharmonic at $f_{exc}/2$ and harmonics of the excitation frequency and of the subharmonic. The amplitude patterns for the generated harmonic and subharmonic frequencies are shown in figure 6.31. Clearly, both delaminations can be detected. However, the amplitudes found above the delamination centred on the plate are much higher than the ones found above the second delamination. This is evidently due to the fact that one delamination is positioned in an anti-node of the generated standing wave pattern while the other one is positioned in a node and thus less efficiently excited than the first one. Moreover, the second delamination is only detected in the amplitude patterns for the harmonics of the excitation frequency and not in the amplitude patterns for the subharmonic frequency and its harmonics. An explanation can be found in the normalized maximum amplitude response for the top surface of composite samples, containing only one of these two delaminations. These normalized maximum amplitude responses were already displayed in figure 6.17(a) for the delamination centred on the plate and in figure 6.17(d) for the second delamination. From these figures, it is clear that clapping of the first delamination gives rise to the generation of a subharmonic at frequency $f_{exc}/2$ and harmonics of the excitation frequency and the subharmonic frequency,

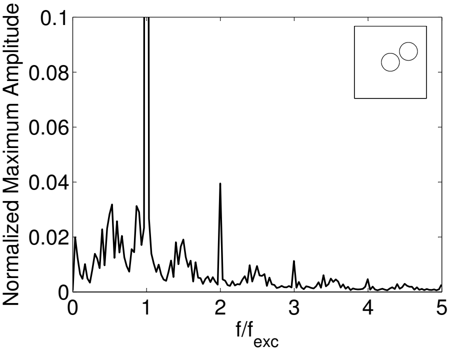

Figure 6.30: Normalized maximum amplitude response for the top surface of a composite plate with two circular delaminations with radius 5 mm at a depth of 0.4 mm. The first delamination is centred on the plate, the centre of the second one has (x, y)-coordinates $(10, 6)$ mm. The position of both delaminations within the sample is illustrated in the top right corner of the figure.

while activation of the second delamination only leads to the generation of harmonics of the excitation frequency. For a given excitation amplitude the energy at the central delamination suffices to initiate a trampoline effect, while the energy at the second delamination remains below the subharmonic activation threshold. When both delaminations are present in one and the same sample, harmonics of the excitation frequency, but also the subharmonic frequency $f_{exc}/2$ and its harmonics will be generated in a global sense. However, evidences of this subharmonic frequency and its harmonics will only be found above the delamination centred on the plate, while evidences of the harmonics of the excitation frequency will be found above both delaminations. Therefore, to detect all possible defects it is necessary to study the amplitude patterns for every generated subharmonic or harmonic frequency.

In conclusion, the study of the detection of multiple defects thus reveals two major problems. First, not all delaminations are equally well detected. Delaminations in a node line of the created standing wave pattern are much more difficult to detect than delaminations elsewhere. Second, when investigating the amplitude patterns of the excited subharmonic and harmonic frequencies, it is essential that multiple amplitude patterns are studied in order to detect all possible defects. If we want all delaminations to be detected equally well and represent the results in just one graph, we can use a sweep excitation and study the scaling subtracted normal displacements at the top surface of the sample as we did in the previous sections. The maximum amplitude plot of the scaling subtracted normal displacements at the top surface of the composite sample

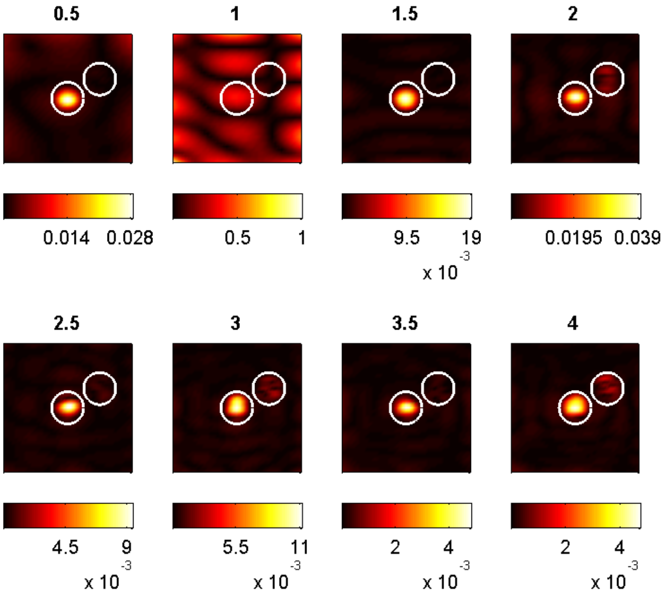

Figure 6.31: Simulated amplitude patterns for the fundamental frequency f_{exc}, second, third and fourth harmonic of this frequency, the subharmonic frequency $f_{exc}/2$ and the third, fifth and seventh harmonic of this subharmonic frequency in a 2 mm thick composite plate with two circular delaminations with radius 5 mm at a depth of 0.4 mm. The first delamination is centred on the plate, while the centre of the second one has (x, y)-coordinates $(10, 6)$ mm. The circles indicate the position of the delaminations. Low amplitudes are shown in black. The value above each figure represents the ratio f/f_{exc}.

containing two circular delaminations obtained by using sweep signal (6.10) is displayed in figure 6.32. It is obvious that, using a sweep signal in combination with SSM, both delaminations are equally well detected.

In figure 6.32, the maximum amplitudes of the scaling subtracted normal displacements above the two delaminations have approximately the same values because of the fact that both delaminations are located at the same depth. In section 6.4.3 we showed that the deeper the delamination is located into the sample, the more difficult it is to detect the delamination using a sweep excitation in combination with SSM (see figure 6.23). Therefore, if two delaminations are located at different delamination depths inside the same composite plate, we expect the amplitudes of the scaling subtracted normal displacements at the top surface of the sample above the delamination closest to the top surface to be higher than the scaling subtracted normal displacements at the top surface

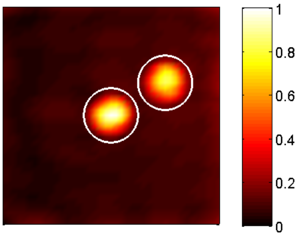

Figure 6.32: Maximum amplitude plot of the scaling subtracted normal displacements at the top surface of a composite sample with two circular delaminations of radius 5 mm and located at a depth of 0.4 mm. The dimensions of the sample are 40 mm × 40 mm × 2 mm. The first delamination is centred on the plate and the centre of the second delamination has (x, y)-coordinates $(10, 6)$ mm. The circles indicate the position of both delaminations. High values are shown in white, low values are shown in black.

above the deeper delamination. This is indeed observed in figure 6.33 where the maximum amplitude plots of the scaling subtracted normal displacements at the top surface of two composite plates, each containing two circular delaminations of radius 5 mm, are displayed. The (x, y)-coordinates of the centre of the delaminations are the same as in the previous case, but the two delaminations are now at different depths. The delamination centred on the plate is in both samples located at a depth of 0.4 mm, while the off-centre delamination is located a little bit deeper, i.e. at a depth of 0.6 mm in the first plate and 0.8 mm in the second plate. We clearly see that in both plates the amplitudes above the second delamination are much smaller than the amplitudes above the central delamination. Moreover, the deeper the second delamination, the smaller the observed amplitudes. Consequently, by using a sweep excitation in combination with SSM we can get an idea of the depths of the various delaminations in a composite sample relative to each other.

Finally, a composite plate with two overlapping circular delaminations at different depth is analysed using a sweep excitation in combination with SSM. The plate has the same dimensions as before and contains two circular delaminations of radius 5 mm. The first delamination is centred on the plate and located at a depth of 0.4 mm, the second delamination is at a depth of 0.8 mm and the (x, y)-coordinates of its centre are $(5, 3)$ mm. The maximum amplitude plot of the scaling subtracted normal displacements at the top surface of the plate is displayed in figure 6.34. High amplitudes are found in a zone bordered by the two circles indicating the position of the delaminations. Since the amplitudes in the left part of this zone are higher than the ones in the right

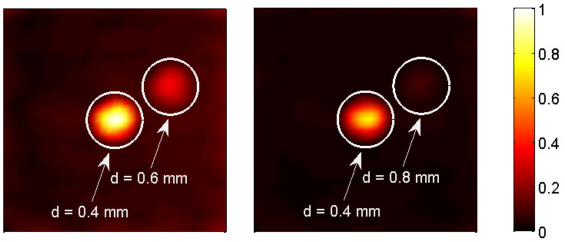

Figure 6.33: Maximum amplitude plots of the scaling subtracted normal displacements at the top surface of two composite samples with two circular delaminations of radius 5 mm. The dimensions of the samples are 40 mm × 40 mm × 2 mm. The first delamination is centred on the plate and the centre of the second delamination has (x, y)-coordinates $(10, 6)$ mm. The delamination centred on the plate is at a depth of 0.4 mm, while the off-centre delamination is at a depth of 0.6 mm in the left figure and 0.8 mm in the right figure. The circles indicate the position of both delaminations. High values are shown in white, low values are shown in black.

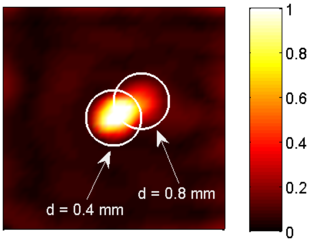

Figure 6.34: Maximum amplitude plot of the scaling subtracted normal displacements at the top surface of a composite sample with two overlapping circular delaminations of radius 5 mm. The dimensions of the sample are 40 mm × 40 mm × 2 mm. The first delamination is centred on the plate and the centre of the second delamination has (x, y)-coordinates $(5, 3)$ mm. The delamination centred on the plate is at a depth of 0.4 mm, while the second delamination is at a depth of 0.8 mm. The circles indicate the position of both delaminations. High values are shown in white, low values are shown in black.

part, we can infer that the plate contains two independent delaminations with the left one located closest to the top surface (assuming both delaminations have the same 'nonlinear' parameters).

6.6 Surface breaking cracks

Apart from the investigation of closed delaminations, it is also possible to simulate the nonlinear effects of a surface breaking crack on the wave propagation using the above described model. In this section, we will illustrate the generation of harmonics in an aluminium bar containing such a crack and we will show that these harmonics are being radiated into the surrounding air.

6.6.1 Generation of harmonics

To illustrate the generation of harmonics we investigated an aluminium bar with a length of 20 cm, and a width and height of 40 mm. A vertical 'surface breaking' crack is located in the centre of the top surface of the aluminium bar and is modelled as a semi-circle with radius 15 mm. Since the crack is semi-circular, its depth and half length on the surface are equal to the radius. The actual implementation of the sample in Comsol is similar to the implementation of a sample containing a delamination. First, a rectangular domain with the dimensions of the aluminium bar is constructed. Then a horizontal semi-cylinder with radius 15 mm and length 10 cm is added, so that the right surface of the semi-cylinder coincides with the right surface of the rectangular domain. Subtracting the semi-cylinder from the rectangular bar, two 'model' domains are created. Domain 1 is the remaining part of the rectangular bar and domain 2 is the semi-cylinder itself. The left surface of the semi-cylinder represents then the crack interface. The geometry is illustrated in figure 6.35.

An acoustic/ultrasonic line source was introduced in the model by implementing a particular boundary condition at the left boundary (i.e. small x-values) of the bottom surface of the aluminium bar. The excitation source considered is a continuously applied sinusoidal out-of-plane displacement at frequency $f_{exc} = 25420$ Hz for the entire duration of the simulation. Using this single frequency excitation, a typical standing wave pattern is created in the aluminium sample. As with the simulations for closed delaminations, virtual spring-damper elements are introduced between the interfaces of the crack. In order to prevent overlap between the two interfaces the spring constant k_1^* and the damping constant γ^*, both introduced in section 6.3, are chosen a bit higher than in the previous simulations, i.e. respectively equal to $5 \cdot 10^{13}$ N/m^3 and 10^8 Ns/m^3. The other parameters used in the spring forces (6.3) and damping forces (6.7) are set equal to the parameters used in the previous simulations.

In order to see if the surface breaking crack is clapping for a sufficiently high excitation amplitude, we can analyse the time signals of the in-plane x-displacements of two points on the top surface of the sample, with the first

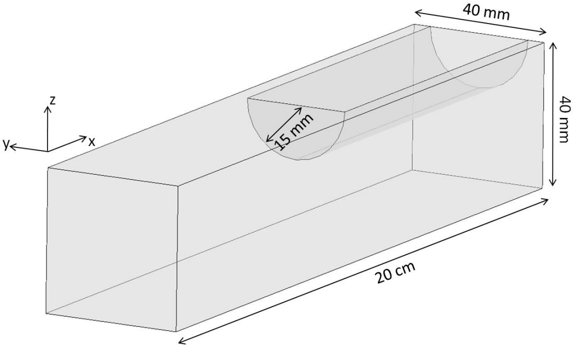

Figure 6.35: Illustration of the geometry used in the COMSOL simulation for surface breaking cracks. The model contains an aluminium bar of dimensions 20 cm × 40 mm × 40 mm and a semi-cylinder made of the same aluminium material with a radius of 15 mm and a height of 10 cm. The left surface of the semi-cylinder represents the crack interface.

point just to the right and the second point just to the left of the crack. These displacements are shown at the left hand side of figure 6.36. The full line represents the x-displacement of a point just to the right of the crack, the dotted line represents the x-displacement of a point just to the left of the crack. The displacement signals reveal that within each excitation period, the two sides of the crack move jointly for an extended period of time (closed crack) and separate for the rest of the time (open crack). This alternating clapping behaviour results in the creation of harmonics of the excitation frequency. This is indeed shown at the right hand side of figure 6.36, where the normalized frequency spectra of the x-displacements of the two points right next to the crack's interface are given. We clearly see the generation of higher harmonics at both positions.

To get an idea of all generated harmonics and not just those generated at a specific location, we studied the normalized maximum amplitude response obtained by temporally Fourier transforming the x-displacements at all positions on the top surface of the aluminium sample and identifying the maximum amplitude over this surface for each response frequency. In figure 6.37, these normalized maximum amplitude responses are displayed for a high and a low excitation amplitude. In case of a low excitation amplitude (figure 6.37(a)), the amplitude is too low to open the crack and no harmonics are generated. In case of a high excitation amplitude (figure 6.37(b)), the amplitude suffices to open the contact, resulting in the generation of harmonics of the excitation frequency (in correspondence to the results from figure 6.36).

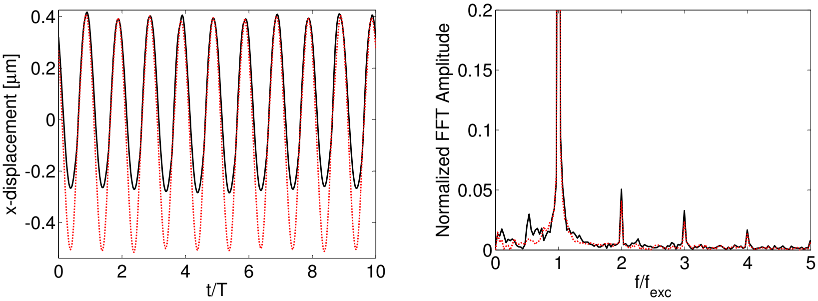

Figure 6.36: Simulation results for a 20 cm × 40 mm × 40 mm aluminium bar with a surface breaking crack. LEFT: Simulated (in-plane) x-displacement response signals at a point on the top surface of the bar just to the right of the crack (full line) and a point just to the left of the crack (dotted line). RIGHT: Simulated normalized displacement frequency spectra for a point on the top surface of the bar just to the right of the crack (full line) and a point just to the left of the crack (dotted line).

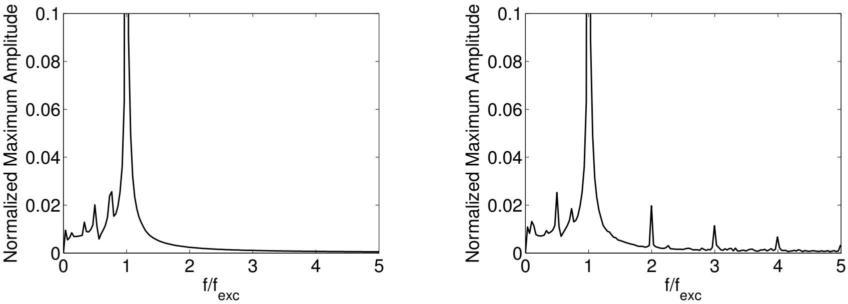

(a)

(b)

Figure 6.37: Normalized maximum amplitude response for the top surface of an aluminium bar with a surface breaking crack in case of (a) a low excitation amplitude and (b) a high excitation amplitude. The normalized maximum amplitude response was obtained by temporally Fourier transforming the x-displacements at the top surface of the aluminium sample and identifying the maximum amplitude for each response frequency.

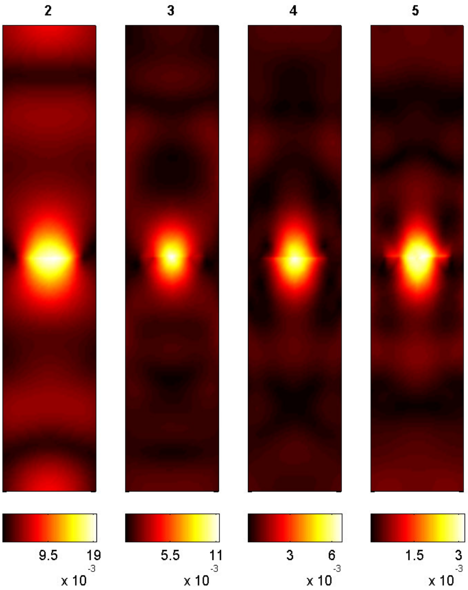

Figure 6.38: Simulated amplitude patterns for the second, third, fourth and fifth harmonic of the excitation frequency in a 20 cm × 40 mm × 40 mm aluminium bar with a surface breaking crack centred on the top surface. The amplitude patterns were obtained by temporally Fourier transforming the x-displacements at the top surface of the sample and filtering the spatially distributed response at the second, third, fourth and fifth harmonic. The colour scales are normalized according to the maximum amplitude of the x-displacements at the fundamental frequency. Low amplitudes are shown in black. The value above each figure represents the ratio f/f_{exc}.

In the case of sub-surface delaminations, we have shown that the exact position of the defects could be determined by studying the amplitude patterns of the excited harmonic frequencies. We now verify if the exact location of a surface breaking crack is also detectable using the same analysis method. Therefore, we calculated the amplitude patterns obtained by temporally Fourier transforming the x-displacements at the top surface of the sample and filtering the spatially distributed response at the second, third, fourth and fifth harmonic. The results are visualized in figure 6.38, and confirm that the highest amplitudes are indeed found around the location of the crack. The position of the crack can thus indeed be determined by a nonlinear spectroscopic analysis of the (in-plane) x-displacements, scanned over the surface of the sample.

In our setup, the crack is oriented along the y-axis, causing the interfaces of the crack to mainly move and clap in the x-direction. Therefore, until now, only the

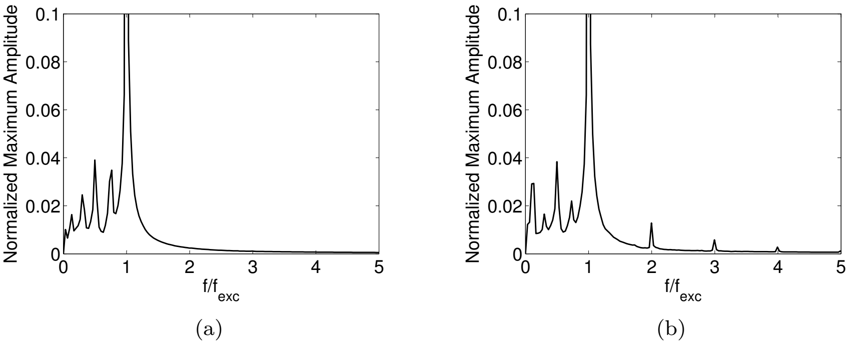

(a) (b)

Figure 6.39: Normalized maximum amplitude response for the top surface of an aluminium bar with a surface breaking crack in case of (a) a low excitation amplitude and (b) a high excitation amplitude. The normalized maximum amplitude response was obtained by temporally Fourier transforming the normal displacements at the top surface of the aluminium sample and identifying the maximum amplitude for each response frequency.

x-displacements were used to determine the harmonics generation and the exact location of the crack. Given the fact that out-of-plane displacements are generally easier to measure than the in-plane components, we also examined the possibility of detecting surface breaking cracks based on the normal displacements at the top surface. The normalized maximum amplitude (global) response of the normal displacements at the top surface is plotted in figure 6.39 in case of a low (figure 6.39(a)) and a high (figure 6.39(b)) excitation amplitude and shows evidences of a second harmonic of the excitation frequency and some very small higher harmonics if the excitation amplitude is high enough. In figure 6.40, the simulated amplitude patterns for the second, third, fourth and fifth harmonic using the normal displacements are shown. As for the x-displacements, the highest amplitudes are found in the neighbourhood of the crack, indicating that the crack can also be detected based on the normal or out-of-plane component of the displacement at the top surface.

Due to the nonlinear behaviour of a surface breaking crack at high excitation amplitudes, the use of the scaling subtraction method can again be proposed to determine the location of a crack. To illustrate this, we excite the above considered sample using a sweep signal (cfr equation (6.10)) successively with a low and a high excitation amplitude, similar to what was done for closed delaminations. In each simulation, we will determine the in-plane x-displacements and the out-of-plane normal displacements at the top surface of the sample. Subtracting the scaled local responses for the low excitation

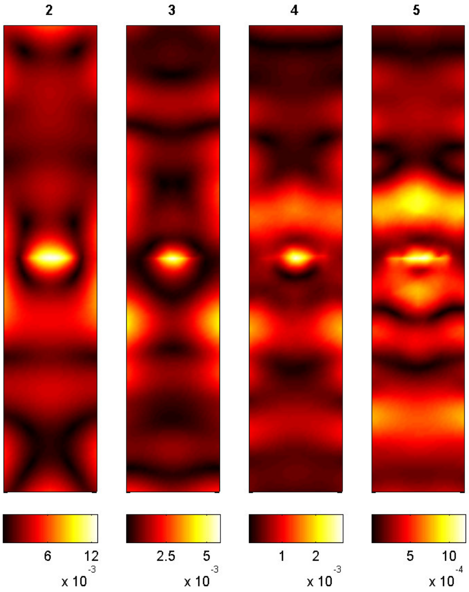

Figure 6.40: Simulated amplitude patterns for the second, third, fourth and fifth harmonic of the excitation frequency in a 20 cm × 40 mm × 40 mm aluminium bar with a surface breaking crack centred on the top surface. The amplitude patterns were obtained by temporally Fourier transforming the normal displacements at the top surface of the sample and filtering the spatially distributed response at the second, third, fourth and fifth harmonic. The colour scales are normalized according to the maximum amplitude of the normal displacements at the fundamental frequency. Low amplitudes are shown in black. The value above each figure represents the ratio f/f_{exc}.

amplitude from the results for the high excitation amplitude, the local nonlinear features resulting from the crack's behaviour can be extracted from the signals. In figure 6.41, the maximum amplitude plots of the subtracted signals are plotted in the neighbourhood of the crack. High values indicate the positions where most of the nonlinearity occurs and these positions indeed correspond to the location of the crack. The simulations imply that the resolution in the out-of-plane component is better than for the in-plane component and may be attributed to a different efficiency in radiation of the nonlinear components in both directions.

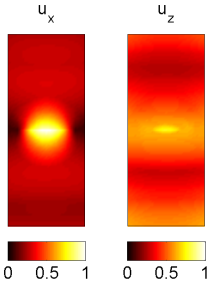

Figure 6.41: Maximum amplitude plot of the scaling subtracted tangential (u_x) and normal (u_z) displacements at the top surface of a 20 cm × 40 mm × 40 mm aluminium bar with a surface breaking crack centred on the bar. The results are plotted in the neighbourhood of the crack. High values are shown in white, low values are shown in black. The colour scale in each figure is normalized according to its maximum value.

6.6.2 Nonlinear air-coupled emission

In the above parameter study, we have clearly demonstrated that the clapping behaviour of delaminations and surface breaking cracks in materials gives rise to nonlinear features at the defect location, as has been reported in several journal papers by the group of Solodov and Busse [13, 27, 30]. In addition, Solodov et al. [28] recently demonstrated that the nonlinear vibrations cause high-frequency ultrasonic radiation into the surrounding air, which is often referred to as Nonlinear Air-Coupled Emission (NACE). In that way, NACE can be used as an alternative method to locate and visualize defects in nonlinear NDT.

In Ref. [29], Solodov and co-workers experimentally demonstrated the feasibility of NACE by nonlinear defects. To achieve this, they generated a Lamb wave at a specific frequency in a cracked rod of carbon fiber reinforced plastic (CFRP) and they investigated the airborne acoustic fields at the fundamental frequency and at some harmonics radiated by the cracked rod. Figure 6.42 shows images of the airborne acoustic fields at the fundamental frequency (figure 6.42(a)) and at its second harmonic (figure 6.42(b)). The fundamental frequency field illustrates a typical radiation pattern (slightly perturbed by the presence of the crack) observed in the air surrounding a specimen in which a leaky Lamb wave is propagating. The second harmonic field shows a typical NACE directivity pattern. Once the leaky Lamb wave propagating in the CFRP specimen encounters the surface breaking crack, the clapping phenomenon is initiated and harmonics are being generated at the defect location. The defect now behaves as a localized source of nonlinear emission and the harmonics are being radiated

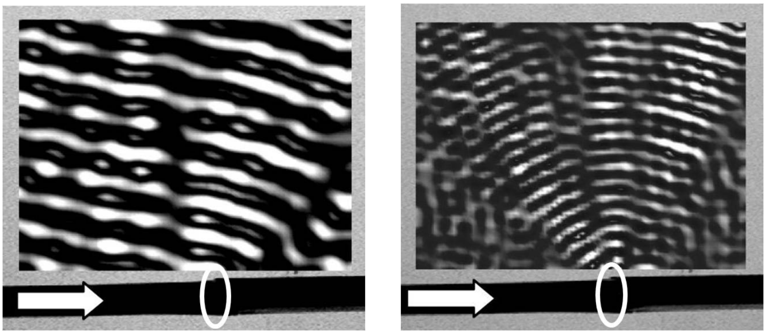

(a) (b)

Figure 6.42: Airborne field (a) at the fundamental frequency and (b) at its second harmonic radiated by a cracked CFRP specimen in which a Lamb wave is propagating from left to right (indicated by the arrow). The ellipse indicates the position of the crack. These figures are taken from Solodov et al. [29].

into the ambient air starting from the crack's position. As can be seen in the figure, no radiation is shown from outside the defect, of which the position in the plate is indicated by the white ellipse.

Using the developed finite element models, the feasibility of NACE by nonlinear defects can also be illustrated numerically by bridging the time domain solution from this chapter and the spectral solution from chapter 4. As such, we can examine the radiation patterns in air above the aluminium bar with surface breaking crack. An illustration of the geometry used for this simulation is displayed in figure 6.43. First, a standing wave at a frequency of $f_{exc} = 25420$ Hz is created in the aluminium bar (similar to the previous simulations) and the normal and x-displacements are determined on the dashed line in the centre of the top surface using the 3D time domain solution of the aluminium bar. These displacements are then temporally Fourier transformed to determine the response of both displacement components on the dashed line at a fixed response frequency. Finally, the calculated responses at a certain frequency are used as a boundary condition in the 2D spectral solution of the air above the aluminium sample allowing to determine the radiation pattern at specific frequencies.

Figure 6.44 shows images of the radiation patterns above the aluminium bar at the fundamental frequency and at its second, third and fourth harmonic. The fundamental frequency field illustrates a regular radiation pattern created by the standing wave in the aluminium bar. In this case, no evidence of the presence of a crack is found. The harmonic fields, however, show typical NACE

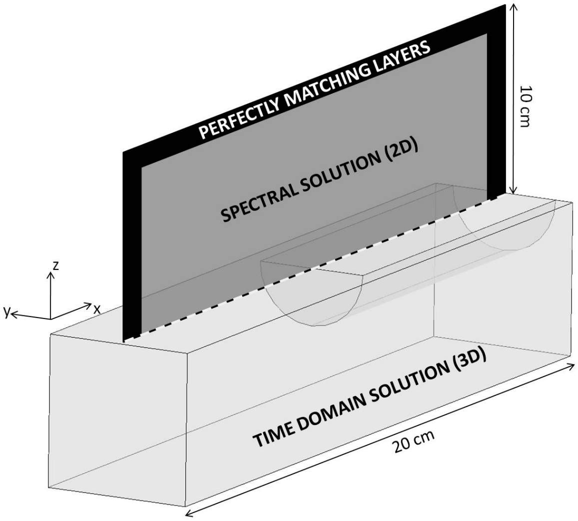

Figure 6.43: Illustration of the bridging of the time domain solution from this chapter and the spectral solution from chapter 4 in order to determine the radiation pattern in air above the aluminium bar with surface breaking crack. First, the normal and tangential displacements are determined on the dashed line. These displacements are then temporally Fourier transformed to determine the response of both displacement components on the dashed line at a fixed frequency. Finally, the response at a certain frequency is used as a boundary condition in the spectral solution to determine the radiation pattern.

radiation patterns showing radiation from the harmonics into the ambient air, starting from the position of the crack at $x = 10$ cm, and no radiation from outside the defect. Even though the setup is not completely the same as the one used in the experiments of Solodov (e.g. standing wave instead of Lamb wave), the simulations qualitatively provide similar results and therefore confirm the ability of using NACE to detect the location of surface breaking cracks.

6.7 Conclusion

A three-dimensional finite element model has been developed in order to simulate composite materials containing a single circular delamination. The model was used to obtain a better understanding and analysis of the macroscopic nonlinear behaviour that can be observed at the component level. The model makes use of local node splitting and the nonlinear behaviour of the closed delamination

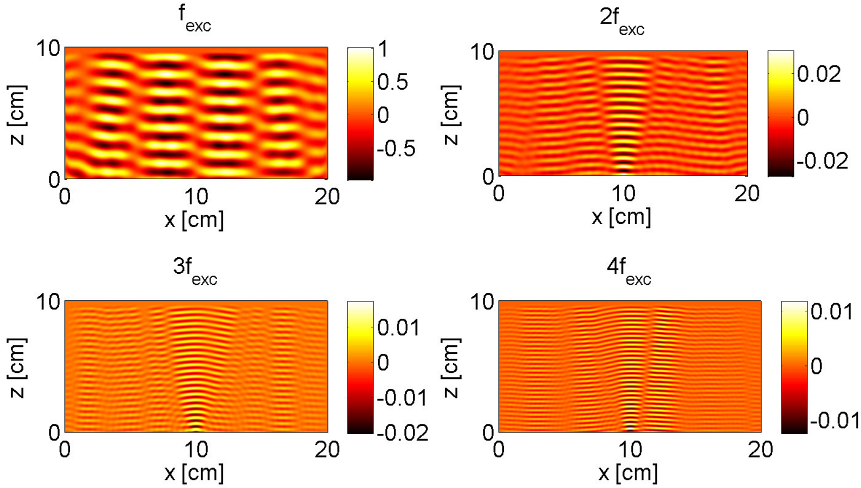

Figure 6.44: Radiation patterns in air above the aluminium bar with surface breaking crack at the fundamental frequency and at its second, third and fourth harmonic. The crack is positioned at $x = 10$ cm. The fundamental frequency field shows no evidence of the presence of the crack. The harmonic fields show radiation of the harmonics into the ambient air, starting from the crack's position.

is implemented by means of spring-damper elements with local activation thresholds at the delamination interface.

Numerical experiments were performed using the finite element simulation method to describe and interpret the clapping phenomenon that can be observed at and above the delamination interface. The model was first qualitatively validated against simulation [21] and experimental observations [12, 13, 21, 27, 30] of existing situations by showing that subharmonics and harmonics of the excitation frequency, and harmonics of the subharmonic components are generated by the delamination if the excitation amplitude is large enough to overcome the local activation thresholds.

By means of an extensive parametric study, we showed that subharmonics are efficiently excited if the delamination is close to the top surface of the sample. For delaminations deeper into the sample, only harmonics are generated. By exploiting then the flexibility of the finite element code, we also illustrated the potential to detect the shape, position, depth and orientation of a delamination by studying the amplitude patterns of the excited subharmonic and harmonic frequencies using a single frequency excitation. This method, however, has a severe drawback. If a delamination is located in a node of the wave pattern created by exciting the sample using a single frequency, it is almost impossible to detect the delamination. Therefore, an alternative method based on a sweep excitation in combination with the scaling subtraction method was proposed. It was shown that with this method, the signal-to-noise ratio of the detected nonlinear contributions can be significantly increased.

The developed model also allows to predict nonlinear spectroscopic features for composite plates containing multiple delaminations. Numerical simulations showed that all delaminations inside a composite plate can be detected using the two methods described above. Using a sweep excitation in combination with the scaling subtraction method, it is even possible to infer the different depths of the delaminations relative to each other.

In the last part of this chapter, we implemented surface breaking cracks in the described model. Numerical simulations showed that harmonics are also generated by this type of defects. Studying the amplitude patterns of the generated harmonic frequencies or using the scaling subtraction method, the exact location of the surface breaking crack can be detected. We also demonstrated that the harmonics generated by the surface breaking crack are being radiated into the ambient air, starting from the position of the crack.

Further advancements to improve the interpretation should consist in studying the eigenmode pattern of the membrane above the delamination, and in further examining the radiation patterns in air above different types of surface breaking cracks and delaminations. As always, the goal of these numerical studies is to help optimizing acoustic and ultrasonic techniques and experiments for applications in non-destructive testing.

Bibliography

[1] *COMSOL Multiphysics, Structural Mechanics Module, User's Guide, Version 3.3*, 2006.

[2] *COMSOL Multiphysics User's Guide, Version 3.3*, 2006.

[3] Antonaci, P., Bocca, P., Bruno, C., Gliozzi, A., and Scalerandi, M. Non destructive characterization of concrete joints using the scaling subtraction method. *Key Eng. Mat. 417-418* (2010), 41–44.

[4] Antonaci, P., Bruno, C., Bocca, P., Scalerandi, M., and Gliozzi, A. Nonlinear ultrasonic evaluation of load effects on discontinuities in concrete. *Cement Concrete Res. 40* (2010), 340–346.

[5] Antonaci, P., Bruno, C., Gliozzi, A., and Scalerandi, M. Evolution of damage-induced nonlinearity in proximity of discontinuities in concrete. *Int. J. Solids Struct. 47* (2010), 1603–1610.

[6] Antonaci, P., Bruno, C., Gliozzi, A., and Scalerandi, M. Monitoring evolution of compressive damage in concrete with linear and nonlinear ultrasonic methods. *Cement Concrete Res. 40* (2010), 1106–1113.

[7] Bruno, C., Antonaci, P., Bocca, P., Gliozzi, A., and Scalerandi, M. Linking elastic nonlinearity and cracks growth in mortar samples. *Key Eng. Mat. 417-418* (2010), 293–296.

[8] Bruno, C., Gliozzi, A., Scalerandi, M., and Antonaci, P. Analysis of elastic nonlinearity using the scaling subtraction method. *Phys. Rev. B. 79* (2009).

[9] Delrue, S., and Van Den Abeele, K. Finite element simulations of contact acoustic nonlinearities (CANs). In *Proceedings of the 5th International Conference on Emerging Technologies in Non-Destructive Testing* (Ioannina, September 2011).

[10] Delrue, S., and Van Den Abeele, K. Three-dimensional finite element simulation of closed delaminations in composite materials. *Ultrasonics 52* (2011), 315–324.

[11] Guyer, R., and Johnson, P. *Nonlinear Mesoscopic Elasticity : The Complex Behaviour of Granular Media Including Rocks and Soil.* Wiley-VCH, 2009.

[12] Korshak, B., Solodov, I., and Ballad, E. DC effects, sub-harmonics, stochasticity and "memory" for contact acoustic non-linearity. *Ultrasonics 40* (2002), 707–713.

[13] Krohn, N., Stoessel, R., and Busse, G. Acoustic non-linearity for defect selective imaging. *Ultrasonics 40* (2002), 633–637.

[14] Müller, I. Clapping in delaminated sandwich-beams due to forced oscillations. *Comput. Mech. 39* (2007), 113–126.

[15] Müller, I., Konyukhov, A., Vielsack, P., and Schweizerhof, K. Parameter estimation for finite element analyses of stationary oscillations of a vibro-impacting system. *Eng. Struct. 27* (2005), 191–201.

[16] Ohara, Y., Endo, H., Hashimoto, Y., Shintaku, Y., and Yamanaka, K. Monitoring growth of closed fatigue crack using subharmonic phased array. *Review of Quantitative Nondestructive Evaluation 29* (2010), 903–909.

[17] Ohara, Y., Endo, H., Mihara, T., and Yamanaka, K. Ultrasonic measurement of closed stress corrosion crack depth using subharmonic phased array. *Jpn. J. Appl. Phys. 48* (2009).

[18] Ohara, Y., Mihara, T., Sasaki, R., Ogata, T., Yamamoto, S., Kishimoto, Y., and Yamanaka, K. Imaging of closed cracks using nonlinear response of elastic waves at subharmonic frequency. *Appl. Phys. Lett. 90* (2007).

[19] Ohara, Y., Yamamoto, S., Mihara, T., and Yamanaka, K. Ultrasonic evaluation of closed cracks using subharmonic phased array. *Jpn. J. Appl. Phys. 47* (2008), 3908–3915.

[20] Sarens, B., Kalogiannakis, G., and Glorieux, C. Full-field imaging of nonclassical acoustic nonlinearity. *Appl. Phys. Lett. 91* (2007).

[21] Sarens, B., Verstraeten, B., Glorieux, C., Kalogiannakis, G., and Van Hemelrijck, D. Investigation of contact acoustic nonlinearity in delaminations by shearographic imaging, laser doppler vibrometric scanning and finite difference modeling. *IEEE T. Ultrason. Ferr. 57* (2010), 1383–1395.

[22] Scalerandi, M., Gliozzi, A., Antonaci, P., Bruno, C., and Bocca, P. Elastic conditioning, memory and relaxation induced by the presence of cracks in concrete. *Key Eng. Mat. 417-418* (2010), 253–256.

[23] Scalerandi, M., Gliozzi, A., Bruno, C., Masera, D., and Bocca, P. A scaling method to enhance detection of a nonlinear elastic response. *Appl. Phys. Lett. 92* (2008).

[24] Scalerandi, M., Gliozzi, A., Bruno, C., and Van Den Abeele, K. Nonlinear acoustic time reversal imaging using the scaling subtraction method. *J. Phys. D. Appl. Phys. 41* (2008).

[25] Shkerdin, G., and Glorieux, C. Lamb mode conversion in a plate with a delamination. *J. Acoust. Soc. Am. 116* (2004), 2089–2100.

[26] Shkerdin, G., and Glorieux, C. Lamb mode conversion in an absorptive bi-layer with a delamination. *J. Acoust. Soc. Am. 118* (2005), 2253–2264.

[27] Solodov, I. Ultrasonics of non-linear contacts: propagation, reflection and NDE-applications. *Ultrasonics 36* (1998), 383–390.

[28] Solodov, I., and Busse, G. Nonlinear air-coupled emission: The signature to reveal and image microdamage in solid materials. *Appl. Phys. Lett. 91* (2007), 251910.

[29] Solodov, I., Döring, D., and Busse, G. Air-coupled vibrometry for measurements in classical and nonclassical nonlinear acoustics. In *Proceedings of the XIV International Conference on Nonlinear Elasticity in Materials* (Lisbon, June 2009).

[30] Solodov, I., Krohn, N., and Busse, G. CAN: an example of nonclassical acoustic nonlinearity in solids. *Ultrasonics 40* (2002), 621–625.

[31] Van Den Abeele, K., Carmeliet, J., Ten Cate, J., and Johnson, P. Nonlinear elastic wave spectroscopy (NEWS) techniques to discern material damage, Part II: Single-mode nonlinear resonance acoustic spectroscopy. *Res. Nondestruct. Eval. 12* (2000), 31–42.

[32] Van Den Abeele, K., Johnson, P., and Sutin, A. Nonlinear elastic wave spectroscopy (NEWS) techniques to discern material damage, Part I: Nonlinear wave modulation spectroscopy (NWMS). *Res. Nondestruct. Eval. 12* (2000), 17–30.

[33] Yamanaka, K., Mihara, T., and Tsuji, T. Evaluation of closed cracks by model analysis of subharmonic ultrasound. *Jpn. J. Appl. Phys. 43* (2004), 3082–3087.

[34] Yamanaka, K., and Ohara, Y. Selectivity enhancement of subharmonic phased array for crack evaluation (SPACE). *Review of Quantitative Nondestructive Evaluation 28* (2009), 824–831.

[35] Zak, A., Krawczuk, M., and Ostachowicz, W. Vibration of a laminated composite plate with closing delamination. *J. Intel. Mat. Syst. Str. 12* (2001), 545–551.

Chapter 7

Conclusion

As mentioned in the introduction of this work, the main goal of the thesis was to develop numerical simulation tools for the description of elastic wave propagation phenomena in view of an optimization of quantitative ultrasonic NDT techniques. In this work we particularly focused on NCU and NEWS techniques to support the qualitative process of gathering observable facts concerning wave propagation in solid materials and we assisted in the design and testing of localization using TRA. Due to the improvement of commercially available software tools in the last few years, one of these software packages, COMSOL Multiphysics, was used for the numerical simulations.

In this chapter, the main conclusions of the individual chapters concerning air-coupled ultrasonic non-destructive testing, time reversed acoustics and nonlinear ultrasonic spectroscopy of delaminations and cracks are summarized and we elaborate on suggestions for further research.

7.1 Air-coupled ultrasonic non-destructive testing

In the introduction we pointed out the high need for a more practical realization of ultrasonic techniques. A significant step in that direction can be achieved by avoiding contact fluids between the transducer and the material to be tested, as is the case in air-coupled non-destructive testing.

In chapter 4, several air-coupled experiments were simulated using two distinctive methods. The first simulation is based on a ray tracing (shadow) method approach. This method entails serious simplifications as divergence, diffraction, scattering and any other frequency dependent effects are not taken into account. However, for the simplest experiments discussed in chapter 4, the method leads to a good qualitative interpretation of the experimental results. The second method uses a spectral solution with addition of perfectly matching layers and has been implemented in Comsol Multiphysics. This method aims to be much closer to a description of the reality, as the geometry includes reflection, mode conversion, frequency effects, plate resonance distributions, etc.

Various cases of air-coupled inspection of materials were modelled. The first case consists of air-coupled single-sided pitch-catch inspection of an aluminium bar with a circular borehole. In this setup, transmitter and receiver are both positioned at oblique angles at the same side of the test object. We have shown that the simulation results are in qualitative good agreement with the observations implying that both simulation methods can be beneficial for the interpretation of air-coupled experiments and for the prediction of the effects of experimental parameters which are hard to vary in real conditions. In this respect, we studied the effect of changing the vertical position of a circular defect, we elaborated on the danger of using pure Lamb waves and we studied the influence of the orientation of a rectangular inclusion.

Due to the fact that the finite element model gives rise to more realistic simulations with respect to the shadow method, the first model has also been used for the implementation of more complex problems. We considered two particular examples (plate with varying thickness and LED-rail) and proposed air-coupled ultrasonic techniques for the non-destructive testing of both samples. The results of the finite element model may help in guiding the design, further development and optimization of these inspection methods.

7.2 Time reversed acoustics

Besides the detection of defects using for example air-coupled ultrasonic NDT, there is also a high need for localization schemes for quantitative material and defect characterization. In this work we studied in particular the time reversal technique, with the goal to enhance its potential. In this technique, a recording signal is re-emitted in a sample in a time reversed fashion to focus back in space and time to the source or to scatterers acting as sources, enabling to find the exact location of the defects.

In chapter 5 we focused on the investigation of one particular TR technique: single-channel reciprocal TR. To demonstrate the feasibility and usefulness of this technique we adapted and extended the finite element model that was initially developed for the simulation of air-coupled experiments. Using the finite element model, we provided numerical supporting evidence of the ability of single-channel reciprocal TR to focus energy in a multi-reverberant solid medium. Different situations were studied, illustrating multi-component TR and TR in multiple points.

In order to allow single-channel reciprocal TR focusing in non-reverberant samples, we investigated a technique using a chaotic cavity transducer, which consists of a transducer glued on a cavity of chaotic shape. This technique was initially introduced for imaging in fluids, but we extended it to applications dealing with elastic waves in solids. We were able to show that, due to the large number of reflections inside the chaotic cavity, a nice quality focus can be obtained in non-reverberant samples.

Furthermore, our numerical simulations demonstrated that chaotic cavity transducers allow to create a virtual transducer array with only one transducer, enabling to focus in an arbitrary point of a medium by applying specific time delays to the different elements of the virtual array. In particular, we illustrated multi-component TR in a non-reverberant medium by using a virtual phased array. In a 2D solid material, TR focusing along the horizontal (vertical) displacement component is achieved if the time delays are determined using the transversal (longitudinal) wave velocity. For 3D solid materials, the proper choice of time delays becomes more complicated. The wave speed distribution in the sample needs to be known exactly, in order to calculate the time shifts of the different signals.

7.3 Nonlinear ultrasonic spectroscopy of delaminations and cracks

Again referring to the introduction, conventional ultrasonic NDT techniques are normally based on reflection, diffraction and scattering of acoustic waves by defects (e.g. air-coupled experiments discussed in chapter 4). For incipient damage in the form of delaminations and cracks, traditional linear ultrasonic techniques fail to detect the defect and new techniques with a more sensitive detection of performance degradation are required.

In chapter 6 we developed and investigated the results of a finite element time domain model for the nonlinear ultrasonic spectroscopy of delaminations and cracks. The model makes use of local node splitting at the defect's interface and the nonlinear constitutive behaviour of the defect is implemented by means of spring-damper elements with local activation thresholds at the delamination interface.

We first studied the behaviour of a delamination in a composite material. We showed that clapping phenomena can be observed at and above the delamination interface, resulting in the generation of harmonics and subharmonics of the excitation frequency. An extensive parametric study illustrated the potential to detect the shape, position, depth and orientation of one or multiple delaminations by studying the amplitude patterns of the generated subharmonic and harmonic frequencies in the surface scan response signals using a single frequency excitation. To increase the signal-to-noise ratio of the detected nonlinear contributions we proposed an alternative method using a sweep excitation in combination with the scaling subtraction method. The latter method showed better and dependable results in all exemplary cases that were considered.

We also demonstrated that surface breaking cracks can be easily implemented in the described model. It was shown that these defects behave in a similar way to the delaminations and, as a consequence, the same detection and localization techniques can be utilized. Using a bridging of the different developed finite element models (spectral solution and time domain solution) we were able to illustrate that the nonlinear vibration of a surface breaking crack causes radiation of harmonics into the surrounding air.

7.4 Suggestions for future research

The research work described in a doctoral thesis is never fully finished. Solutions to initial problems always suggest further developments, enhancements and new problems. This is not different in the case of the work presented here. We conclude the manuscript by suggesting a few extensions of our work, without being exclusive.

First, the developed numerical simulation models can be used for the implementation of a variety of other and more complex situations. As an example, we already modelled two such cases (plate with a section of varying thickness and LED-rail) related to air-coupled ultrasonic inspection of materials. However, there are also various possibilities concerning TRA (e.g. embedded chaotic cavities, 3D simulations, etc.) and NEWS experiments (e.g. different delamination and crack shapes and positions, spatially dependent spring constants in the spring-damper elements, etc.). The obtained results on the NCU examples testify that complex problems lead to complex interpretations, and that a realistic numerical model is essential in the interpretation of the experimental observations, and in the guidance of an appropriate experimental design.

Second, a bridging between the developed models in all chapters needs to be investigated. Doing so, we could, for instance, model the detection of nonlinear defects using air-coupled techniques (e.g. using NACE), implement air-coupled time reversal techniques, use time reversal to focus energy on clapping delaminations and cracks, etc. However, in order to apply the finite element frequency domain model from chapters 4 and 5 with nonlinear defects, we will have to transform all equations (adapted for the use of PMLs) back to the time domain. A first attempt to do this in COMSOL failed as we encountered an instability in the code. Further investigation is needed.

Third, based on the potential of the simulation methods, the new NDT techniques should be introduced to various industrial partners and companies to perform feasibility studies for the implementation of the proposed technologies on realistic test cases. Direct contacts with end-users of NDT technologies can lead to a further development and optimizing of several NDT techniques.

Curriculum vitae

Personal data

Name: Delrue
First name: Steven
Adress: Forestiersstraat 31, 8530 Harelbeke, Belgium
Nationality: Belgian
Date of birth: June 22, 1985
Place of birth: Waregem, Belgium

Education

- **1997-2003:** Secondary school: Sciences-Mathematics (8h) at Sint-Jan Berchmanscollege, Avelgem, Belgium
- **2003-2005:** Candidate in mathematics, Catholic University of Leuven campus Kortrijk, Belgium
- **2005-2007:** Master in mathematics, Catholic University of Leuven, Belgium
- **July 2007:** Degree in mathematics (with great distinction), Catholic University of Leuven, Belgium
  Master thesis (dutch): *Granulatie in rode reuzen.* Promotor: J. De Ridder.
- **February 2008:** Aggregated for teaching mathematics in secondary education (with distinction), Catholic University of Leuven, Belgium
- **2007-2011:** PhD student at wave propagation and signal processing research group, Catholic University of Leuven campus Kortrijk, Belgium

List of publications

Publications in internationally reviewed scientific journals

Delrue, S., Van Den Abeele, K., Blomme, E., Deveugele, J., Lust, P. and Bou Matar, O. Two-dimensional simulation of the single-sided air-coupled ultrasonic pitch-catch technique for non-destructive testing. *Ultrasonics 50* (2010), 188-196.

Delrue, S. and Van Den Abeele, K. Three-dimensional finite element simulation of closed delaminations in composite materials. *Ultrasonics 52* (2011), 315-324.

Publications at international conferences and symposia

Bou Matar, O., Li, Y., Delrue, S. and Van Den Abeele, K. Optimization of chaotic cavity transducers to nonlinear elastic imaging. In *Proceedings of the 10th French Congress on Acoustics* (Lyon, April 2010).

Delrue, S. and Van Den Abeele, K. Finite element simulations of contact acoustic nonlinearities (CANs). In *Proceedings of the 5th International Conference on Emerging Technologies in Non-Destructive Testing* (Ioannina, September 2011).

Communications at international conferences and symposia

Geeraert, M., Janssen, E., Delrue, S., Bou Matar, O., Blomme, E., De Gersem, H. and Van Den Abeele, K. Simulations of nonlinear ultrasonic NDT of plate-like structures. Oral presentation at *XIII International Conference on Nonlinear Elasticity in Materials, Aix-en-Provence, France* (June 22-27, 2008).

Delrue, S., Van Den Abeele, K., Blomme, E., Deveugele, J., Lust, P. and Bou Matar, O. Single-sided air-coupled ultrasonic NDT of thick plates. Oral presentation at *Acoustics'08, Paris, France* (June 29-July 4, 2008).

Geeraert, M., Janssen, E., Delrue, S., Bou Matar, O., Blomme, E., De Gersem, H. and Van Den Abeele, K. Simulations of nonlinear ultrasonic NDT of plate-like structures. Oral presentation at *Acoustics'08, Paris, France* (June 29-July 4, 2008).

Li, Y., Bou Matar, O., Delrue, S. and Van Den Abeele, K. Optimization of chaotic cavities transducers for time reversal nonlinear elastic wave spectroscopy. Oral presentation at *International Conference on Ultrasound ICU2009, Santiago, Chile* (January 11-17, 2009).

Delrue, S., Van Den Abeele, K., Blomme, E., Lust, P. and Bou Matar, O. Simulation for optimization of air-coupled ultrasonic nondestructive testing in plates with defects. Oral presentation at *International Conference on Ultrasound, Santiago, Chile* (January 11-17, 2009).

Bou Matar, O., Li, Y., Van Den Abeele, K. and Delrue, S. Nonlinear elastic imaging with a chaotic cavity transducer. Oral presentation at *XIV International Conference on Nonlinear Elasticity in Materials, Lisbon, Portugal* (June 1-5, 2009).

Delrue, S. and Van Den Abeele, K. Nonlinear finite element simulation of closed delaminations in composite materials. Oral presentation at *10th French Congress of Acoustics, Lyon, France* (April 12-16, 2010).

Bou Matar, O., Delrue, S. and Van Den Abeele, K. Optimization of chaotic cavity transducers to nonlinear elastic imaging. Oral presentation at *10th French Congress of Acoustics, Lyon, France* (April 12-16, 2010).

Delrue, S. and Van Den Abeele, K. Finite difference simulations of closed delaminations in composite materials. Oral presentation at *XV International Conference on Nonlinear Elasticity in Materials, Otranto, Italy* (July 4-11, 2010).

Van Damme, B., Delrue, S., Van Den Abeele, K. and Bou Matar, O. Time reversal in media with high damping using a chaotic cavity - Simulations and experiments. Oral presentation at *XV International Conference on Nonlinear Elasticity in Materials, Otranto, Italy* (July 4-11, 2010).

Delrue, S. and Van Den Abeele, K. A simulation study of contact acoustic nonlinearity (CAN). Oral presentation at *XVI International Conference on Nonlinear Elasticity in Materials, Prague, Czech Republic* (June 5-11, 2011).

Delrue, S. and Van Den Abeele, K. Finite element simulations of contact acoustic nonlinearities (CAN). Oral presentation at *5th International Conference on Emerging Technologies in NDT, Ioannina, Greece* (September 19-21, 2011).

Communications at other conferences and symposia

Delrue, S., Van Den Abeele, K., Blomme, E., Deveugele, J., Lust, P. and Bou Matar, O. Single-sided air-coupled ultrasonic NDT of thick plates. Poster presentation at *Research Meeting KUL Association WEST, Kortrijk, Belgium* (October 25, 2008).

Delrue, S., Van Den Abeele, K., Blomme, E., Deveugele, J., Lust, P. and Bou Matar, O. Simulations for ultrasonic non-destructive testing. Poster presentation at *Research Day KULAK, Kortrijk, Belgium* (February 24, 2011).

Blomme, E., Bilcke, M., Calu, G., Lust, P., Naert, H., Verslype, S., Vandenbussche, J., Loret, F., De Craemer, R., Delrue, S. and Van Den Abeele, K. Air-coupled ultrasonic NDT. Poster presentation at *Aircraft Integrated Structural Health Assessment II (AISHA II) Open Project Meeting, Leuven, Belgium* (October 28, 2011).

Arenberg Doctoral School of Science, Engineering & Technology
K.U.Leuven Kulak
Subfaculty of Science
Wave Propagation and Signal Processing Research Group
E. Sabbelaan 53
B-8500 Kortrijk

KATHOLIEKE UNIVERSITEIT
LEUVEN

ASSOCIATIE K.U.LEUVEN